Functional Nano-Structures Using Atomic Layer Deposition

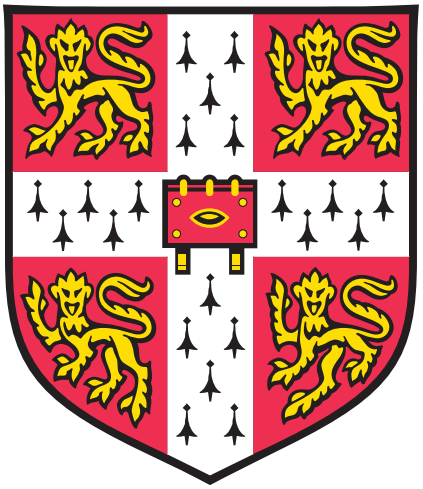

Pedro Manuel Salgård Cunha

A dissertation submitted for the degree of Doctor of Philosophy
August 2013

University of Cambridge
Department of Physics
Cavendish Laboratory
Trinity College

Dedicated to my father

Dedikerad till pappa

Declaration

This dissertation is the result of my own work and includes nothing which is the outcome of work done in collaboration except where specifically indicated in the text. I declare that no part of this work has been submitted for a degree or any other qualification at this or any other university. This dissertation does not exceed the word limit of 60,000 words set by the Physics and Chemistry Degree Committee.

Cambridge, August 2013

Pedro M. Salgård Cunha

Acknowledgements

This thesis is the result of work carried out between October 2009 and August 2013 with the Thin Films and Interfaces Group at the Cavendish Laboratory, Cambridge UK. The completion of this thesis has only been possible with the help of numerous people, and thanks to the finanical support provided by the UK Engineering and Physical Sciences Research Council and Trinity College.

I would like to start by thanking my supervisor Prof. Dr. Ullrich Steiner for giving me the opportunity to carry out my PhD in an excellent research environment. His support, enthusiasm and wealth of knowledge have guided me throughout this research. I would also like to thank Ulli for allowing me to pursue my Atlantic crossing as well as providing me with extra financial support when I really needed it.

My next thanks go to the members of the Thin Films and Interfaces Group both past and present for their support and friendship over the last seven years. Special thanks go to Sven Hüttner, Silvia Vignolini, Nataliya Yufa, Mathias Kolle and Ed Crossland for their invaluable help and companionship.

My thanks also to a number of people for their help with measurements and characterisations. Cate Ducati and JJ for TEM imaging, Yana Vaynzof for XPS measurements, Alessandro Sepe for scattering measurements and Kevin Musselman for valuable discussions.

I would like to express my gratitude to the support staff of the Biological and Soft Systems Sector and the Cambridge Nanoscience Centre, in particular Suresh Mistry, Pete Bone, Owen Dunn, Ian Ganney, Sue Murkett, Sue Gymer and Tom Mitchell. Special thanks go to Tom for his extensive knowledge and for making the many hours spent in the cleanroom more enjoyable. I also wish to thank Prof. Sir Mark Welland for allowing me access to the office and facilities of the Nanoscience Centre and Dr. Sachiko Kusukawa for her continued support during my time at Trinity College.

An extra large thank you to Maik Scherer. Not only for being a very good friend but also for making the PhD much more enjoyable through a number of fruitful collaborations and daily discussions.

To my parents for always being there for me. Thank you for encouraging me in all my endeavours and for your constant support and love. To Emma, the love of my life, for being there by my side throughout this journey.

Abstract

Functional Nano-Structures Using Atomic Layer Deposition

Pedro M. Salgård Cunha

This thesis is a study of the crossover between the fields of atomic layer deposition, block copolymer self-assembly and photovoltaics. The central research question is how the technique of atomic layer deposition (ALD) can be incorporated into the creation of nano-structured functional materials and devices, specifically in the areas of photovoltaics and biomimetics.

The work aims to explore the capabilities of ALD as a strategy for overcoming two main challenges: the creation of extremely thin conformal metal oxide layers and the replication of complex high surface area templates. In these areas of fabrication on the nano-scale, ALD has consistently been shown to achieve more conformal depositions of higher quality and with greater thickness control than other thin film experimental techniques.

Rather than understanding these challenges in their narrowest sense, the thesis seeks to explore the full range of possibilities inherent to the ALD process for a number of quite different applications, all of which are linked by their reliance on self-assembled templates or the creation of functional photovoltaic structures.

The thesis begins by providing three background chapters. *Chapter 1* covers photovoltaics, with an emphasis on liquid and solid-state electrolyte dye-sensitised solar cells. *Chapter 2* is concerned with the self-assembly of microphase separating diblock copolymers and covers the special case of the gyroid morphology which is utilised extensively in the thesis. *Chapter 3* describes the ALD technique. It deals with the physical and chemical underpinnings of this process, as well as its application for the coating of non-ideal substrates such as polymeric and high-aspect-ratio structures. *Chapter 4* then introduces the key experimental techniques and methods utilised throughout the research.

These introductory sections serve as the foundation for the four major experimental chapters of the thesis. *Chapter 5* reports on the formation of gyroid-structured core-shell $Cu/Cu_2O/CuO$ solar cells via the post-deposition thermal oxidation of electrodeposited copper. *Chapter 6* deals with the replication of gyroid-structured polystyrene templates using metal oxides deposited via ALD, for use in dye-sensitised solar cells. The chapter presents a novel ozone-based functionalisation scheme which overcomes the inherent difficulty of ALD nucleation on polymer surfaces.

Chapter 7 covers two projects which are ongoing. One is focused on the application of ALD for the deposition of metal sulphides, and primarily describes the safety and experimental considerations for the installation of H_2S as the sulphur source for this process. The other is concerned with the deposition of ultra-thin titania compact layers for dye-sensitised solar cells using ALD. *Chapter 8* reports on the use of ALD in the biomimetic replication of the spectral response of the wing scales of the *Papilio Blumei* butterfly.

Contents

1 Introduction

One of the most fundamental technological challenges which has appeared over the last three decades is the supply and demand of energy. The world's energy usage has risen steeply in this period with an increase of 39 % since 1990 to a total energy usage of 142 000 TW h in 2008. The general increase in energy usage in the western world is compounded by a significant financial expansion in Africa and Asia, especially in China and the Middle East, which have seen an increase in energy usage of 146 % and 170 % respectively since 1990, compared to 20 % and 7 % for the USA and the European Union over the same time period. The world's energy usage is expected to continue to rise at an increasing rate to a predicted usage of 327 000 TW h by 2050.

A significant fraction of the energy, about 87 %, is currently supplied by fossil and nuclear fuels. Besides the environmental impact of the use of fossil fuels and the inherent issues of long-term storage and processing of nuclear waste, the main argument for moving away from these energy sources is the limitation of available resources. The total remaining energy from fossil fuels is estimated to be 4×10^{22} J, with the majority of these fuels being expensive and difficult to extract. The equivalent amount of nuclear fuels assuming current reactor configurations is estimated to be 2×10^{22} J. This should be compared to the total influx of energy from the sun which is approximately $3 \times 10^{24}\,\mathrm{J\,yr^{-1}}$. Even though it is not possible to capture most of this incident irradiation, collection of about 0.02 % would be sufficient to cover the earth's current energy need.

Driven by this requirement for alternatives to fossil and nuclear fuels, significant research efforts have been made over the last two decades to develop new systems for renewable energy. Together with geothermal energy, solar energy is one of the few renewable energy sources that can have a significant impact on the world's energy supply in the foreseeable future. However solar energy has two main drawbacks: cost and raw material for the fabrication. The main type of solar cell used today is the monocrystalline silicon solar cell. Although these solar cells are capable of converting 15 % to 20 % of the incident solar light on a modular level, the production costs are considered relatively high. The use of silicon and other materials such as silver for electrical contacts also imposes limits on their future use due tp the limited amount of these resources available on earth. As such a large portion of photovoltaic (PV) research has shifted to solar cell technologies that have intrinsically lower maximum efficiencies but also have much lower predicted production costs. Two of these emerging technologies are organic photovoltaics (OPV) and organic/inorganic hybrid photovoltaics such as the dye-sensitised solar cell. Both of these solar cell types benefit hugely from an increased internal surface area, which enhances light absorption and therefore power conversion efficiencies.

A high surface area can be achieved by structuring the active material on the nanometre length scale. Nano-structuring can also lead to new, interesting material properties and physical effects which stem from the accessibility of both the bulk and the surface of

the active material. The main route currently used for the fabrication of well-defined structures on the nano-scale relies on the use of a number of lithographic techniques such as electron-beam, x-ray and deep ultra-violet lithography and nano-imprint lithography [1, 2]. These fabrication techniques are all top-down approaches which have a number of drawbacks such as extended fabrication times, the requirement for expensive fabrication equipment, and limitations in resolution. Moreover these techniques are not well-adapted for the fabrication of complicated, for example three-dimensional, structures. Recently bottom-up fabrication protocols have been developed which overcome the problems outline above. In general these protocols rely on self-assembly, which removes the need for an expensive external experimental setup.

From the large range of fabrication routes that employ self-assembly to achieve nano-structuring, it is possible to define three categories. The first category involves routes that rely on the fine-tuning of experimental parameters, either extrinsic parameters such as deposition conditions or intrinsic parameters such as material composition, to achieve self-assembly of the active material itself. Although a number of materials display this type of self-assembly into for example nano-wires and nano-tubes [3, 4] they have limited applicability in industry. One exception are conjugated semiconducting polymers which have shown promise in roll-to-roll processing [5, 6]. The second approach utilises non-functional materials, such as copolymers, as structure-directing agents, to pattern one or more functional materials. For copolymers this is normally achieved by selective swelling of the copolymer blocks with for example nanoparticles. The main limitation of this fabrication route is the increasing number of degrees of freedom with increasing number of components which can make control of the final nanoscale structure difficult [7, 8].

The third and final approach utilises the self-assembly of templates and their subsequent replication with the active material. The main advantage of this approach is the separation of the fabrication route into a template step and a replication step which allows the self-assembly of the template and the fabrication of the active material to be optimised separately. Given the separation of the template fabrication and the replication a range of different replication techniques can be used, including electrochemistry, sol-gel and atomic layer deposition. One particular set of self-assembled templates that has shown promise is the voided diblock copolymer template. Once the copolymer has been allowed to reach its equilibrium morphology, the porous template is formed by selective removal of one of the blocks. Of the diblock copolymer morphologies the double-gyroid phase shows the most promise since both blocks are continuous, allowing the formation of a self-supportive scaffold of an active material with a high specific surface area and a narrow pore distribution. A schematic of a generalised fabrication route employing a block copolymer template with the gyroid morphology is shown in Figure 1.1.

With decreasing feature sizes of fabricated nano-structures, as well as increasing aspect ratios, stricter requirements are placed upon experimental processes, especially thin film techniques, in terms of conformity and thickness control. One technique that has been shown to cope well with these increasingly stringent requirements is atomic layer deposition (ALD). Since it relies on substrate/gas phase interactions it allows

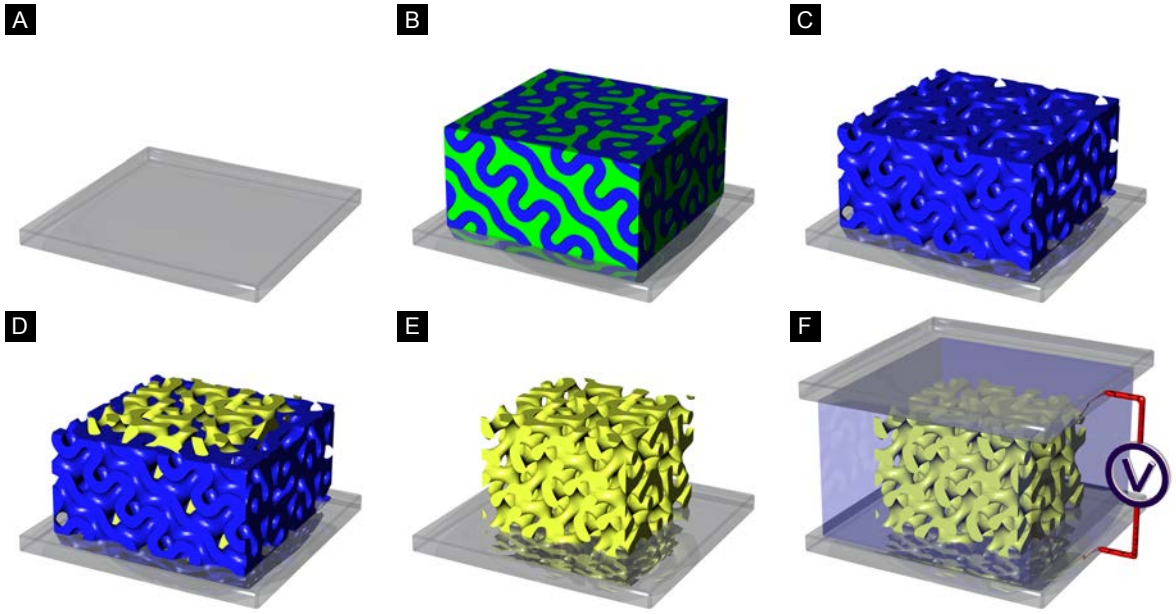

Figure 1.1: Generic fabrication route using diblock copolymer templates which display the double-gyroid morphology. **(A)** Functionalisation of the substrate using for example piranha etching and silinisation. **(B)** Spin-coating and thermal annealing of thin block copolymer film to reach the equilibrium double-gyroid morphology. **(C)** Removal of the minority phase to produce a porous template. **(D)** Replication of the template using for example electrochemical or atomic layer deposition. **(E)** Removal of the polymeric template and post-processing of the replica including thermal treatments. **(F)** Assembly of the double-gyroid-structured replica into a functional nano-structured device.

for high conformality even on high-aspect-ratio samples with complicated geometries whilst maintaining a sub-nanometre thickness resolution.

This thesis aims to study the interplay between these three areas: photovoltaics, block copolymer templates and atomic layer deposition. The thesis will begin by giving an overview of the field of photovoltaics or solar cells in *Chapter 2*. The working principles of a traditional silicon solar cell will be described as well as the concept of hybrid solar cells which are the main focus of this thesis. Particular emphasis is given to the dye-sensitised solar cell (DSSC). The theoretical framework for the self-assembly of covalently bonded diblock copolymers, which are used as templates for the main two studies in this thesis, will be outlined in *Chapter 3*. The chapter will also describe the nano-scale morphologies adopted by equilibrium diblock copolymers with focus on the tri-continuous double-gyroid morphology. Given that atomic layer deposition is used to a varying degree in every chapter in this thesis, *Chapter 4* has been dedicated to this experimental technique. As well as the working principles of ALD, its uses within the field of solar cells will be highlighted. ALD growth on non-ideal substrates and under non-ideal conditions, such as high-aspect-ratio polymeric templates and low deposition temperatures, features frequently in this thesis and as such the current

understanding of ALD growth under these conditions will be described. *Chapter 5* covers the experimental fabrication and characterisation techniques used in this thesis.

Chapter 6 describes the replication of double-gyroid-structured polystyrene thin film templates using electrochemical deposition of copper and the subsequent thermal oxidation of the self-supportive copper scaffolds for use in solar cells. The morphological changes occurring during the oxidation, including the formation of novel core-shell structures, will be studied using electron microscopy and scattering techniques. The characteristics of the devices fabricated from the oxidised copper network will also be studied as a function of the thermal oxidation protocols. In *Chapter 7* the replication of double-gyroid-structured templates by TiO_2, Al_2O_3 and ZnO using ALD will be described. Particular focus will be given to the requirement for surface modification to achieve dense and uniform ALD nucleation on the polymeric templates, and a novel gas phase modification technique used for the functionalisation will be detailed. The chapter concludes by reporting on dye-sensitised solar cells fabricated from ALD replicated TiO_2 scaffolds.

Chapter 8 outlines two projects which utilise ALD for photovoltaic applications. The first part of this chapter describes the upgrade of our commercial ALD reactor to utilise H_2S for the deposition of metal sulphides. It describes the engineering considerations needed to fulfil the stringent safety requirements regarding H_2S. Initial results from the deposition of ZnS will also be presented. The second part of this chapter reports on the use of ALD to deposit TiO_2 compact or blocking layers for mainly dye-sensitised solar cells. Initial results suggest that ultra-thin TiO_2 layers deposited below 200 °C are a potential substitute for compact layers normally formed using spray pyrolysis at elevated temperatures. The thesis concludes by describing the use of ALD in the field of biomimetics in *Chapter 9*. The spectral response of the colourful *Papilio blumei* butterfly is successfully replicated using an all-inorganic fabrication route comprising electrochemistry and ALD. The chapter also describes a synthetically stronger optical response caused by a small modification of the structure presented by the butterfly.

2 Fundamentals of solar cells

This chapter will provide an overview of the concepts fundamental to photovoltaic devices or solar cells. It will begin by introducing the operational principles of traditional silicon solar cells. The focus will then shift to hetero-junction solar cells in which the absorption of an incident photon leads to the formation of a long-lived electron/hole pair, or exciton. Next, the chapter will introduce the concept of a bulk hetero-junction, describing how it overcomes some of the drawbacks of bilayer hetero-junction devices. Examples of all-organic and hybrid bulk hetero-junctions will be given. The chapter will conclude with a very common hybrid hetero-junction, the dye-sensitised solar cell. Both liquid and solid-state electrolyte cells will be described, together with the advantages and disadvantages of these device geometries.

2.1 Conventional photovoltaic devices

The word *photovoltaic* stems from the Greek word *photo* meaning 'light' and *voltaic* designating 'electricity formed by chemical action'. As such the photovoltaic effect describes a process in which an electric potential difference is formed as a consequence of light irradiation. This effect is the basis for the operating principles of a solar cell. For the effective operation of a solar cell with a high conversion between solar energy and electrical energy two physical processes have to be optimised: the generation of charge carriers via the absorption of incident photons; and the separation and transport of these charge carriers to macroscopic electrodes connected to an external load.

The generation of charge carriers is caused by the absorption of an incident photon and the subsequent photoexcitation of an electron to a higher electronic state, given that the energy of the photon ($h\nu$) is higher than the electronic potential barrier [9]. Normally this barrier is given by the band gap of the material and as such the requirement is that $h\nu > E_{\text{bandgap}}$. This means that the effectiveness of this first step is governed by the electronic structure of the absorbing material. When the light source employed is the sun, the electronic structure should be such that the absorption matches the spectrum of the sun as closely as possible. Strategies to ensure and to enhance the overlap between material absorption and the solar spectrum include the use of multi-junction solar cells [10] in which multiple materials with varying electronic structures are used to widen the absorption window. The dye-sensitised solar cell is constructed for this purpose (Section 2.4).

The most common solar cell in use today is the silicon solar cell. This utilises a planar interface between n- and p-type doped silicon to extract the charge carriers. Assuming that $h\nu > E_{\text{bandgap}}$, an electron will be promoted from the valence band to the conduction band. Absorption can take place within the bulk of either layer of the silicon homo-junction. For the absorption coefficient of silicon, an active layer of a few 100 µm is required for complete absorption. The separation of the essentially free

electron and hole charge carriers is aided by the generation of an electric field at the junction interface due to the equilibration of Fermi levels. This electric field moves electrons and holes to opposite macroscopic collecting electrodes.

These operating principles are described for the case of the silicon solar cell, but they apply for any solar cell consisting of a high crystalline inorganic semiconductor homo-junction. One of the main disadvantages of high-performing silicon solar cells is the requirement for high crystallinity and purity, which stems from the fact that electrons and holes co-exist in the same material volume and will easily recombine if defects and impurities are present. Even though significant efforts have been made over the last two decades to alleviate this requirement by the introduction of multi-crystalline devices [11] and silicon hetero-structures [12], the high cost associated with material purity and high processing temperatures remains one of the limiting factors for the use of silicon solar cells in large scale power generation and for their introduction into the mainstream consumer product market. This high cost has accelerated research into alternative low cost solar cell concepts which can utilise cheaper materials and fabrication techniques.

2.2 Excitonic solar cells

Existing solar cell concepts can be categorised as either p-n homo-junctions or excitonic solar cells [13]. The physical mode of operation of excitonic solar cells (XSC) is intrinsically different from homo-junction solar cells such as silicon p-n junctions. The main difference between the excitonic and homo-junction solar cell is the way in which the absorption of an incident photon leads to the generation of free charge carriers. In both cases, the generation of an electron/hole pair forms an *excitonic* state due to the Coulomb interaction between the electron and the hole. In highly crystalline inorganic semiconductors such as silicon the formed exciton is very quickly dissociated at room temperature due to the small excitonic binding energy which amounts to a few meV. However in excitonic systems such as organic materials, the absence of strong dielectric screening leads to a long-lived bound state that does not dissociate at room temperature. An additional event is required to form free charge carriers since the absorption of an incident photon does not in itself automatically lead to the generation of free carriers.

One of the easiest ways to fulfil this additional requirement for separation of the bound electron and hole is to introduce another material in close proximity to the absorbing material. If chosen correctly, i.e. with appropriate band energy levels or molecular energy levels, the transfer of either an electron or a hole across this newly-formed interface is energetically favourable. The generated free charges are then transported to the external electrodes in the respective materials. The work functions of the electrodes are chosen relative to the band energy levels of the materials to aid charge extraction. This interface between an electron conducting or donor material and hole conducting or acceptor material is called a *hetero-junction* and a schematic of the operating principles of such an interface is shown in Figure 2.1.

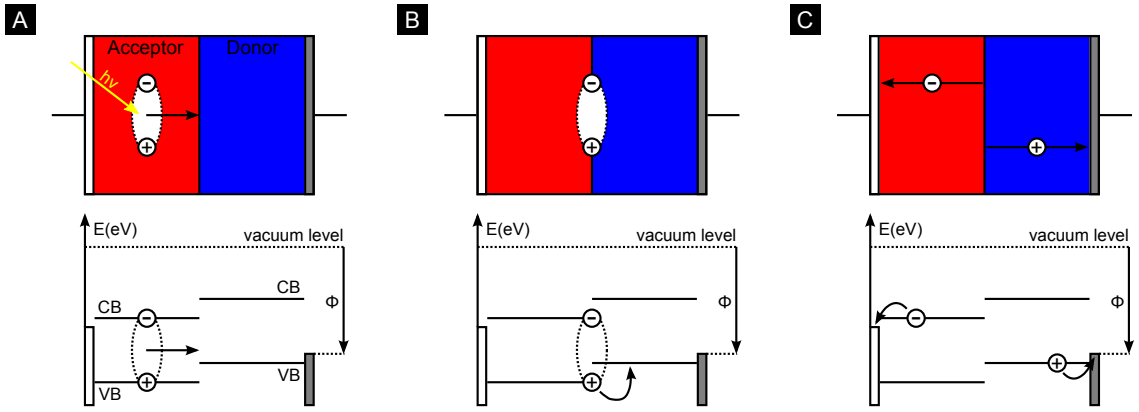

Figure 2.1: Schematic of excitonic generation in a hetero-junction solar cell. **(A)** An incident photon is absorbed by the solar cell, leading to the generation of an excitonic electron/hole pair that diffuses towards an acceptor/donor interface. **(B)** The interface aids the separation of the exciton into free charge carriers. **(C)** The free charge carriers are transported to the macroscopic electrodes to drive an external load.

Two main figures of merit exist for excitonic solar cells: the power conversion efficiency (PCE) and the external quantum efficiency (EQE). The PCE simply gives the ratio between the maximum power density of the device and the incident power density. The EQE gives a ratio between the measured electrical current and the number of incident photons. For an EQE of 100 % every photon that is incident on the solar cell leads to charge collection. EQE values of more than 100 % are possible if an absorbed photon facilitates the generation of more than one electron [14]. The mechanism for charge extraction in an XSC relies on three separate steps, namely: photon absorption, exciton dissociation and charge collection. The EQE can be considered as a product of the efficiencies of these three steps [15].

$$\mathrm{EQE} = \eta_\mathrm{A}\ \eta_\mathrm{D}\ \eta_\mathrm{C} \tag{2.1}$$

The efficiency of light absorption (the fraction of photons absorbed in the active material) is denoted by η_A. Three factors may cause the coefficient to be lower than unity: the reflection of the incident light off the surface of the active layer or other solar cell components; the absorption of light in non-active parts of the solar cell such as liquid electrolytes; or the inclusion of an active layer which is too thin to achieve complete absorption. A high value of η_A corresponds to a length scale of 100 nm to several µm, since this range of active material thicknesses is usually required for absorption to reach a value close to unity. The exciton dissociation efficiency (η_D) is defined as the fraction of excitons that reach an hetero-junction interface without recombining and then successfully dissociate. A low value of η_D is one of the main drawbacks of XSCs, since the exciton diffusion length prior to recombination is on the order of tens of nanometres [16]. As such only absorption events within 10 nm to 20 nm of a hetero-junction will contribute to the generated current. But at the same time a high value of η_A is needed which corresponds to a length scale of 100 nm to several µm. The charge

collection efficiency, η_C, is mainly limited by the mobility of charge carriers through the two materials in the hetero-junction but also by recombination events taking place after exciton dissociation.

2.3 Bulk hetero-junctions

The non-commensurate length scales needed to optimise η_A and η_D [17] can be resolved by nano-structuring the device to form what is called a bulk hetero-junction, which is described in the next section (Section 2.3).

The definition of a *bulk hetero-junction* is a hetero-junction where the donor-acceptor interface is not confined to a single planar interface somewhere inside the active regions of the device but is located throughout the bulk of the device. The two components of the XSC are finely dispersed throughout its entire thickness. For a bulk hetero-junction XSC to perform optimally three criteria have to be met:

1. The average size of the domains of any absorbing component has to be on the order of the exciton diffusion length (giving a high η_D).
2. Continuous pathways for charge transport must exist in both components (giving a high η_C.)
3. The amount of active material must be sufficient for the absorption to approach unity (giving a high η_A).

Although structuring the solar cell on the 10 nm length leads to an increased η_D, it can also lead to a decreased η_C. This is due to recombination caused by back electron transfer across the hetero-junction interface, an effect which is compounded in an XSC by the close spatial proximity of the dissociated free charge carriers. The charge extraction pathways should therefore be kept as short as possible with a high charge carrier mobility to ensure that the time-scales for charge extraction are short compared to any recombination event.

As we have already seen from the requirements for high η_A, η_E and η_C, the morphology of the XSC on the nanometer length scale can strongly influence the overall device performance. Figure 2.2 shows a number of possible interfacial schemes ranging from a single planar hetero-junction to a fully interdigitated junction which would conceptually offer the highest device performance.

As described in the introduction, a number of self-assembly based fabrication schemes are available for achieving nanoscale architectures not feasible using traditional lithographic techniques. These can broadly be divided into two categories.

1) A single step process consisting of the co-deposition of the active constituent components which self-assemble in-situ. 2) A two step process consisting of the self-assembly of one active component and the subsequent infiltration of the other active component

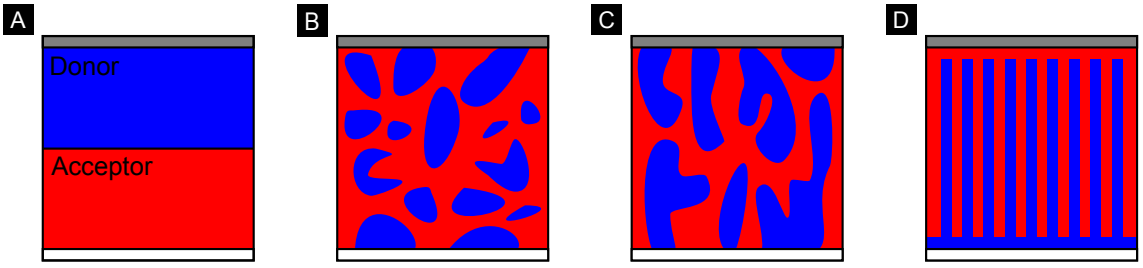

Figure 2.2: Hetero-junction morphologies. **(A)** A bi-layer hetero-junction suffers from the large distance required for exciton diffusion which increases the probability of recombination. **(B)** A bulk hetero-junction blend reduces the distance for exciton diffusion but instead suffers from non-direct conduction pathways to the electrodes and island formation. **(C)** If care is taken in the blend preparation, island formation can be avoided and the number of continuous pathways increased. **(D)** Idealised fully interdigitated donor/acceptor bulk hetero-junction which displays short distances for exciton diffusion and fully continuous direct transport pathways.

or components. The self-assembly could be achieved by the use of a structure-directing agent or via a template approach.

There are a number of existing material systems which are capable of forming a bulk hetero-junction. They can be divided into all-organic hetero-junctions and hybrid organic/inorganic hetero-junctions. All-organic solar cells normally fall under category (1) whereas hybrid solar cell fall under category (2).

The following sections will deal in turn with all-organic and hybrid junctions. We will then turn our focus to the dye-sensitised solar cell as an example of a hybrid device.

2.3.1 All-organic hetero-junctions

The simplest strategy for forming organic bulk hetero-junctions is to deposit a combination of two polymers or a polymer and a small molecule onto a substrate, for example via spin-coating or blade-coating from a common solvent. Before the solvent has evaporated, de-mixing of the two components leads to the formation of the hetero-junction. This morphology is then preserved in the glassy state of the polymers formed upon complete solvent removal.

One of the most common components for organic hetero-junction blends is an electron accepting derivative of C_{60} ((6,6)-phenyl C61-butyric acid methyl ester or PCBM). The first devices incorporating PCBM were produced by Saricfiti *et al.* in 1993 [17]. In these samples PCBM was evaporated on an poly(2-methoxy-5-(2-ethyl-hexyloxy)-1,4-phenylene-vinylene) (PPV) layer in a bilayer configuration. Developments have since then extended the library of polymer/PCBM blends to include, for example, P3HT/PCBM and F8TBT/PCBM. State-of-the-art organic solar cells reach power conversion efficiencies of over 8 % [18].

Although the approach is conceptually very simple, a number of experimental parameters affect the morphology, domain size and interconnectedness of the polymer blend. Common parameters include interactions between the solvent and the acceptor and donor materials, interactions between the two materials themselves, and interaction of both the solvent and the material with the substrate. Experimental methods such as deposition technique, solvent removal and annealing protocols may also affect the structure [15]. Given the large range of parameters, achieving two optimally interconnected networks with the required lateral length scale of approximately 10 nm (Figure 2.2D) can prove very difficult [19].

One method of addressing this difficulty is the use of block copolymers which incorporate the acceptor and donor material as the constituent blocks of the polymer. The length scale at which block copolymers (of a molecular weight of 10s of $\mathrm{kg\,mol^{-1}}$) naturally undergo microphase separation lends itself well to the fabrication of bulk hetero-junctions since this length scale is commensurate with the exciton diffusion length. However different issues arise when using conjugated block copolymers to fabricate hetero-junctions, principally the crystallisation of both or either of the constituent blocks which can interfere with or completely hamper the microphase separation.

2.3.2 Hybrid organic/inorganic hetero-junctions

The relatively simple mixing method described for all-organic hetero-junctions can also be applied in the formation of hybrid junctions. A range of differently shaped nanoparticles such as rods, spheres and tetrapods can be mixed with various polymers to form a hybrid hetero-junction upon annealing. Elongated particles such as rods and tetrapods allow for a more directed charge extraction compared to spherical nanoparticles. Examples of polymers used in this method include MEH-PPV and P3HT [20]. Common materials for the nanoparticles are CdS and CdSe [20] both of which have an absorption spectrum in the visible range which can extend the absorption efficiency of the device. A power conversion efficiency of about 2 % has been achieved [20].

Another common approach for the fabrication of hybrid devices follows the second route described in Section 2.3, in which one component is structured in the first step and the other component is infiltrated/backfilled in the second step. The most common scheme involves the structuring of metal-oxide nanoparticles such as titanium dioxide (TiO_2). TiO_2 has the advantage of being non-toxic and abundant. Titania nanoparticles, used in a large range of applications including photocatalysis [21, 22] and photovoltaics, are normally fabricated using a sol-gel process. Titania pastes, which include a polymer binding agent such as cellulose, are commercially available, and thin films ranging from less than 1 µm to 10s of µm with a porosity of approximately 60 % can easily be achieved upon high temperature annealing [23]. However, bulk hetero-junctions fabricated using TiO_2 scaffolds and conjugated polymers such as P3HT and MEH-PPV suffer from low power conversion efficiencies and EQEs [24]. These issues arise due to the disordered network of the titania mesoporous film, which with its wide pore size distribution prevents complete infiltration of the macro-molecules into the network [25].

2.4 Dye-sensitised solar cells

The first dye-sensitised solar cells that exploited a bulk hetero-junction were developed by Grätzel and O'Regan in the 1990s [23]. The benefit of dye-sensitised solar cells is that the size requirements imposed on the structure by the exciton diffusion length can be completely avoided if the absorption is confined to the charge separating interface .

In a dye-sensitised solar cell, shown in Figure 2.3 below, a wide band gap metal oxide semiconductor which has a limited absorption in the visible spectrum is sensitised by the conformal coating of its surface with a thin layer of organic or inorganic dye [26]. Absorption of an incident photon creates an excited oxidised state in the dye and an electron is injected into the TiO_2 scaffold providing that its conduction band lies below the redox potential of the dye. The dye is then reduced via an electron transfer from the surrounding electron donating material. Suitable electron-donating materials fall into two categories: liquid electrolytes, commonly containing an iodine/iodide (I^-/I_3^-) redox couple (Figure 2.3A,B); and solid-state electrolytes containing a hole conducting material, normally polymers as described in Section 2.4.1 (Figure 2.3C,D).

In the liquid electrolyte cell the oxidised redox couple is reduced at the macroscopic counter electrode, thus completing the electric circuit via an external load. The maximum achievable potential for this device configuration is the difference between the redox potential of the electrolyte and the sub-band edge states of the semiconducting scaffold. Two main recombination events lower the overall device efficiency: the back-transfer of injected electrons either to the oxidised dye or to the oxidised species in the electrolyte.

The main conceptual difference between the dye-sensitised solar cell and other hybrid devices is the introduction in the former of a thin absorbing mono-layer at the donor/acceptor interface. This increases the exciton dissociation efficiency since diffusion is not required, but at the same time leads to difficulties in achieving complete light absorption. The solution to this problem is to nano-structure the solar cell, thus increasing the amount of dye per unit area of the device. For example, given the absorption coefficient of the commonly used N719 dye (α=13 900 $\mathrm{mol^{-1}\,cm^{-1}}$) [27], approximately a 1000-fold increase in surface area compared to a flat junction is needed to achieve an absorption efficiency close to unity. The roughness factor (the increase in surface area per micrometer of porous film thickness) of commonly used mesoporous titania electrodes is between 100 and 140 [23]. As such a film thickness of approximately 7 µm to 10 µm is required for near complete absorption. However an increase in the film thickness also increases the probability of recombination according to either of the two loss mechanisms described below (Figure 2.3B(4,5) and Figure 2.3D(3,4)), thereby lowering the charge collection efficiency. This demonstrates that great care must be taken in device design to optimise the EQE and thereby the overall power conversion efficiency.

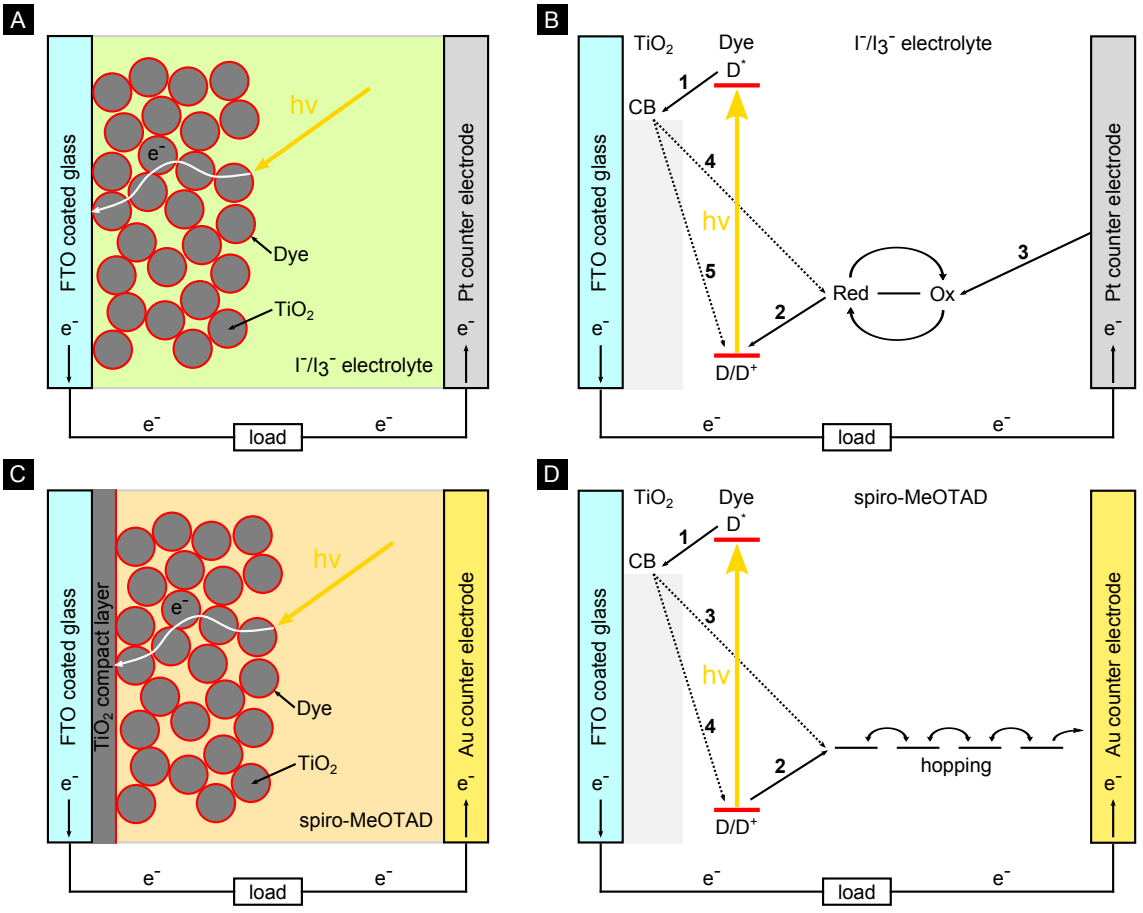

Figure 2.3: Hetero-junction morphologies. **(A)** A sensitised mesoporous TiO_2 network in contact with a I^-/I_3^- liquid electrolyte. **(B)** Band diagram of a liquid electrolyte DSSC. **(1)** The absorption of an incident photon leads to the oxidation of a dye molecule and injection of an electron into the TiO_2 conduction band. **(2)** The reduction of the dye by electron injection from the redox couple which is left in an oxidised state. **(3)** The reduction of a redox couple by an electron which has been passed through the external load. Recombination can occur between electrons in the TiO_2 scaffold and **(4)** the oxidised redox couple or **(5)** the oxidised dye. **(C)** A sensitised mesoporous TiO_2 network on a titania compact layer in contact with a hole-conducting spiro-MeOTAD solid-state electrolyte. **(D)** Band diagram of a solid-state electrolyte DSSC. **(1)** The absorption of an incident photon leads to oxidation of the dye and injection of an electron into the TiO_2 conduction band. **(2)** Reduction of the dye by hole injection into spiro-MeOTAD. Recombination can occur between electrons in the TiO_2 scaffold and **(3)** the holes in the spiro-MeOTAD or **(4)** the oxidised dye.

A number of excellent reviews cover aspects of both dye and electrolyte design [26, 28, 29]. In short, these reviews conclude that any process which aids in electron extraction such as dye regeneration and carrier transport must occur over a time scale

significantly shorter than detrimental processes, such as electron back-transfer from the TiO_2 conduction band to the dye and recombination events between free carriers.

Optimisation of the various components of the DSSC has led to recorded photon-to-electron conversion efficiencies of over 90 % at the absorption maximum of the dye [30]. The current record power conversion efficiency for liquid electrolyte cells is 12.3 % and is held by a device consisting of a 5 µm thick titania mesoporous electrode with a 5 µm scattering layer, a novel zinc porphyrin dye cosensitised with a Y123 dye and a Co(II/III)tris(bipyridyl)-based redox electrolyte [31]. A significant portion of current research efforts focuses on the design of new, more stable and more broadband dyes [32] and new electrolyte concepts. This is unsurprising given the low costs associated with the fabrication of meso-porous nano-particular titania electrodes. These research efforts are aimed at fine-tuning the pre-existing and highly successful model of the dye-sensitised solar cell. A second area of research is invested in the design of novel electrodes. Advances in this area include the use of non-standard nano-particular titania electrodes and the fabrication of devices which incorporate other metal oxides.

2.4.1 Solid-state electrolyte cells

As the power conversion efficiencies of DSSCs have increased, and as commercialisation has become more desirable, part of the current research focus has shifted towards properties such as long term stability and low manufacturing costs. One of the outcomes of this research focus has been greater investment in the development of the solid-state electrolyte cell, which shows several benefits in comparison to the liquid-electrolyte DSSC described above. One of the main drawbacks of DSSCs lies in the lack of stability of the constituent components. Examples of these instabilities include the tendency of the dyes to be bleached on exposure to light and the volatility and corrosiveness of the liquid electrolyte. The use of a liquid electrolyte also requires effective sealing of the device and the use of costly precious metals as counter electrodes. As these problems impede commercialisation attempts, research into the replacement of the liquid electrolyte with a solid-state hole transporting counterpart has gained further prominence.

The two major candidates to replace the liquid electrolyte are small molecule organic semiconductors and wide band gap semiconductor compounds such as CuSCN and CuI. Of the various compounds studied, 2,2',7,7'-tetrakis(N,N-di-methoxypheny-amine)-9,9'-spirobifluorene (spiro-MeOTAD) (Figure 5.2C) has been shown successfully to fulfil the requirements of a liquid electrolyte replacement [33]. These requirements include low molecular weight to aid infiltration; good transport properties; and energy levels that match those of the dyes employed.

The operating behaviour of a solid-state DSSC (ssDSSC) containing spiro-MeOTAD, is very similar to its liquid electrolyte counterpart with the main difference being the way in which the oxidised dye is regenerated. The electron transfer now takes place from the surrounding hole conducting material, or in other words via an injection of a hole into the hole conducting material. In the case of small molecule organic semiconductors

such as spiro-MeOTAD, the charge transfer through the electrolyte to the electrode takes place via a hopping mechanism.

Since the first use of spiro-MeOTAD in a DSSC by Bach *et al.* in 1998 [33, 34], a number of experimental advances have further extended the efficiency of spiro-MeOTAD-containing solar cells. The three main routes pursued are the use of additives such as lithium bistrifluoromethylsulfonylamine (Li-TFSI), the fine-tuning of the amount of these additives to improve the transport properties of the spiro-MeOTAD, and the improvement of the infiltration of the spiro-MeOTAD into the titania mesoporous scaffold which is commonly achieved by altering the parameters of the infiltration method, such as spin-coating speeds and times.

2.5 Alternatives to nanoparticular TiO_2 electrodes

The final section of this chapter gives a short overview of a number of different reported approaches to the creation of mesoporous TiO_2 and other metal oxide scaffolds for DSSC devices.

The majority of fabrication routes found in the literature can be categorised into electrochemical deposition in porous templates [35], hydro- and solvothermal synthesis [36], oxidation of titanium metal [37] and the use of structure-directing agents in combination with e.g. sol gel [38, 39].

One of the most common approaches uses sol gel synthesis together with any number of structure-directing agents, such as block copolymers. The combination of two commercially scalable fabrication techniques makes this route interesting from an industrial point of view. The structuring agent of choice is the commercially available triblock copolymer P123, poly(ethylene glycol)-b-poly(propylene glycol)-b-poly(ethylene glycol). Efficiencies up to 10 % have been reported by Wei *et al.* for liquid electrolyte cells with TiO_2 scaffolds fabricated through this approach [40]. Examples for ssDSSC devices include results by Zukalova *et al.* [39] which demonstrate 1 µm thick films with an efficiency of 4 %.

Another less frequently used fabrication route, interesting because of its potential of scalability, is the oxidation of titanium foils to produce high aspect ratio wires or tubes [37] with dimensions on the nanoscale. DSSCs using TiO_2 nanotubes have shown efficiencies up to 3 % [41].

The least scalable of the fabrication schemes is electrochemical deposition. Despite the lack of potential for scalability, this fabrication scheme is promising from a research point of view due to its versatility. A large range of different metals and metal oxides can be deposited using including titania for use in DSSCs [35]. A variety of templates can also be used including polycarbonate membranes [42], alumina membranes [43], colloidal crystals [44] and voided block copolymer thin films [35, 45–48].

The large range of feasible materials allows for the investigation of new device fabrica-

tion routes. These could include more complex structures created by the the deposition of metals and their post-deposition thermal oxidation to their corresponding oxides [48]. A number of materials have also been studied as an alternative to TiO_2 [49, 50], of which ZnO has gained the most interest with state-of-the-art efficiencies reaching up to 7 % [51].

One technique used for the fabrication of TiO_2 scaffolds that has so far received relatively little attention is atomic layer deposition (Chapter 4). This technique is combined with self-assembled double-gyroid polystyrene templates (Section 3.2) in Chapter 7 to produce high surface area titania electrodes.

3 Block copolymer self-assembly

Block copolymers, and in particular their use as templates, form an integral part of this thesis. It is therefore important to understand the underlying physical principles that lead to their self-assembly. The chapter begins by contrasting melts of homopolymers with melts of block copolymers, showing how the additional constraint of the covalent bond in the block copolymers leads to phase separation on the nanometre length scale into morphologies with high order. It then moves to focus on the double-gyroid block copolymer morphology which is of particular interest as a template for nanofabrication due to its highly ordered networked structure. Methods for describing and visualising the double-gyroid morphology are detailed. The chapter concludes by describing the self-assembly of block copolymers under non-ideal conditions, especially the deposition of thin polymer films on solid substrates.

3.1 Introduction to copolymer self-assembly

Polymers are a subset of the material class of macromolecules in which repeat units, or monomers (Figure 3.1A), are covalently bonded together into linear or branched systems. Copolymers are arrangements of two or more chemically distinct monomers and can be ordered or random in configuration. Block copolymers are a sub-class of copolymers, and consist of homopolymer chains (Figure 3.1B), or blocks, of different chemical compositions covalently bonded together (Figure 3.1C). Depending on how the blocks are arranged, a number of different block copolymer structures can be realised. The most common block copolymer architectures are diblocks P(A-b-B) and triblocks P(A-b-B-b-A), P(A-b-B-b-C) (Figure 3.1D). The diblock copolymer structure is the system used in this thesis.

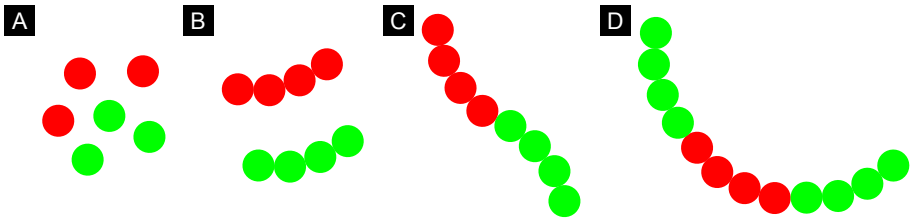

Figure 3.1: Polymer configurations. **(A)** Monomers **(B)** Homopolymers **(C)** Diblock copolymers **(D)** Triblock copolymers

3.1.1 Homopolymer blends

While a mixture of two different monomers, A and B, tends to form a homogeneous phase, a mixture of polymers made up from the same monomers A and B tends to

undergo macro phase separation upon lowering of the temperature of the system. This difference was explained by Flory and Huggins [52, 53] who used a mean field theory to model the thermodynamics of polymer blends. The polymer blend system is characterised by five parameters which describe the polymers: the degrees of polymerisation N_A, N_B; the relative volume fractions of each homopolymer ϕ_A, ϕ_B; and the Flory-Huggins interaction parameter χ.

The macro phase separation of polymer blends is driven by the competition between the energetic and entropic contributions to the Gibb's free energy where the energetic contribution (i.e. the energy of mixing) is proportional to the number of monomers in the system and the entropic contribution is proportional to the number of polymer chains. The Gibb's free energy of mixing for a blend of homopolymers A and B is,

$$\Delta G_{\mathrm{mix}} = \Delta H_{\mathrm{mix}} - T\Delta S_{\mathrm{mix}}. \tag{3.1}$$

Flory and Huggins modelled the blend as a lattice in which each monomer occupies one lattice site. The result of applying mean field theory to this model is the Flory-Huggins free energy description which takes into account enthalpic and entropic contributions to the free energy due to monomer interactions,

$$\frac{\Delta G_{\mathrm{mix}}}{k_{\mathrm{B}}T} = \chi\phi_{\mathrm{A}}\phi_{\mathrm{B}} + \frac{\phi_{\mathrm{A}}}{N_{\mathrm{A}}}\ln\phi_{\mathrm{A}} + \frac{\phi_{\mathrm{B}}}{N_{\mathrm{B}}}\ln\phi_{\mathrm{B}} \tag{3.2}$$

where χ is the Flory-Huggins interaction parameter [52], $N_{\mathrm{A,B}}$ are the degrees of polymerisation and $\phi_{\mathrm{A,B}}$ are the relative volume fractions of polymers A and B. The overall free energy of the system governs whether the blend forms a homogeneously mixed phase or whether spontaneous phase separation occurs. For $\Delta G_{\mathrm{mix}} < 0$ phase separation is energetically favourable whereas for $\Delta G_{\mathrm{mix}} > 0$ the stable phase will be a homogeneous mixture. The enthalpic contribution, which describes the nearest-neighbour monomer interactions, can be either negative, promoting mixing, or positive, opposing mixing. The entropic term which is derived by applying Boltzmann's entropy formula to the lattice model is always negative i.e. it promotes mixing. A simple model for the interaction parameter χ based on Van-der Waals interactions alone is given by

$$\chi = \frac{Z}{k_{\mathrm{B}}T}\,\epsilon_{\mathrm{AB}} - \frac{1}{2}(\epsilon_{\mathrm{AA}} + \epsilon_{\mathrm{BB}})) \tag{3.3}$$

where Z is the number of nearest neighbours in the lattice model and ϵ_{AB}, ϵ_{AA} and ϵ_{BB} are the interaction energies between the A and B monomers. Empirically, the interaction parameter is often found to vary as $\chi = \mathrm{A}/T + \mathrm{B}$. In contrast to the enthalpy of mixing ΔH_{mix}, which is proportional to χ, the entropy of mixing ΔS_{mix} which favours the mixing of the two monomers, is proportional to the total degree of polymerisation. This means that polymer mixing is controlled by the product χN, the segregation strength, instead of just χ as for a monomer blend. By using the expression for the free energy given by Equation (3.2), the binodal and spinodal curves

and stability conditions for blends can be calculated by minimisation of the free energy. One specific case exists for $N = N_A = N_B$. By differentiating $G(\phi_A, \chi, N)$ with respect to N it can be shown that for $\chi N < 2$ a blend is stable for any ϕ_A, and for $\chi N > 2$ some values of ϕ_A will lead to phase separation.

3.1.2 Diblock copolymer blends

As with blends of homopolymers, the phase separation of block copolymers is driven by the incompatibility of the chemically different monomers that constitute the blocks. The main difference is the covalent bonding between the A-block and the B-block which leads to local phase separation and self-assembly into A-rich and B-rich regions. The morphology that the blend adopts is determined by the relative volume fractions of the two blocks ϕ_A and ϕ_B and the segregation strength χN. The length scale of phase separation is determined by the total degree of polymerisation of the block copolymer N.

For a symmetric diblock copolymer ($\phi_A = \phi_B$) the adopted morphology is a lamellar structure with alternating A-rich and B-rich regions of a particular lamellar spacing. As the volume fraction of one of the blocks is increased, the block copolymer becomes more asymmetric and begins to adopt structures with a higher degree of curvature. The bicontinuous *Fddd* phase [54], the tricontinuous double-gyroid phase (see Section 3.2), hexagonally packed cylinders, body-centred cubic (BCC) and close-packed spheres are all observed as the volume of either block is increased or decreased (Figure 3.2).

Unlike the homopolymer blends, the free energy of diblock copolymers must take into account the entropic forces caused by covalent bonding between the blocks. For small χ (high T) the mixing due to entropy outweighs the demixing due to enthalpy and the copolymer blend adopts a homogeneously mixed disordered phase, where the free energy per chain can be approximated by the A-B interfacial energy as shown in Equation (3.4) [56].

$$\frac{\Delta G_{\text{dis}}}{k_B T} = \chi \phi_A \phi_B N \tag{3.4}$$

As the temperature is lowered, the enthalpic contribution to the free energy increases and the system tries to minimise the contact between unlike blocks by the formation of phase separated regions. The polymers in these regions are stretched, compared to the random coil configuration of homopolymer blends, which means that there will be an entropic contribution to the free energy in the form of an elastic Hookian term. Equation (3.5) shows the free energy for the lamellar phase, where $N_A = N_B$ [56].

$$\frac{\Delta G_{\text{lam}}}{k_B T} = \frac{3(\lambda/2)^2}{2Na^2} + \frac{\gamma A}{k_B T} \tag{3.5}$$

The first term corresponds to the stretching of a polymer chain to half the lamellar

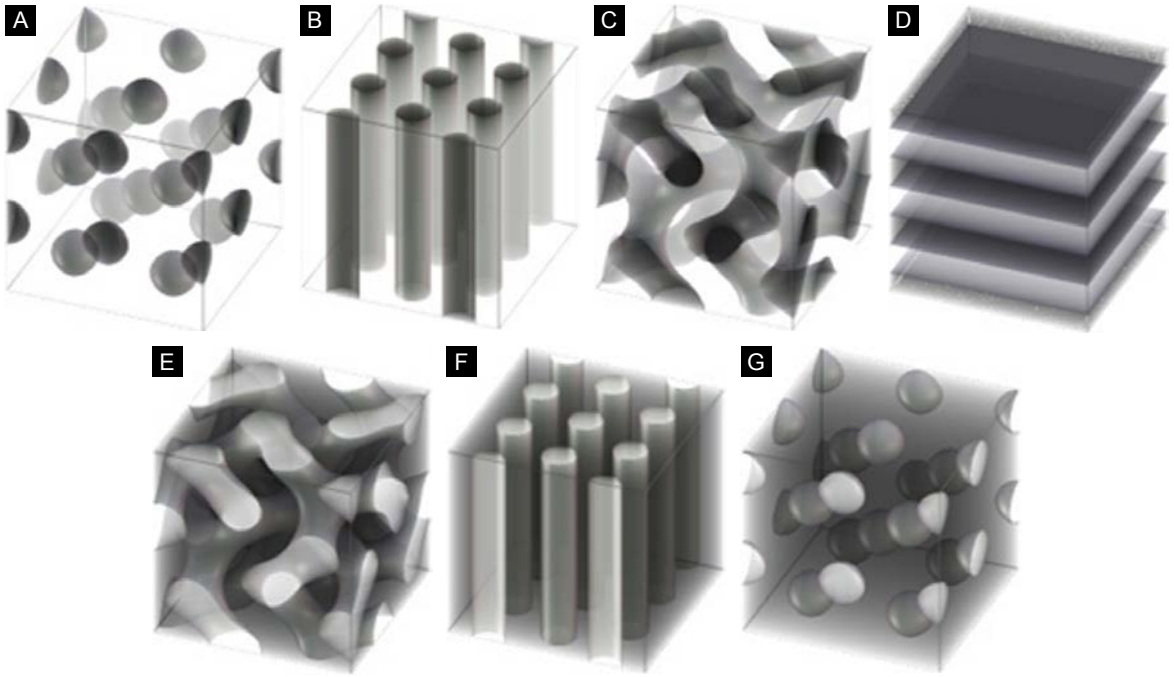

Figure 3.2: Equilibrium microphase separated morphologies of diblock copolymers. In **A** - **C** one of the two components is in minority, whereas in **D** both components have the same volume and in **E** - **G** the other component is in minority. **(A)** Body-centred cubic **(B)** Hexagonally close-packed cylinders **(C)** Double-gyroid **(D)** Lamallae **(E)** Double-gyroid **(F)** Hexagonally close-packed cylinders **(G)** Body-centred cubic. Modified from [55].

spacing ($\lambda/2$). The second term is the enthalpic repulsion at the A-B interface expressed as the product of the chain contact area $A = Na^3/(\lambda/2)$ and the interfacial tension $\gamma = (k_\mathrm{B}T/a^2)\sqrt{\chi}$ which can be calculated from theoretical work on polymer-polymer interfaces. Minimisation of the free energy with respect to λ in the strong segregation limit yields an expression for the equilibrium lamellar spacing [56],

$$\lambda_0 \approx a\chi^{1/6}N^{2/3} \propto N^{2/3} \tag{3.6}$$

which is in good agreement with experimental work by Hashimoto *et al.* [57].

A critical value of χN for the order-disorder transition can be estimated by equating the free energy of a disordered polymer melt $G_\mathrm{dis}(\phi_\mathrm{A} = \phi_\mathrm{B} = 1/2) = k_\mathrm{B}T\chi N/4$, with the free energy of the lamellar phase $G_\mathrm{lam}(\lambda_0)$. The estimation yields a value of $\chi N \approx 10.4$ which is in good agreement with a more accurate value of $\chi N = 10.5$ predicted using self-consistent mean field theory [58, 59]. Thus for $\chi N > 10.5$ (i.e. low temperatures, high molecular weights, or strong incompatibility between the polymer blocks) we expect a symmetric ($\phi_\mathrm{A} = \phi_\mathrm{B}$) block copolymer to micro phase separate into a lamellar arrangement with a period λ_0.

This simple calculation does not provide any information about the composition profile at the interface between the A-rich and B-rich regions, for which self-consistent mean

field theories are required. It is possible to define three different regimes describing increasingly sharp composition profiles: the weak ($\chi N \approx 10$), intermediate ($\chi N \approx 10$ to 100) and strong ($\chi N > 100$) segregation limits. The weak and strong segregation limits have been treated and unified by Matsen, Bates and Schick [58, 59] who calculated theoretical phase diagrams for diblock copolymer systems (Figure 3.3B). These predictions agree well with experimental work by Khandpur *et al.* [60] as seen in Figure 3.3A.

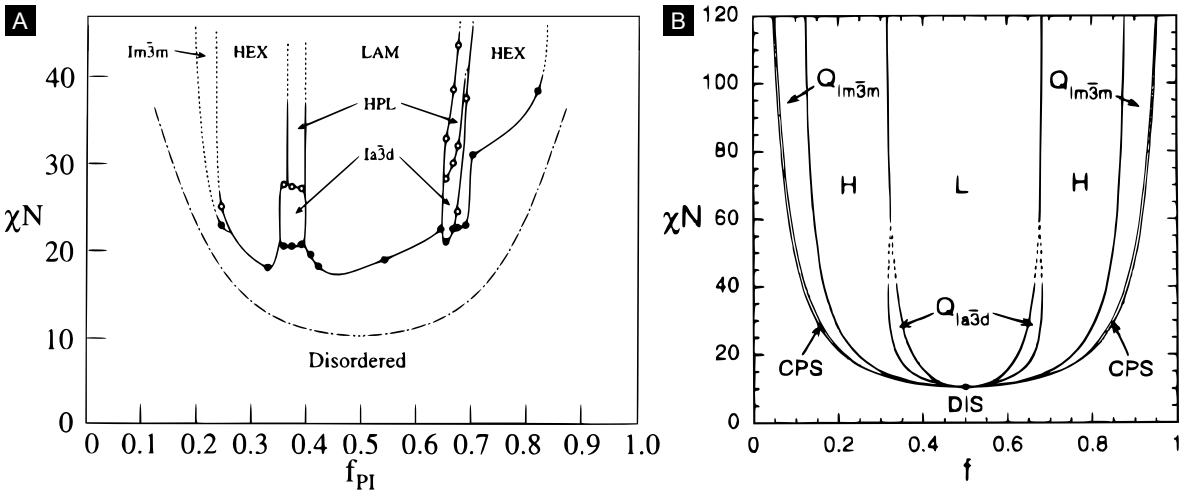

Figure 3.3: Diblock copolymer phase diagrams. **(A)** Experimentally determined phase diagram of polystyrene-b-poly(isoprene). Modified from Khandpur *et al.* [60] **(B)** Calculated phase diagram using mean field theory. Modified from Matsen *et al.* [59]

3.1.3 Phase separation of non-ideal systems

The theory of micro phase separation of block copolymers described in Section 3.1.2 assumes that both the polymers and the environment surrounding the polymer system are ideal. However real polymers are very seldom ideal and certain considerations have to be made when dealing with their phase separation and self-assembly. This section will cover polymer polydispersity, the properties of thin polymer films, and their effects on polymer self-assembly.

The range of molecular weights in a polymer melt is characterised by the polydispersity index, $PDI = M_\mathrm{w}/M_\mathrm{n}$, where M_w and M_n are the weight average molecular weight and the number average molecular weight respectively. Both simulation and experimental studies have shown that an increased polydispersity can affect the achieved equilibrium morphology as well as the domain spacing and system properties such as the long-range domain order. For example, using self-consistent mean field theory, Matsen *et al.* and Cooke *et al.* showed a shift in the boundaries between the equilibrium morphologies in the phase diagram, the appearance of co-existence regions and the lack of long-range order [61, 62]. Experimental studies confirm that systems with high polydispersity

form ordered morphologies but that these can be different from their monodisperse counterparts as confirmed by Lynd *et al.* [63].

The idealised theory of micro phase separation only accounts for local interactions between neighbouring polymer chains and intensive properties such as the system's temperature. In other words the system is considered to be very large and the interactions between the polymer and its surroundings are assumed not to affect self-assembly. However in practice when block copolymers are used as templates or scaffolds they are very frequently fabricated as thin films on solid substrates. This means that the constituent blocks of the copolymer will interact with both the free surface at the air/polymer interface and the substrate. These interactions can cause the formation of non-bulk equilibrium morphologies, or alternatively can alter the orientation of the intrinsic morphology.

One very common example of this is the self-assembly of cylinder-forming block copolymers in thin films. The preferential interaction, or wetting, between either block and the substrate can cause the formation of cylinders parallel to the substrate surface. This preferential wetting of either block is normally unwanted for device fabrication since continuity of both blocks is required.

3.2 The gyroid morphology

Of all the possible block copolymer morphologies, hexagonally close-packed cylinders and the double-gyroid morphology are the two most commonly used as templates for the fabrication of nano-structured active materials [35, 45–48, 64–66]. The major drawback with the cylindrical morphology is the lack of interconnectedness between neighbouring cylinders which frequently leads to the collapse and clumping of the replicated nanowires upon removal of the template, especially for high-aspect-ratio polymer templates. The gyroid-structured replicas are far less mechanically sensitive to experimental conditions such as solvent evaporation, and are less likely to collapse during processing [45]. This stability is due to the networked structure of the gyroid morphology which gives it a greater mechanical robustness than the individual hexagonally close-packed cylinders.

This section gives an overview of the gyroid phase of diblock copolymers including the double-gyroid morphology displayed by the polymer templates used in the thesis.

3.2.1 The double-gyroid surface

The interfaces between the phase separated regions of block copolymers (Section 3.1.2) are described by a surface which has an approximately constant mean curvature $H = \frac{1}{2}(k_1 + k_2) = \text{const}$. These surfaces of constant mean curvature are called intermaterial dividing surfaces (IMDS). Depending on the connectedness of the equilibrium morphology achieved, the surfaces can be categorised into either unconnected (close-packed

cylinders, close-packed spheres etc.) or connected with various degrees of continuity. Connected surfaces are further distinguished by the number of distinct continuous phases.

Because of the lack of analytical solutions to most IMDSs (exceptions do exist [67]) the concept of level surfaces are used to model them. Level surfaces are functions which satisfy the equation

$$F(x, y, z) = t = \text{const} \tag{3.7}$$

where the shape and geometry of the surface is determined by $F(x, y, z)$ and the constant t determines the volume fractions of the two volumes separated by the level surface [68]. Because of the triply periodic nature of the level surfaces they can be described by a three-dimensional Fourier series.

By using the lowest allowed Fourier components hkl of the single-gyroid space group ($I4_132$), we get an approximate expression for its level surface.

$$\sin\left(\frac{2\pi}{a}x\right)\cos\left(\frac{2\pi}{a}y\right) + \sin\left(\frac{2\pi}{a}y\right)\cos\left(\frac{2\pi}{a}z\right) + \sin\left(\frac{2\pi}{a}z\right)\cos\left(\frac{2\pi}{a}x\right) = t = \text{const} \tag{3.8}$$

The single-gyroid and its associated dividing surface separates space into two physically distinct regions. If the value of the constant t is zero, the two volumes separated by the IMDS are equal. As $|t|$ increases the ratio of the two volumes increases, up to a value of $|t| = \sqrt{2}$ at which for larger $|t|$ the surface is no longer connected. Single-gyroid structures are not very common in nature but were recently found in butterflies, where they act as photonic crystals to produce the iridescent colours of the wing scales [69, 70].

Although the double-gyroid was first discovered in surfactant systems [71], it was first seen in copolymer systems by Thomas *et al.* in 1986 [72] in a polystyrene-polyisoprene copolymer and has since then been found in many systems including diblock and triblock copolymers [73, 74]. The double-gyroid surface divides the unit cell into three volumes separated by two single-gyroid level surfaces. The volume between the two single-gyroid surfaces forms the matrix of the block copolymer, with the other two volumes forming two separate networks within the matrix as seen in Figure 3.4A. When the double-gyroid is found in a diblock copolymer system, the two networks are chemically equivalent but are unconnected. An example of this can be seen in work by Finnemore *et al.* who used a double-gyroid PS-PI system with the PI networks removed, as a template for the growth of calcite ($CaCO_3$) [65, 75]. Finnemore reported that under certain conditions, calcite crystal growth took place in only one of the networks, thus showing the lack of connectivity between these two networks. It is possible to achieve a configuration in which all three networks in a double-gyroid are unconnected and chemically distinct. This can be accomplished using a triblock copolymer, for example PS-b-PI-b-PLA, where the PS forms the first network, and the PI and the PLA form

the second and third networks, which in this case are chemically distinct.

The level surface for the double-gyroid can be constructed as the square of the level surface of a single-gyroid (SG).

$$F(x, y, z) = [F_{\mathrm{SG}}(x, y, z)]^2 = t^2 = t^* = \mathrm{const} \tag{3.9}$$

As was the case for the limits of $|t|$ in the single-gyroid level surface, the equivalent limit for the double-gyroid beyond which the networks are no longer connected is $|t^*| < 1.414$.

In order to simulate the level surfaces of the double-gyroid and to construct the 3D models which are used in this thesis, an implementation of the level surface was performed in Matlab. The code for this was written and kindly provided by **Maik Scherer** [66].

The matrix or majority phase of a diblock copolymer, which corresponds to the volume enclosed between the two single-gyroid level surfaces, occupies approximately 65 % of the total volume. The volume that surrounds the majority phase, which corresponds to the remaining two distinct networks, is called the minority phase. Figure 3.4A shows eight unit cells of the double-gyroid with the majority phase coloured in blue and the minority phases coloured in green. The continuity of both minority networks and the fact that they are not interconnected is shown in Figure 3.4B. The networks are coloured in two shades of green for clarity.

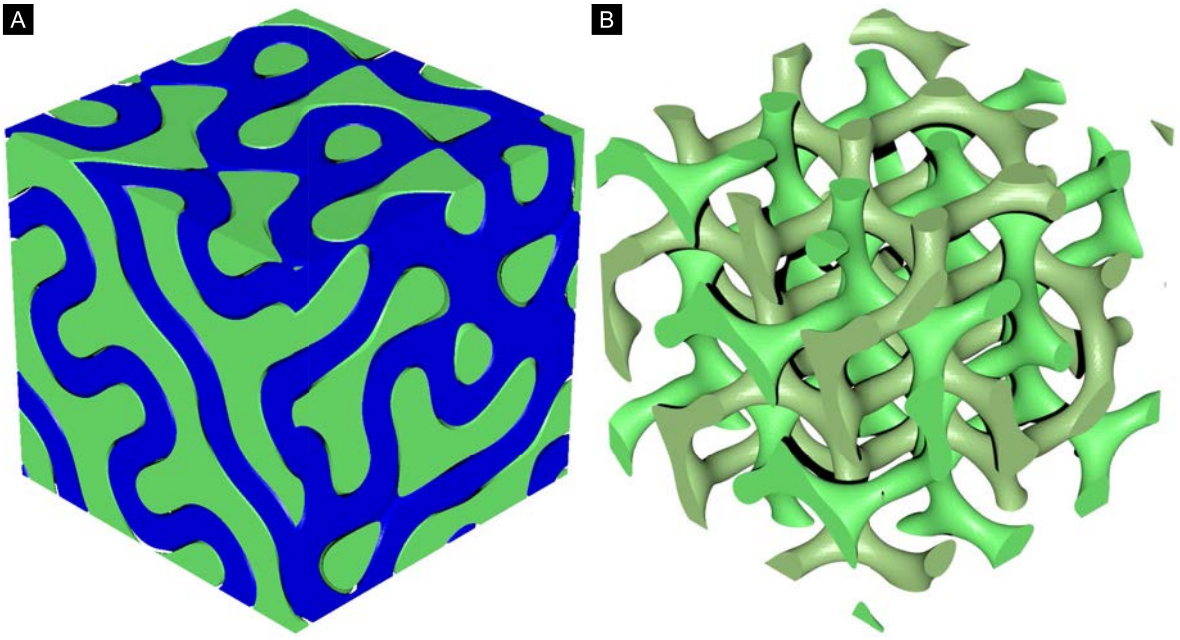

Figure 3.4: Simulation of the double-gyroid morphology. **(A)** Double-gyroid with a blue majority phase and green minority phases. The minority networks occupy 38.5 % of the volume. **(B)** The two minority phases of a combined volume fraction of 15 % displayed in two shades of green to show that the two networks are continuous and non-intersecting.

A number of other very interesting morphologies have been shown to exist in block copolymers, both theoretically and experimentally, including the alternating [76] and core-shell double gyroids [77] found in triblock copolymers and the *Fddd* [54] and the *Pnna* [78] morphologies.

3.2.2 Achieving the gyroid phase

There are a number of routes to the formation of a diblock copolymer system that displays the double-gyroid as its equilibrium morphology. They can broadly be divided into either the modification of commercially available or easy to synthesise block copolymers, or the direct synthesis of a block copolymer with the correct volume fractions. The former route relies on the addition of low molecular weight polymers or small molecules to one of the copolymer blocks in order to alter its volume fraction and therefore the position of the block copolymer in its phase diagram, for example from a cylindrical to a double-gyroid morphology. For this route to be successful the addition must be selective, in other words it must be ensured that the additional component only goes into the intended block. This can be achieved by tuning the miscibility of the additive in the copolymer blocks [75, 79, 80]. Another way to achieve this is by facilitating specific interactions, such as hydrogen bonding, between the additive and one copolymer block [81, 82].

In this thesis the direct synthesis route is used. This avoids the problems attached to the modification route. However direct synthesis introduces other potential difficulties, of which the largest is the reliance upon synthetic chemistry to achieve the correct volume fraction. The direct synthesis route employed in this thesis is described in Section 5.5.

3.2.3 The double-gyroid in thin films

As mentioned in Section 3.1.2, one of the most interesting morphologies of diblock copolymers is the double-gyroid morphology due to the continuity of both its majority and minority phases. A number of theoretical and experimental studies have been carried out on the formation of the double-gyroid morphology in thin films [66, 83–85]. The studies report that polymers which tend to form the gyroid-morphology in the bulk also adopt this structure in thin films. However for thin films, interfacial effects such as non-porous wetting layers at the polymer-substrate interface are more frequent. The studies also show that when ultra-thin films are used (film thickness of less than twice the gyroid period) they do not adopt their usual gyroid morphology.

So far only two polymer systems, a poly(4-flouro styrene)-b-poly(lactic acid) and a polystyrene/poly(4-flouro styrene)-b-poly(lactic acid) diblock copolymer, have been shown to produce thin films that are porous at both interfaces upon removal of one of the constituent polymers. In the work by Crossland *et al.* [35, 45, 64, 86, 87] the porosity of the substrate/polymer interface is maintained by the intrinsic roughness of

the FTO-coated glass substrate [64].

The second of these polymer systems, produced by Scherer *et al.* [66], did not show this porosity at the substrate/polymer interface despite the roughness of the FTO-coated substrate. Instead the surface had to be chemically modified using a self-assembled monolayer to create a neutral surface which allowed equal wetting both the P(F)S and PLA. The same polymer system is used extensively in this thesis (Chapter 6 and Chapter 7) and the surface functionalisation is described in Section 5.6.1.

4 Atomic layer deposition

This chapter will cover the main experimental technique used in this thesis, atomic layer deposition (ALD). The first part of the chapter describes the physical and chemical underpinnings and the development of ALD. It then moves to outline current understanding of the physics of ALD growth on polymer and high-aspect-ratio surfaces. The properties of the main three deposited materials will be described. The chapter sets a foundation for the majority of the experimental work reported in this thesis.

4.1 Introduction

As miniaturisation has become increasingly important in the semiconductor industry, the requirement for thin film deposition techniques which offer conformal, large area depositions has become one of the key aspects of the process line. A number of thin film deposition techniques including chemical vapour deposition (CVD) and pulsed laser deposition (PLD) offer solutions to this challenge. However no other technique rivals the conformality achieved by atomic layer deposition on high-aspect-ratio structures.

Besides these industrial applications ALD has remained a very important deposition technique in the research community since its invention in the 1960s, and the number of publications which utilise ALD increases every year. In this thesis, ALD has been employed in the replication of porous block copolymer gyroid templates with Al_2O_3, TiO_2 and ZnO (Chapter 7); in the fabrication of solid state dye-sensitised solar cells from ALD-deposited TiO_2 mesoporous scaffolds (Chapter 7); for the deposition of ZnO as an n-type component in p-type double-gyroid-structured cuprous oxide solar cells (Chapter 6); and for deposition of TiO_2 compact layers for dye-sensitised solar cells (Chapter 8). ALD has also been used in the biomimicry of the *papilio blumei* butterfly to produce a colour response close to the biological counterpart as well as a stronger, more striking optical response (Chapter 9).

As evidenced by the list of projects undertaken, with their varying potential applications and varying technological challenges, ALD has proven to be a very versatile technique. Along with the research progress achieved during this thesis, a significant amount of time has also been dedicated to the installation and establishment of ALD as a useful tool within the University of Cambridge and especially the Physics department where we now have about twenty regular users including one major commercial user and an average machine run time of 30 h to 40 h per week.

The chapter will start by outlining the physical and chemical processes involved in ALD, taking the deposition of aluminium oxide as an example. It will then give a short overview of the development of ALD and some of the technological and research advancements made to date, especially those connected to solar cells which are the

main research goal of this thesis. It will also cover the properties of some of the the most commonly-used metal oxides: aluminium oxide, titanium dioxide and zinc oxide.

Since the majority of the projects use ALD for depositions on polymeric substrates and/or high-aspect-ratio structures, the current physical understanding of deposition on such surfaces based on experimental studies and modelling will be covered. This is followed by a description of the specific ALD reactor used in this research, and the physical properties of the deposited materials, including deposition rates, refractive indices, material purities and crystal structures, as a function of deposition temperature.

4.2 Fundamentals of ALD

ALD is a thin film coating technique which employs gas-solid self-terminating reactions of gaseous precursors with a substrate. It offers extremely good thickness control with sub-nanometre resolution and superior conformality both over large areas and on high-aspect-ratio surfaces. ALD as a deposition technique is a conceptual advancement from chemical vapour deposition (CVD). In CVD two or more precursors are simultaneously entered into the reaction chamber and allowed to react. The limitations of CVD are that the growth rate is too high for successful application in nano-porous high-aspect-ratio templates and that the deposited film thickness is only a function of interaction time between the precursors and the substrate and as such is not discrete or quantised.

ALD presents a solution to this problem by dividing the reaction up into two half-cycles (for a binary reaction). Only one of the constituent reactants at a time is allowed to interact with the substrate. The interactions can either be temporally or spatially separated, with temporal separation being the standard configuration in ALD reactors. Spatial separation is mostly used in ALD reactors for industrial applications for which more specialised types of processes are required (such as roll-to-roll depositions [88]). Regardless of the type of separation, the distinctive feature of ALD is that the film growth happens in a cyclic manner and therefore is quantised.

The ALD process relies on the sequential introduction of two or more precursors into the reaction chamber. Each precursor is allowed to chemisorb from the gas phase onto the substrate and the surface coverage is allowed to reach unity by precursor self-saturation. This self-saturation is what leads to the self-limiting behaviour of ALD and is what, in combination with the cyclic nature of ALD, enables precise thickness control. Between each sequential precursor, the reaction chamber is purged with an inert gas to remove unreacted precursor molecules and to remove by-products formed during the chemisorption reaction. A reaction scheme for the deposition of Al_2O_3 is shown in Figure 4.1.

This deposition uses trimethyl aluminium (TMA) and water as the precursors with methane as the reaction by-product. In Step 1 the TMA is allowed to react with the functional groups present on the substrate surface, in this case -OH groups. For the reaction to be considered self-limiting, no further absorption should take place once all available -OH groups, bar groups not accessible due to steric hindrance, have partaken

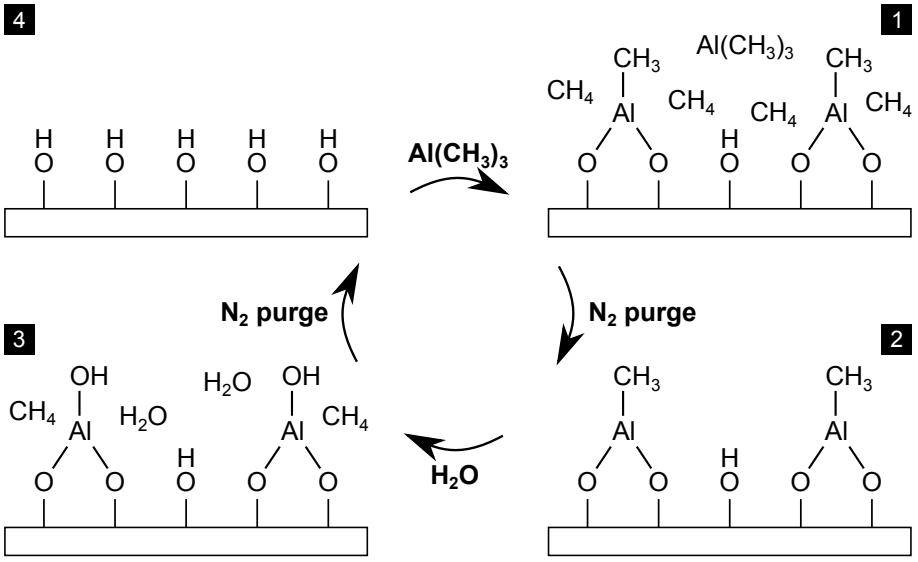

Figure 4.1: Schematic of Al_2O_3 deposition by Atomic Layer Deposition. The precursors used are trimethyl aluminium (TMA) and water. **(1)** TMA molecules are chemisorbed onto the surface. **(2)** Unreacted TMA molecules and methane by-products are removed by a nitrogen purge. **(3)** Water is chemisorbed onto the monolayer of TMA. **(4)** Unreacted water molecules and methane are removed by a nitrogen purge. Each cycle deposits one (possibly partial) monolayer of Al_2O_3.

in chemisorption. This is true for TMA even for extended exposure times. However it is not true for all precursors, meaning that multilayer formation is possible especially at low deposition temperatures [89]. In the ALD reaction, the subsequent inert gas purge removes unused gas molecules and reaction by-products (Step 2). The second half-cycle consists of an H_2O pulse which is allowed to react with the remaining exposed methyl groups (Step 3). This chemisorption of water leads to the formation of a (possibly partial) monolayer of Al_2O_3 and the layer of -OH groups used in the next reaction cycle. The water pulse is normally longer than the primary precursor pulse to allow the reaction to reach a yield of one. The second inert gas purge removes excess water and the methane by-product (Step 4). Due to potential hydrogen bonding between unreacted water molecules and surface hydroxyl groups, especially at low temperatures where the water sticking coefficient is high, the second half-cycle purge is normally longer than the first half-cycle purge. In this thesis, whenever ALD reactions are described, the first half-cycle is considered to use the metal-containing precursor and the second half-cycle the oxygen or sulphur source. The metal-containing precursor is named the primary precursor whereas the oxygen or sulphur containing precursor is named the secondary precursor.

The reaction scheme described above depends upon the physical properties of the precursors including their reactivity, thermal stability, and volatility, all of which are a function of the reaction temperature. The range of temperatures for which these properties are favourable for self-limited ALD growth is called the ALD window, shown in Figure 4.2.

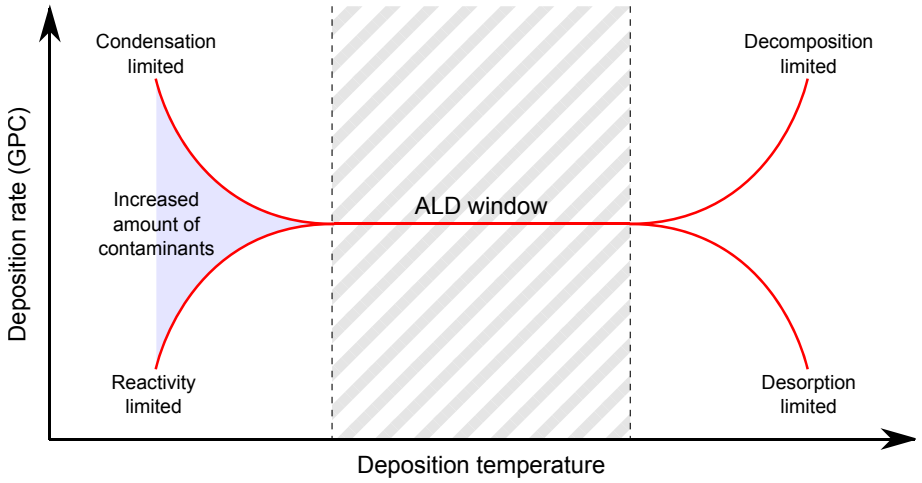

Figure 4.2: General temperature dependence of the ALD deposition rate. The range of temperatures for which the ALD growth is self-terminating and approximately linear with temperature is called the ALD window. Below the ALD window temperature, precursor condensation and limited reactivity can lead to incorporation of impurities.

At temperatures below this window, limited precursor reactivity and precursor condensation can lead to both under- and over-saturated absorption respectively. Condensation can cause unwanted CVD-like growth, and an increased incorporation of impurities due to unreacted ligands or reaction by-products. At temperatures above the ALD window, precursor decomposition and desorption can also cause increased and decreased growth rates.

Most standard ALD reactors operate with an inert carrier gas in viscous flow. The pressure is normally approximately 1 mbar which is a trade-off between entrainment and gas interdiffusion. Above 1 mbar the mean free path between carrier gas molecules is too small for effective purging. Below 1 mbar the interdiffusion of stagnant precursor molecules in the carrier gas is decreased. A pressure of 1 mbar is chosen as a compromise between the two factors.

Throughout this thesis it is assumed that the ALD processes discussed are thermal processes, in other words that the energy required for the self-terminating reactions of *both* precursors to take place is supplied by the thermal environment of the ALD reaction chamber. This is opposed to plasma-enhanced ALD where the energy for at least one of the precursor chemisorption reactions is supplied via an direct or indirect plasma of the secondary precursor.

4.3 Development of ALD

ALD has its origin in experiments carried out by Finnish and Russian scientists in the 1960s and 1970s. The most commonly accepted origin of ALD stems from a technique

called 'atomic layer epitaxy' (ALE) developed by Suntola *et al.* in 1974 [90]. They initially demonstrated thin film growth based on elemental precursors: ZnS from Zn/S, SnO_2 from Sn/O_2 and GaP from Ga/P [90]. They also developed protocols for the use of compound materials such as Ta_2O_5 from $TaCl_5/H_2O$, Zn(Mn)S from $Zn(Mn)Cl_2/H_2S$ and Al_2O_3 from $AlCl_3/H_2O$ [91].

Besides ALE, the technique has been described by other terms such as 'binary reaction sequence chemistry' and 'molecular deposition' [92, 93]. The transition from ALE to ALD stems from the fact that most films grown using the earlier technique were not in fact epitaxial to the supporting substrate. The change was also enforced due to the preference for amorphous films for barrier and dielectric layers, which by their very nature are not epitaxial.

The refinement of ALD as a thin film technique has its roots in its early and continuous application for commercial processes, especially in the semiconductor industry. The first application of ALD in an industrial process was the fabrication of thin film electroluminescent displays in which both the insulating layers and the active layer, consisting of manganese doped zinc sulphide. The emergence and growth of a large scale semiconductor industry led to further developments of ALD [94–96].

In the last decade the uses of ALD for various nanotechnology applications have increased exponentially and have gone far beyond diffusion barrier layers [97] and pin-hole free dielectrics [98], the two areas for which ALD had traditionally been employed. More recent applications of ALD range from the modification of the properties of MEMS [99] and NEMS [100], to the creation of thin film transparent conductive oxides (TCO) [101], photonics [102] and photovoltaics [103].

4.4 ALD for photovoltaics

Photovoltaics plays an important role in the work of this thesis and as such the following section will cover some of the advances and applications of ALD for solar cells and related areas. This section is not meant as an extensive review of ALD use in photovoltaics and the reader is referred to the comprehensive reviews on the topic by Kessells *et al.* [103] and Bakke *et al.* [104].

The deposition of thin and ultra-thin layers by ALD for photovoltaic applications has been applied to a variety of solar cells concepts including crystalline and amorphous silicon, copper indium gallium selenide (CIGS), organic and dye-sensitised solar cells. The specific application of ALD can be split into three main directions: 1) the deposition of passivation, barrier and buffer layers; 2) the deposition of transparent conductive oxides and blocking layers; and 3) the deposition of sensitizers and photoanodes.

The first reported application of ALD in photovoltaics dates back to 1994 when Bedair *et al.* deposited GaAs, AlGaAs and AlAs as multi-junction absorbers [105]. Work on ZnSe for CIGS buffer layers [106] and doped ZnO TCOs followed these results [107]. The most significant advancement of ALD and its application into PV research has

however taken place over the last decade. This short overview will mainly focus on advances made for DSSCs. For applications of ALD in other types of solar cells such as silicon, CIGS and organic solar cells the reader is referred to a number of reviews on the topic [103, 104].

4.4.1 ALD in dye-sensitised solar cells

ALD has been used to advance and in some instances improve most of the constituent components of a traditional dye-sensitised solar cell ranging from barrier layers on TiO_2 mesostructures [108] to TCOs [109] and TiO_2 blocking layers [110], fully ALD deposited TiO_2 and ZnO photoanodes [111, 112] and thin film inorganic sensitisers [113, 114].

Barrier layers

One of the main limiting factors of DSSCs is the transport of charge carriers through the n-type mesoporous scaffold. Recombination of electron and hole charge carriers at the photoanode and dye or electrolyte interfaces leads to a low short-circuit current and poor device performance. The addition of a barrier layer on the surface of the photoanode can lower the probability of recombination by causing a longer diffusion length of electrons in the photoanode compared to the barrier layer. However the barrier layer also leads to a reduced injection of charge carriers into the photoanode. A thick layer leads to a lowered injection current since the electron tunnelling rate through the barrier layer decays exponentially with barrier thickness [115]. As such, a compromise has to be found between charge recombination and charge injection which depends on the barrier layer thickness. The layer thickness is typically on the order of a few nanometers. The requirement for fine control in layer thickness makes ALD one of the few deposition techniques capable of barrier layer growth on high-aspect-ratio structures.

A large variety of materials have been used as thin film barrier layers for mesoporous photoanode scaffolds. These materials include ALD deposited Al_2O_3, TiO_2, HfO_2 and ZrO_2. The most common choice of material represented in the literature is Al_2O_3 deposited using trimethyl aluminium (TMA) and water [116–118]. The increased power conversion efficiency seen when using alumina barrier layers is linked to the high energy barrier of recombination of the TiO_2/Al_2O_3 interface, the high work function of the Al_2O_3 and finally the low energy barrier of injection between the Al_2O_3 and the sensitising dye [116].

A difficulty which presents itself with the use of ALD on high-aspect-ratio structures such as the mesoporous nanoparticle networks used in DSSCs is that very long precursor exposure times are required (Section 4.6.3). A long exposure time is required to reach a surface saturation close to unity in each cycle and thereby to ensure a conformal coating within the entire structure. Depending on the number of cycles, this may result in a very long fabrication time. This problem is partially overcome in the case of alumina

barrier layers by the fact that the optimal performance of the device is achieved by the use of very thin films consisting of fewer than twenty cycles [118].

Contrary to the idea that an ultra-thin barrier layer would have little impact on the recombination rate, a single ALD layer of Al_2O_3 has been shown to lead to improved results [119]. Such a layer does not form a conformal coating on the photoanode surface, but it is reasoned that the improved performance stems from steric hindrance which prevents the dye molecules from absorbing on the TiO_2 surface [120], which leads to a reduced recombination rate.

Other methods such as sol-gel chemistries can also be used to fabricate Al_2O_3 barrier layers for DSSCs. ALD deposited layers perform similarly to these methods with an efficiency of 6.5 % for equivalent thicknesses of photoanodes [119, 120]. However ALD has the advantage that it is a gas phase deposition technique that can be carried out at relatively low temperatures, which makes it very suitable for temperature sensitive plastic substrates.

Blocking layers and TCOs

ALD has also been used to fabricate large area TCOs and blocking (compact) layers. TCOs are normally fabricated by the deposition of tin-doped indium oxide (ITO) or various doped thin films of ZnO and SnO such as aluminium- (AZO), indium- (IZO), gallium-doped zinc oxide and antimony-doped tin oxide (ATO) [121]. The deposition of ITO has been extensively studied by Martinson and co-workers who have developed a route to ITO via ALD. The ITO is grown using cyclopentadienyl (InCp), tetrakisdimethylamido tin (TDMASn) and water at a relatively low temperature of approximately 220 °C [109]. They report a mobility and resistivity of $110\,\mathrm{cm^2\,V^{-1}\,s}$ and $4.0 \times 10^{-4}\,\Omega\,\mathrm{cm}$ respectively for an approximately 40 nm thick film of ITO grown at 150 °C [109]. This corresponds favourably to ITO grown by other deposition techniques such as pulsed laser deposition and sputtering [122].

A large number of publications record the deposition of doped ZnO and SnO_2 compounds [123]. The most commonly deposited compound is aluminium-doped ZnO, created when ZnO deposition cycles (diethylzinc and water) are replaced with Al_2O_3 cycles. By varying the frequency of the Al_2O_3 cycles, the concentration of aluminium oxide can be adjusted from 0 % to 100 %. Recent advances in the fabrication of thin doped ZnO films by ALD have resulted in film properties that lie within an order of magnitude of ITO and FTO fabricated through traditional techniques. The state of the art doped ZnO thin films deposited by ALD have a reported resistivity and mobility of $9.8 \times 10^{-4}\,\Omega\,\mathrm{cm}$ and $11.2\,\mathrm{cm^2\,V^{-1}\,s}$ respectively. One of the drawbacks with these types of TCOs is the lowered performance seen for very thin films [124]. This limits the applicability of these films for high-aspect-ratio porous substrates.

Arguably, the use of ALD for the deposition of TCOs on high-aspect-ratio substrates could significantly increase device performance since it limits the distance of electron transport. The macroscopic TCO electrode could effectively be extended into the

mesoporous network. This concept was realised by Martinson *et al.* [109] when they deposited ITO (according to the protocol above) onto porous alumina membranes followed by a thin layer of amorphous titania, thus creating a new DSSC device structure. They report the increased performance of devices that include the deposited TCO compared to devices in which it is absent.

The traditional way of depositing compact or blocking layers for DSSCs is by using spray pyrolysis, a technique which has two major disadvantages. A high processing temperature is required to sinter and crystallise the formed titania, and thick films are required to avoid pin-holes and shorting pathways through the film. Hamann *et al.* [111] used ALD to deposit TiO_2 from titanium isopropoxide and water at 200 °C on FTO substrates and report very low dark-current densities indicating the pin-hole free nature of the TiO_2. A study was published recently by Kim *et al.* which shows that ultra-thin compact layers (<10 nm) deposited by ALD demonstrate comparable or better device performance compared to traditional routes for compact layer fabrication [125].

Photoanodes

ALD has also been used to deposit the photoanode itself. Martinson *et al.* [126] deposited ZnO on porous alumina membranes which exhibited faster transport compared to nanoparticle networks. Hamann *et al.* used silica aerogels to fabricate high surface area TiO_2 and ZnO photoanodes [111, 112]. Devices using these photoanodes displayed power conversion efficiencies over 5 %. One of the main studies in this thesis focuses on this specific use of ALD to replicate high-aspect-ratio polymer templates for use in solar cells (Chapter 7).

Sensitisers

The final and perhaps most interesting application of ALD for DSSCs is inorganic sensitizers or absorbers. However, to date there are still very few examples of ALD deposited absorbers. The main reason for this is most likely that useful inorganic absorbers consist of compounds such as sulphur which are more difficult to deposit using ALD than simple metal oxides. The method for depositing sulphides by ALD uses H_2S, a toxic and highly flammable gas, as a replacement for water, thus limiting the number of ALD reactors capable of depositing these materials.

Goossens *et al.* have reported on the deposition of Cu_xS and $CuInS_2$ by ALD [127]. These absorbing materials were used in mesoporous heterojunction solar cells. TiO_2 nanoparticle networks conformally infiltrated with Cu_xS and $CuInS_2$ displayed power conversion efficiencies of 4 %. Another thin film absorber which was very recently deposited on TiO_2 DSSCs is antimony sulphide (Sb_2S_3, stibnite) [128]. The research of Yang *et al.* built upon work by Grätzel *et al.* who used chemical bath deposition to deposit thin layers of stibnite on TiO_2 scaffolds in TiO_2/P3HT heterojunction devices [129]. Grätzel *et al.* report an impressive efficiency of 5 %. However the bath deposition

technique fails to address the persistent problem of a lack of control in the exact thickness and conformality of the deposit, a problem that ALD can overcome. In the work by Yang and co-workers they apply ALD grown stibnite to solar cells consisting of a TiO_2 mesoporous scaffold and a CuSCN hole conductor. A 9 nm thick layer of ALD grown stibnite on the surface of an approximately 2 µm thick TiO_2 film resulted in an efficiency of 2.6 % [114].

4.5 ALD materials

A large range of materials have been deposited using ALD including metals, organic compounds, organic/metallic hybrids and metal ceramics such as oxides, nitrides, selenides, sulphides and tellurides [130] (Figure 4.3). To ensure that the precursor properties of reactivity, thermal stability and volatility are suitable at a given deposition temperature, the ligands surrounding the central atom can be altered. The most common ligands are halides, alkyls, cyclopentadienyls and alkooxides. For more detailed information about ALD precursors see the reviews by Puurunen *et al.* and Miikkulainen *et al.* [130, 131].

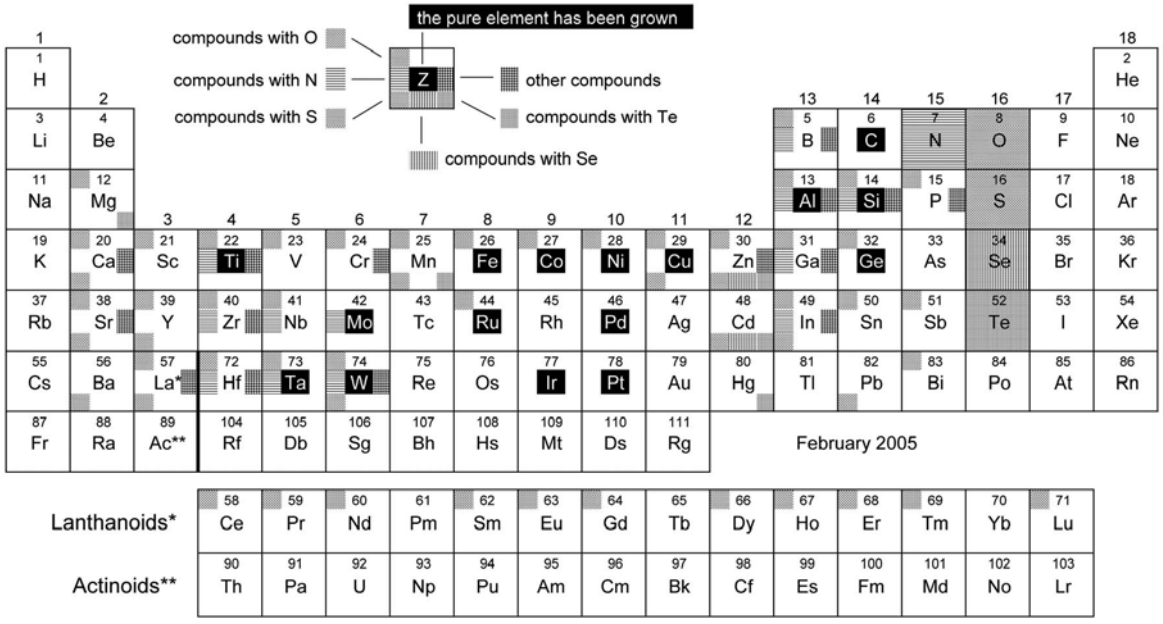

Figure 4.3: Periodic table displaying the different material compounds possible to deposit using ALD. Modified from Miikkulainen *et al.* [131]. Correct as of December 2010.

Halides are the oldest class of precursors and they have been studied extensively. The main benefits of halide reactants are that they are available for a large range of metals, that they are highly reactive and thermally stable and that the molecules are relatively small. The main disadvantages of halides are that most of them are solids at room temperature, that the by-products are corrosive, e.g. HCl from $TiCl_4$, and that

the thermal stability means that ligands can remain as impurities in the films after deposition. One of the few halides which is liquid at room temperate is $TiCl_4$.

Within the alkyl class of ligands are the common aluminium and zinc precursors trimethyl aluminium and diethylzinc. Since these are true organometallic compounds they are very reactive even at low deposition temperatures. The by-products are normally inert saturated hydrocarbons. The main drawbacks are that rather few elements have been synthesised as alkyls and that they have a relatively poor thermal stability.

More recently synthesised precursors have included cyclopentadienyls, alkoxides and beta-diketonates. Cyclopentadienyls and beta-diketonates have the benefit that they can be synthesised for alkaline earth metals. Alkoxides are now normally used together with other halides to deposit ternary compounds. However, these three types of precursor deposit only a limited range of materials, predominantly oxides, sulphides and metals.

There are a range of secondary precursors. The most common ones for oxides are water, hydrogen peroxide, molecular oxygen, ozone and oxygen radicals. For sulphides, selenides and nitrides, H_2S, H_2Se and HN_3 respectively are commonly used.

The following sections will cover the deposition of Al_2O_3, TiO_2 and ZnO in more detail, as these are the three main materials used in this thesis.

4.5.1 ALD Al_2O_3

The process of depositing Al_2O_3 from trimethyl aluminium (TMA) and water (H_2O) is normally considered to be closest to the ideal ALD process for three reasons: 1) the TMA/H_2O process is a thermal ALD which remains feasible even at low temperatures [132]; 2) the process deposits a metal oxide using water as the secondary precursor, i.e. the most commonly deposited inorganic material and the most frequently used oxygen source; 3) the reactions are fully self-terminating and the gaseous reaction by-product (methane) is relatively inert.

The reaction of the TMA with surface -OH groups has been shown to proceed with ligand exchange which produces Al-O bonds and releases methane [133] at temperatures between 80 °C and 300 °C [134]. The reaction between TMA and H_2O is described by two half-reactions, presented in Equations (4.1) and (4.2).

$$\|Al - OH\ (s) + Al(CH_3)_3\ (g) \rightarrow \|Al - O - Al(CH_3)_2\ (s) + CH_4\ (g) \tag{4.1}$$

$$\|Al - O - Al(CH_3)_2\ (s) + 2H_2O\ (g) \rightarrow \|Al - O - Al(OH)_2\ (s) + CH_4\ (g) \tag{4.2}$$

Given pulse and purge times long enough to ensure surface saturation, further lengthening of the TMA and H_2O pulses and purges does not alter the number of deposited species and therefore does not affect the deposition per cycle, as seen in Figure 4.4 [98]. The TMA chemisorption is also self-terminating with respect to the pressure of the TMA [135].

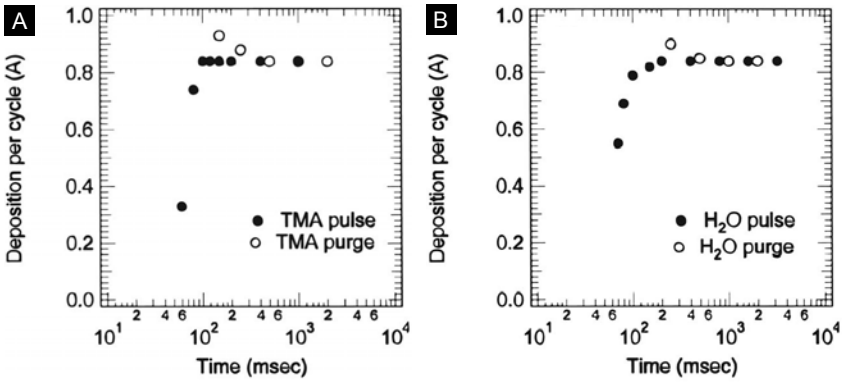

Figure 4.4: Growth rates of Al_2O_3 for varying TMA and H_2O pulse lengths at a deposition temperature of 300 °C. **(A)** The H_2O pulse and purge are kept constant and the TMA pulse and purge are varied. **(B)** The TMA pulse and purge are kept constant and the H_2O pulse and purge are varied. Modified from [98].

The amount of Al_2O_3 deposited per ALD cycle (growth per cycle) decreases with increasing deposition temperature [136]. This is due to a reduction in the number of available -OH groups at high temperatures due to the formation of oxygen bridges [137], rather than a change in the inherent reaction mechanism [134]. The average deposition rate within the ALD window is approximately 0.11 Å per cycle. The deposition of Al_2O_3 is amorphous for deposition temperatures ranging from room temperature to 300 °C, above which the trimethyl aluminium thermally decomposes.

4.5.2 ALD TiO_2

A number of precursors are available for the deposition of TiO_2, including titanium tetrachloride ($TiCl_4$), titanium isopropoxide (TTIP) and tetrakis(dimethyl)titanium (TDMAT). In this thesis, $TiCl_4$ with either H_2O or H_2O_2 is the main precursor used. A thermal range of 80 °C to 400 °C has been studied by Aarik *et al.* and Triani *et al.* [89, 138], and a few examples of TiO_2 depositions at lower temperatures have also been reported [139]. The deposition rate ranges from 0.4 Å to 0.8 Å per cycle depending on deposition temperature. Aarik and Triani showed that the increasing growth rate with decreasing deposition temperatures is most likely caused by the incorporation of reaction by-products or unreacted precursor ligands into the deposition. The inclusion of these chlorine-containing species leads to an increasing amount of chlorine impurities with decreasing temperatures. At 80 °C TiO_2 films deposited on Si contained 3.3 at% Cl, whereas deposition at 100 °C, 120 °C, 160 °C displayed chlorine impurities of 1.8 at%, 1.5 at% and 0.4 at% respectively [89, 138].

Aarik *et al.* showed that the reaction mechanism between $TiCl_4$ and water varies with deposition temperature. Between 100 °C and 150 °C $TiCl_4$ reacts with one surface -OH group.

$$\|\mathrm{Ti-OH\ (s)} + \mathrm{TiCl_4\ (g)} \rightarrow \|\mathrm{Ti-O-TiCl_3\ (s)} + \mathrm{HCl\ (g)} \tag{4.3}$$

The following H_2O pulse then removes three chlorine ligands to recover the initial single hydroxyl group.

$$\|\mathrm{Ti-O-TiCl_3\ (s)} + \mathrm{2H_2O\ (g)} \rightarrow \|\mathrm{Ti-O-TiO(OH)\ (s)} + \mathrm{3HCl\ (g)} \tag{4.4}$$

For higher temperatures deposition can also occur via the formation of intermediate volatile surface species, $(TiOH)_xCl_{4-x}$, which can cause agglomeration phenomena [140] as well as influence the conditions under which crystallisation occurs.

The deposition temperature also affects the crystallographic structure and surface roughness of the deposited TiO_2. Below 165 °C smooth amorphous films are obtained [138]. For higher temperatures the surface roughness increases and the films are mainly anatase until 350 °C at which point the rutile TiO_2 phase becomes dominant [138]. TiO_2 can also be deposited from $TiCl_4$ and hydrogen peroxide (H_2O_2). Aarik *et al.* have shown that the use of H_2O_2 enables a more complete removal of the chlorine ligands, thus forming more hydroxyl groups per cycle and leading to an increase in the deposition rate [141].

4.5.3 ALD ZnO

Zinc oxide is most commonly deposited from diethylzinc (DEZ) and water. The deposition of ZnO using these two precursors from 20 °C to 350 °C has been studied by Suntola *et al.* [142], Konagai *et al.* [143] and Nam *et al.* [139]. They show that self-limited growth occurs throughout the entire temperature range. However surface morphology and crystal orientation are strongly dependent on deposition temperature. At very low temperatures (below 100 °C) the films display a single crystalline (002) direction. Between 100 °C and 165 °C the (100) and (101) directions are dominant whereas for temperatures above 165 °C the (002) direction again dominates. This observed crystallinity, even at room temperature, is explained by the high ionic strength between zinc and oxygen. Amorphous ALD deposited ZnO films have been reported but only for thicknesses below 4 nm [144, 145].

The deposition of ZnO proceeds according to Equation (4.5) and Equation (4.6) with a reaction by-product of ethane.

$$\|\mathrm{Zn-OH\ (s)} + \mathrm{Zn(C_2H_5)_2\ (g)} \rightarrow \|\mathrm{Zn-O-ZnC_2H_5\ (s)} + \mathrm{C_2H_6\ (g)} \tag{4.5}$$

$$\|\mathrm{Zn-O-ZnC_2H_5\ (s)} + \mathrm{H_2O\ (g)} \rightarrow \|\mathrm{Zn-O-Zn-OH\ (s)} + \mathrm{C_2H_6\ (g)} \tag{4.6}$$

According to the existing literature, the deposition rate of ZnO across the ALD window varies from 1.2 Å/cycle at room temperature to 0.5 Å at 350 °C displaying a maximum deposition rate of just below 1.7 Å/cycle at approximately 140 °C.

4.6 Non-ideal ALD substrates

ALD films grown on inorganic, planar, high-temperature stable substrates with a high native density of suitable functional groups, such as silicon with a native oxide layer, all display similar properties to the materials described in the previous three sections. However most of the substrates used in this study are not planar, inorganic substrates with a high temperature stability. Instead they consist of thin polymeric films with a glass transition temperature of 100 °C or below. Moreover some of the substrates exhibit high-aspect-ratios and surfaces with very few or no functional groups. This section will look at the properties of non-ideal substrates by focusing on the current physical understanding of area-selective ALD, ALD on polymers and ALD on high-aspect-ratio structures.

4.6.1 Area-selective ALD

Area-selective ALD looks at ways to decrease the deposition rate or alternatively to prevent deposition in certain areas of the substrate entirely, as well as to promote growth on substrates normally void of functional groups. This is interesting for the purposes of this thesis since it gives an understanding of the importance of the functional groups required on the substrate surface in order for the deposition to nucleate and grow uniformly.

Selective growth is normally achieved by the functionalisation of the deposition surface with self-assembled monolayers (SAMs) which incorporate end-groups inert to ALD. This method has been used to achieve near complete area-selective growth for SAMs of a sufficient thickness [146]. An alternative route to area selectivity is the application of poly(methyl methacrylate) (PMMA) to the substrate. It has been shown that PMMA is sufficiently inert to prevent ALD growth of ZnO for up to 1200 cycles, and PMMA has been patterned via photo-lithography to achieve area selectivity [147].

Functionalisation can also be used to enhance growth on otherwise inert substrates. Nitrogen dioxide/trimethyl aluminium and nitroaniline have been used to functionalise carbon nanotubes in order to allow growth of both Al_2O_3 and HfO_2 [148] and ozone has been used to promote growth on the otherwise extremely inert graphene [149].

4.6.2 ALD on polymers

Until recently, ALD was not carried out on thermally sensitive surfaces such as polymers since they decompose or soften at the temperatures required for most ALD processes. In addition most polymers do not contain the functional surface groups required for uniform nucleation and growth.

The mechanism by which ALD proceeds on polymers has been studied by Puttaswamy *et al.* and Wilson *et al.* [150, 151]. Wilson and co-workers spin-coated various polymers

on QCM sensors and monitored the mass uptake caused by the TMA and water pulses during the deposition of Al_2O_3. Their main observation is that the diffusion of the reactants in and out of the film during the pulse and purge steps has a strong influence on the nucleation mechanism, as can be seen from the schematic in Figure 4.5.

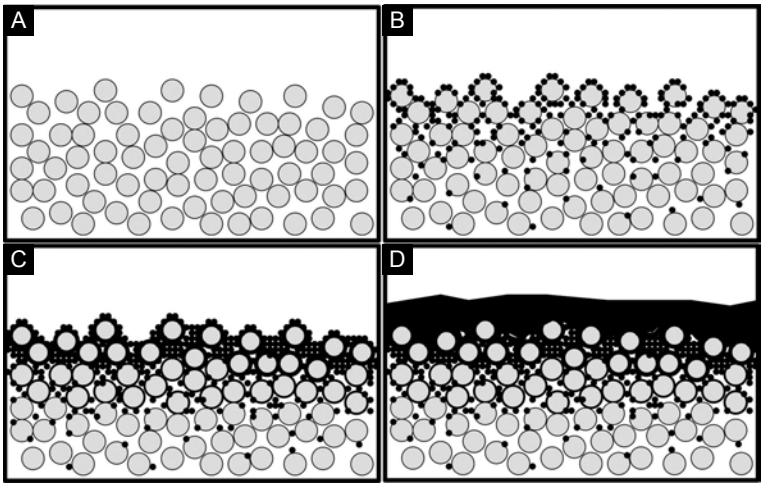

Figure 4.5: Model for ALD growth on polymer surfaces. **(A)** Cross-section through a polymer film where the polymer chains are represented by circles. **(B)** The incomplete removal of TMA molecules during the purge cycle leads to the formation of Al_2O_3 clusters during the H_2O pulse. **(C)** An increasing number of cycles causes the clusters to coalesce and fill the voids between polymer chains. **(D)** Beyond a certain cycle threshold, TMA diffusion into the polymer is prevented and a dense Al_2O_3 film grows on top of the polymer surface. Modified from Wilson *et al.* [151].

An incomplete removal of the primary reactant from the sub-surface region of the polymer during the purge step leads to the formation of nucleation clusters in the near surface region during the chemisorption of the secondary precursor. These clusters promote further nucleation and growth, and they will eventually coalesce and form a continuous film. This continuous film prevents further diffusion of reactants into the polymer and the deposition proceeds according to the standard ALD growth mechanism. The reduced diffusion through continuous thin films has in fact been exploited to encapsulate moisture sensitive devices such as CIGS and organic solar cells and organic light emitting diodes [152].

Puttaswamy *et al.* used x-ray photoelectron spectroscopy (XPS) to determine the delay in continuous growth of Al_2O_3 (using TMA and water) on polystyrene surfaces. They showed a delay of 40 cycles before aluminium could be detected using XPS. The high surface roughness, measured by atomic force microscopy, of Al_2O_3 growth on smooth spin-coated polystyrene films indicates an island growth mode [130] which can be caused by both a low density of functional surface groups and by sub-surface nucleation as described above.

4.6.3 ALD on high-aspect-ratio surfaces

Two of the main projects in this thesis employ the growth of conformal ALD coatings on high-aspect-ratio (HAR) structures. As such it is necessary to understand what factors influence ALD growth and how the important parameters of purge time and precursor dose scale with the aspect ratio of the structure. ALD deposition inside HAR structures has been studied extensively by George *et al.* [153], Gordon *et al.* [154], Detavernier *et al.* [155], Knez *et al.* [95] and Karuturi *et al.* [156, 157] and the reader is referred to these publications for more detailed descriptions.

Since ALD is a technique that relies on gas-phase reactions, it is conceptually easy to understand that an increased distance between the gas reservoir and the reaction sites necessitates an increased exposure time. The increased exposure time required to allow the self-terminating reactions to reach a coverage close to unity is accompanied by an increasing purge time to allow for the complete removal of unreacted reactants and reaction by-products.

At the pressures normally used for ALD, the dimensions of the pores of the HAR structures used in this work are much smaller than the mean free path of the precursor and the by-product molecules. As such, the reactants are in free molecular flow and the transport of precursors into and out of the structure is governed by Knudsen diffusion where molecules travel ballistically between interactions with the template surface.

Al_2O_3 depositions inside HAR porous alumina membranes by Elam *et al.* [153] confirmed that conformal coatings inside HAR structures are indeed dependent on reactant exposure times. For a membrane (pores accessible from both sides) with a pore size of 65 nm and a thickness of 50 µm (aspect ratio $>$ 500:1), exposure times of more than 30 s were required for a conformal coating throughout the membrane compared to less then 1 s for a planar surface.

Depositions of ZnO in HAR alumina membranes also showed a similar behaviour [153]. Energy-dispersive x-ray spectroscopy used to determine the coverage as a function of depth found that the integrated coverage (the total amount of ZnO deposited) scales as $t^{1/2}$ where t is the exposure time. This demonstrates that the reactant flow is limited by diffusion and can be understood by kinetic gas theory.

Monte Carlo simulation of diffusion in a one-dimensional pore showed that the total exposure time, T, scales as $1/k^2$.

$$k = 2.1 \times 10^3 \; P^{1/2} m^{-1/4} N^{-1/2} a^{-1} \tag{4.7}$$

P is the pressure (Torr), m is the atomic mass (amu) of the precursor molecule, N (cm^{-2}) is the surface density of accessible sites and $a = L/d$ is the aspect ratio with d and L being the diameter and length of the pore respectively. This implies $T \propto (L/d)^2$, i.e. the required pulse time scales as the square of the aspect ratio.

Gordon *et al.* [154] used gas conductance equations to derive an analytical expression for the exposure times required to reach a coverage of unity as a function of aspect

ratio. This approach is in agreement with the work by Elam and co-workers and it also shows that the required exposure time scales as the square of the aspect ratio. The required exposure time, t, is given by

$$t = \frac{S}{P\,\Gamma}\sqrt{2\pi mkT}\left(1 + \frac{19}{4}a + \frac{3}{2}a^2\right), \tag{4.8}$$

where S is the saturated surface density, P is the partial pressure of the reactant, Γ is the reactive sticking coefficient, m is the mass of the precursor molecules, k is Boltzmann's constant and T is the deposition temperature. For high-aspect-ratios, the a^2 term in $(1 + (19/4)a + (3/2)a^2)$ dominates and the required time is proportional to the aspect ratio squared.

ALD has previously been used to coat a number of HAR nano-structures. The most common are the alumina membranes described above, into which a large number of materials have been deposited including Al_2O_3, ZnO, TiO_2, Fe_2O_3 [158], Ni and Co [159] and Sb_2S_3 [128] to name a few. ALD has also been used to coat high-aspect-ratio MEMS devices [160], track-etched poly(carbonate) membranes [161], colloidal arrays [162] and recently ultra-HAR aerogels [163].

To date, most experimental studies and simulations have looked at systems where the pore diameter is much larger than the diameter of the diffusing precursor molecules, effectively treating them as point particles. On this basis, it is possible to make the assumption that only the aspect ratio of the system will affect the required diffusion time. However the work by Kucheyev *et al.* supports the idea that depositions in porous systems, with a pore diameter below 30 nm, do not proceed solely via Knudsen diffusion [164]. The measured penetration depths inside silica aerogel monoliths with pore diameters of 18 nm and 27 nm suggest that other processes such as physisorption between the precursor and by-product molecules and the pore walls can limit the deposition depth. Kucheyev *et al.* argue that even a small increase in residence times due to physisorption can significantly lower the effective diffusion coefficient through the pores. They also found that increasing exposure times did not lead to a correspondingly increased penetration depth. They argue that one possible explanation for this behaviour is that confinement could lead to increased precursor decomposition even at deposition temperatures where the precursor is normally stable.

Non-ideal ALD depositions in high-aspect-ratio templates have also been reported by Karuturi *et al.* who studied TiO_2 depositions at 70 °C in colloidal templates [156, 157]. Even though the aspect ratios of the templates mean that the deposition is Knudsen limited, Karuturi reported non-ideal ALD growth with non-uniform thicknesses, which varied with exposure time and the precursor concentration.

4.7 Properties of deposited materials

The ALD system used for all of the materials deposited in this thesis is a Beneq TFS200 reactor which is equipped with three liquid precursor lines as well as a number of gas precursor lines and a hot source capable of heating solid or low vapour pressure liquid precursors to 200 °C. An inert carrier gas flow of 200 SCCM of 6N N_2 was used unless otherwise specified. The normal reactor base pressure was 1.3 mbar. All precursors were kept at 20 °C and were allowed to evaporate unassisted.

Throughout this work the deposition rates, refractive indices and in some cases impurities and crystal structures of the deposited Al_2O_3, TiO_2 and ZnO have been characterised on planar silicon substrates. Prior to deposition, the silicon substrates were cleaned by piranha etching (3:1 H_2SO_4:H_2O_2 at 80 °C) for 10 min. The deposition rates were normally determined by at least four different films with thicknesses varying from 100 to 1000 cycles. Film thicknesses and refractive indices were determined by spectroscopic ellipsometry (Woollam α-SE). The refractive indices, unless otherwise specified, were measured for films consisting of 1000 cycles to ensure that the bulk regime for refractive index had been reached. They are quoted for a wavelength of 632.8 nm. The elemental analysis was carried out using energy-dispersive x-ray spectroscopy (Section 5.2.1).

The next three sections will cover the properties of Al_2O_3, TiO_2 and ZnO depositions on silicon substrates,detail their dependence on deposition temperature, and show how they compare to literature values. For depositions of Al_2O_3, TiO_2 and ZnO on non-planar substrates see Chapter 7.

4.7.1 Al_2O_3

Aluminium oxide was deposited from +97 % trimethyl aluminium (TMA) and 18 MΩ DI water. The pulse times for the TMA and the water were both 250 ms for planar substrates. Purge times for the TMA and water pulses varied as a function of deposition temperature between 250 ms and 10 s, and 250 ms and 15 s respectively.

The growth rate of Al_2O_3 on silicon (Figure 4.6A) is relatively constant at approximately 1.1 A per cycle from 60 °C to 250 °C, with a decreased growth rate at higher temperatures due to a decreased density of -OH groups. The deposition rates agree with literature values (Section 4.5.1). As expected, the refractive index (Figure 4.6B) increases with increasing deposition temperatures and reaches a maximum value of 1.63 at 300 °C.

4.7.2 TiO_2

In this thesis, titanium dioxide was mainly deposited from +99.5 % titanium tetrachloride ($TiCl_4$) and 18 MΩ DI water. The pulse times for the $TiCl_4$ and the water were

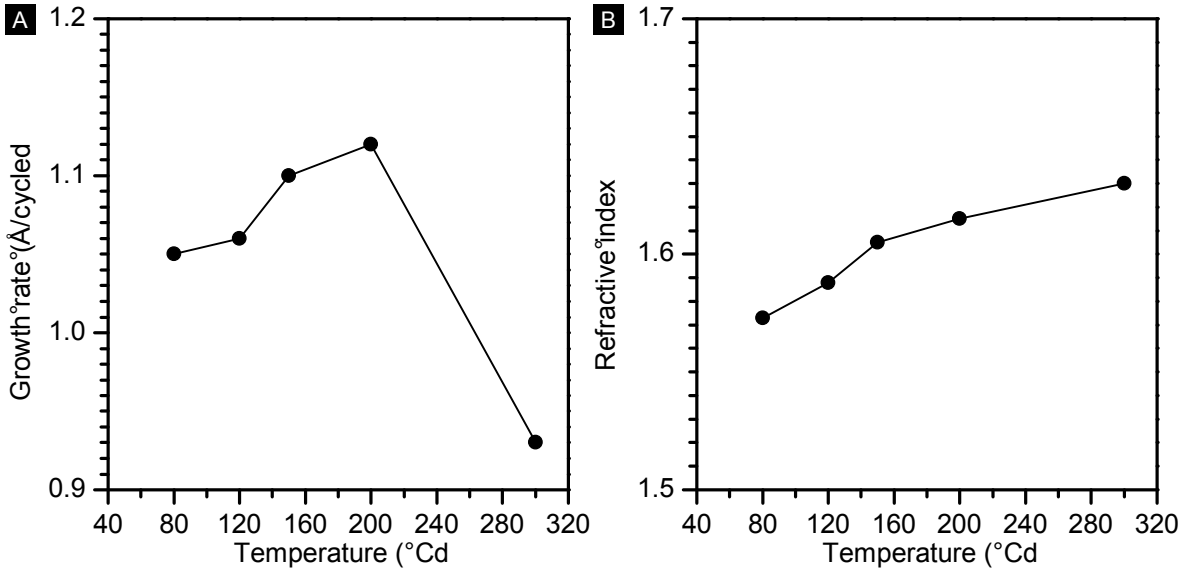

Figure 4.6: Temperature dependence of the growth of Al_2O_3 on silicon. The Al_2O_3 was deposited from +97 % trimethyl aluminium (TMA) and 18 MΩ DI water. **(A)** Growth rate of Al_2O_3. **(B)** Refractive index of Al_2O_3.

350 ms and 250 ms respectively for planar substrates. The purge times for the $TiCl_4$ and water pulses varied between 500 ms and 15 s, and 250 ms and 20 s respectively. The growth rate of TiO_2 on silicon substrates as a function of deposition temperature is shown in Figure 4.7A. The measured rates are consistent with literature values (section 4.5.2). The refractive index (Figure 4.7B) varies from 2.29 at 60 °C to 2.45 at 300 °C. As expected from the crystallographic transition at approximately 165 °C [138], a step change in refractive index is also seen between 150 °C and 200 °C.

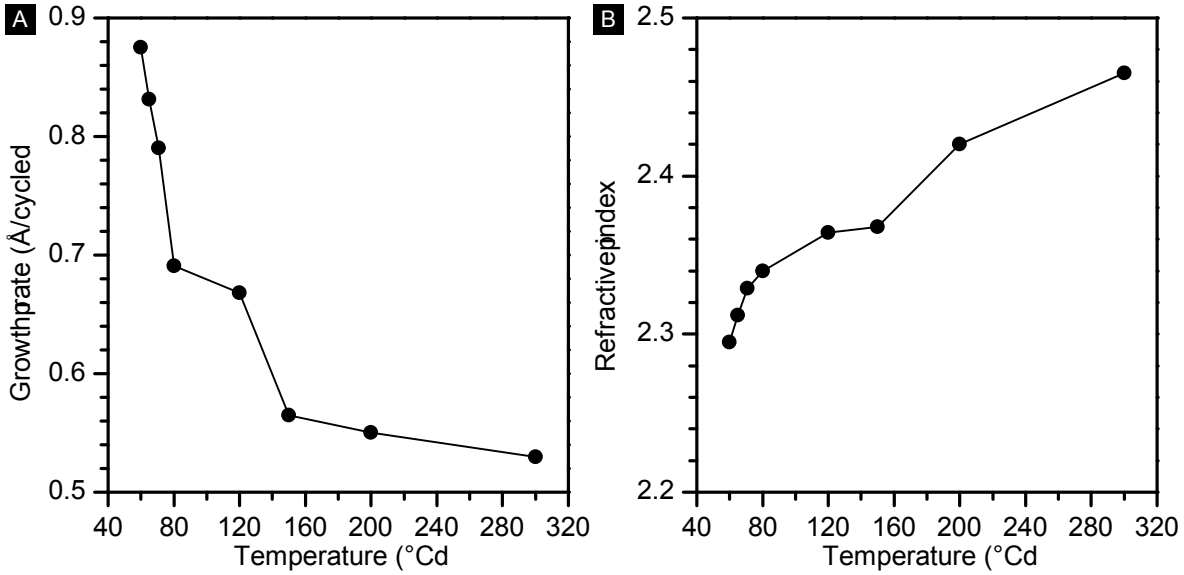

Figure 4.7: Temperature dependence of the growth of TiO_2 on silicon. The titania was deposited from +99.5 % titanium tetrachloride ($TiCl_4$) and 18 MΩ DI water. **(A)** Growth rate of TiO_2. **(B)** Refractive index of TiO_2.

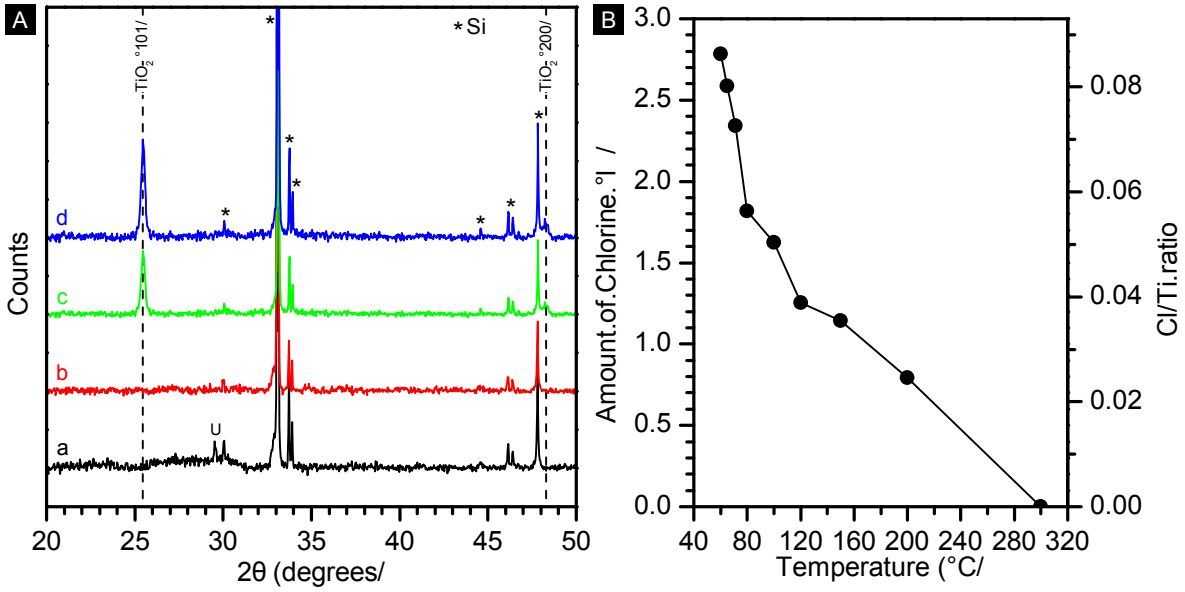

Figure 4.8: XRD and EDX spectra of ALD deposited TiO_2. **(A)** All film thicknesses were 100 nm deposited on a Si substrate. **(a)** - **(d)** show the XRD spectra for deposition temperatures of 100 °C, 150 °C, 200 °C and 300 °C respectively. One peak at 100 °C is unidentified and is denoted by U. **(B)** Chlorine contaminations as a function of deposition temperature. EDX spectra were acquired at 15 keV with an integration time of 5 min.

Measurements using EDX confirmed that the only elemental impurity is chlorine. Figure 4.8B shows the chlorine content as atomic percent and as a chlorine/titanium ratio, both as a function of deposition temperature. As expected from the literature, a significant amount of chlorine was detected at low deposition temperatures with the highest chlorine concentration of 2.8 % at 60 °C. At 200 °C the amount of chlorine was 0.8 % and at 300 °C the ratio was below the detection limit of our EDX.

The crystallinity of the TiO_2 growth as a function of deposition temperature is shown in Figure 4.8A. These spectra are consistent with the amorphous/crystalline transition taking place between 150 °C and 200 °C. Above 200 °C the anatase TiO_2 phase with the (101) direction normal to the surface dominates.

4.7.3 ZnO

Zinc oxide was deposited from +95 % diethylzinc (DEZ) and 18 MΩ DI water. For planar substrates, pulse times for the DEZ and the water were 350 ms and 250 ms respectively. Equivalent purge times for the DEZ and water varied between 500 ms and 10 s, and 250 ms and 15 s. The deposition rates display a maximum of 2.2 Å/cycle at approximately 150 °C, decreasing for both higher and lower temperatures (Figure 4.9A). This behaviour is consistent with the deposition rates described in Section 4.5.3. The refractive index also follows a similar trend to the growth rate with a maximum of 2.02 at 150 °C and lower refractive indices at both lower and higher deposition temperatures.

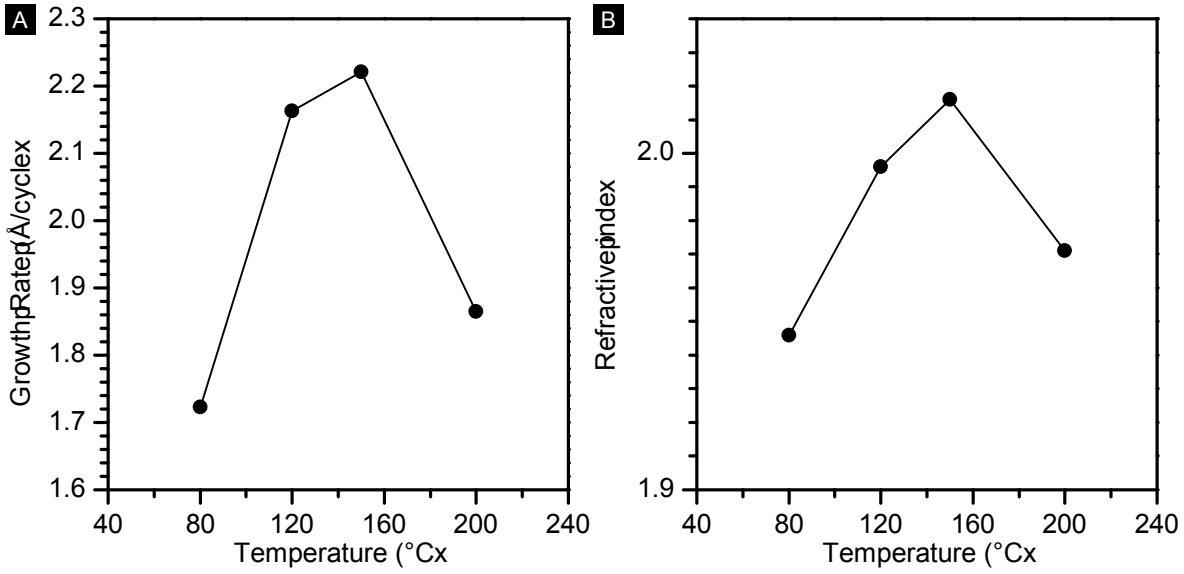

Figure 4.9: Temperature dependence of the growth of ZnO on silicon. The ZnO was deposited from +95 % diethylzinc (DEZ) and 18 MΩ DI water. **(A)** Growth rate of ZnO. **(B)** Refractive index of ZnO.

The deposited ZnO is crystalline for all deposition temperatures, as seen in Figure 4.10, except for very thin films (20 nm) deposited at 80 °C. To exclude the possibility that the film thickness could affect the crystallisation behaviour, the number of deposition cycles was varied to produce films that were 100 nm thick. The main crystallographic orientations are a strong function of both the deposition temperature and the film thickness. The primary and secondary orientations normal to the substrate surface for depositions at 80 °C, 120 °C, 150 °C and 200 °C are (100)/(002) (similar intensities), (100)/(002), (002)/(100) and (100)/(002) respectively. Doubling the film thickness at 80 °C reverses the primary and secondary orientations (Figure 4.10b compared to Figure 4.10c). Interestingly, deposition of 20 nm of ZnO at 80 °C suppresses crystallisation as shown in Figure 4.10a. This has been reported previously for ALD deposited ZnO but only for films thinner than about 15 cycles (3 nm) [144, 145]. We speculate that the reduced deposition temperature combined with a possible increase in impurities extends the film thickness for which this suppression of crystallisation takes place.

Elemental analysis using EDX shows no detectable amount of carbon at any deposition temperature.

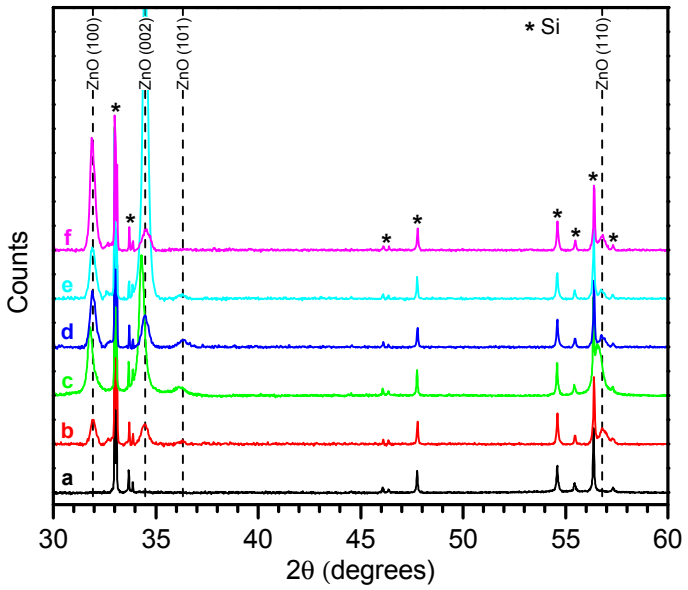

Figure 4.10: XRD spectra of ZnO as a function of temperature and film thickness. All films were deposited on a silicon substrate. **(a)** - **(c)** show XRD spectra for a deposition temperature of 80 °C with film thicknesses of 20 nm, 200 nm and 400 nm respectively. **(d)** - **(f)** show XRD spectra for deposition temperatures of 120 °C, 150 °C and 200 °C respectively with a film thickness of 200 nm.

4.8 Summary

This chapter has introduced a thin film deposition technique called atomic layer deposition. The historical development, including its application to photovoltaics, and the physical and chemical underpinnings of ALD have been described together with the current understanding of depositions on non-ideal surfaces such as polymeric and high-aspect-ratio substrates.

The research methods detailed in the chapter will serve as a foundation for the novel contributions made by this thesis in the fields of photovoltaics and biomimicry.

5 Experimental techniques and methods

This chapter details the experimental techniques and methods used throughout the thesis. The main topics are structural and material characterisations, electrochemistry, solar cell fabrication and characterisation, polymer synthesis and fabrication of porous polymer templates. Methods and techniques which are specific to an individual study will be given in the relevant chapter.

5.1 Structural characterisation

In the presented research, a large range of characterisation techniques are used to determine structural features of fabricated samples. They can be divided into three categories: direct imaging, scattering techniques and optical techniques. The direct imaging techniques range from optical microscopy for resolution of features on the 1 µm to 100 µm length scale, to scanning electron and transmission electron microscopy with a resolution limit of 2 nm and 0.2 nm respectively. The scattering techniques include wide-angle and gracing-incident x-ray scattering and the main optical technique employed is ellipsometry.

5.1.1 Electron microscopy

Electron microscopy is used to image sample features smaller than the diffraction limit of optical microscopy, which is on the order of 0.5 µm depending on illumination wavelength. The increased resolution is achieved by using an accelerated beam of electrons which has a much shorter effective wavelength. Depending on the acceleration voltage and the thickness of the specimen, the interactions between the electrons and the specimen can be designated as either transmission electron microscopy (TEM) or scanning electron microscopy (SEM).

Scanning electron microscopy

The two main detectors used to characterise samples in SEM are a secondary electron detector and a detector for energy-dispersive x-ray spectroscopy (EDX) (Section 5.2.1). The penetration depth and therefore the interaction volume between the sample and the electrons is very small (less than 10 nm) due to the relatively low electron energy. The achievable resolution is a function of the interaction volume, the effective interaction between the sample and the electrons and the spot size of the electron beam. A number of factors can deteriorate the imaging resolution including the charging of the sample by excessive secondary electrons. This is normally overcome by coating the sample with a continuous but very thin (1 nm to 2 nm) metal coating.

Two scanning electron microscopes were used in this thesis: a LEO ULTRA 55 SEM field emission microscope operated at an acceleration voltage of 2 keV to 20 keV; and a high-resolution Hitachi S-5500 field emission microscope operating at 1 keV to 5 keV. Thin metal coatings (Au, Au/Pd or Cr) designed to prevent charging effects were applied using an Emitech K575X Turbo sputter coater. Typical plasma currents and sputtering times were 30 mA and 4 s respectively. Samples were imaged either from the top or in a cross-sectional configuration at 45° or 90°.

Transmission electron microscopy

Transmission electron microscopy was used to achieve atomic imaging resolution of the inorganic samples produced in this thesis. This technique allows for the characterisation of crystal domains, including both size and orientation, in relation to constraints imposed by the fabrication surrounding and geometry such as the size and shape of templates. Two microscopes are used in the thesis. The first is an FEI Philips Tecnai 20 TEM operating at an acceleration voltage of 200 keV using a LaB_6 filament, the second is a JEOL 4000EX high-resolution TEM operating at an acceleration voltage of 400 keV using a LaB_6 source with a maximum resolution of approximately 0.2 nm. Samples to be imaged using TEM were scraped off their supporting substrates onto a copper grid coated with a thin layer of holey amorphous carbon.

5.1.2 Scattering techniques

Various scattering techniques, including WAXS, GI-WAXS and GI-SAXS were used to probe the internal order and to obtain structural information about the fabricated samples. All of the scattering techniques employed rely on the use of a monochromatic beam of x-ray radiation of a wavelength λ, and the recording of the scattered intensity as a function of one or more diffraction angles $\theta_{1,2}$. The measured scattering angle is related to the reciprocal space scattering vector $\mathbf{q}$ as described in Equation (5.1), where $\mathbf{k}_i$ and $\mathbf{k}_f$ are the incident and scattered wave vectors respectively, θ the scattering angle and λ the wavelength of the incident beam.

$$\mathbf{q} = \mathbf{k}_f - \mathbf{k}_i = \frac{4\pi \sin\theta}{\lambda} \tag{5.1}$$

Maximum intensity is achieved for constructive interference from a set of real space lattice points. Given that the spacing of lattice planes in reciprocal space G is related to the spacing in real space d via $G = 2\pi/d$, this leads to the well-known diffraction condition

$$n\lambda = 2d_{hkl} \sin\theta \tag{5.2}$$

where d_{hkl} is the spacing of the lattice planes defined by hkl, and n is the order of the scattering peak. Given the allowed hkl values for known crystallographic structures, the

particular mesoscale morphologies or the atomic-scale order of the measured samples can be determined.

Wide angle x-ray scattering (WAXS)

Wide angle x-ray scattering (commonly known as x-ray diffraction or XRD) is used to probe the composition of crystalline materials. Due to the small real space lattice spacings and therefore large q values, the scattering angles are normally in the range of $2\theta = 15^\circ$ to 80°. The diffraction patterns that are obtained from XRD can be used to identify the specific crystallographic phases present by a comparison of the spectra to those documented in the International Centre for Diffraction (ICDD) Powder Diffraction Database [165]. XRD spectra in this thesis were obtained using a Bruker B1 diffractometer fitted with a PSD LynxEye detector at a illumination wavelength $\lambda = 0.154\,\mathrm{nm}$ (Cu_α). Typical 2θ angles were between 20° and 80°.

Gracing incident wide angle x-ray scattering (GI-WAXS)

Gracing incident wide angle X-ray scattering is a wide-angle detection technique that is used for the characterisation of the crystalline composition of thin films ($<$100 nm). In this research, the measurements were performed at beamline D1, at the Cornell High Energy Synchrotron Source (CHESS) at Cornell University in Ithaca, NY, U.S.A. at a wavelength of 1.17 Å. The beam was focused to a size of 500 µm × 100 µm (horizontal × vertical) at the sample position, with an incident angle of 0.4°. A beam stop was employed for the intense reflected beam and the strong diffuse scattering in the incident plane. A Fujifilm image plate with an area of 2500 × 2000 pixels was used for the detection of the scattered intensity. A GE Typhoon FLA 7000 was used to develop the collected pictures. The measuring time was either 60 s or 120 s and the measured scattering intensities were adjusted to take into account the varied measuring times. The sample-detector distance was 0.25 m for all the samples. The samples were moved out of the beam after each measurement to avoid beam damage. The conversion of the 2D images as well as the construction of 1D profiles were carried out by **Alessandro Sepe** using the GISAXS Analysis Package [166], written within the Igor Pro development environment.

Gracing incident small angle x-ray scattering (GI-SAXS)

Gracing incident small angle x-ray scattering is the small angle analogue to GI-WAXS. It is used in the characterisation of the nano-scale structure of thin films, for example block copolymer morphologies. The sample is illuminated at a very shallow angle, close to the critical angle of the thin film, and the scattered intensity is measured using a two-dimensional detector which allows the extraction of structural information both parallel and perpendicular to the substrate as seen in Figure 5.1. Analysis and modelling of the data can identify both the phase morphology and its orientation relative to the

substrate. All of the known phase morphologies of diblock copolymers have previously been extracted from GI-SAXS data [167–173]. The peak positions corresponding to the double-gyroid morphology are shown in Table 5.1.

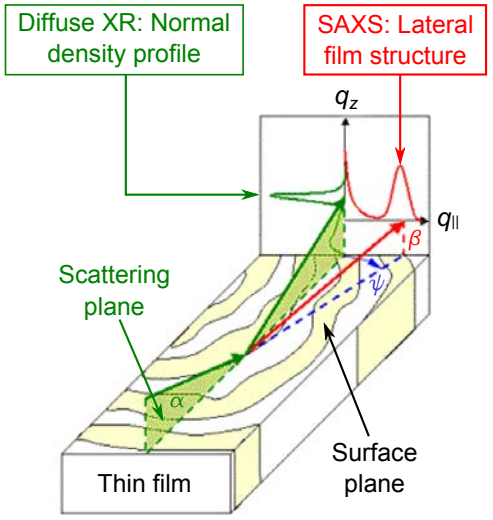

Figure 5.1: Schematic of GI-SAXS scattering configuration. The angles α, β and ψ correspond to the incident, the exit and the in-plane scattering angles respectively. Modified from [174].

Scattering maxima	1	2	3	4	5	6
hkl	211	220	321	400	420	332
q_{hkl}/q_{100}	$\sqrt{6}$	$\sqrt{8}$	$\sqrt{14}$	$\sqrt{16}$	$\sqrt{20}$	$\sqrt{22}$
d_{hkl}/d_{100}	0.408	0.354	0.267	0.250	0.224	0.213

Table 5.1: GI-SAXS peak positions for an undistorted gyroid morphology.

The measurements were performed at beamline D1, at the Cornell High Energy Synchrotron Source (CHESS) at Cornell University in Ithaca, NY, U.S.A. at a wavelength of 1.17 Å. The beam was focused to a size of 500 µm x 100 µm (horizontal x vertical) at the sample position, with an incident angles of 0.11°, 0.15°, 0.18° and 0.20°. A tantalum rod with a diameter of 2 mm served as a beam stop for the intense reflected beam and the strong diffuse scattering in the incident plane. A MedOptics CCD detector was used for the detection of the scattered intensity. It has a pixel size of 47 µm x 47 µm. The measuring time was 3 s. The sample-detector distance was 1.846 m for all samples. The samples were moved out of the beam after each measurement to avoid beam damage. $q_{||} = \sqrt{{q_x}^2 + {q_y}^2}$ and q_z denote the in-plane and the normal components of the scattering vector respectively. For small incident and scattering angles, the coordinates of the 2D detector correspond approximately to q_y and to q_z. The q-space calibration was performed by fitting the characteristic ring arising from the silver behenate scattering signal.

The conversion of the 2D images from pixels to q-values, the construction of 1D profiles and the pattern analysis using the distorted wave Born approximation model [35] were

carried out by **Alessandro Sepe** using the GISAS Analysis Package [166], written within the Igor Pro development environment.

5.1.3 Ellipsometry

Ellipsometry is an optical thin film characterisation technique which is used to determine film properties such as thickness, refractive index and absorption. This is accomplished by measuring the change in polarisation state of a collimated monochromatic beam as it is reflected off the thin film surface. It relies on the fitting of a model based on the Fresnel equations to the measured experimental data [175]. In nulling ellipsometry the polarisation change of the thin film is determined by adjusting a set of linear polarisers and quarter-wave plates such that the intensity of the reflected beam is at a minimum (or nulled). If the incident polarisation is known, the ellipsometric parameters ϕ and Δ of the film can be extracted, and can be used in the modelling to determine the film parameters. If multiple fitting parameters are used, variable-angle (VAE) or spectroscopic (SA) ellipsometry is required.

Two ellipsometers were used in this thesis: a Nanofilm EP3 imaging VASE with a laser illumination of 780 nm and a Woollam α-SE ellipsomter (incident angle fixed at 70°) with a wavelength range from 380 nm to 1000 nm in steps of 2.9 nm.

5.2 Material characterisation

5.2.1 Spectroscopy techniques

Optical spectroscopy

Optical microscopy, which allows for a resolution down to the diffraction limit, was used throughout this thesis to study relatively large features on the 1 µm to 10 µm length scale. However it was most frequently used to determine intrinsic properties of the fabricated structures including transmissivity and reflectivity as described in Section 5.2.2. The setup included an Olympus BX-51 microscope equipped with 5x, 20x, 50x and 100x objectives. The light source was a halogen lamp which together with an Olympus U-LWDC condenser allowed for illumination in both reflection and transmission mode. Optical spectroscopic information was obtained using a OceanOptics QE65 spectrometer with a wavelength range of 200 nm to 1000 nm and collected through a single mode optical fiber with a core diameter of 50 µm. For reflection measurements a silver mirror with a reflectivity of more than 97 % was used as reference. For transmission measurements the device substrate was used as the reference. Data collection and analysis was performed in Igor.

Electron spectroscopy

X-ray photoelectron spectroscopy (XPS) X-ray photoelectron spectroscopy is a spectroscopic technique which is used to measure elemental composition, chemical and electronic states of a material. The spectra are acquired by subjecting the sample to a beam of x-rays in an ultra-high vacuum environment and measuring the number of electrons which escape from the top 1 nm to 10 nm of the sample and determining their kinetic energy. XPS can detect elements with atomic number of 3 (Li) and above with a detection limit in the parts per thousand range. The probing depth of XPS is on the order of nanometres.

A standard XPS spectrum consists of a plot of the number of electrons versus their binding energy. The spectrum and the measured XPS peaks can be used to identify the elements that exist in the sample and to determine their atomic percentages. The binding energy of the ejected electrons can be determined according to Equation (5.3)

$$E_{\text{binding}} = E_{\text{photon}} - (E_{\text{kinetic}} + \phi) \tag{5.3}$$

where E_{binding} is the electron binding energy, E_{photon} is the energy of the x-ray photons, E_{kinetic} is the measured electron energy and ϕ is the work function of the spectrometer.

The XPS measurements were carried out in an ultra-high vacuum chamber of an ESCALAB 250Xi XPS system fitted with an XR6 monochromated Al K_α X-ray source ($h\nu = 1486.6\,\text{eV}$) with a 900 µm × 200 µm spot size. The depth profiling was carried out using an Ar^+ ion gun at an ion energy of 3000 eV in 5 s exposures.

Auger electron spectroscopy (AES) In Auger electron spectroscopy the source of primary radiation which ionises the atoms can consist of either an electron beam or soft x-rays, however the process by which electrons are liberated from the surface is different from XPS. In AES the electrons are ejected as a consequence of the radiationless de-excitation of the ionised atom to its ground state. AES has a comparable depth value to XPS but a higher lateral resolution of 10 nm to 100 nm (compared to 1 µm to 100 µm for XPS).

In this study soft x-rays rather than electrons are used as the ionisation source. The Auger spectroscopy measurements were carried out on the XPS system described above. The XPS and Auger measurements were carried out by **Yana Vaynzof**.

Energy-dispersive x-ray spectroscopy (EDX)

Energy-dispersive x-ray spectroscopy is used in conjunction with SEM for elemental analysis. Its penetration depth is limited by the penetration depth of the electrons in the SEM compared to the shallow penetration depth of XPS (approximately 5 nm). It normally offers less accuracy compared to XPS but has the added advantage that it probes average properties of the sample. The accuracy of EDX can be limited by a

number of factors including element peak overlaps and inhomogeneities of the sample. EDX spectra were obtained using an Oxford Instruments INCA system with an SEM acceleration voltage of 15 keV and a working distance of 7 mm. Integration times were in the range of 1 min to 10 min.

5.2.2 Band structure characterisation

A full understanding of the band structure and properties such as conduction type of a fabricated structure or material allows for the correct choice of complementary device materials. This is especially true for nano-structured materials where confinement can produce material properties that are significantly different from their bulk equivalents [176]. The band structure can either be determined by measuring the positions of both the valence and conduction bands, or the positions of one of these two and the band gap. The latter approach is used in this thesis, and the conduction type of the fabricated material is also characterised.

Band gap

The most common method to determine the band gap of a semiconductor relies on the measurement of its absorption coefficient as a function of wavelength. The measured transmittance and reflectance is connected to the absorption coefficient α and the single surface reflection R via Equation (5.4) and Equation (5.5), where i_0 and d are the incident intensity and the film thickness respectively. Care has to be taken so that the transmission and reflection are mostly interference-free.

$$\tilde{T} = \frac{I_{\text{trans}}}{I_0} = \frac{(1-R)^2 \mathrm{e}^{-\alpha d}}{1 - R^2 \mathrm{e}^{-2\alpha d}} \tag{5.4}$$

$$\tilde{R} = \frac{I_{\text{refl}}}{I_0} = R\left(1 + \frac{(1-R)^2 \mathrm{e}^{-2\alpha d}}{1 - R^2 \mathrm{e}^{-2\alpha d}}\right) \tag{5.5}$$

The absorption coefficient can be extracted from the measured quantities $\tilde{T}$ and $\tilde{R}$ and Equation (5.4) and Equation (5.5).

$$\alpha(\lambda) = \frac{1}{d} \ln\left(\frac{1 + \tilde{R}^2 - 2\tilde{R} - \tilde{T}^2 + \sqrt{(1 + \tilde{R}^2 - 2\tilde{R} - \tilde{T}^2)^2 + 4\tilde{T}^2}}{2\tilde{T}}\right) \tag{5.6}$$

Depending on the type of transition of the semiconductor, the absorption coefficient scales according to Equation (5.7)

$$\alpha(\hbar\omega) \propto (\hbar\omega - E_{\text{g}})^n \tag{5.7}$$

where E_g is the semiconductor band gap and the exponent n is equal to 3/2, 1/2, 3 and 2 for direct forbidden, direct allowed, indirect forbidden and indirect allowed transitions respectively [177]. The band gap can be obtained from a linear fit on a plot of $(\alpha\hbar\omega)^{1/n}$ versus $\hbar\omega$ or what is called a Tauc plot. The band gap is found by determining the intersection between the linear fit and $(\alpha\hbar\omega)^{1/n} = 0$.

Conduction type

The conduction types of the structures fabricated in this thesis were determined using an electrochemical method. The polarity of the measured photocurrent was monitored under chopped (40 mHz) AM1.5G illumination whilst scanning the applied bias from 0 V to 400 mV at a scan rate of 10 mV s. A cathodic or anodic photocurrent corresponds to a p-type or n-type structure respectively. The electrochemical setup used was a standard three-electrode electrochemical cell (as described in Section 5.3.1) connected to an Autolab PGSTAT302N potentiostat with a 0.5 M $NaSO_4$ electrolyte, a platinum counter electrode and a silver wire coated with silver chloride as the reference electrode. The reference electrode was calibrated relative to a saturated calomel electrode (SCE) in 0.5 M $NaSO_4$ solution and its potential was 160 mV higher than the SCE.

5.3 Electrochemistry

Electrochemistry is a subset of chemistry which studies both chemical reactions caused by the interaction between an electron conductor and an electrolyte, and the generation of electrical current due to chemical reactions. It features in a large range of different applications, from deposition of metals and metal oxides [178], to characterisation techniques such as surface area measurements, to the determination of semiconductor band structures, and electrochemical impedance spectroscopy [179, 180].

5.3.1 Principles of electrochemical deposition

One of the most common experimental electrochemical setups, and the setup used in this thesis, is the so-called three-electrode setup. It consists of an electrochemical cell containing a liquid electrolyte of the species of interest, with three electrodes immersed into the electrolyte. The conductive surface on which the deposition or the characterisation takes place is called the working electrode and it is placed in close proximity to the counter electrode which is used to complete the electrical circuit. The counter electrode is normally made from highly electroactive materials such as inert precious metals in order to reduce the required overpotential. In the case of the electroplating of metals, a counter electrode of the deposited metal is used to maintain a constant concentration of the electroactive species in the electrolyte. To determine the electrochemical potential applied to the working electrode, a reference electrode with a known potential offset to the Standard Hydrogen Electrode (SHE) is placed near the working

electrode. The reference electrode used in this thesis is a Saturated Calomel Electrode (SCE) which has a redox potential of 0.2444 V versus SHE at 25 °C. The electrochemical cell is connected to a Autolab PGSTAT302N potentio/galvanostat that supplies the voltage/current and measures the produced current/voltage.

The process of electrochemical deposition normally proceeds by passing a charge q through the electrochemical cell, causing the precipitation of insoluble species at the surface of the working electrode . The deposition thickness of a passed charge q is given by:

$$d = \frac{q}{A}\frac{1}{zF}\frac{m_{\mathrm{w}}}{\rho}\frac{\eta}{\phi} \tag{5.8}$$

where z is the number of electrons involved in the reaction, F is Faraday's constant, N_{A} is Avogadro's number, m_{w} and ρ are the molecular weight and density of the deposited material respectively, A is the area of the working electrode, η is the faradaic efficiency and ϕ is the porosity of any potential template.

For the deposition to take place, two conditions have to be fulfilled: the electrolyte has to be in contact with the conducting working electrode and the applied potential must be such that it is thermodynamically favourable for the deposition to take place. Deposition only takes place when the applied potential E, is larger ($E > E_{\mathrm{redox}}$) (for oxidation reactions) or smaller ($E < E_{\mathrm{redox}}$) (for reduction reactions) than the redox potential of the redox couple $M^{n+} + ne^- \rightarrow M$ [178].

Besides the thermodynamical aspects of the deposition, the kinetics of both the electrochemical reaction and the electrolyte have to be taken into account especially for porous high-aspect-ratio templates as used in this thesis. The kinetics are governed by the Butler-Volmer equation and the Nernst-Planck equation for the electrochemical reactions and electrolyte respectively [181].

5.3.2 Deposition of metals and metal oxides

The electrochemical deposition of metals proceeds via the simple faradaic reaction of reduction of metal cations at the cathode.

$$M^{n+} + ne^- \rightarrow M^0 \tag{5.9}$$

A large range of metals and metal alloys can be deposited using electrochemistry including Au, Ag, Pt, Zn, Fe, Cu, Zn, Cr and their alloys. For a detailed description of the electrodeposition of metals and metal alloys see [178]. Metal depositions are normally dense, homogeneous and smooth which means that they obey Equation (5.8) and they proceed without any intermediate steps which leads to a low concentration of impurities. Metal depositions are also less sensitive to experimental conditions such as pH than depositions of metal oxides such as those described below.

A large range of conducting or semiconducting metal oxides have been deposited using electrochemistry including ZnO, TiO_2, Cu_2O and NiO [178]. However the deposition of metal oxides is more complicated than their metal counterparts, and both reductive and oxidative depositions can take place [182]. In reductive depositions, the growth proceeds either by the precipitation of metal hydroxides due a local lowering of the electrolyte pH [183] or by the direct reduction of the oxidised state of the metal cation into the corresponding metal oxide [184]. Similarly, for oxidative depositions the growth of metal oxides can take place either by a decrease in the local pH and subsequent precipitation of the metal oxide (caused by a reduction of species in the electrolyte) or the anodic oxidation of a cation to its higher oxidation state. Since depositions of metal oxides are generally caused by precipitation induced by other chemical reactions, precise control of experimental parameters such as pH and temperature are normally needed. This compounds the difficulty of replicating the kinds of porous polymer templates which are central to the research of this thesis.

5.4 Solar cell fabrication

5.4.1 Dye-sensitised solar cell device assembly

The fabrication and assembly of both liquid electrolyte and solid-state electrolyte dye-sensitised solar cells based on TiO_2 mesoporous scaffolds have been extensively covered in the literature and only the most important experimental parameters are described below.

TiO_2 compact layer

Prior to deposition of the TiO_2 compact layers, the FTO-coated glass substrates (FTO) for the solid-state DSSCs (Section 5.4.1) were masked using Scotch tape, and the FTO was etched using zinc powder and 2M HCl to produce a 14 mm×14 mm device substrate with an active area of 10 mm×14 mm. The samples were rinsed with excess amounts of DI water and ethanol, and sonicated in a 2 % Hellmanex soap solution, acetone and isopropanol prior to O_2 plasma cleaning for 10 min (Diener Femto plasma cleaner, 100 W). The device substrates for the liquid electrolyte DSSCs were unetched 14 mm×20 mm FTO. The substrates were covered with a TiO_2 compact layer either by spray pyrolysis of a 0.1 M titaniumbis(acetylacetone) (TAA) solution in ethanol at 300 °C [185] or by atomic layer deposition as described in Section 8.2.

Mesoporous TiO_2 electrodes

The standard mesoporous nanoparticular TiO_2 scaffolds were fabricated by spin-coating from a solution of commercially available TiO_2 paste (Dyesol 18 NTR) and ethanol (1 g:1.5 mL). 50 µL cm^{-2} of solution spun at 1500 RPM produced films approximately

1.5 µm thick. Titania electrodes were also fabricated by atomic layer deposition as described in Chapter 7.

Two different dyes were employed in this thesis, a ruthenium-based dye (N719) and an all-organic indolene dye (D149), shown in Figure 5.2A,B. Besides being more environmentally friendly to produce, the indolene dye also has a five-fold increase in its absorption coefficient compared to N719 [186]. This is exploited in solid-state electrolyte DSSC devices where the D149 dye is commonly used to achieve high incident light absorption despite a limited maximum device thickness which is due to problems with infiltration of the hole-conducting material.

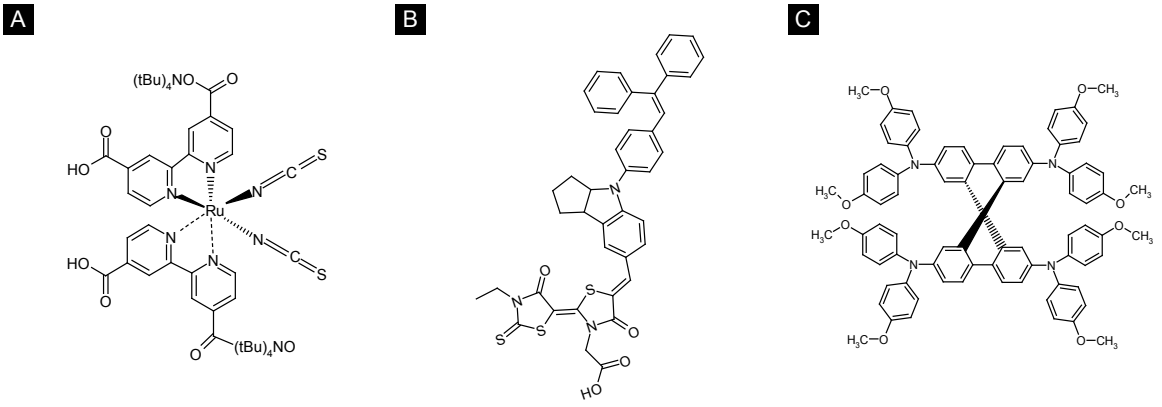

Figure 5.2: Sensitising dyes and hole-conducting materials used in this thesis. **(A)** N719 dye (cis-bis(isothiocyanato)bis(2,20-bipyridil-4,40-dicarboxylate) ruthenium (II) bis-tetra-nbuthylammonium) **(B)** D149, all-organic indolene dye **(C)** spiro-MeOTAD hole-conductor (2,2'7,7'-tetrakis(N,N-dimethoxypheny-amine)-9,9'-spirobifluorene)

Prior to sensitisation and device assembly, the TiO_2 scaffolds were subjected to a standard $TiCl_4$ treatment [187] to increase surface area and material purity. The samples were immersed in a freshly made 40 mM $TiCl_4$ aqueous solution, prepared from a 2 M $TiCl_4$ stock solution, and heated to 70 °C for 30 min. After rinsing in DI water the samples were annealed at 550 °C for 30 min in air.

Liquid electrolyte DSSC

The TiO_2 electrodes were sensitised overnight by heating them to 70 °C for 5 min and were then directly immersed in an acetonitrile:tert-butyl alcohol (1:1 vol:vol) solution of 0.5 mM of cis-bis(isothiocyanato)bis(2,20-bipyridil-4,40-dicarboxylate) ruthenium (II) bis-tetra-nbuthylammonium dye (N719) (Figure 5.2A). After sensitisation, the samples were rinsed with acetonitrile and sandwiched with a platinised FTO counter electrode using a 50 µm Surlyn spacer as shown in Figure 5.3A. The platinised FTO electrodes were fabricated by spin-coating with a 50 mM hexachloroplatinic acid solution in isopropanol and heating at 450 °C for 20 min.

The devices were filled with a non-volatile iodide/triiodide electrolyte ('Robust') con-

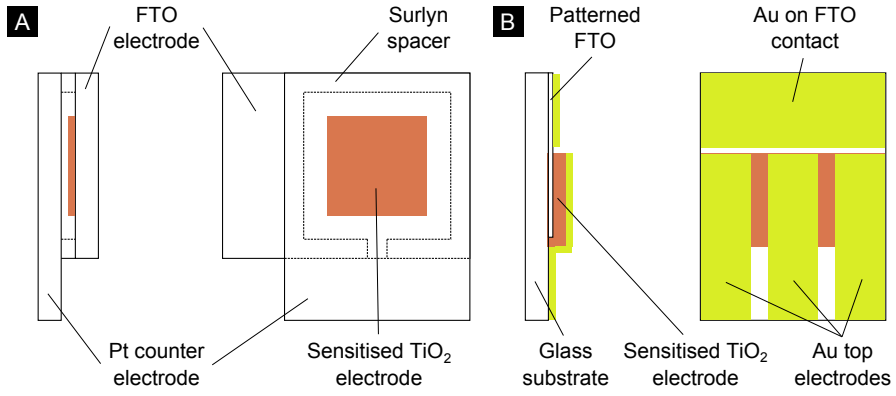

Figure 5.3: Schematic of dye-sensitised solar cell device fabrication. **(A)** Liquid electrolyte DSSC. The sensitised TiO_2 electrode is sandwiched using a platinised FTO counter electrode and a 50 µm Surlyn spacer and infiltrated with an iodine/iodide electrolyte. **(B)** Solid-state electrolyte DSSC. The FTO electrode is patterned prior to assembly of the TiO_2 mesoporous film. Gold bottom and top electrodes are evaporated on the device.

sisting of 0.8 M PMII, 0.15 M iodine, 0.1 M GuNCS and 0.5 M NMBI in 3-methoxypropionitrile using vacuum back filling [188]. The filling hole was sealed using a two component epoxy (Hardman Double Bubble). The illumination area for device measurements was defined by acircular mask with an area of 0.05 mm^2.

Solid-state electrolyte DSSC

The titania electrodes were heated to 70 °C and immediately immersed in an all-organic indolene dye (D149) (Figure 5.2A) (0.3 mM in 1:1 acetonitrile:tert-butanol) for 3 h. The electrodes were back-filled with a solid-state organic molecular hole-transporter 2,2',7,7'-tetrakis(N,N-di-methoxypheny-amine)-9,9'-spirobi-fluorine (Spiro-MeOTAD) (Figure 5.2C) [33, 34]. The hole-conductor was infiltrated by spreading 25 µL cm^{-2} of a Spiro-MeOTAD solution (90 mM spiro-MeOTAD + 1.54 M 4-tert-butylpyridine + 0.6 M Li bis(trifluoromethanesulfonyl)imide in a chlorobenzene and acetonitrile mixture (CB:ACN 21.9:1)) across the device, allowing it to infiltrate for 15 s before spin-coating for 1 min at 2000 RPM to improve the infiltration and to remove excess solution [189]. A 150 nm thick gold top electrode was e-beam evaporated (Kurt Lesker, 99.999 % Au) onto the device through a shadow mask. The active area of the device (approximately 0.1 cm^2) was defined by the overlap of the top electrode and the TiO_2 film. A schematic of an assembled device is shown in Figure 5.3B.

5.4.2 Cu_2O solar cell device assembly

Liquid electrolyte devices

Non-aqueous electrolyte For the non-aqueous photoelectrochemical experiments, acetonitrile, $LiClO_4$, bis(pentamethylcyclopentadienyl) cobalt(II) (decamethylcobaltocene, $Me_{10}CoCp_2{}^0$) and bis(pentamethylcyclopentadienyl) cobalt(III) hexafluorophosphate (decamethylcobaltocenium, $Me_{10}CoCp_2{}^+ \cdot PF_6$) were all used as received. All chemical handling took place in a Bruker glovebox (<0.1ppm O2) as did solution processing and device assembly. The solar cells were assembled using a 300 µm thick parafilm spacer and a platinized FTO counter electrode (50 mM H_2PtCl_6 isopropanol solution spin-coated at 2000 RPM and annealed at 450 °C for 20 min). Devices were dried at 60 °C for 2 h prior to assembly to remove any trace amounts of water. The electrolyte consisted of 1.0 M $LiClO_4$ – 0.020 M $Me_{10}CoCp_2{}^+$ – 0.002 M $Me_{10}CoCp_2{}^0$ in acetonitrile and was introduced into the device using a syringe needle. The devices were further sealed with a two-component epoxy (Hardman Double Bubble) to improve their integrity and stability. To improve the conductivity between the measurement rig (Section 5.4.3) and the device, silver dag (Agar Silver Paint) was applied to both top and bottom electrodes.

Aqueous electrolyte The electrolyte for the aqueous devices consisted of LiI (0.5 M), I_2 (0.05 M) and tert-butylpyridine (0.5 M) in dry acetonitrile. The LiI, I_2 and tert-butylpyridine were used as received. The remainder of the fabrication procedure was identical to the non-aqueous electrolyte devices.

Solid-state electrolyte devices

Zinc oxide Zinc oxide was deposited inside the gyroid-structured electrodes using ALD from diethylzinc (DEZ) and 18 MΩ DI water at 120 °C. The deposition scheme was according to Table 5.2. A top electrode of 40 nm of aluminium and 130 nm of gold was deposited using a Kurt Lesker e-beam evaporator (99.999% Al and 99.999% Au, base pressure of approximately 1×10^{-6} torr).

	Precursor	Pulse (s)	Purge (s)
Step 1	DEZ	20	180
Step 2	H_2O	20	180

Table 5.2: Pulsing scheme for depositions of ZnO inside gyroid-structured Cu_2O electrodes.

PCBM and spiro-MeOTAD PCBM and spiro were infiltrated into the porous Cu_2O/Cu electrodes by a two step spin-coating procedure to improve the pore filling.

25 µL cm^{-2} of a 5 % solution of PCBM or spiro was spread on the sample and allowed to wet it for 10 s before spin-coating at 1000 RPM (acceleration 300 RPM/s^2) for 1 min. The same procedure was then repeated with a higher concentration solution (10 %). The PCBM was dissolved in chlorobenzene and stirred overnight to ensure complete dissolution. The spiro-MeOTAD solution contained 45 mM spiro-MeOTAD, 0.77 M 4-tert-butylpyridine and 0.3 M Li bis(trifluoromethanesulfonyl)imide in a chlorobenzene and acetonitrile mixture (CB:ACN 21.9:1). Top electrodes of 150 nm of gold were deposited using a Kurt Lesker e-beam evaporator (99.999% Au, base pressure approximately 1×10^{-6} torr).

5.4.3 Device characterisation

A number of figures of merit can be determined for a solar cell. The **short circuit current (I_{sc})** is the current density of the device with no bias applied. The **open circuit voltage (V_{oc})** is the bias at which the measured current density is zero. The **power output** of the device is the product of the current density at a given bias ($P_{out} = I \times V$). A maximum in power output ($P_{out,max}$) is reached between short circuit (0 V bias) and the open circuit voltage. The **fill factor (FF)** is the ratio between the maximum power output and the product of the short circuit current and the open circuit voltage ($FF = P_{out,max}/(I_{sc} \times V_{oc})$. A low fill factor could indicate parasitic resistive losses such as a series shunt resistance or recombination losses. The **power conversion efficiency (η)** is the ratio between the maximum power output and the power input from the incident illumination.

$$\eta = \frac{P_{out,max}}{P_{in}} = \frac{I_{sc} V_{oc} FF}{P_{in}} \tag{5.10}$$

The **external quantum efficiency (EQE)** is a measure of how effective the conversion is between incident photons and electrons delivered to the external load, $EQE(\lambda) = n_{electron}(\lambda)/n_{photon}(\lambda)$. It is possible to achieve EQEs above unity if the absorption of a single photon leads to the generation of multiple electrons [14]. When measuring the internal quantum efficiency, the EQE is compensated for losses such as reflections off the top of the device and the active material, and electrolyte absorption.

The EQE was measured by illuminating the device with a halogen lamp spectrally resolved by a monochromator, at an intensity on the order of 0.1 mW cm^{-2} at each wavelength interval. The illumination spot size was approximately 2 mm^2. The photocurrent was measured by a Kiethley 237 source meter. The incident photon flux on the device was measured in parallel with a reference silicon diode. The spectral dependence of the power incident on the devices was calibrated with a calibrated silicon photodiode. The simulated AM 1.5 solar illumination was generated by a 300 W Oriel solar simulator fitted with a AM 1.5 filter. The intensity of the solar simulator was calibrated using a Si calibration diode purchased from and calibrated at the Fraunhofer Institute for Solar Energy Systems (Freiburg, Germany). Measurements of both I-V curves and EQE was carried out using a purpose-built LabView software.

5.5 Polymer synthesis

The diblock copolymers used in this thesis were synthesised by **Maik Scherer**. This section will only give a short description of the synthesis procedure. For a more detailed description see Scherer's PhD thesis [66] or any of the reviews on the topic [190, 191].

The polymers were synthesised using a bi-functional initiator in a two step process. In the first step, poly(styrene) or a copolymer of poly(styrene) and poly(4-fluorostyrene) was synthesised by atom transfer radical polymerisation (ATRP). The second step involved the synthesis of a poly(lactide) block using organocatalytic ring-opening polymerisation (ROP). The synthesis procedure is shown in Reaction 5.1 [192].

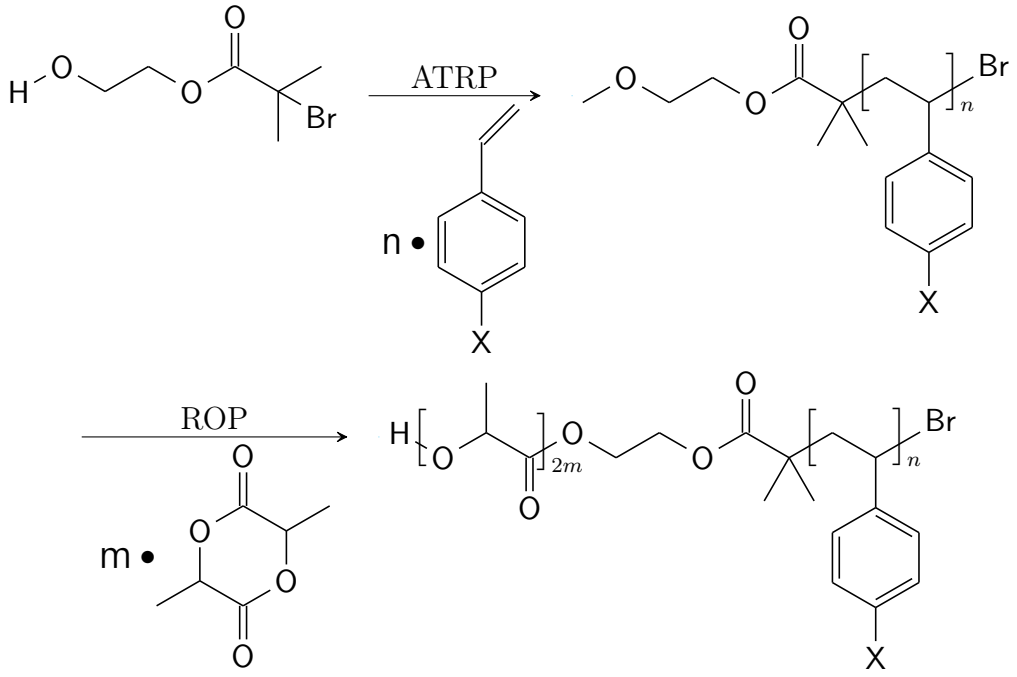

Reaction 5.1: Schematic for the synthesis of poly(4-X-styrene)-poly(lactic acid) diblock copolymers using ATRP and ROP with a HEBIB initiator.

Atom transfer radical polymerisation was developed by Wang and Matyjaszewski [193] and has become the main replacement for living (ionic) polymerisation [194]. It has industrial applications due to the possibility of fast synthesis of high molecular weight polymers. ATRP consists of a number of components including the monomer, an initiator, a catalyst and optionally a solvent and an additive. In this case, the monomers used for the synthesis were styrene and 4-fluorostyrene. The initiator was β-hydroxylethyl α-bromoisobutyrate (HEBIB) synthesised according to White *et al.* and the catalyst was CuBr [195].

Ring-opening polymerisation is used to polymerise cyclic monomers [196]. Organocatalytic ROP allows for a high degree of control of molecular weights and leads to low polydispersities. It consists of the monomers, an initiator, an organocatalyst and optional additives. The monomer used for the synthesis of poly(lactide) was 3,6-dimethyl-1,4-dioxane-2,5-dione (D,L-lactide). The catalysts were bis(3,5-trifluoromethyl)phenyl

cyclohexylthiourea (thiourea), synthesised according to Pratt *et al.* [197] and 1,8-diazabicyclo[5.4.0]undec-7-ene (DBU). The initiator used was the macroinitiator formed during the synthesis of the styrenic polymer.

Two polymers with different molecular weights and poly(lactic acid) volume fractions, synthesised according to the scheme above, were used in this thesis. The polymers and their molecular weights, volume fractions and equilibrium morphologies are displayed in Table 5.3.

Sample	M_n^{PFS} (kg mol^{-1})	f_{PLA} (%)	Morphology
PS128	33	37.00	Worm-like bicontinuous
PS192	14	38.25	Double-gyroid

Table 5.3: Properties of the diblock copolymers used in this thesis.

5.6 Polymer template fabrication

The following section describes the various steps required for the fabrication of nanoporous thin film polymer templates on FTO-coated glass substrates using block copolymers. Certain studies in this thesis will employ modified versions of this protocol and this will be indicated in the relevant chapters.

5.6.1 Surface modification

Flourine-doped tin oxide coated glass (FTO) (Solaronix, 15Ω/□) was piranha cleaned for 15 min (3:1 H_2SO_4:H_2O_2 at 80 °C), rinsed with copious amounts of DI water and further sonicated in DI water for 10 min. The hydrophilic substrates were treated in 0.1 % octyltrichloro silane (OTS) in cyclohexane for 8 s and then dried with dry N_2. This prcoess creates a partial self-assembled monolayer on the surface of the FTO which promotes equal wetting of the two block copolymer components.

5.6.2 Thin film preparation

The thesis uses two different diblock copolymers denoted by PS192 ans PS128 (Section 5.5). The equilibrium morphologies of PS192 and PS128 are the double-gyroid Chapter 3 and cylindrical morphologies respectively and they have poly(lactic acid) volume fractions of 38.25 % and 37 %. The thermal annealing protocols described below were carried out in a home-made heated brass chamber controlled by a West 6100+ thermal controller, situated inside a Binder vacuum oven. The home-made chamber and the vacuum oven were pre-heated to 90 °C and 85 °C respectively. Before starting the thermal annealing protocols, the vacuum oven was purged by evacuating it to a

pressure below 10 mbar and subsequently pressurising it with dry N_2 to 900 mbar. The purging procedure was repeated three times. After the thermal annealing the samples were quickly removed from the vacuum oven and quenched to room temperature on an aluminium block.

PS192

A solution of PS192 (11 % wt/vol in toluene) was spin-coated on the FTO substrate (2 µL cm^{-2}) at 200 RPM to 1000 RPM to produce films 1 µm to 5 µm thick. The thin films were allowed to reach their equilibrium double-gyroid morphology by thermal annealing in which the samples were heated under vacuum to 150 °C at 2.5 °C min^{-1} and then annealed in a N_2 atmosphere at 172 °C (heating rate 2.5 °C min^{-1}) for 30 min before being quenched to room temperature.

PS128

A solution of PS128 (15 % wt/vol in toluene) was spin-coated on the FTO substrate (8 µL cm^{-2}) at 1000 RPM to 3000 RPM to produce films 1 µm to 3 µm thick. The samples were thermally annealed by heating them to 155 °C under vacuum at a heating rate of 2.5 °C min^{-1} and subsequently annealing them for 30 min at 155 °C in a N_2 atmosphere. This heating protocol of a shortened annealing time leads to the formation of a partially ordered worm-like cylindrical morphology instead of the hexagonally close-packed equilibrium morphology expected from the volume fractions of the polystyrene and the poly(lactic acid) blocks (Section 7.3.5).

5.6.3 Voiding of templates

To produce nano-porous templates, the thermally annealed thin films were voided by etching the poly(lactic acid) minority networks. This was achieved by immersing the samples in a basic solution (pH≈14) consisting of 0.1 M NaOH in H_2O:MeOH (1:1). The etching times ranged from 3 h to 15 h. After etching, the samples were first immersed in methanol for 15 min and then rinsed in methanol to remove any residual NaOH before being dried in dry N_2.

6 Gyroid-structured Cu_2O solar cells

The main aim of this chapter is to study the feasibility of using post-deposition thermal oxidation of metal nano-structures as electrodes for solar cells. The chapter describes the fabrication of core-shell copper-Cu_2O solar cells. The core-shell device geometry is achieved by the post-deposition thermal oxidation of electroplated copper deposited in gyroid-structured polystyrene templates. The morphological changes observed during the oxidation are described, as is the performance of both solid-state and liquid electrolyte devices fabricated from core-shell photoelectrodes.

6.1 Introduction

In the history of semiconductor physics, copper (I) oxide or cuprous oxide (Cu_2O) has been one of the most frequently studied materials. Investigations have included studies into its use in rectifiers before the introduction of silicon [198] and its use as a platform for experimental observations such as the Wannier exciton series and the dynamic Stark effect of excitons [199]. However its use in photovoltaic devices has been fairly limited.

The potential of cuprous oxide, a non-stoichiometric p-type semiconductor [200], for the design of solar cells has been known and recognized since the 1920s. The research into Cu_2O as a solar cell material was revived during the 1970s [201], but despite renewed interest in the last decade the efficiencies associated with the material have remained low. Despite this, Cu_2O remains a valid and interesting alternative to silicon and other semiconductors because: 1) it is non-toxic (as a bulk material), 2) its starting material, Cu, is abundant on earth [202], 3) its production processes are relatively simple and cheap [203] compared to e.g. the polymers used in OPVs and 4) Cu_2O has a direct band gap of approximately 2 eV (620 nm) [204] which makes it suitable for photovoltaic conversion without the need to include additional light absorbers or sensitisers (as is the case in e.g. dye-sensitised solar cells).

6.1.1 All-solid-state Cu_2O solar cells

Even though theoretical calculations predict an electric power conversion efficiency for Cu_2O-based photovoltaics of approximately 20 % [205], in practice the efficiencies obtained are low because of the difficulty of finding a suitable n-type counterpart to Cu_2O or because of the issues with preparing high quality n-type Cu_2O for homo-junction devices. For Cu_2O/metal Schottky junction devices, interfacial reactions lead to the formation of deleterious metallic copper which effectively turns the device into a Cu_2O/Cu Schottky barrier, lowering the barrier height and therefore the open-circuit voltage to less than 350 mV [203, 206]. The interfacial formation of Cu is also responsible for the low performance displayed by TCO/Cu_2O heterojunctions made from ZnO, SnO_2 or

In_2O_3 [205, 207, 208]. Examples of devices where the formation of Cu has been limited, leading to a higher barrier height, include ZnO/Cu_2O heterojunction solar cells with a reported open circuit voltage of 595 mV and an efficiency of 2 % [205] and Al-doped ZnO/non-doped ZnO/Cu_2O heterojunction solar cells with an open-circuit voltage of 700 mV and an efficiency of 4.04 %. The latter device structure has one of the highest reported efficiencies for a solid-state Cu_2O heterojunction device.

To achieve a high open-circuit voltage, and consequently a high power conversion efficiency, a high barrier has to be formed between the cuprous oxide and the accompanying electron conducting material. Since Cu_2O has a low conduction band energy (−3.2 eV relative to the vacuum) [209], typically only reactive metals would be expected to form a high barrier with Cu_2O. Thallium (Tl) is reported to be the only metal to not reduce Cu_2O to Cu [203]. Cu_2O p-n homo-junctions of high quality have not been reported so far due to the difficulty of producing n-type Cu_2O. Further, few heterojunction materials have the appropriate band-edge offsets relative to Cu_2O to produce a sufficient built-in voltage, e.g. ZnO/Cu_2O junctions only produce 0.75 V to 0.87 V due to band misalignment [210].

6.1.2 Solid/liquid Cu_2O solar cells

An alternative to solid-state devices are liquid electrolyte/semiconductor junctions which have the advantage that the electrolyte can be altered to produce either rectifying or ohmic contacts to a variety of semiconductors [211–214], by tuning the chemical and/or electrical properties of the interface. For Cu_2O the electrolyte has to be chosen carefully since its thermodynamic stability in aqueous environments is limited to a relatively small range of pH and electrochemical potential [215]. Because of this stability issue, a better choice is a non-aqueous electrolyte solvent such as acetonitrile (CH_3CN), where Cu_2O displays limited photo-corrosion [216, 217].

As described in Section 6.1.1, a high barrier between the Cu_2O and the other component in the solar cell is needed to achieve a high open-circuit voltage. For liquid electrolyte/Cu_2O junctions, the redox couple used would need to have a sufficiently negative Nernstian redox potential to produce a large open-circuit voltage and therefore high conversion efficiencies. Since the redox potential of such species is more negative than the reduction potential of water, inert non-aqueous solvents have to be used. One redox couple that produces high barrier heights with Cu_2O is decamethylcobaltocenium/decamethylcobaltocene ($Me_{10}CoCp_2^{+}/Me_{10}CoCp_2^{0}$) abbreviated as ($CoCp^*_2{}^{+}/CoCp^*_2{}^{0}$), which has a formal reduction potential of -1.47V vs. SCE [218]. The use of such a liquid electrolyte would allow for the study of the photovoltage and power conversion efficiency of Cu_2O electrodes which do not suffer from the chemical interfacial reactions normally found in solid-state Cu_2O devices.

Xiang *et al.* studied Cu_2O contacts together with decamethylcobaltocenium/decamethylcobaltocene ($CoCp^*_2{}^{+/0}$) and cobaltocenium/cobaltocene ($CoCp_2{}^{+/0}$) redox electrolytes [219]. In their work, Cu_2O substrates were produced by high-temperature oxidation of copper foils. For Cu_2O photoelectrodes in contact with a $CoCp^*_2{}^{+/0}$ redox

couple they achieved an open-circuit voltage of 820 mV and a short-circuit current of 3.1 mA cm^{-2} under simulated air mass 1.5 illumination, which corresponds to a power conversion efficiency of 1.5 %.

6.1.3 Fabrication of Cu_2O electrodes

Two main fabrication routes exist for the production of high quality and high purity cuprous oxide electrodes for the use in solar cells: thermal oxidation and electrochemical deposition. Thermal oxidation is one of the earliest methods for the fabrication of Cu_2O and it utilises the oxidation of high purity copper foils or films, normally under reduced O_2 pressures (lower than 10^{-6} torr) and at high temperatures (often exceeding 1000 °C). This produces low resistivity p-type, polycrystalline Cu_2O with a large grain size suitable for photovoltaics. The produced cuprous oxide also has high hole mobilities and long minority-carrier diffusion lengths [203, 220].

However this fabrication route is impeded by a number of factors. Following oxidation, the oxygen pressure has to be successively decreased as the furnace cools in order to maintain the Cu_2O phase according to the Cu-O phase diagram [221]. Besides the requirement for a high processing temperature, it has been shown that Cu_2O grown at a high temperature has a high leakage current which can lead to low conversion efficiencies when applied in a solar cell. This has led to a focus of research into the fabrication of Cu_2O at lower temperatures and more ambient conditions. The majority of the fabrication techniques reported in literature produce p-type copper oxide which has been shown to originate from copper vacancies in the Cu_2O [222].

Amongst a number of developed fabrication techniques, including magnetron sputtering, pulsed laser deposition, chemical vapour deposition and atomic layer deposition, electro-deposition [223, 224] has received a significant interest due to its simplicity, low processing temperatures and low cost as well as the possibility to modify its material properties by altering deposition parameters such as pH and electrolyte temperature. An added benefit is that deposition of n-type Cu_2O from acidic aqueous electrolytes has been reported, which in theory would allow for the fabrication of Cu_2O heterojunction devices [225].

The majority of the properties of electrochemically deposited copper have been reported to be similar to those obtained by thermal oxidation. The exceptions are higher resistivities of $10^4\,\Omega$ cm to $10^6\,\Omega$ cm [226] and small diffusion lengths of minority carriers [227]. These two drawbacks of electrodeposited Cu_2O films limit the obtainable device performance since they hamper charge extraction and lead to a low quantum efficiency above 500 nm.

6.1.4 Nano-structuring Cu_2O solar cells

The obvious solution to the problem of the high resistivity of electrochemically deposited Cu_2O is to reduce the thickness of the Cu_2O electrode, but this leads to a

lowered absorption of incident photons. Like the organic solar cells described in Chapter 2 this can be partially solved by nano-structuring the Cu_2O. However in all-oxide Cu_2O-containing solar cells, such as Cu_2O/ZnO devices, intrinsic properties of the cuprous oxide limit the achievable device performance. Musselman *et al.* [228] showed that even though nano-structuring can aid in the collection of minority carriers, which is normally limited by low electron mobilities, the length scale associated with nano-structuring prevents the formation of a depletion layer comparable to that of bilayer devices, thus resulting in a lowered V_{OC} and reduced device performance.

This need to adjust the length scale of the nano-structures to the width of the intrinsic depletion layer has also been shown for silicon solar cells [229]. There are a number of routes to improving the open-circuit voltage including the reduction of the density of recombination centres, the careful design of the nano-structured geometry and the introduction of interfacial barrier layers. However the work by Musselman *et al.* suggests that the main limitation is the depletion width and that an increase in mobility via doping is required to overcome this issue. Even though examples of doping in bilayer devices exist [230, 231], there have been no reports of direct doping for electrochemically deposited Cu_2O nano-structures. Examples of post-deposition gas phase doping exist in the literature [232, 233] however none have been reported for nano-structured cuprous oxide.

These results by Musselman *et al.* seem to be contradictory to results by Chen *et al.* [234] who report an open-circuit voltage of 0.5 V for a ZnO/Cu_2O device. However it is believed that this device geometry is different from the one described by Musselman *et al.* The high temperature annealing of the device is thought to reduce the Cu_2O at the ZnO/Cu_2O interface to copper, and it is this reduction, accompanied by the thermodynamically expected oxidation of the Cu_2O to CuO, which leads to the formation of a Cu_2O/Cu/ZnO device architecture [208, 235, 236].

Based on the research by Musselman into the nano-structuring of all-oxide Cu_2O solar cells and the associated limitations, two directions were taken in this chapter. Firstly the ZnO or other n-type material was replaced with a liquid electrolyte as described in Section 6.1.2 which allowed for a larger scope to alter the band-offset between the Cu_2O and the secondary device component. Secondly the device geometry was changed from the relatively simple Cu_2O/ZnO (or any n-type material) structure to a more complicated nano-structured geometry which utilises more than two materials [225].

The combination of these two directions can conceptually be realised as a core/shell electrode surrounded by a liquid electrolyte. As described in Section 6.1.1, the formation of deleterious copper in bilayer all-oxide Cu_2O solar cells can lower the barrier height and therefore the device performance. However if cleverly designed, a Cu_2O/copper junction can aid in charge extraction and increase device performance.

A device geometry with this design was constructed by Shao *et al.* Their devices use photo-electrodes consisting of mixtures of electro-deposited Cu_2O and copper. This was achieved by controlling the pH of the electrolyte used for the deposition [237]. The photoelectrode was surrounded by a LiI/I_2 liquid electrolyte and presented an overall efficiency of 3.13 % with an open-circuit voltage of 0.56 V and a short-circuit current

of 11.3 mA cm^{-2}. The device relies on the injection of electrons from the Cu_2O to the copper, which has enhanced electron transport properties, and the transport of the excitonic hole via a redox couple in the liquid electrolyte. The main mechanism of a Cu_2O/Cu junction is the electron injection from Cu_2O into Cu for $\hbar\nu > E_g$ and the hole emission from Cu into Cu_2O when $\hbar\nu < E_g$ [209, 238].

6.1.5 Block copolymer templating

The work reported by Shao *et al.* although very interesting, has certain limitations. Firstly the presented structures are not truly nano-structured. Instead the photoelectrodes consist of 2 µm to 3 µm spherical deposits with a copper core and a Cu_2O shell. This requires a relatively thick Cu_2O shell to achieve complete absorption and as such the device performance can still be limited by transport through the Cu_2O. Secondly the electrochemical deposition of the copper and Cu_2O is not performed in a template. This offers only limited control over feature sizes and structural order. Thirdly, deposition parameters such as temperature, concentration and pH can affect the ratio of deposited copper and Cu_2O. Fourthly the use of an aqueous liquid electrolyte causes problems with the stability of the photoelectrode Section 6.1.2 and a reduction of the device performance with time.

In this chapter we have taken a different approach in which double-gyroid-structured polymeric nano-porous templates (Chapter 3) are replicated using electrochemical deposition of copper followed by a subsequent thermal oxidation. This fabrication procedure offers a number of advantages. Firstly the use of a template offers great control over feature sizes as well as repeatability between subsequent samples and experiments. Secondly a nano-porous template enables the creation of a replica with a high surface area to volume ratio. From the perspective of photovoltaics, this allows for the combination of high photon absorption with proximity between the site of exciton generation and the electrodes (as previously described in Chapter 2). Thirdly the separation of the formation of the cuprous oxide from the deposition of the copper offers more control of the oxide thickness and of the ratio between the formed Cu_2O and CuO. This also allows for more freedom with regards to for example doping, as a variety of atmospheres can be used besides oxygen for the thermal treatment.

The fabrication procedure for the nano-structured Cu/Cu_2O/CuO solar cells used in this chapter is shown in Figure 6.1.

The electrochemical deposition of copper into the self-assembled double-gyroid templates and the subsequent thermal oxidation require the introduction of two concepts which are covered in the following two sections: the Kirkendall effect and electroplating in nanopores.

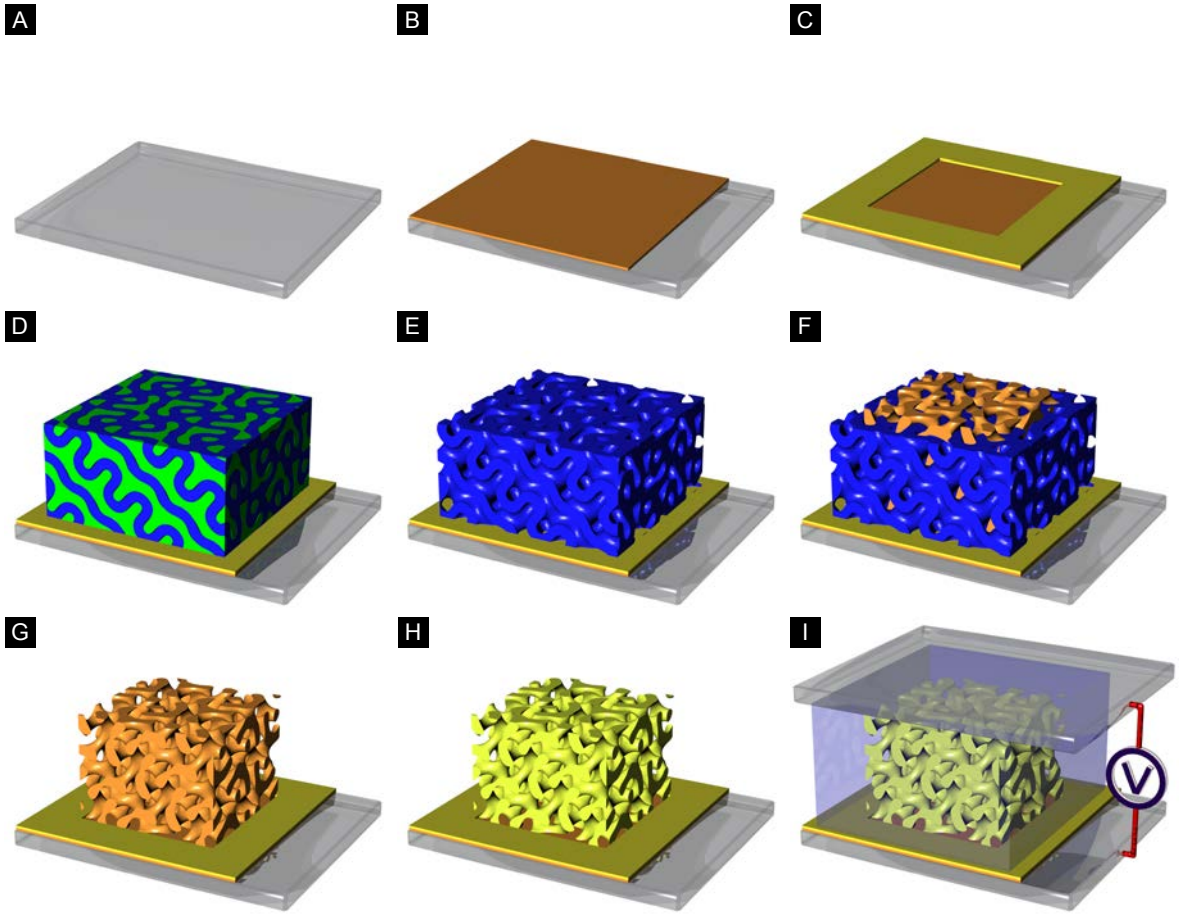

Figure 6.1: Schematic of device fabrication. **(A)** Piranha cleaning of FTO substrate. **(B)** Evaporation of copper compact layer. **(C)** Fabrication of SU-8 mask using photo lithography. **(D)** Spin-coating and thermal annealing of polystyrene-b-poly(lactic acid) diblock copolymer. **(E)** Removal of poly(lactic acid) network using mild base. **(F)** Electrochemical deposition of copper into the porous polystyrene template. **(G)** In-template oxidation of copper deposit and removal of polystyrene template. **(H)** Post-deposition thermal oxidation of gyroid-structured copper network. **(I)** Assembly of solar cell using solid-state or liquid electrolyte.

The nano-scale Kirkendall effect

The Kirkendall effect was first observed in bulk samples where the diffusion of Zn and Cu is different at a Cu and CuZn interface [239]. This difference in atomic diffusion is counterbalanced by a flux of vacancies which if allowed to saturate could lead to the formation of voids. In bulk samples where an equilibrium vacancy concentration can be maintained, void formation is not necessarily seen. However in nano-sized geometries such as nanospheres and nanowires, the vacancies are confined within the structures and can accumulate, supersaturate and condense into a void.

In this study, this process of void formation is called the nano-scale Kirkendall effect

or nKDE. For the oxidation of metal nano-structures into their corresponding metal oxides, the difference in diffusion rates between the oxygen into the structure and that of the metal atoms towards the gas/solid interface is what drives the Kirkendall effect. A large number of metal nanoparticles, including copper, cobalt and nickel, have been shown to undergo the transformation to metal oxide shells with a central void [240]. Other environments have been used to form hollow nanocrystals, including solutions of sulphur and selenium which lead to the formation of metal chalcogenides. However the Kirkendall effect is not limited to solid/gas systems, and there are solid/solid systems that also undergo the Kirkendall effect, for example ZnO/Al_2O_3 core/shell nanowires which form hollow spinel $ZnAl_2O_4$ structures [241].

The Kirkendall effect is also apparent in other nano-sized structures such as nanowires and tricontinuous double-gyroid networks [48]. Given that multiple nuclei of voids can form in one of these structures at different places, the final nano-tubular geometry is a strong function of the characteristic length scale of the nano-structure and of processing parameters such as temperature. An example of this variation in geometries is the oxidation of nickel nanowires with a diameter of 80 nm or larger [242]. They form bamboo-like structures upon annealing due to the high temperature required for their full oxidation.

There are a few examples of copper nanowires that display a tubular morphology upon oxidation [243, 244]. However no examples exist in the literature of the formation of a copper oxide nano-tubular morphology upon the oxidation of nanowires with a diameter smaller than 50 nm.

Electroplating of copper in porous templates

There are a number of routes to the creation of copper nanowires and these can roughly be categorised into liquid based synthesis routes such as hydrothermal synthesis [245] and electrochemical deposition of copper in various templates [246, 247]. Electrochemical deposition of copper is usually performed in commercially available porous alumina membranes (PAM) or track-etch polycarbonate membranes which have a pore diameter ranging from 20 nm to 500 nm. Examples of deposition in sub-20 nm pores include growth in mesoporous silica templates [248].

Special considerations have to be made when using electrochemistry to deposit materials in nano-porous high-aspect-ratio templates due to electrolyte diffusion. Valizadeh *et al.* studied the deposition of cobalt in track etched membranes and determined equations that compare the electrolyte concentration in the bulk to the concentrations at the openings of the pores and at the electrode surface, and show how these concentrations relate to the deposition current as a function of time [249].

It is safe to assume that the equations will hold for the deposition of copper. However care has to be taken when applying them to depositions in the double-gyroid morphology. Rather than consisting of individual well-separated nano-pores, as for a track-etched membrane, the gyroid consists of interconnected pores where the openings

of the pores are in close proximity to each other. However no further effort was taken in this thesis to validate the equations (given below) for a template of gyroid morphology.

It is possible to show that the deposition current in an array of nanopores is described by

$$I = nF\left(\frac{D}{\pi r}\right)^{1/2}\left(c^b - c^m\right)\left\{1 - \exp\left[\frac{4N\pi^3(Dt\pi)^{1/2}}{4L + \pi r}\frac{c^b}{c^b - c^m}\right]\right\} \tag{6.1}$$

where n is the number of electrons involved in the reaction, F is the Faraday constant, D is the diffusion coefficient of species in the electrolyte, r is the radius of the nanopore, c^b is the bulk concentration, c^m is the concentration at the entrance of the nanopore, N is the nanopore density and t is the deposition time. Two deposition regimes can be identified: for short time-scales the current is limited by a linear or Cottrell time-dependant diffusion with $i \propto t^{-1/2}$ whereas for long time-scales, the system is limited by spherical diffusion and the steady-state current per nanopore is

$$I = \frac{4\pi nFDc^b r^2}{4L + \pi r} \tag{6.2}$$

which gives a current density of

$$J = \frac{I}{\pi r^2} = \frac{4nFDc^b}{4L + \pi r} \propto \frac{1}{L + r}. \tag{6.3}$$

This shows that deposition inside a high-aspect-ratio template, as is the case in this study, results in a lowered deposition current, given a fixed deposition potential. The change in deposition current with time results in the characteristic current trace shown in Figure 6.2.

As explained in Section 5.3, deposition of the copper was mainly carried out galvanostatically. Thus assuming that the current density remains constant and rearranging Equation (6.3) the following expression is found for the minimum required bulk electrolyte concentration. It should also be taken into account that the diffusion of Cu^{+2} ions is a function of the concentration of the $CuSO_4$.

$$c^b = \frac{J}{4nFD}\left(4L + \pi r\right) \tag{6.4}$$

The steady-state current is a result of the spherical diffusion which allows more electroactive species to reach the electrode surface per unit time and therefore yields a high current per unit area. Based on this steady state current, the cyclic voltammogram trace is expected to display an S-shaped sigmoidal shape [250], as is also seen for the redox reaction of copper in the gyroid-structured templates (Section 6.3.1).

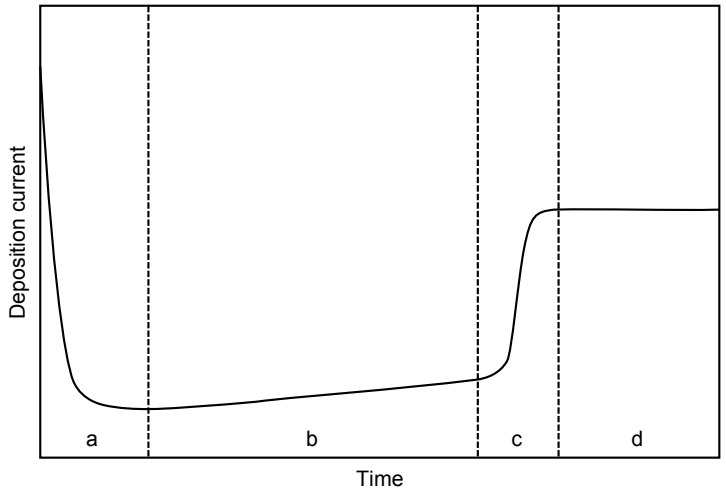

Figure 6.2: Theoretical chronoamperometry trace of depositions inside an array of nano-pores. **(a)** Mass-transport limited Cottrell diffusion regime. **(b)** Steady-state spherical diffusion regime. The current increases approximately linearly due to the progressively shorter nanopore length. **(c)** Over-growth regime where growth takes place past the top surface of the template. **(d)** Flat film regime where the over-growth from neighbouring pores has coalesced.

6.2 Experimental methods

6.2.1 Materials

The chemicals and materials listed in Table 6.1 were used as received unless otherwise specified.

Chemical	Purity (%)[a]	Abbreviation
Acetonitrile, anhydrous	99.8 (SA)	–
Aluminium	99.999 (KL)	–
Bis(pentamethylcyclopentadienyl) cobalt(II)	– (SA)	–
Bis(pentamethylcyclopentadienyl) cobalt(III) PF_6	– (SA)	–
Boric acid	99.5 (SA)	–
Chlorobenzene, anhydrous	99.8 (SA)	–
Copper	99.999 (KL)	–
Copper sulphate	99 (SA)	–
Diethylzinc	95 (SA)	DEZ
Flourine–doped tin oxide (FTO) coated glass	15 Ω/□ (SR)	FTO
Gold	99.999 (KL)	–
Hexachloricoplatinic acid	99.9 (SA)	–

continued

Chemical	Purity (%)[a]	Abbreviation
Iodine	99.8 (SA)	–
Lithium bis(trifluoromethanesulfonyl)imide	– (SA)	–
Lithium iodide	99.99 (SA)	–
Lithium perchlorate	99.99 (SA)	–
Methanol, laboratory reagant grade	– (FS)	–
Oxygen	99.999 (BOC)	–
Phenyl C_{61} butyric acid methyl ester	99.5 (SA)	PCBM
Spiro–MeOTAD hole conducting material	– (SR)	Spiro
SU–8 2000.5	– (MC)	–
Tert–butylpyridine	96 (SA)	–
Toluene, anhydrous	99.8 (SA)	–
Trimethylaluminium	97 (SA)	TMA
Water, deionised	18 MΩ	DI water

[a] Suppliers are given in brackets: Fisher Scientific, FS; Sigma Aldrich, SA; Greiner Bio-One, GBO; Solaronix, SR.

Table 6.1: Chemicals and materials used in this part of the study.

6.2.2 Sample fabrication

The substrate fabrication consists of six individual steps described in the following sections and the normal fabrication time for approximately 25 substrates is roughly two days. Figure 6.3 shows the various steps in the device fabrication and will be referenced in the section on device preparation below.

Substrate preparation

Substrates consisting of fluorine-doped tin oxide (FTO) coated glass (Solaronix, sheet resistance 15 Ω/□) are cleaned by piranha etching for 15 min (3:1 H_2SO_4:H_2O_2 at 80 °C) and subsequently vigorously rinsed with plenty of DI water (18 MΩ) and then sonicated in DI water for 10 min to remove any piranha residues. The cleaned substrates are prescribed, to facilitate easy separation at the end of substrate fabrication, into 10 mm × 14 mm sized samples and each sample is masked with Kapton tape to produce an active area of 10 mm × 10 mm (Figure 6.3A).

Cu_2O compact layer

The samples are coated with 30 nm of copper using a Kurt Lesker e-beam evaporator at a rate of 1 Å s^{-1}. The normal operating pressure is 10^{-6} torr and the source was

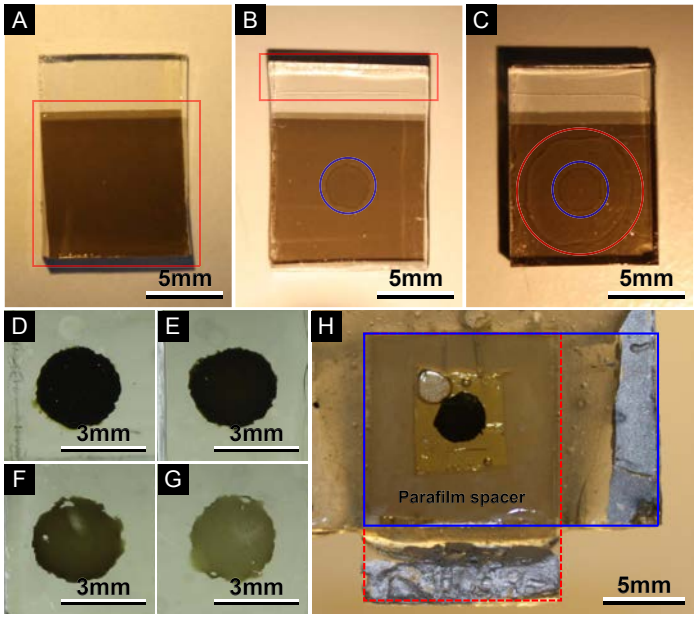

Figure 6.3: Sample fabrication of gyroid-structured $Cu/Cu_2O/$ solar cells. **(A)** Copper compact layer evaporated on FTO substrate (red square). **(B)** Patterning of circular device area (blue circle) using SU-8. Prior to exposure SU-8 along one edge is removed to ensure good electrical contact (red rectangle). **(C)** Spin-coating of gyroid-forming polymer (red circle). The patterned device area is visible (blue circle). **(D)** – **(G)** Electrochemical deposition of copper subjected to various thermal oxidation protocols. **(D)** As-deposited copper (P1). **(E)** 70 °C for 1 h in O_2 (P3). **(F)** 2 h for 2 h in air (P7). **(G)** 350 °C for 2 h in air (P9). **(H)** Liquid electrolyte device assembled using a gyroid-structured copper electrode (dashed red rectangle), a platinised counter electrode (blue rectangle), and a 300 µm parafilm spacer.

99.999 % copper. Once exposed to air, a thin Cu_2O layer is formed on the surface of the copper compact layer, as expected from copper oxidation in air at room temperature [251] (Figure 6.3A).

Surface functionalisation

The substrates are plasma etched under a 50 W air plasma at a pressure of 0.6 mbar for 15 s using a Diener MRC 100 plasma etcher to render the substrates hydrophilic. Substrates are used as is or are silinised for 8 s in a solution of 0.1 % octyltrichlorosilane (OTS) in dry cyclohexane.

SU-8 mask

The substrates were covered with SU-8 photo-resist (Microchem 2000.5 resist, approximately 1 mL cm^{-2}) and spin-coated at 6000 RPM (acceleration of 500 RPM/s^2) for 45 s. Prior to the pre-exposure bake, the SU-8 along one edge of the substrates was removed using acetone to expose the underlying FTO and thus to provide good electrical contact for the subsequent electro-deposition and device characterisation (Figure 6.3B). The substrates were pre-baked for 1 min at 65 °C, 1 min at 90 °C and 1 min at 65 °C and exposed in an MJB4 mask aligner (SUSS MicroTec MJB4, λ >350 nm) using various circular masks with diameters of 0.9 mm, 2.5 mm and 4.5 mm. The masks were fabricated by laser printing on overhead transparency sheets. Before development of the SU-8, the substrates were post-baked with the same parameters as the pre-bake. The SU-8 was developed in propylene glycol methyl ether acetate (PGMEA) for 40 s under light agitation, rinsed with fresh PGMEA and dried with dry N_2. The final sample is shown in Figure 6.3B.

Thin polymer film self-assembly

The double-gyroid thin films were spin-coated on the SU-8 covered samples and thermally annealed to achieve the double-gyroid morphology as previously described in Section 5.6 (Figure 6.3C). Once annealed the templates were voided as described in Section 5.6.3 for 1 h to 10 h depending on the film thicknesses [87]. If the samples are exposed to the alkaline NaOH solution for extended periods of time, the underlying copper compact layer is oxidised, eventually leading to the removal of the Cu_2O/Cu layer which detaches the polymer film [252]. As such the etching time of the poly(lactic acid) block was calibrated using an electrochemical method developed by Crossland *et al.* [87].

Electrochemical deposition of copper

Copper was deposited inside the voided polymeric templates by potentiostatic and galvanostatic electrochemical deposition in a standard 3-electrode electrochemical cell at room temperature, using a polished copper counter electrode and a saturated calomel reference electrode (SCE). The electrolyte consisted of an aqueous solution of 0.1 M $CuSO_4$ and 0.2 M H_3BO_4. Prior to deposition the samples were dipped in methanol six times (1 s per dip) to promote the infiltration of the electrolyte into the hydrophobic polystyrene templates by the exchange of the low surface methanol with the aqueous electrolyte. The samples were left in the plating solution for 30 s prior to deposition to achieve an equilibrium open-circuit potential of approximately 0.05 V. The deposition consists of two steps: a nucleation step for 1 s and a subsequent deposition step. The nucleation and deposition steps were carried out at -1 V and -0.3 V for the potentiostatic deposition. For the galvanostatic deposition, the corresponding current densities for the nucleation and deposition steps were 250 mA cm^{-2} and 25 mA cm^{-2} respectively. A gyroid-structured copper film deposited through an SU-8 mask is shown

in Figure 6.3D.

Thermal annealing

Prior to device assembly the samples were exposed to various thermal annealing protocols. For a detailed description of the protocols see Section 6.3.2. The majority of the samples were annealed in an Elite tube furnace from 50 °C to 400 °C under either air, 99.999 % N_2 or 99.999 % O_2 atmospheres. Heating rates ranged from 0.1 °C min^{-1} to 10 °C min^{-1}. Samples were annealed either with the polymeric template in place or removed before annealing. The polymer templates were removed by immersing the samples in dimethylformamide (DMF) for 30 min and then rinsing them with acetone before drying them with dry N_2. Large area samples were annealed on a large area programmable hotplate. Annealing temperatures and heating rates were within the same range as for samples annealed in the tube furnace.

6.2.3 Solar cell characterisation

The solar cells were assembled and characterised according to Section 5.4.2 and Section 5.4.3. An assembled device is shown in Figure 6.3H.

6.3 Results and discussion

The sample fabrication and characterisation of the double-gyroid-structured Cu/Cu_2O electrodes and devices can be divided into three sections which will be covered below: 1) Fabrication of free-standing, morphologically intact copper/Cu_2O gyroid-structured electrodes including the electrochemical deposition of copper and in-template thermal treatment; 2) Post-deposition thermal oxidation of the fabricated gyroid network at various temperatures and times. This section will cover how the morphology as well as the composition and crystallographic structure of the samples change with the various oxidation procedures; 3) Fabrication and characterisation of solar cells as a function of oxidation temperature and time. This includes band structure and optical measurements as well as measurements of device performances including both light and dark I-V behaviour and EQE.

6.3.1 Fabrication of stable Cu/Cu_2O gyroid networks

Electrochemical deposition of copper

To aid the electrochemical deposition, three modifications were made to the standard fabrication route of porous polystyrene templates described in Section 5.6.

Firstly the FTO-coated glass substrates were coated with a thin, 30 nm layer of copper by e-beam evaporation as described in Section 6.2.2. This layer serves two purposes. Once oxidised in the subsequent thermal treatments, the layer serves as the Cu_2O compact layer in the assembled devices (Section 5.4.2). Secondly it is used to promote a more uniform deposition of copper compared to the bare FTO substrate.

Secondly the standard functionalisation scheme described in Section 5.6.1 was modified. Due to the very low stability of the Cu/Cu_2O compact layer in the piranha clean, this step was replaced by plasma etching under a 50 W air plasma (Diener MRC 100, 0.6 mbar) for 15 s to render the substrates hydrophilic. The substrates changed from a contact angle of $>90°$ to $<90°$ after plasma etching.

However the functionalisation of the substrates for 8 s in 0.1 % OTS in dry cyclohexane did not produce reproducible results with the expected porous film/substrate interface [66], which is required for electrochemical deposition. This is thought to be caused by a different initial density of -OH groups after plasma etching compared to piranha etching which affects the formation of the OTS self-assembled monolayer. Attempts with shorter and longer functionalisation times did not lead to improved results.

Instead a different approach was taken where the hydrophilic substrates were used directly after the plasma etching step. This led to a wetting layer of poly(lactic acid) on the copper/Cu_2O compact layer which guarantees continuity between the PLA block and the substrate. The main drawback of this functionalisation route is the etching of this PLA wetting layer during the template voiding which tends to detach the thin polymer films from the substrates.

Thirdly, and partially as a solution to this drawback, the substrate was covered with an SU-8 mask (Section 6.2.2). The SU-8 mask serves three purposes: it makes subsequent electrochemical depositions more uniform, homogeneous and repeatable since the growth is confined to a small area; it defines a region with a well-known area which assures that the active area for measurements of device characteristics remains the same between subsequent devices; and it ensures that the polymer film adheres well to the substrate despite the modified surface functionalisation described above. This enhanced adhesion is caused by the wetting of the hydrophobic SU-8 by the polystyrene portion of the block copolymer. Depending on which part of the project the samples were used for, the circular active area was chosen to have a diameter of 0.9 mm, 2.5 mm or 4.5 mm. A sample with an SU-8 masked active area can be seen in Figure 6.3B.

Figure 6.4 shows an SEM cross-section of a double-gyroid-structured polymer template assembled on the $Cu_2O/Cu/FTO$ substrate prior to the electrochemical deposition. It shows the highly-ordered morphology achieved by the use of block copolymer templates and also the 11 nm characteristic length scale which gives rise to high surface area. For electrochemical deposition in a porous template, the main requirement is that the interface between the conducting substrate and the template is continuous and fully porous, whereas the template/air interface only has to be sufficiently porous to allow for electrolyte infiltration. As seen in Figure 6.4B, the porosity of the double-gyroid is continuous all the way down to the substrate and the template/air interface in Figure 6.4C displays sufficient porosity.

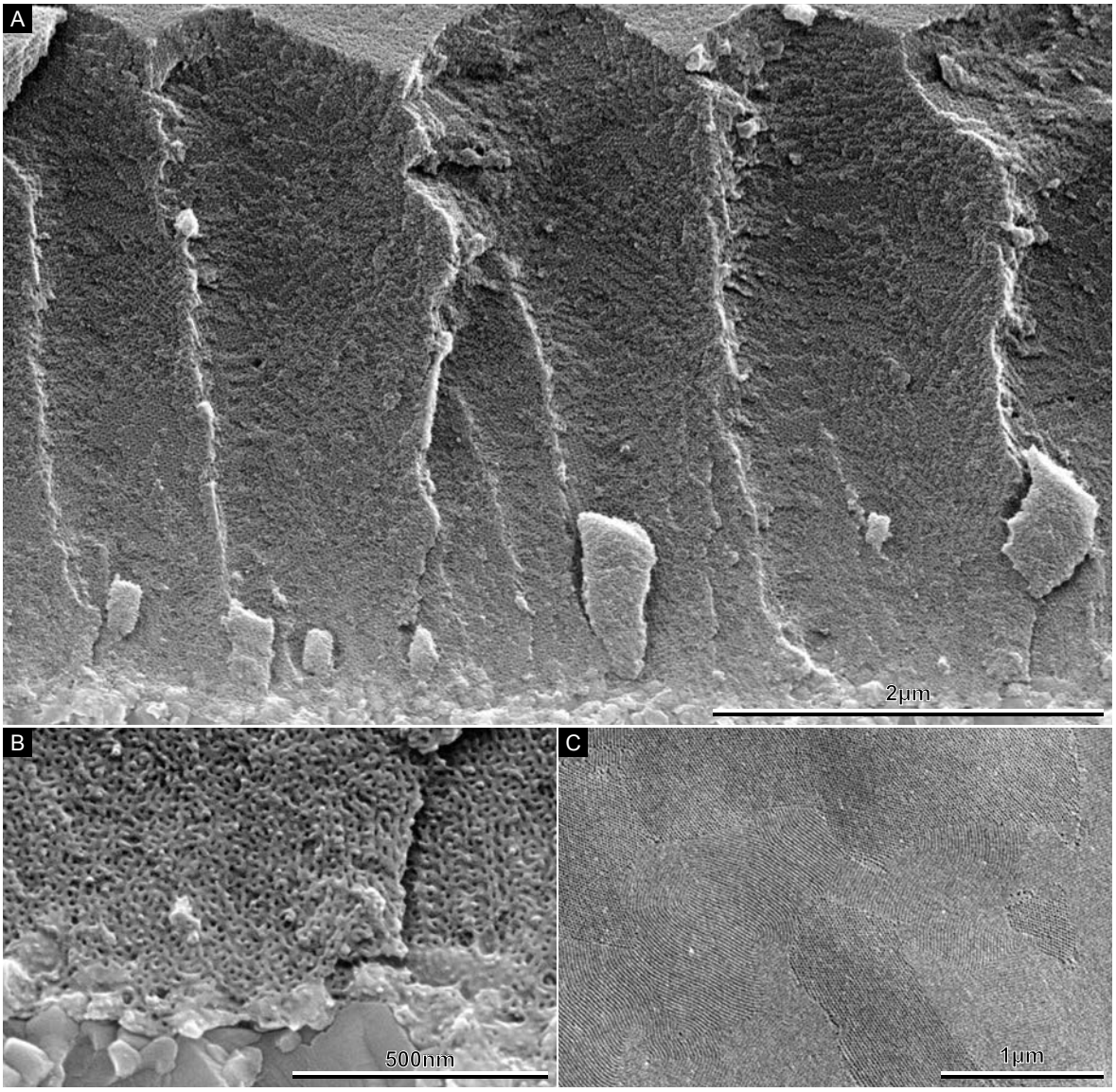

Figure 6.4: Double-gyroid-structured nanoporous polystyrene template **(A)** Cross-sectional view of a voided double-gyroid polystyrene thin film template. **(B)** View of the bottom of the film in **A** displaying the continuous porosity. **(C)** View of the partially porous free-surface of the film in **A**.

The electrolyte for the copper deposition which consisted of $CuSO_4$ and H_3BO_4 was chosen after discussion with **Dishant Mahendru** and consultation of protocols found in the literature [253]. As described in Section 6.1.5, a minimum electrolyte concentration is needed for galvanostatic depositions inside nanoporous templates. Even though in this case the geometric current density, the applied current divided by the area of the SU-8 mask, is $10\,\mathrm{mA\,cm^{-2}}$ the effective current density is higher due to the porosity of the template. The cross-sectional area fraction of the pores in the double-gyroid templates is approximately equal to the volume fraction of the pores, in other words 38.5 %, giving an effective current density of $25\,\mathrm{mA\,cm^{-2}}$.

Given the fixed current density and a pore length of 10 µm (which is the upper limit used in this study taking into account the extra distance due to the complex geometries of the gyroid network), a pore radius of 5.5 nm and a diffusion coefficient of Cu^{+2} ions of $5 \times 10^{-6}\,cm^2\,s^{-1}$ [254], the minimum bulk concentration needed for a steady-state deposition at the bottom of the template is 10 mM. This is an order of magnitude below the concentration used in this study. However one of the disadvantages of a high concentration of $CuSO_4$ is the formation of large nuclei with a low nucleation density [255]. The concentration of boric acid was also increased compared to literature values, which improves the electrolyte conductivity and lowers the cathode over-voltage [256] as well as counteracting the lowered nucleation density caused by the high concentration of $CuSO_4$ [255]. The aqueous electrolyte used for all electrochemical depositions of copper contained 0.1 M $CuSO_4$ and 0.2 M H_3BO_4. The solution had a pH of 3.

Based on protocols in the literature for the electrochemical deposition of copper [256], the deposition into the polymer templates was initially performed potentiostatically at approximately −0.3 V (vs. SCE). A typical cyclic voltammogram of the Cu_2O/Cu/FTO substrate in the aqueous electrolyte can be seen in Figure 6.5A.

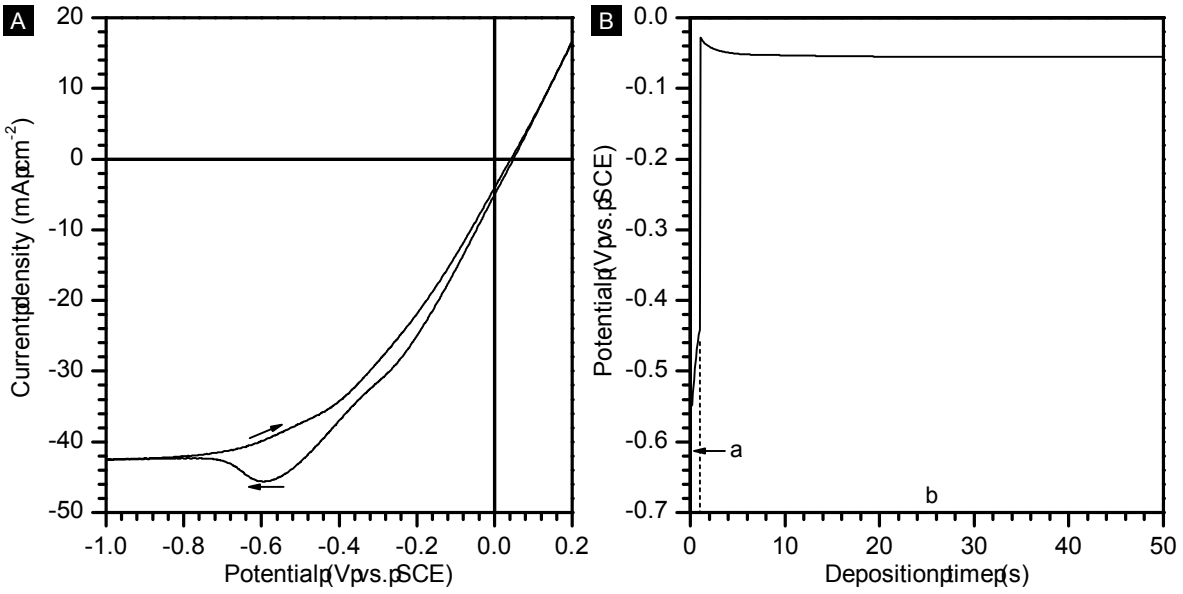

Figure 6.5: Electrochemical deposition of copper. **(A)** Cyclic voltammogram of a Cu_2O/Cu/FTO substrate working electrode in contact with a copper sulphate containing electrolyte. A sigmoidal shape of the current response is clearly seen. **(B)** Typical trace of the galvanostatic deposition of copper inside the polystyrene templates. Region **a** and **b** correspond to the nucleation and deposition steps respectively.

However potentiostatic depositions led to a non-uniform growth (Figure 6.6A) which was thought to be due to problems with sparse nucleation of the copper growth on the Cu_2O/Cu/FTO substrate. The low nucleation density led to the pronounced formation of spherical growth fronts as seen in Figure 6.6A. It has been reported that a short nucleation step at a more negative potential would increase the number of nucleation sites and improve the deposition uniformity [66]. However the application of a nucle-

ation step of −1 V for 1 s did not improve the nucleation density and the deposition uniformity.

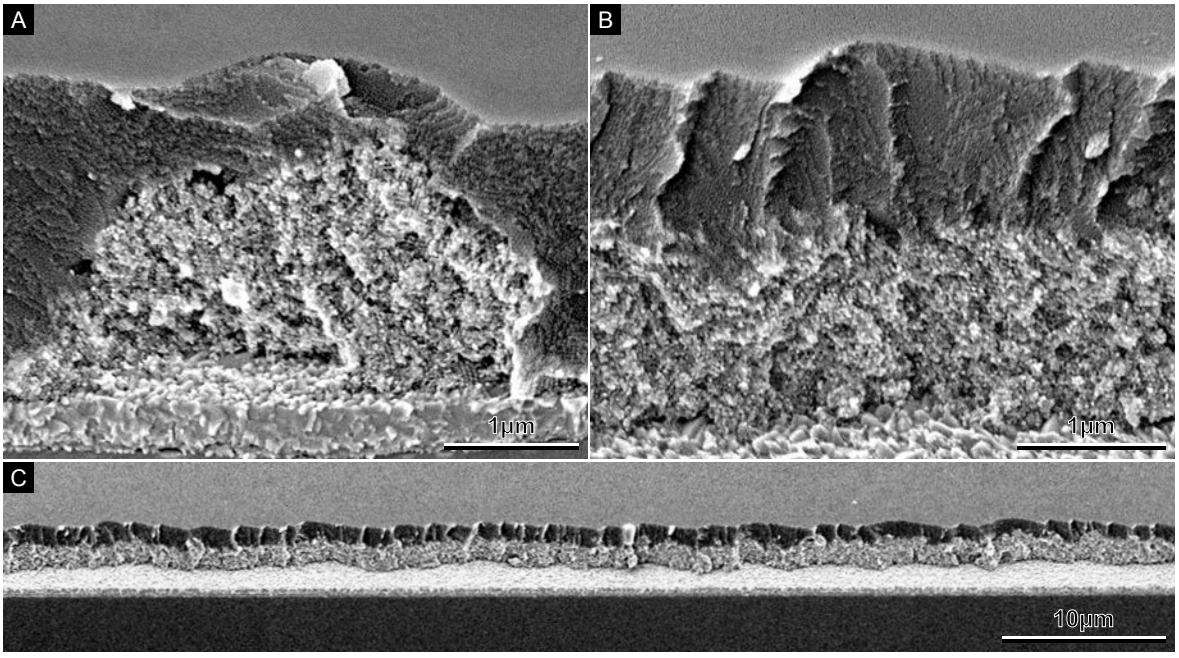

Figure 6.6: Electrochemical deposition of copper in nano-structured template. **(A)** Potentiostatic deposition of copper inside the gyroid template displaying a low nucleation density and therefore pronounced spherical growth fronts. **(B)** Galvanostatic deposition of copper inside the gyroid template displaying a uniform growth. **(C)** Low magnification view of **B** showing uniformity over large areas.

Even though the deposition of copper is feasible over a relatively large range of potentials and processing parameters such as electrolyte composition and temperature, the deposition of uniform thin films can be difficult. The unwanted morphologies shown in Figure 6.7A-I have been encountered throughout this study.

Due to the poor results seen for potentiostatic depositions inside the polymer templates, galvanostatic deposition was chosen instead and was found to be a much more successful deposition technique. Based on the current densities observed for potentiostatic depositions at −0.3 V, an effective current density of 25 mA cm^{-2} is used throughout this project. An effective current density of 250 mA cm^{-2} is applied for 1 s during the nucleation step. The nucleation current density was chosen by qualitatively comparing the uniformity of depositions at various current densities and nucleation times. Using these optimised parameters, the copper deposition display a uniform nucleation and growth through the polymer template (Figure 6.6B). The deposition is also uniform in thickness over large areas (Figure 6.6C) which is important for comparing device performances. A typical voltage vs. time trace for the galvanostatic depositions is shown in Figure 6.5B.

The growth rate during galvanostatic deposition on a flat device substrate with the

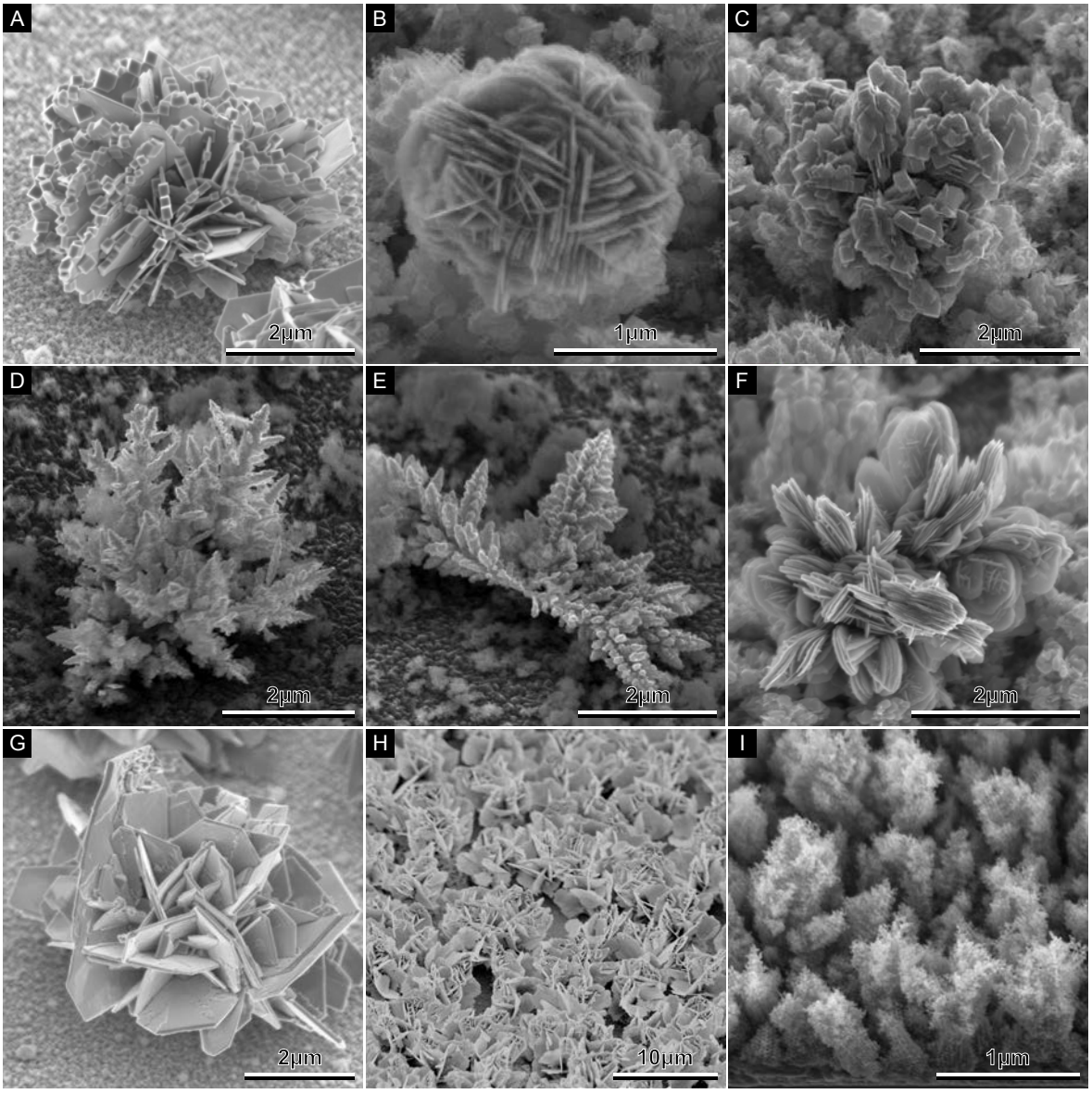

Figure 6.7: Unwanted growth morphologies encountered during copper deposition. **(A) - (G)** Non-templated growth morphologies. **(H)** Lower magnification view of **G**. **(I)** Dendritic-like growth through a double-gyroid-structured template.

copper compact layer was $0.36\,\mathrm{nm\,mC^{-1}\,cm^{-2}}$, which corresponds to a deposition efficiency of 98 %, assuming a molecular weight and density of copper of $63.55\,\mathrm{g\,mol^{-1}}$ and $8.96\,\mathrm{g\,cm^{-3}}$ respectively. The growth rate inside the polymeric templates was determined by thickness measurements using SEM to be $0.93 \pm 0.02\,\mathrm{nm\,mC^{-1}\,cm^{-2}}$, given the molecular weight and density above and a template void fraction of 38.5 % [66]. This gave an in-template growth efficiency of 97 %, indicating that there appear to be no problems such as diffusion limitations associated with in-template deposition. Normal deposition times range from 10 s to 200 s producing films with thicknesses of approximately 150 nm to 2 µm. A typical trace of the measured potential versus time

can be seen in Figure 6.5B. The measured potential reaches steady-state after approximately 15 s which is confirmed by a linear growth rate. After the deposition, the films are rinsed in methanol and then water for 5 min to remove any residual electrolyte and finally dried with dry N_2.

Stability of the copper gyroids

The next fabrication step before the thermal oxidation is to remove the polymeric template used for the copper deposition. Given that the templates are spin-coated from toluene, this was the initial choice of solvent. Initial attempts to remove the template using toluene resulted in two problems: incomplete dissolution of the template and stability issues of the copper deposition. The toluene surprisingly proved insufficient to remove all of the polymer template, and polymer residues were seen whilst imaging in the SEM (Figure 6.8A). Dimethylformamide (DMF) was therefore chosen as an alternative to toluene and successfully removes the polystyrene template in 30 min.

Removal of the template using either toluene or DMF results in the morphology seen in Figure 6.8B. The samples display a disordered nano particular morphology in comparison to to the highly ordered strut-like appearance expected from copper depositions inside the polymer templates. The characteristic length scale of the copper network seen after template removal has also increased to 20 nm to 30 nm which is larger than the 11 nm expected from the pore diameter of the double-gyroid template. This change in morphology is observed as early as within 1 h of template removal.

Such a morphological change of nano-scale copper has been observed previously for the room temperature oxidation of copper nanowires [257]. We believe that besides increased oxidation due to the high surface area of the copper network, the observed distortion is caused by a process, well-known for electro-deposited copper, called self-annealing. This process appears even at room temperature and causes the removal of stresses from the deposit by coarsening of the copper nano-crystallites [258, 259]. It is this coarsening that leads to the destruction of the expected ordered structure and the increase in observed length scales. The very fast self-annealing displayed in our samples is most likely due to the very small feature sizes of the copper gyroid. The small feature sizes also cause the samples to have a very high surface to volume ratio, which can make any surface contributions to the self-annealing more pronounced. The exothermic oxidation of copper to copper oxide in air will also locally heat the structure which could accelerate the self-annealing process.

It was observed that certain parts of the gyroid-structured copper films, normally the top surface, remained intact after template removal in DMF and showed the expected 11 nm ordered morphology (Figure 6.8B). The reason for this increased stability of the copper structure is thought to be due to the oxidation of the upper most parts of the copper deposition which are in contact with air through the porous template. The oxidation of the copper surface with the template still in place allows for the morphology to remain intact due to the mechanical confinement offered by the template.

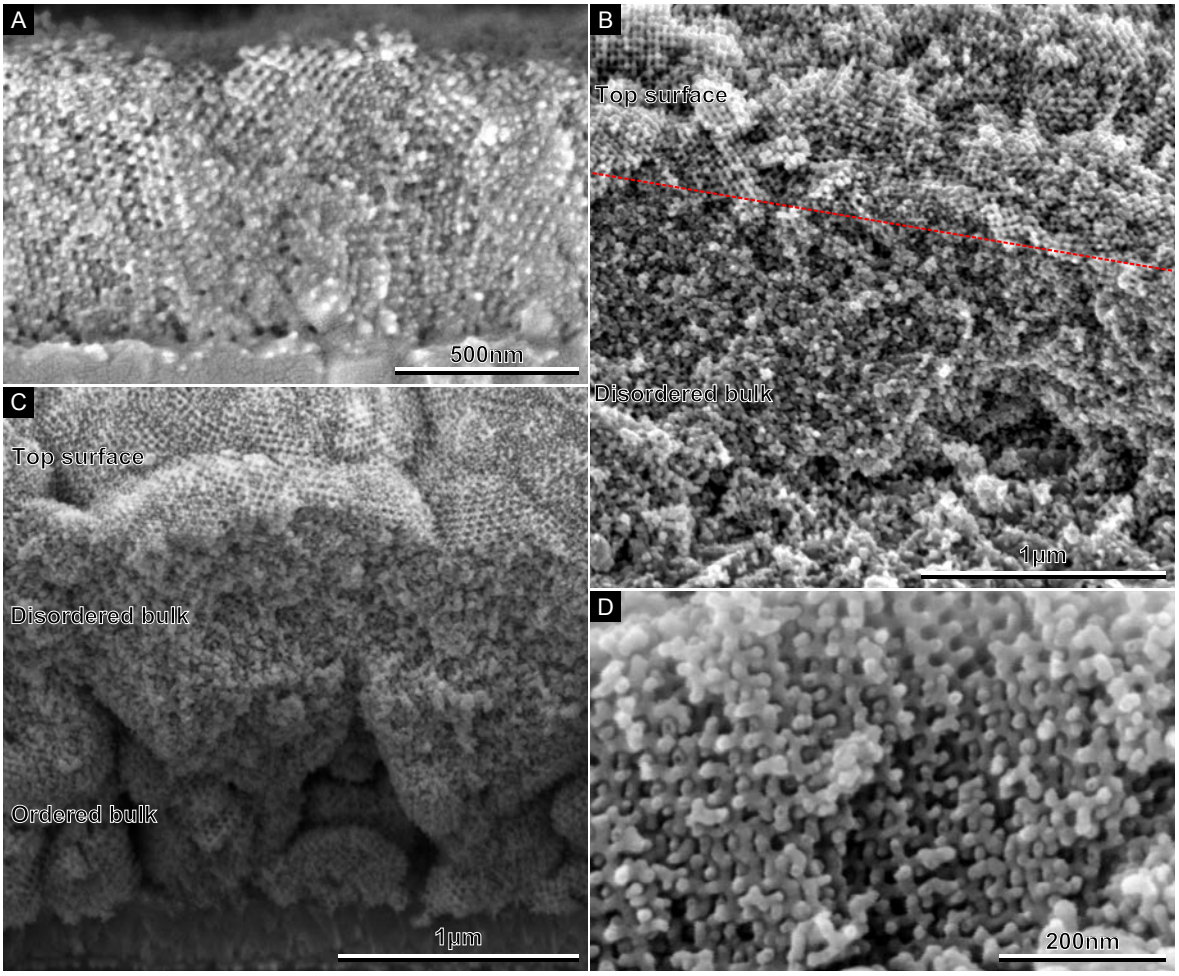

Figure 6.8: Instability of the copper gyroid upon removal of the polystyrene template. **(A)** Use of toluene proved insufficient to fully remove the polystyrene template as can be seen by the regions with lack of porosity. **(B)** The bulk of the gyroid-structured thin film restructures upon removal of the template and the high order is lost. Only the top of the film remains intact after being exposed to air through the pores in the template. **(C)** Order is also maintained further into the film if the copper deposition is not homogeneous. **(D)** After the in-polymer oxidation of the copper at 70 °C in O_2, the order of the replica is maintained in the bulk upon template removal.

The surface oxidation also appears to prevent self-annealing upon template removal which suggests that self-annealing is a mainly surface-driven process in our nanostructures. Further evidence for this explanation is found when observing SEM cross-sections of samples in which the copper deposition is not homogeneous but voids are present (as shown in Figure 6.8C). As expected, the top surface retains the gyroid morphology whereas the bulk of the sample reorders. However due to the voids present in the template, the region nearest to the substrate is also exposed to air and its surface oxidises, preventing it from reordering upon template removal.

Given the hypothesis that the loss of order and coarsening seen upon removal of the polymer template is compounded by local heating of the nano-structure due to the exothermic oxidation of the copper, initial attempts were made to remove the template at temperatures lower than room temperature. Successful removal of the template at reduced temperatures relies on the use of a good solvent for polystyrene that has a low melting point.

Toluene had already been shown not to be a sufficient solvent and was therefore disregarded. Three other solvents, acetone, dimehtylformamide and diethyl ether, which have melting points of $-95\,°C$, $-60\,°C$ and $-116\,°C$ respectively, were used instead. Liquid nitrogen was added to the solvent and the mixture was allowed to return to its liquid phase. The as-deposited samples were immersed in the cooled solvent for 15 min and then removed and dried with dry N_2. Attempts were also made in which small amounts of H_2O_2 (melting point is $-52\,°C$ for a 50 % in water mixture) were added to the solvent to allow the copper to oxidise at a reduced temperature. The reason for this procedure was to allow the outer surface to oxidise simultaneously with the template removal and therefore stabilise the gyroid structure. However none of these attempts to remove the template at a reduced temperature proved successful in retaining the expected highly ordered morphology of the copper.

Based on the results which show that the native surface oxidation of the gyroid-structure copper network prior to the removal of the polystyrene template leads to improved stability, an annealing protocol was devised in which all of the surface of the copper deposition was partially oxidised in-situ in the polymer template. This was achieved by thermally annealing the samples in a tube furnace at 70 °C for 1 h under an oxygen (99.999 %) atmosphere. The oxygen diffuses through the polystyrene polymer matrix and oxidises the copper at the copper/polymer interface. This in-template oxidation method is made possible by the relatively high diffusion rate of oxygen through polystyrene of the molecular weight used in the templates ($30\,kg\,mol^{-1}$) [260].

The relatively low oxidation temperature of 70 °C was chosen because of the lowered glass transition temperature ($T_g \approx 75\,°C$) of the voided block copolymer template Section 7.3.1 [74]. Above this temperature the top surface and the non-replicated regions of the polymer template reorder and become non-porous, limiting the diffusion of oxygen. After this low temperature partial oxidation, the template was removed by immersion in DMF for 30 min and then the samples were rinsed in acetone before drying in a stream of dry N_2. The 70 °C oxidation procedure successfully retained the ordered, 11 nm morphology expected from the double-gyroid template and the resulting negative copper/Cu_2O replica of the template is shown in Figure 6.8D.

6.3.2 Post-deposition thermal oxidation of Cu/Cu_2O gyroids

The following section first details the thermal annealing protocols used, and then introduces the results of these protocols. The results will be grouped and presented for each experimental technique. This is due to the large number of parameters associated with the thermal oxidation procedure combined with the large range of experimental

techniques. The section will conclude with a summary that combines results from the different experimental techniques to explain the morphological changes seen for the various thermal oxidation protocols.

Thermal annealing protocols

To understand fully how the morphology and material properties of the gyroid-structured copper network change under various oxidation/annealing protocols, samples were studied using SEM, TEM, XRD, XPS, Auger spectroscopy, GI-SAXS and optical spectroscopy. The thermal annealing protocols used in this work together with the experimental parameters used for each protocol are displayed in Table 6.2.

Protocol	Step 1			Step 2			Step 3		
#	T/°C	t/min	Gas	T/°C	t/min	Gas	T/°C	t/min	Gas
P1	As-deposited copper gyroid								
P2	As-deposited copper gyroid and template removal								
P3	70	60	O_2	Template removal			-	-	-
P4	70	60	O_2	-	-	-	-	-	-
P5	70	60	O_2	Template removal			70	480	Air
P6	70	60	O_2	70	480	Air	Template removal		
P7	70	60	O_2	Template removal			225	120	Air
P8	70	60	O_2	225	120	Air	Template removal		
P9	70	60	O_2	Template removal			350	120	Air
P10	70	60	O_2	350	120	Air	Template removal		

Table 6.2: Thermal oxidation protocols used to modify double-gyroid stuctured copper networks.

The first protocol (P1) corresponds to a sample with the as-deposited copper but without the template removed. The second protocol (P2) is P1 with the polystyrene template removed using DMF. P3 and P4 are the partial in-template thermal oxidation after and before the template removal respectively. Protocols with additional thermal treatment steps all include this initial 70 °C oxidation step. These additional annealing temperatures were chosen as 70 °C, 225 °C and 350 °C. The two latter temperatures are based on values from the literature for the thermal oxidation of copper nano-structures into Cu_2O and CuO respectively [261]. The thermal oxidations at 70 °C, 225 °C and 350 °C were also performed both after and before polystyrene template removal. P5, P7, and P9 correspond to annealing after template removal at the three temperatures; P6, P8, P10 to annealing before. The reason for annealing the samples both before and after template removal is that experimental evidence indicates that the Kirkendall formation of a nanotubular double-gyroid network (Section 6.1.5) is suppressed when

the annealing of a double-gyroid-structured metal network takes place inside a template which offers mechanical confinement.

Images for protocols P1, P3, P7 and P9, taken with illumination from behind the samples, are shown in Figure 6.3D,E,F,G.

X-ray diffraction

X-ray diffraction is used to study crystallographic changes as a function of the employed thermal oxidation protocols. Figure 6.9 shows the XRD spectra for as-deposited copper with the polystyrene template still in place (P1) and with the template removed (P2), and the thermal annealing protocols P3, P5, P7 and P9 (Section 6.3.2). The as-deposited sample (P1) in Figure 6.9a shows, as expected, peaks for (200) and mainly (111) copper.

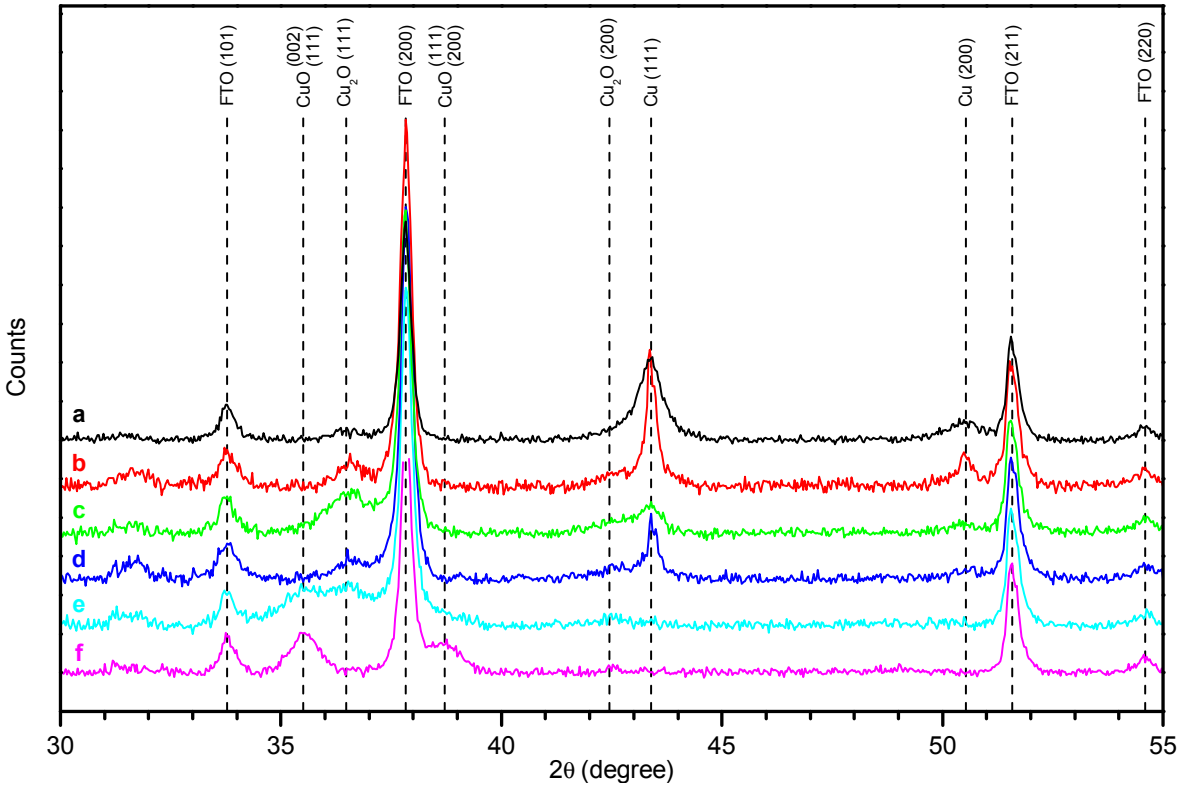

Figure 6.9: XRD spectra of the thermal oxidation of gyroid-structured copper. Thermal oxidations of spectra **c** – **f** were carried out after template removal. **(a)** As-deposited copper inside the polymer template (P1). **(b)** As-deposited copper after template removal (P2) **(c)** Sample annealed at 70 °C under O_2 for 1 h (P3). **(d)** Sample annealed at 70 °C under air for 8 h (P5). **(e)** Sample annealed at 225 °C under air for 2 h (P7). **(f)** Sample annealed at 350 °C under air for 2 h (P9).

These two peaks are seen together with minor peaks for (111) and (200) Cu_2O due to

the oxidation of the top of the gyroid copper deposition through the porous network of the polystyrene template prior to template removal, as described in Section 6.3.1.

Removal of the polymer template without the in-template thermal oxidation leads to coarsening of the copper network and loss of order as described in Section 6.3.1. The coarsening is also observed in Figure 6.9b where the expected oxidation upon template removal is shown by an increase in the (111) Cu_2O peak. The (111) and (200) copper peaks display a decreased full width at half maximum (FWHM) which is due to a coarsening of the copper crystallites.

As the samples are annealed at 70 °C in O_2 (P3) (Figure 6.9c), the intensity of the (111) and (200) copper peaks are reduced as the intensity of mainly the (111) Cu_2O peak increases. This is consistent with the surface oxidation of the copper gyroid into Cu_2O that takes place during the in-template oxidation. The observed weak (111) and (002) CuO peaks are due to the further oxidation of Cu_2O into CuO which is known to take place at room temperature when a Cu_2O surface is exposed to moisture in the air [251]. These peaks for Cu_2O and CuO are normally not visible for the thermal oxidation of flat copper films. They appear for the gyroid-structured samples due to the high surface area and therefore high surface-to-volume ratio of the copper network, which means that a higher ratio of Cu_2O and CuO to copper volumes can be achieved through annealing.

When samples are annealed according to P5, the XRD spectrum in Figure 6.9d is seen. Compared to P3, an increase in both the (111) and (200) copper peaks are seen together with a reduction in the (111) Cu_2O peak. This indicates a reduction of the Cu_2O formed during P3 to copper when the sample is thermally annealed for extended periods of time in air. The copper to oxygen ratios of P3 and P5 as measured by EDX appear virtually unchanged (Section 6.3.2). This suggests that the increase in copper should be accompanied by an increase in the amount of CuO according to Reaction 6.1 for the amount of oxygen to remain unchanged, but no noticeable increase in the (002) and (111) CuO peak is observed in Figure 6.9d for which we have no explanation. However the conversion of Cu_2O to CuO and Cu for extended annealing times is supported by the fact that CuO is thermodynamically more stable at 70 °C compared to Cu_2O.

$$\mathsf{Cu_2O} \longrightarrow \mathsf{Cu} + \mathsf{CuO}$$

Reaction 6.1: Transformation of Cu_2O to Cu and CuO.

The increase in the (111) Cu peak appears to be associated with an increase in crystallite size due to a reduction of its FWHM. Application of the Scherrer formula to the (111) Cu peaks for P3 and P5 results in a measure of the increase in crystallite size. Care has to be taken however to use these values quantitatively since use of the Scherrer formula relies on prior knowledge of the crystallite shape. Given the confinement caused by the polymer template, the copper crystallites formed during the electrochemical growth are expected to be elongated, which can indeed be seen in Figure 6.16C. We believe that the reduction in FWHM is due to an 'Oswald ripening'-type process in

which some crystallites grow at the expense of neighbouring ones, which increases their aspect ratio and therefore decreases their FWHM. One could argue that the decrease in the FWHM could also be due to a coarsening and reordering of the gyroid-structure network similar to that seen in the untreated copper networks in Section 6.3.1. However SEM imaging (Section 6.3.2) shows that the double-gyroid morphology is maintained.

When the sample is further annealed at 225 °C (P7) (Figure 6.9e) the (111) and (200) copper peaks completely disappear and instead the (111) and (002) CuO and (111) and (200) Cu_2O peaks become more prominent, which is consistent with further and complete oxidation of the copper. The ratio between the (111) CuO and (111) Cu_2O peaks appears to be one to one which suggests a similar scattering volume of the two oxides.

Samples that are finally annealed at 350 °C (P9) (Figure 6.9f) display mainly (111), (002) and (200) CuO peaks. As the as-deposited copper samples are thermally annealed an additional peak appears at approximately $2\theta = 31.5°$ that does not correspond to known peaks for FTO, Cu, Cu_2O or $Cu(OH)_2$. So far we have no explanation for this peak.

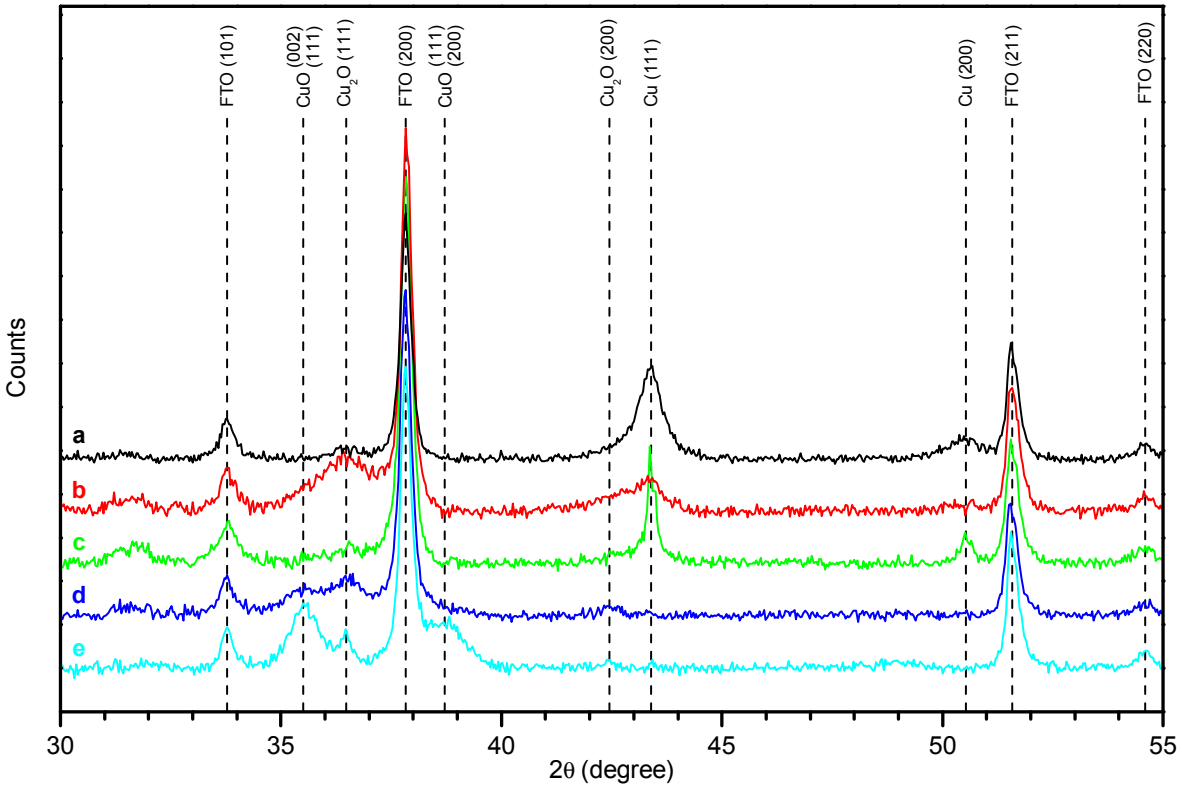

Figure 6.10: XRD spectra of thermal oxidation of gyroid-structured copper. Thermal oxidations for spectra **c** – **e** were carried out before template removal. **(a)** As-deposited copper inside the polymer template (P1). **(b)** Sample annealed at 70 °C under O_2 for 1 h with the template left in place (P4). **(c)** Sample annealed at 70 °C under air for 8 h (P6). **(d)** Sample annealed at 225 °C under air for 2 h (P8). **(e)** Sample annealed at 350 °C under air for 2 h (P10).

The difference between annealing protocols (P6, P8, P10) and (P5, P7, P9) is that the thermal annealing is done before and after the removal of the polystyrene template respectively. The XRD spectra for samples annealed with the template in place (P6, P8, P10) are shown in Figure 6.10. Relatively small differences are seen for thermal annealing before and after the template removal. They are more easily noticed by comparing (P5, P6), (P7, P8) and (P9, P10) as is shown in Figure 6.11. This figure also includes XRD measurements of the in-template annealing of the copper gyroid with and without template removal (P3 and P4).

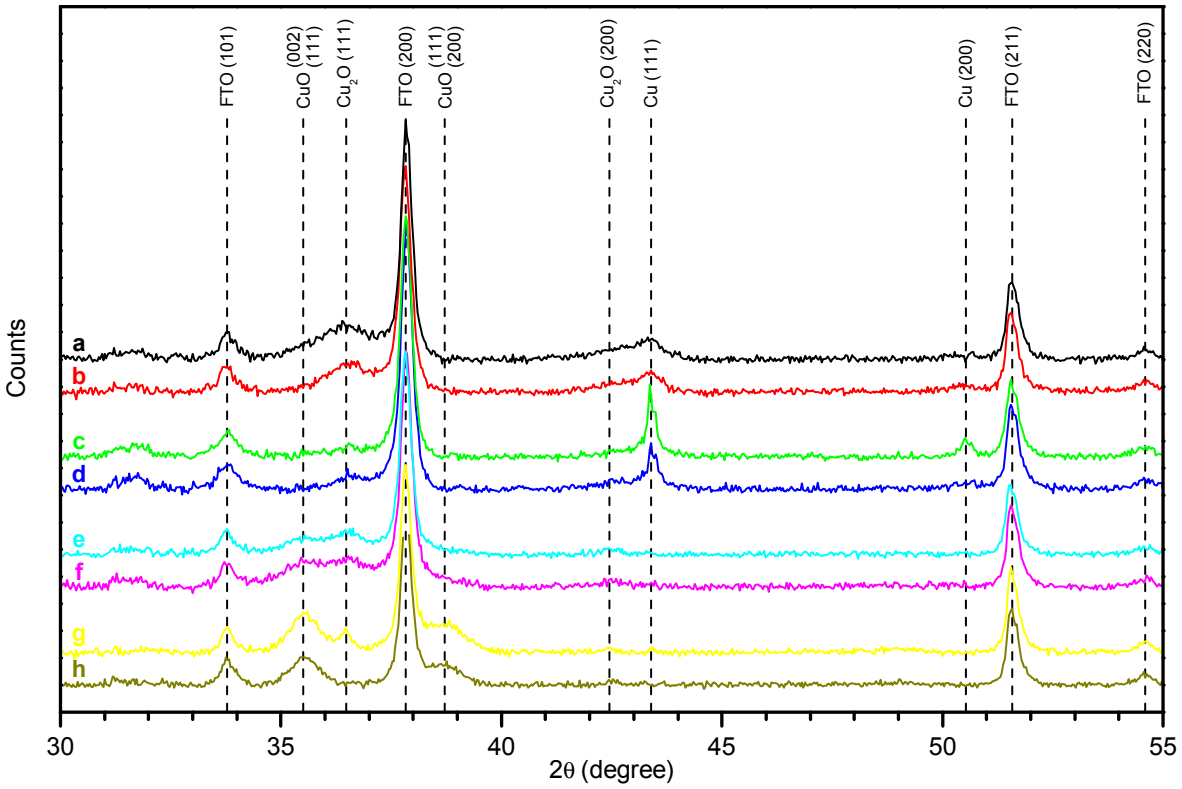

Figure 6.11: XRD spectra of thermal oxidation protocols before and after template removal. Spectra **a**, **c**, **e** and **g** show thermal oxidation before template removal and spectra **b**, **d**, **f** and **h** show thermal oxidation after template removal. Thermal oxidation protocols for spectra (**a**,**b**), (**c**,**d**), (**e**,**f**) and (**g**,**h**) are (P3, P4), (P5, P6), (P7, P8) and (P9, P10) respectively.

The fact that no difference is observed between Figure 6.11a and Figure 6.11b shows that the oxidation of the copper gyroid takes place in the in-template thermal annealing at 70 °C and no apparent oxidation takes place once the template has been removed. However for the extended oxidation at 70 °C (P5, P6) seen in Figure 6.11c,d, a pronounced difference can be observed. The sample annealed with the template in place (P6; Figure 6.11c) displays a larger increase in the (111) and (220) copper peaks and decrease in the (111) Cu_2O peak compared to the sample annealed with the template removed (P5; Figure 6.11d). This is explained by the competition between Reaction 6.1 and the oxidation of the copper. When annealed inside the template, the reduced expo-

sure to oxygen due to lowered diffusion through the template will favour Reaction 6.1 and a larger amount of copper will be observed.

For the samples annealed at 225 °C (P7, P8; Figure 6.11e,f) and 350 °C (P9, P10; Figure 6.11g,h) a larger (111) Cu_2O peak can be seen for the samples annealed inside the template (P7, P9; Figure 6.11e,g). This is similarly explained by the reduced amount of oxygen for P7 and P9 due to the presence of the template, which leads to the reduced oxidation of Cu_2O into CuO.

Figure 6.12 compares the thermal oxidation of 100 nm copper thin films and approximately 1 µm thick gyroid-structured copper films, annealed according to P5, P7 and P9. As expected from the high surface area to volume ratio of the gyroid-structured samples, thin surface oxidation of the copper indicated by the (111) Cu_2O peak in Figure 6.12b and the (111) and (002) CuO peaks in Figure 6.12d, are more pronounced in these samples. The thin flat films annealed at 225 °C and 350 °C also display peaks with a narrower full width at half maximum ((111) Cu_2O and (111), (200) and (002) CuO) which is explained by the lower confinement in the thin film compared to the gyroid-structured copper and thus the formation of larger crystallites.

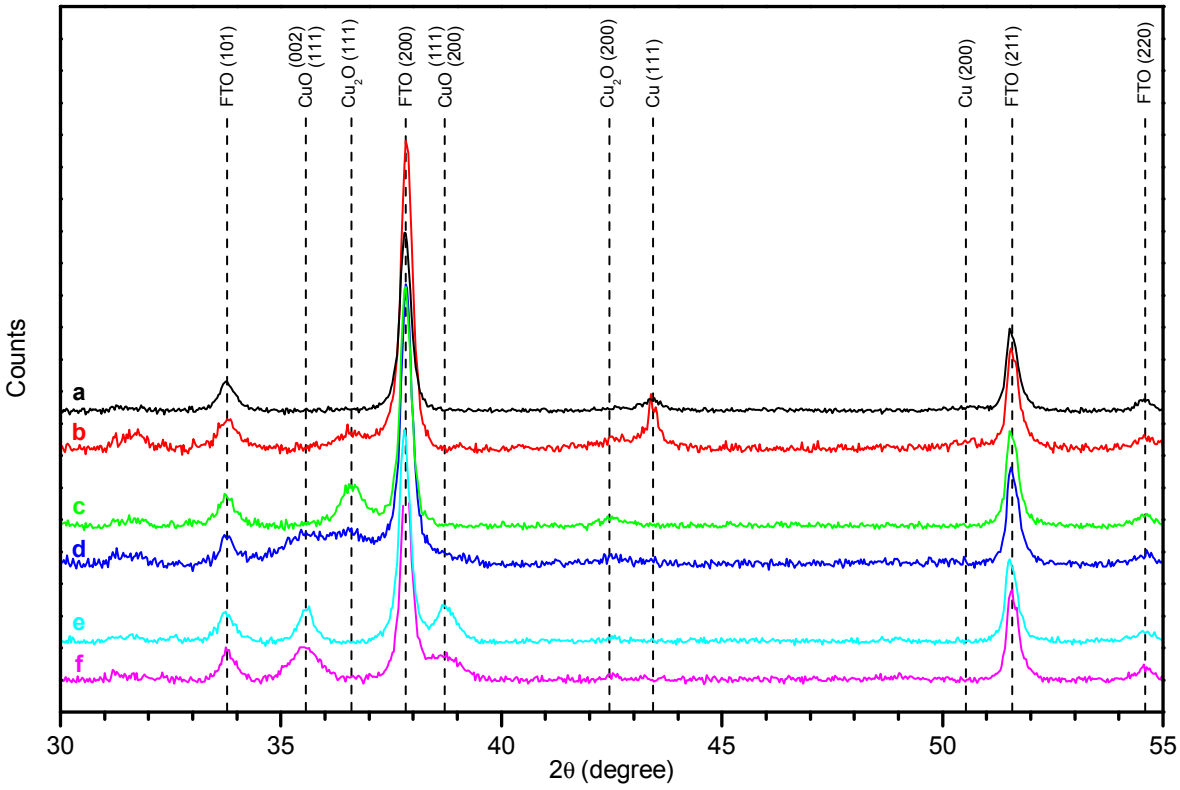

Figure 6.12: XRD spectra of thermal oxidation protocols for flat and gyroid-structured copper films. Spectra **a**, **c**, **e** show thermal oxidation of 100 nm flat copper films and spectra **b**, **d**, **f** show thermal oxidation of gyroid-structured copper films after template removal. Thermal annealing protocols for spectra (**a**,**b**), (**c**,**d**) and (**e**,**f**) are P5, P7 and P9 respectively.

Energy-dispersive x-ray spectroscopy

Energy-dispersive x-ray spectroscopy is used as a complement to XPS to determine the stoichiometry and composition of the gyroid-structured copper for various thermal oxidation protocols. As mentioned in Section 5.2.1, EDX probes average properties with a penetration depth of hundreds of nanometres, which is an advantage compared to XPS for which the penetration depth is approximately 5 nm (although argon milling can be used to depth profile samples). However care has to be taken when using EDX due to its lower compositional accuracy compared to XPS.

Figure 6.13 shows EDX spectra taken for protocols P1, P3, P5, P7 and P9. The as-deposited sample (P1) displays mainly a copper peak with a small oxygen peak, as expected due to the oxidation of the top of the copper network through the porous template upon exposure to air. This is also consistent with XRD measurements (Section 6.3.2). The onset of a peak at 0.4 keV is a carbon peak which together with the fluorine peak at 0.7 keV is attributed to the fluorinated polystyrene template. As the sample is annealed according to P3 at 70 °C, an increased oxygen peak is seen which is consistent with the in-template oxidation of the surface of the copper gyroid. The carbon and fluorine peaks are absent due to the removal of the template. Extended annealing at 70 °C (P5) does not lead to an increased oxygen peak. This, in combination with the XRD spectrum seen for P5 (see Figure 6.9), indicates that the extended oxidation protocol does not cause further oxidation compared to P3 but instead produces a transformation of the Cu_2O to Cu and CuO according to Reaction 6.1. Annealing at increasing temperatures in air (P7 and P9) leads to the further oxidation of the sample to a mixture of Cu_2O and CuO at 225 °C and pure CuO at 350 °C.

The atomic fractions of copper, oxygen and tin for the different oxidation protocols are shown in Table 6.3. Since the samples are fabricated on FTO, the oxygen contribution due to the tin dioxide has been subtracted and the corrected amounts of oxygen are displayed together with the measured value. This does not take into account any potential dopants in the FTO. These values together with data from TEM images can be used to estimate the thicknesses of the various shells present in the core/shell configuration. This will be covered in detail in Section 6.3.2.

Protocol #	Tin (%)	Copper (%)	Oxygen (%)	Oxygen (corr.) (%)
P1	12.8	61.1	26.1	0.5
P3	11.5	52.2	36.3	13.3
P5	11.7	53.0	35.3	11.9
P7	10.4	43.8	45.8	25.0
P9	12.7	30.6	56.7	31.3

Table 6.3: Composition of thermally oxidised double-gyroid-structured copper networks. The values are atomic percentages.

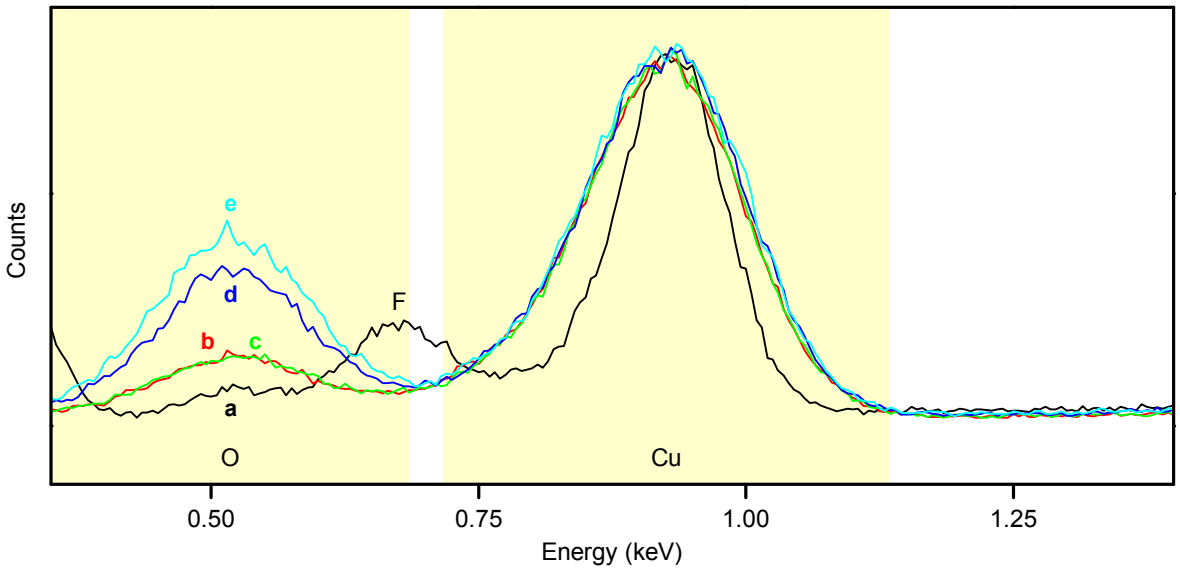

Figure 6.13: EDX spectra of thermally annealed gyroid-structured copper. The spectra have been normalised to the copper L-line at 0.93 keV. **(a)** As-deposited gyroid-structured copper (P1). **(b)** Thermally annealed at 70 °C in O_2 for 1 h (P3). **(c)** Thermally annealed at 70 °C in air for 8 h (P5). **(d)** Thermally annealed at 225 °C in air for 2 h (P7). **(e)** Thermally annealed at 350 °C in air for 2 h (P9).

Electron microscopy

This section will present and describe the scanning and transmission electron microscopy images taken throughout this study with specific focus on samples subjected to the thermal oxidation protocols described in Table 6.2. The nano-porous gyroid-structured polystyrene template prior to the electrochemical deposition of copper and the cross-section of gyroid-structured copper with the template left in place are shown in Figure 6.4 and Figure 6.6 respectively.

Scanning electron micrographs (SEM) of oxidation protocols P3, P5, P7 and P9 are shown in Figure 6.14. Figure 6.14A shows the copper network after in-template oxidation at 70 °C (P3). The gyroid-structured replica of the polymer template can clearly be seen, and the order and porosity is maintained due to oxidation in the O_2 atmosphere as previously described in more detail in Section 6.3.1. Some pore-widening is already seen at this low oxidation temperature. As the samples are further annealed at 70 °C for extended periods of time in air (P5), sample cross-sections similar to the one depicted in Figure 6.14B are seen. The cross-section displays a mixture of regions very similar to those seen for protocol P3 in Figure 6.14A (top left corner) and the formation of wider nano-tubes caused by the nano-scale Kirkendall effect. This formation of a partial nano-tubular morphology at just 70 °C is believed to be due to the formation of bamboo-like non-connected voids in the gyroid network similar to those seen for the oxidation of nickel [242]. Upon fracturing of these samples for cross-sectional SEM imaging, the struts preferentially break at one of these voids.

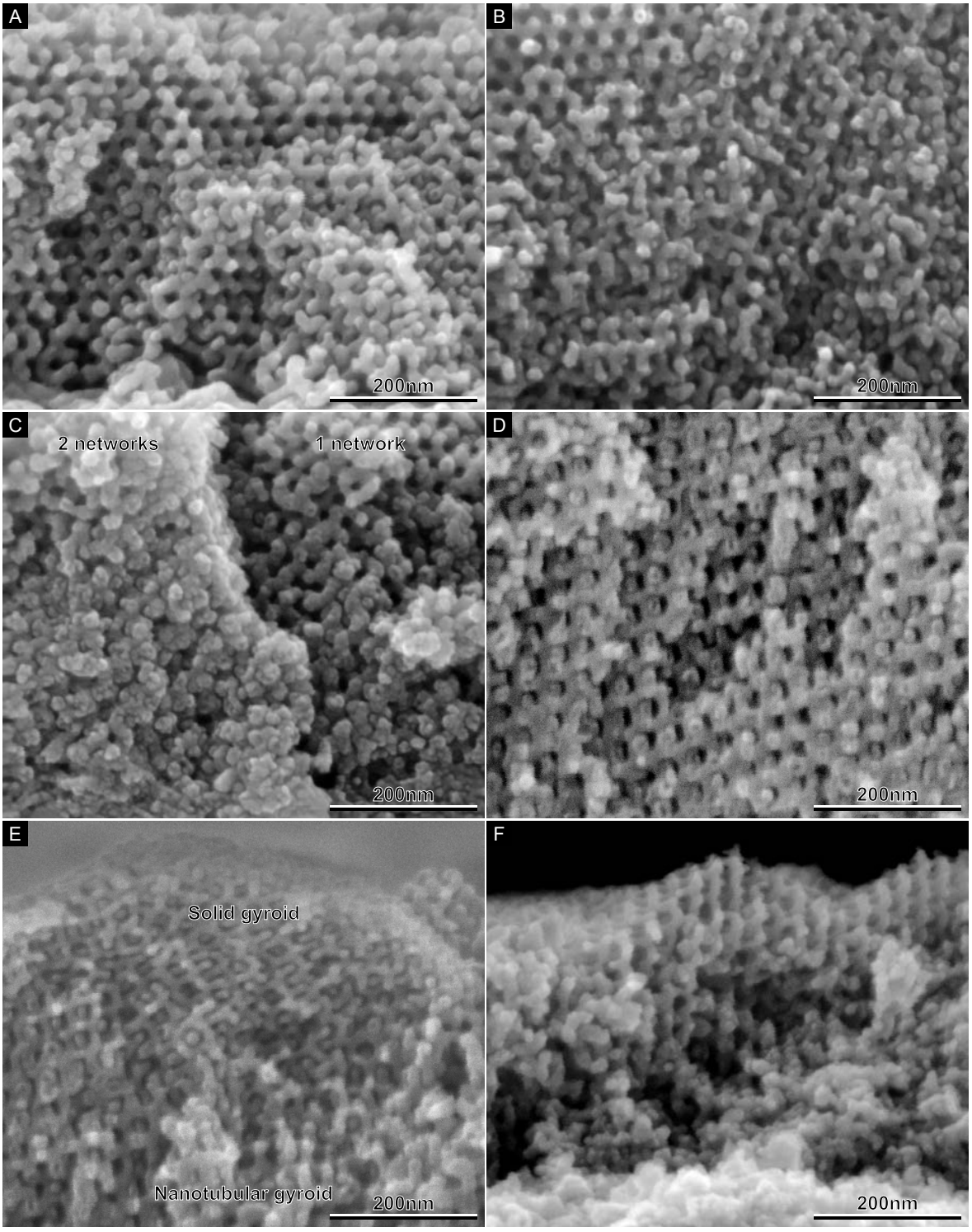

Figure 6.14: Scanning electron microscopy images of thermally annealed gyroid-structured copper. **(A)** Sample thermally annealed at 70 °C in O_2 for 1 h (P3). **(B)** Sample thermally annealed at 70 °C in air for 8 h (P5). **(C)** Sample thermally annealed at 225 °C in air for 2 h (P7). **(D)** Identical annealing protocol to **C** but before template removal (P8) **(E)** Identical annealing protocol to **C** showing intermittent regions that do not form a nano-tubular network. **(F)** Sample thermally annealed at 350 °C in air for 2 h (P9).

When the samples are annealed at 225 °C in air for 2 h (P7) (Figure 6.14C) the entire gyroid network forms a nano-tubular structure with a significant widening of the gyroid strut diameter. The diameter is widened to the extent that a large fraction of the porosity of the sample is lost. In the left half of Figure 6.14C, both of the minority gyroid networks remain present and the lowered porosity is clearly visible as is the appearance of surface roughness of the network struts. In the right half of Figure 6.14C, only one of the networks is present, which allows us to determine that the outer and inner diameter of the nano-tubes are approximately 18 nm and 7 nm respectively. It has previously been reported that the oxidation of metals inside a template which offers mechanical confinement leads to a reduced tube diameter [48]. In this study, this is also observed for the oxidation of copper, as shown by the increased porosity of Figure 6.14D (P8) compared to Figure 6.14C (P7). The surface roughness seen in Figure 6.14C is also reduced when the oxidation takes place with the polymer template in situ.

It was noticed that throughout the samples annealed according to P7, the top surface included regions that appeared not to have fully oxidised, since no nano-tubular morphology could be seen. One such region and its interface to a fully oxidised region is shown in Figure 6.14E. However XRD of samples oxidised at 225 °C (Figure 6.9E) shows no presence of copper, which suggests that these regions have indeed oxidised, but that no widening of the strut diameter due to the Kirkendall effect has taken place. We believe that this absence of the nKDE is due to the two-step oxidation at 70 °C and 225 °C, but the physical background of this observation has not been further investigated. Finally, the ordered morphology remains intact when the samples are oxidised at 350 °C in air for 2 h (P9). A nano-tubular morphology is also seen at this oxidation temperature as shown in Figure 6.14F.

SEM images taken of the top surface of samples oxidised according to P3, P5, P7 and P9 are shown in Figure 6.15. Samples that were annealed in the template at 70 °C (P3) are displayed in Figure 6.15A. The replica of the polymer template is clearly visible and the measured strut diameter is approximately 13 nm. The increase in the strut diameter from 11 nm to 13 nm is due the oxidation of the outer surface of the copper network. As the samples were annealed at 70 °C without the template for long periods of time (P5) (Figure 6.15B), regions that display further coarsening of the struts can be seen, which agree with the cross-sectional view (Figure 6.14B). The top surface view of samples annealed according to P7 display large areas where the strut diameter has significantly widened to a measured value of 19 nm compared to the 11 nm of the polymer template, which is due to the nano-scale Kirkendall effect (Figure 6.15C). However regions are also visible where no apparent oxidation has taken place, which can also be seen in the cross-sectional images (Figure 6.14E). Annealing at 350 °C according to P9 (Figure 6.15D) maintains the high order seen in Figure 6.15A and is also in agreement with the cross-sectional images in Figure 6.14F. On average a less pronounced widening of the strut is seen at this oxidation temperature compared to oxidation at 225 °C.

Transmission electron microscopy (TEM) images of oxidation protocols P1, P3 and P7 are displayed in Figure 6.16. The majority of the as-deposited copper rearranges

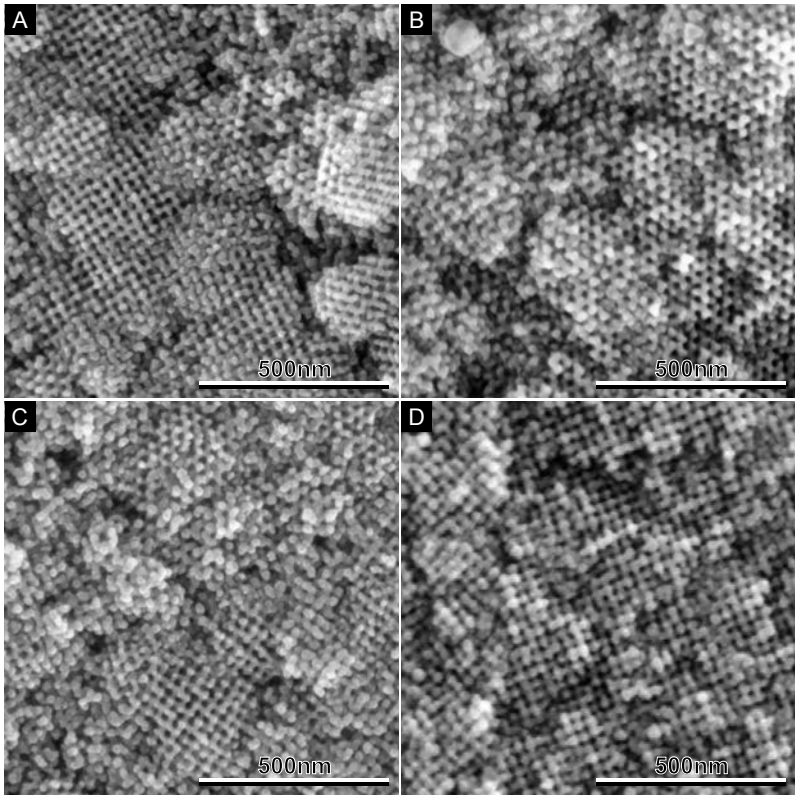

Figure 6.15: Top view of scanning electron microscopy images of thermally oxidised gyroid-structured copper. **(A)** Sample thermally annealed at 70 °C in O_2 for 1 h (P3). **(B)** Sample thermally annealed at 70 °C in air for 8 h (P5). **(C)** Sample thermally annealed at 225 °C in air for 2 h (P7). **(D)** Sample thermally annealed at 350 °C in air for 2 h (P9).

itself upon removal of the template without the 70 °C in-template annealing protocol (Section 6.3.1). However, it is possible to find regions where the ordered morphology of the gyroid and the expected 11 nm strut diameter is maintained, as shown in Figure 6.16A,B,C.

Figure 6.16A,B show the (100) plane of the gyroid morphology. The average strut diameter is estimated to be 11 nm which agrees well with SEM measurements of polymer templates replicated using platinum, and with AFM measurements of the polymer template itself [66]. A high magnification view of a single strut is seen in Figure 6.16C and shows that that the electrochemical deposition of copper inside the gyroid template creates elongated crystallites that completely fill the template pore with a length of approximately 30 nm. As the samples undergo the in-template oxidation and the polymer template is removed (P3), a slight coarsening of the copper struts is observed as seen in Figure 6.16D,E,F. This agrees with measurements taken from SEM images (Figure 6.14A) and is explained by the oxidation of the outer surface of the copper gyroid network to cuprous oxide and CuO which both have a lower density compared to copper (ρ_{Cu} =8.96 g cm^{-3}, ρ_{Cu_2O} =6.00 g cm^{-3}, ρ_{CuO} =6.31 g cm^{-3}). No re-crystallisation of the copper appears to take place during the low temperature annealing, with the

copper core of the gyroid still displaying crystallites that extend for approximately 30 nm as seen in Figure 6.16E.

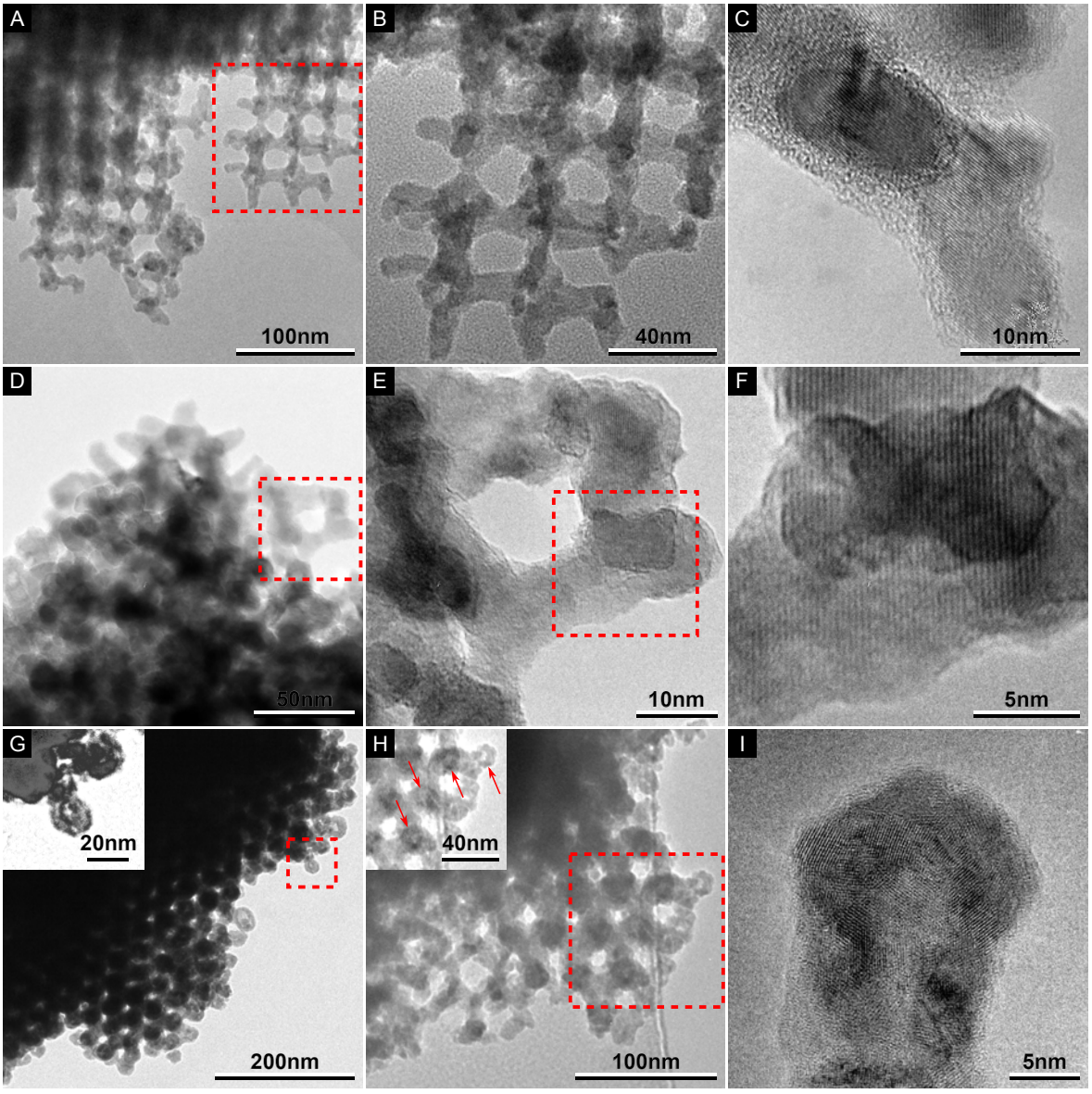

Figure 6.16: Transmission electron microscopy images of thermally oxidised gyroid-structured copper. **(A)**, **(B)** and **(C)** are as-deposited copper samples with the template removed (P2). **(B)** Higher magnification view of **A** (red square). **(D)**, **(E)** and **(F)** are thermally annealed at 70 °C in O_2 for 1 h (P3). **(E)** Higher magnification view of **D** (red square). **(F)** Higher magnification view of **E** (red square). **(G)**, **(H)** and **(I)** are thermally annealed at 225 °C in air for 2 h (P7). **(G)** The inset (red square) shows an end-on view of a tube formed via the nanoscale Kirkendall effect. **(H)** The inset (red square) shows an end-on view of a an array of tubes, indicated by red arrows, formed via the nanoscale Kirkendall effect. **(I)** A high magnification view of a single nano-tube, with an approximate shell thickness of 6 nm.

Figure 6.16G,H,I show samples that have been oxidised at 225 °C in air for 2 h (P7). Figure 6.16G,H show the (111) plane of the gyroid morphology, and it can clearly be seen that the samples have a lower porosity compared to Figure 6.16B and that the strut diameter has increased. The inset in Figure 6.16G shows a higher magnification view of the red square with a tubular morphology clearly visible. Similarly, the inset in Figure 6.16H shows an array of nano-tubes facing out of the plane. The contrast and brightness of the insets have been modified to optimise the appearance of the nano-tubes. High resolution TEM of a single gyroid strut is seen in Figure 6.16I. The shell does not form a complete circle since the strut is in plane in the bottom part of the image and then curves out of plane towards the middle of the image. An outer diameter and shell thickness of 18 nm to 19 nm and 6 nm to 7 nm respectively can be measured in the image. These two values agree with measurements from SEM images (Figure 6.14).

GI-SAXS

Gracing incident small angle x-ray scattering (GI-SAXS) is used to gain quantitative insight into the morphological changes that occur during the oxidation protocols. The sample configuration used for the GI-SAXS measurements is shown in Figure 6.17. The red line denotes the scan direction for the measurements. The reason for the division of the samples into lines is that this enables more uniform copper depositions and in turn allows for more accurate GI-SAXS measurements to be taken. Figure 6.18A,C shows two-dimensional GI-SAXS patterns with the corresponding Bragg reflections for samples oxidised according to protocols P3 and P7. The patterns, collected at an incident angle of 0.15°, are caused by scattering of the direct and reflected x-ray beams from the sample. One-dimensional intensity profiles along the q_y directions, shown in Figure 6.18B,D for Figure 6.18A,C respectively, were also extracted by integration along q_z between the integration limits denoted by the blue lines in Figure 6.18A,C. The limits were chosen to cover a q_z range where the transmission function of the gyroid has a maximum, such that the scattering is dominated by the structure of the films. Overlayed on the 1D intensity profiles are dashed lines which correspond to the scattering peaks of a double-gyroid network (space group $Ia\bar{3}d$) with a unit cell size of 43 nm.

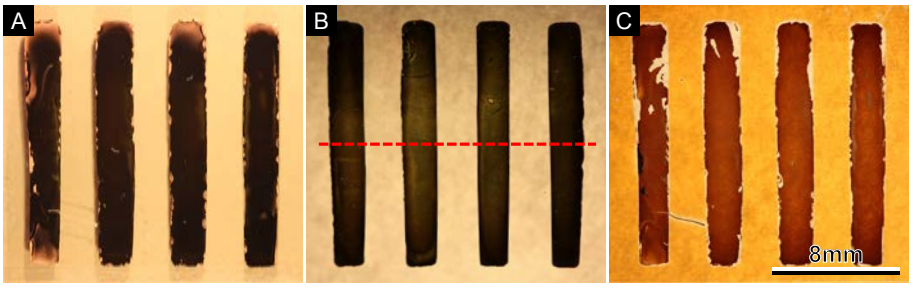

Figure 6.17: Sample fabrication for GI-SAXS measurements. The red line denotes the scan direction. **(A)** Annealing protocol P1. **(B)** Annealing protocol P3. **(C)** Annealing protocol P7.

The two scattering peaks seen in Figure 6.18B have a positional ratio of $\sqrt{2} : \sqrt{6}$ in q space and are thus attributed to the (110) and (211) spacings of the double-gyroid morphology. The scattering signal attributed to the (211) reflection is centred at $q_y \approx 0.033\,\text{Å}^{-1}$ which corresponds to a d_{211} inter-domain spacing of approximately 19 nm. The positions of the (211) and (110) scattering peaks give a unit cell size of $a = 45.5$ nm, which is fractionally larger than the unit cell size of the polymer template as measured by AFM. However we believe that this variation of 5 % is within the experimental error of the GI-SAXS measurements.

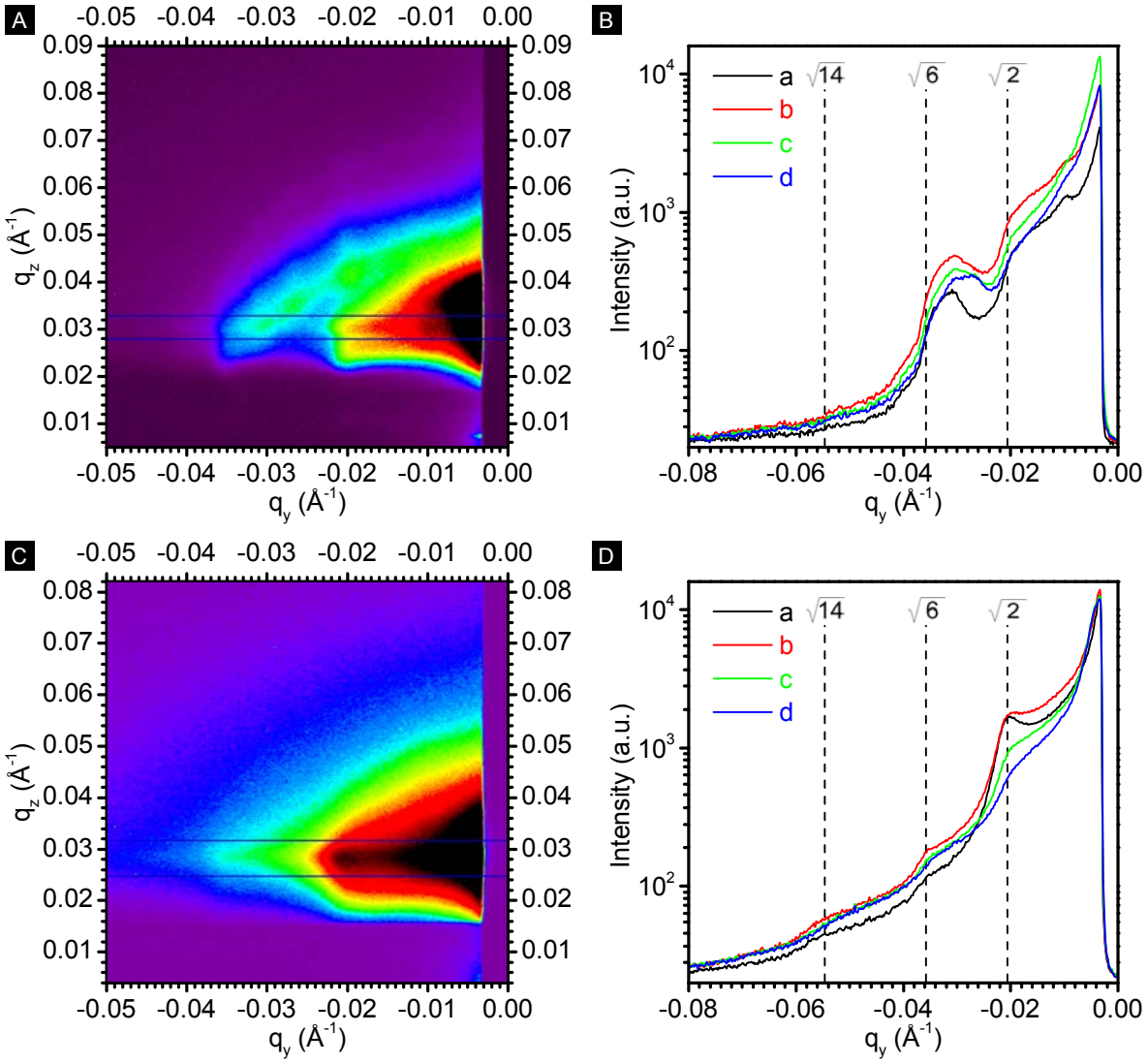

Figure 6.18: Gracing incident small angle x-ray scattering measurements. **(A),(C)** Two-dimensional GI-SAXS patterns of samples oxidised according to P3 and P7 respectively. The incident angle is 0.15°. **(B),(D)** One-dimensional intensity profiles along q_y formed by integration between the two boundary lines in **A** and **C** respectively. The traces correspond to an increasing incident angle and therefore penetration depth of **(a)** 0.11°, **(b)** 0.15°, **(c)** 0.18° and **(d)** 0.2°. The dashed lines show the positions of the $Ia\bar{3}d$ scattering peaks for a unit cell size of 43 nm.

Given that a widening of the gyroid struts is expected due to the oxidation of the outer layer of the copper gyroid into Cu_2O and CuO, one could expect to detect this using GI-SAXS. The estimated strut diameter after the P3 oxidation based on EDX measurements is approximately 13 nm with an 8 nm copper core. However the scattering contrast between copper and Cu_2O/CuO is very small so GI-SAXS will be unable to distinguish between the shell and the core. A strut outer diameter of 13 nm corresponds to a scattering vector of $q_y = 0.048\,\text{Å}^{-1}$. Although Figure 6.18B appears to show a very weak peak at this position it overlaps with the (321) scattering peak, which for a unit cell size of $a = 45.5$ nm appears at $q_y = 0.052\,\text{Å}^{-1}$. There appears to be a shift of the (211) peak to shorter q-values for the highest incident angle (i.e. the deepest penetration depth), as seen in Figure 6.18Bd.

The 1D intensity profile of the fully oxidised samples (P7) is shown in Figure 6.18D and three Bragg peaks are visible which are positioned at a q ratio of $\sqrt{2} : \sqrt{6} : \sqrt{14}$. The position of the (211) scattering peak at $q_y = 0.0356\,\text{Å}^{-1}$ gives a unit cell size of $a = 43.2$ nm which agrees very well with AFM measurements of the polystyrene polymer template [66]. The increased ratio between the intensities of the $\sqrt{2}$ and $\sqrt{6}$ peaks, is indicative of a structure that retains a double-gyroid-like morphology but displays a distorted $Ia\bar{3}d$ symmetry. The relative increase in the intensity ratio compared to the ratio observed in Figure 6.18Ba is approximately 25 %.

One possible explanation for the observed intensity ratios, which was postulated by Crossland *et al.* [35], is a shift of the two gyroid minority networks relative to each other. However the oxidation of the copper as well as the formation of a nanotubular morphology due to the nanoscale Kirkendall effect, are both isotropic and as such we would not expect to observe a shift of the two gyroid networks relative to each other. Instead we speculate that the observed 'distortion' is due to the significant widening of the gyroid struts from approximately 11 nm for the as-deposited copper to 18 nm to 20 nm for the fully oxidised network. This increased volume of the minority networks could lead to local rearrangements within each unit cell, causing a change in the symmetry and therefore the observed intensity ratios of the scattering peaks. Figure 6.14C also shows that the 225 °C oxidation protocol causes a roughening of the network surface which could contribute to the observed 'distortion'. Furthermore, the depth profiling shows that the asymmetry of the $\sqrt{2}$ and $\sqrt{6}$ peaks is more pronounced at the surface (Figure 6.18Da) where the intensity of the (110) reflection has a maximum.

Based on the TEM images of the nanotubular morphology (Figure 6.16I) one could expect scattering signals at $q_y = 0.033\,\text{Å}^{-1}$ and $q_y = 0.090\,\text{Å}^{-1}$ corresponding to the outer and inner diameter of the gyroid struts of 19 nm and 7 nm respectively. However the scattering peak due to the outer diameter overlaps with the (211) peak. The position of the peak corresponding to the inner diameter lies outside of the measured q range.

XPS and Auger spectroscopy

X-ray photoelectron and auger electron depth-profiling spectra of samples annealed according to protocols P3, P7 and P9 are shown in Figure 6.19. The purpose of the XPS and Auger measurements was to obtain compositional information via depth-profiling and thus determine dimensions of the various parts of the gyroid core/shell structures. The total depth for the profiling is approximately 50 nm. For the samples oxidised at 70 °C for 1 h in O_2 (P3) the XPS and Auger spectra are consistent with a copper core surrounded by a Cu_2O/CuO shell (bottom spectra in Figure 6.19A,B). At 5 s the XPS shows no CuO signal, suggesting a very thin CuO coating consistent with EDX (Section 6.3.2). Due to the overlap between the Cu and Cu_2O peaks in XPS, Auger spectroscopy was used instead (Figure 6.19B. A copper peak appears after approximately 15 s of depth profiling, confirming a core/shell structure.

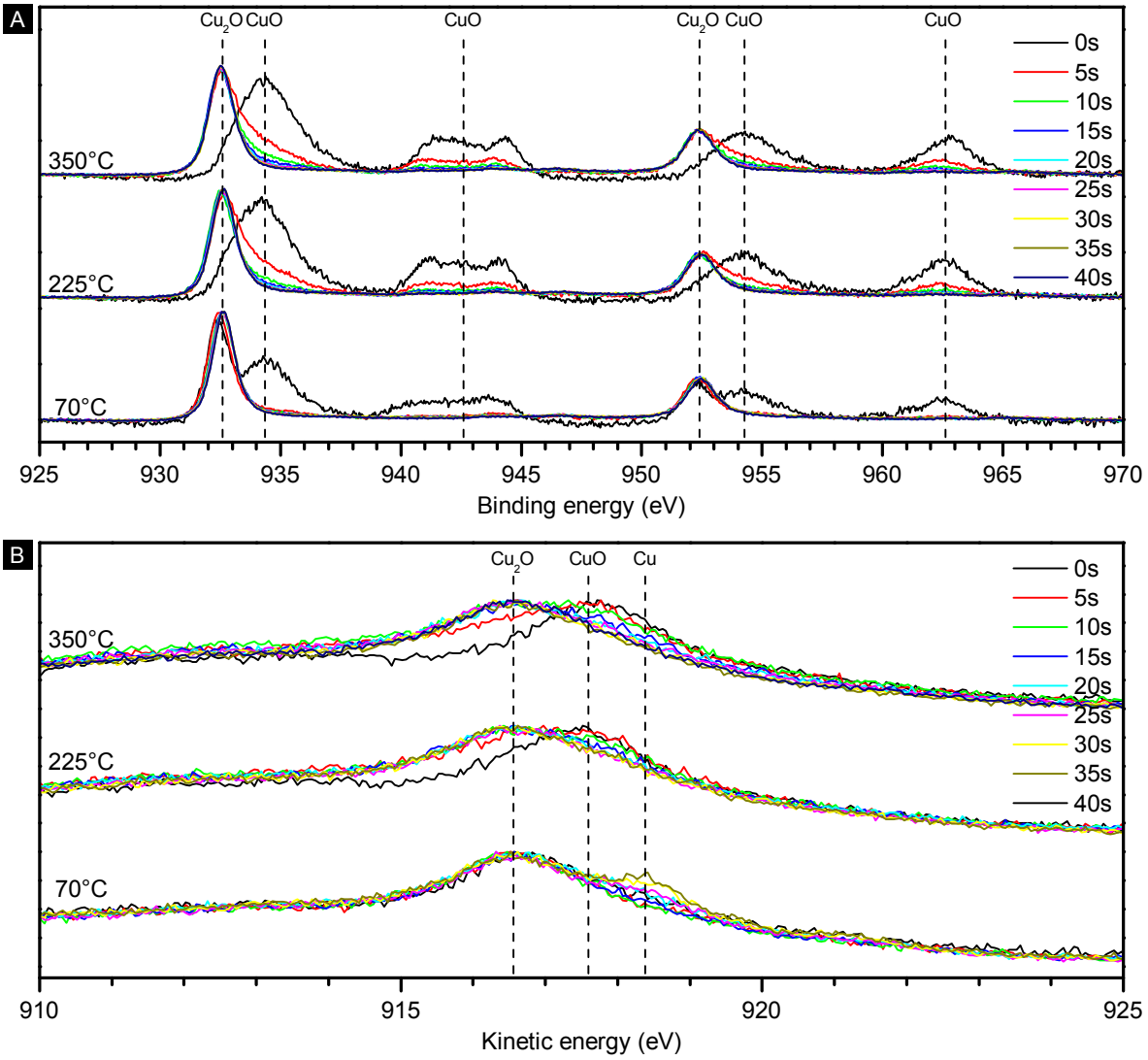

Figure 6.19: **(A)** X-ray photoelectron spectroscopy spectra and **(B)** Auger electron spectroscopy spectra of samples annealed according to protocols P3, P7 and P9.

Despite the apparent match for the P3 sample between the XPS/Auger and EDX measurements, the same does not hold true for the samples oxidised at 225 °C (P7) (middle spectra in Figure 6.19A,B) and 350 °C (P9) (top spectra in Figure 6.19A,B). Both samples show the presence of CuO up until approximately 15 s of depth-profiling which is consistent with a Cu_2O/CuO layer for the P7 sample and fully oxidised CuO in the P9 sample. However the absence of CuO for longer profiling times for both samples and the presence of Cu_2O for the P9 sample are not consistent with the expected EDX and XRD measurements, which showed morphologies of a Cu_2O/CuO core/shell in the P7 sample and a pure CuO structure in the P9 sample. We speculate that the most probable reason for this is a transformation of the CuO into Cu_2O in the UHV of the XPS. This phenomenon of vacuum reduction is well-known and has been shown using XPS, but has normally been reported at elevated temperatures [262, 263]. We believe that the argon millingdepth-profiling and the nano-structuring of the gyroid network lowers the temperature at which the reduction takes place. The extra energetic barrier to reduce the Cu_2O to copper explains why larger amounts of copper are not detected and why all samples display a large amount of Cu_2O. Thus it was not feasible to extract any relevant and quantitative compositional information from the XPS measurements.

Summary of observed changes

This section will give a summary of the morphological and compositional changes observed as the samples undergo the various thermal oxidation treatments listed in Table 6.2.

As-deposited copper sample (P1, P2) The as-deposited copper samples display the expected strut diameter (11 nm) and unit cell size, based on the gyroid polymer template used, as determined by SEM and TEM (Figure 6.16)A-C. Measurements using XRD show a small Cu_2O contribution which is thought to be due to oxidation of the top of each strut through the porous template (Figure 6.9a).

Removal of the template prior to an in-template oxidation step leads to coarsening of the struts and loss of the gyroid network order as seen in SEM (Figure 6.8) and shown by the increase in FWHM of the Cu_2O (111) peak (Figure 6.9b).

Annealing at 70 °C for 1 h in O_2 (P3, P4) Application of the in-template oxidation step leads to a stable gyroid morphology as seen in Figure 6.8d. The increased stability is due to the oxidation of the outermost layer of the copper network as shown by the increase in the Cu_2O and CuO XRD peaks in Figure 6.9c. A schematic of this core/shell structure is shown in Figure 6.20B. Based on an initial diameter of 11 nm and EDX measurements (Section 6.3.2) the copper core of the network is calculated to have a diameter of 8 nm. The core is surrounded by a shell consisting of 1.5 nm Cu_2O coated with 0.75 nm CuO. The thickness of this CuO layer is in agreement with XPS measurements of the room temperature oxidation of copper nanoparticles [264]. The

total diameter of the struts is approximately 12.5 nm which is also in agreement with SEM (Figure 6.14A) and TEM (Figure 6.16D-F) imaging.

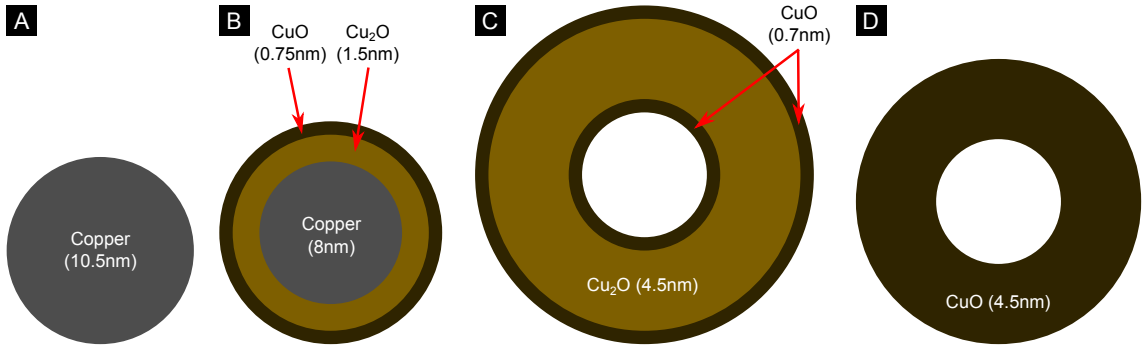

Figure 6.20: Schematic of morphological changes observed upon thermal oxidation. The dimensions correspond to the thickness or diameter of the particular part of the core/shell structure. **(A)** As-deposited copper (P1). **(B)** 70 °C for 1 h in O_2 (P3). Outer diameter is 12.5 nm. **(C)** 225 °C for 2 h in air (P7). Outer and inner diameters are 19 nm and 7 nm respectively. **(D)** 350 °C for 2 h in air (P9). Outer and inner diameters are 16 nm and 7 nm respectively.

Annealing at 70 °C for 8 h in air (P5, P6) Extended annealing at 70 °C of the gyroid networks for 8 h in air does not lead to a noticeable change in their composition as measured by EDX (Table 6.3) and only a small change in the strut diameter coupled with a loss of network order as shown in Figure 6.14B. However XRD measurements (Figure 6.9d) point towards a compositional change with an increase in the amount of copper and a decrease in the amount of Cu_2O via the reaction in Reaction 6.1. The increase in the FWHM of the copper (111) peak (Figure 6.9d) also suggests an increase in the copper crystallite size. Annealing of the network before or after template removal leads to a compositional difference. Oxidation prior to the removal of the template leads to a larger Cu (111) peak as well as a reduced Cu_2O (111) peak (Figure 6.11c compared to Figure 6.11d) which is thought to be due to a reduced amount of oxygen because of diffusion through the polymer template.

Annealing at 225 °C for 2 h in air (P7, P8) Annealing of the gyroid-structured networks at 225 °C for 2 h leads to the formation of a nano-tubular morpholct, as shown in Figure 6.14C and Figure 6.16G-I (Section 6.1.5). The inner and outer diameters of the nanotubular network, as determined by TEM (Figure 6.16I, are 6 nm to 7 nm and 18 nm to 19 nm respectively (Figure 6.20C). It is assumed that both the inside and outside surfaces of the nanotubular network are covered with a thin CuO layer of approximately the same thickness. The measured diameters in combination with EDX measurements allow the thicknesses of these layers to be calculated as 0.7 nm, which agrees with calculations for the samples oxidised at 70 °C. XRD shows that the high temperature oxidation leads to the complete conversion of the copper to Cu_2O and CuO (Figure 6.9e). As with the samples annealed at 70 °C, oxidation at 225 °C before

and after the removal of the template produces a compositional difference. Oxidation prior to template removal causes a larger ratio between the Cu_2O (111) and CuO (111) peaks consistent with a reduced presence of oxygen (Figure 6.11e compared to Figure 6.11f). Oxidation in the presence of the template also reduces the strut widening (Figure 6.14D) due to the mechanical confinement offered by the polystyrene template.

Annealing at 350 °C for 2 h in air (P9, P10) Oxidation at 350 for 2 h also leads to the formation of a nanotubular network (Figure 6.14F). Measurements using SEM show an outer diameter of 16 nm which gives a calculated inner diameter of 7 nm (Figure 6.20D). XRD shows that oxidation without the template in place leads to the complete oxidation of the Cu_2O to CuO (Figure 6.9f). However oxidation with the template in place causes an incomplete oxidation, shown by the presence of a Cu_2O (111) peak (Figure 6.11g.

6.3.3 Cu/Cu_2O gyroid-structured solar cells

Optical spectroscopy

Transmittance and reflectance measurements in the visible spectrum (400 nm to 800 nm) are used to estimate the band gaps of the constituent materials of the copper gyroid samples subjected to the various oxidation protocols. Figure 6.21 shows transmittance and reflectance spectra of samples annealed according to protocols P1, P3, P5; and Figure 6.22 displays samples annealed according to P7 and P9 as well as a summary of protocols P1, P3, P5, P7 and P9 for a sample thickness of 250 ± 25 nm. To avoid contributions due to the copper compact layer described in Section 6.2.2, the measurements for each annealing protocol are referenced to a piece of copper-coated FTO subjected to the same protocol. The following section will only give a brief description of the most interesting features of the spectra, as the main aim of these measurements was to attempt to calculate the band gap.

The transmission spectra for the first three annealing protocols (P1, P3 and P5) display similar shapes to transmittance spectra through copper thin films [265]. To avoid oxidation of the copper networks, the as-deposited samples are kept in the polymer template during the transmittance and reflectance measurements. Interference fringes that are caused by the polymer film are clearly seen in both the reflectance and transmittance spectra (Figure 6.21A,B) which overlap with the spectrum caused by the copper in Figure 6.21Ba. This makes direct measurements of the reflectance and transmittance of a gyroid-structured copper network difficult. Transmittance spectra for protocol P3 and P5 (Figure 6.21D,F) show a red-shift of the wavelength of the maximum transmittance from 500 nm for flat copper films to approximately 525 nm and 560 nm for P3 and P5 respectively (Figure 6.21Da, Figure 6.21Fa). This is thought to be caused by the gyroid-structured copper. This effect has been observed previously for other gyroid-structured metals such as gold and silver [266, 267].

It is also worth noting that the maximum transmittance achievable through the nano-

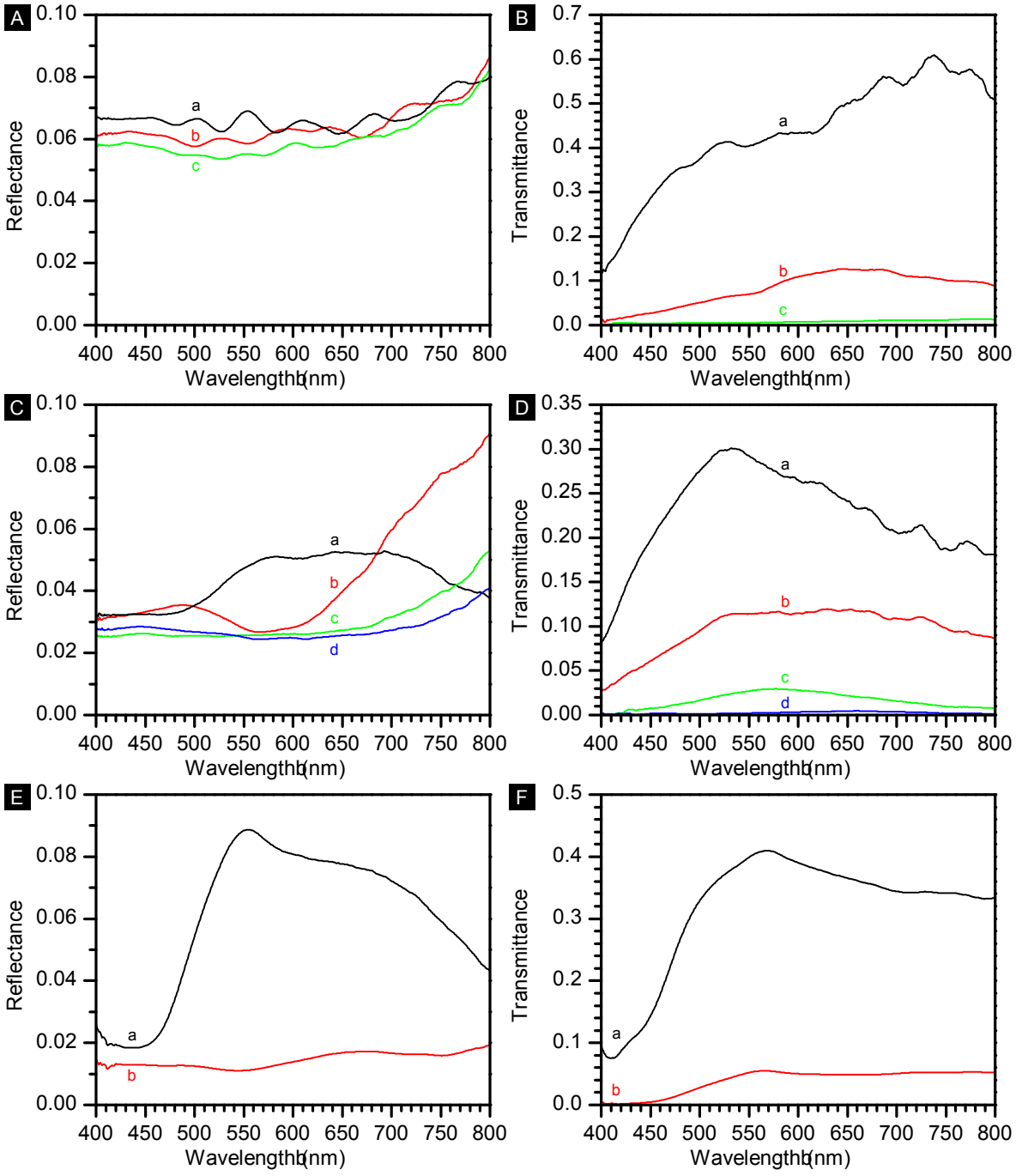

Figure 6.21: Optical reflectance and transmittance spectra of thermally annealed gyroid-structured copper. **(A)**, **(C)** and **(E)** are reflectance spectra. **(B)**, **(D)** and **(F)** are transmittance spectra. **(A)**, **(B)** As-deposited copper with template remaining (P1). **(a)** 130 nm **(b)** 250 nm **(c)** 520 nm. **(C)**, **(D)** Thermally annealed at 70 °C in O_2 for 1 h (P3). **(a)** 120 nm **(b)** 260 nm **(c)** 490 nm **(d)** 970 nm. **(E)**, **(F)** Thermally annealed at 70 °C in air for 8 h (P5). **(a)** 265 nm **(b)** 990 nm.

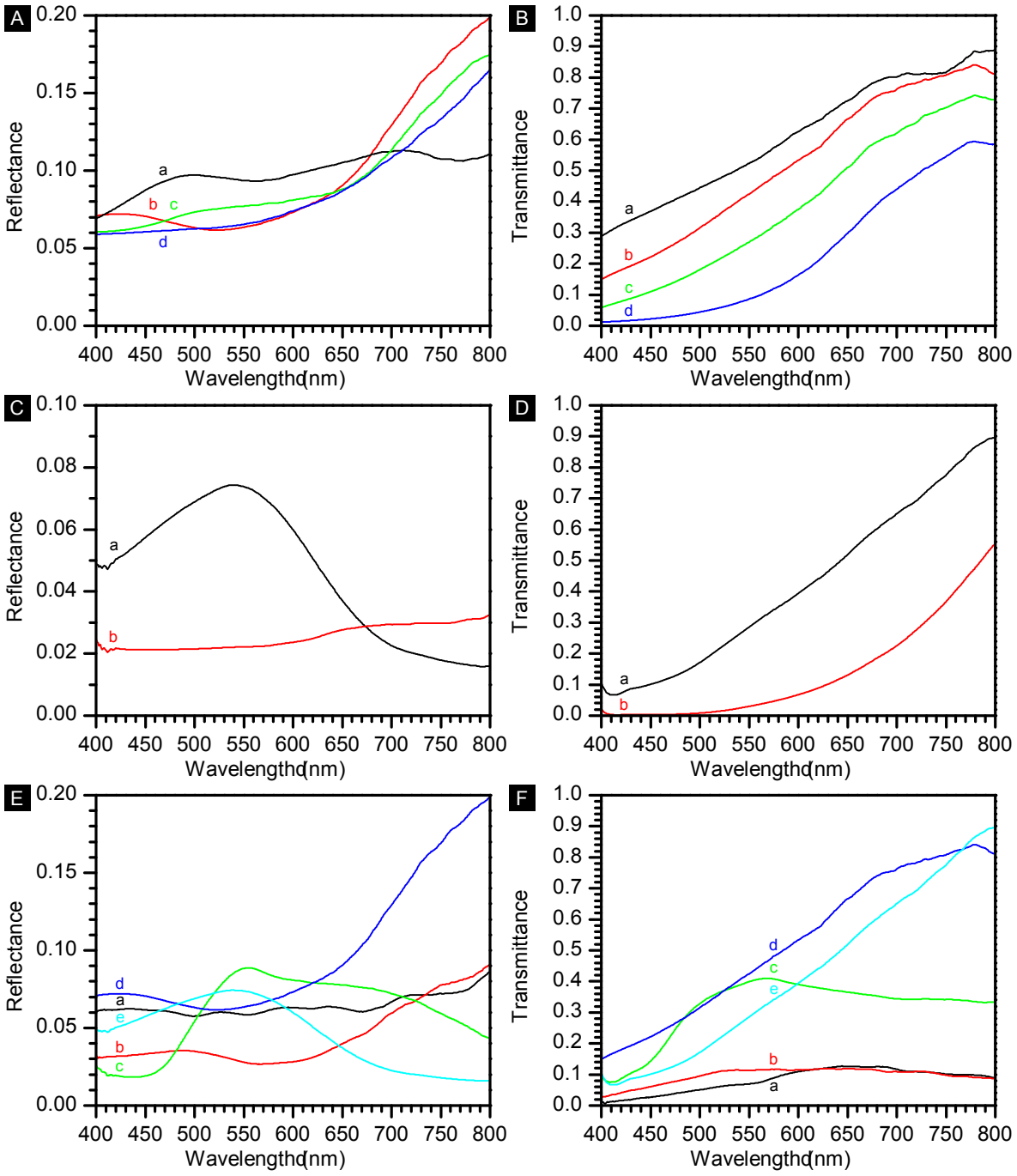

Figure 6.22: Optical reflectance and transmittance spectra of thermally annealed gyroid-structured copper. **(A)**, **(C)** and **(E)** are reflectance spectra. **(B)**, **(D)** and **(F)** are transmittance spectra. **(A)**, **(B)** Thermally annealed at 225 °C in air 2 h (P7). **(a)** 115 nm **(b)** 260 nm **(c)** 515 nm **(d)** 1010 nm. **(C)**, **(D)** Thermally annealed at 350 °C in air for 2 h (P9). **(a)** 235 nm **(b)** 980 nm. **(E)**, **(F)** Thermally annealing of gyroid-structured copper films with thicknesses of approximately 250 nm. **(a)** P1 **(b)** P3 **(c)** P5 **(d)** P7 **(e)** P9.

structured films, which have flat copper film equivalent thicknesses of 50 nm, 30 nm and 30 nm for Figure 6.21Ba,Da,Fa respectively, is higher than flat copper films which have a maximum transmittance of approximately 40 % for a 15 nm thick film [268]. The increased transmittance for samples annealed according to P5 (70 °C for 2 h in air) is believed to be due to the increased crystallite size of these samples (Figure 6.9d).This increased transmittance is also seen in other gyroid-structured metals and is explained by an increased coupling of the incident light with the plasmonic modes present in the nano-structured metal [266]. As the samples are further oxidised according to protocol P7 and P9 (Figure 6.22B,D) a transition is seen towards an increased amount of transmittance for longer wavelengths which is consistent with the full oxidation of the copper into Cu_2O and CuO [265].

The spectra described above were used to calculate Tauc plots for annealing protocols P3, P5, P7 and P9 (Figure 6.23A,B,C,D).

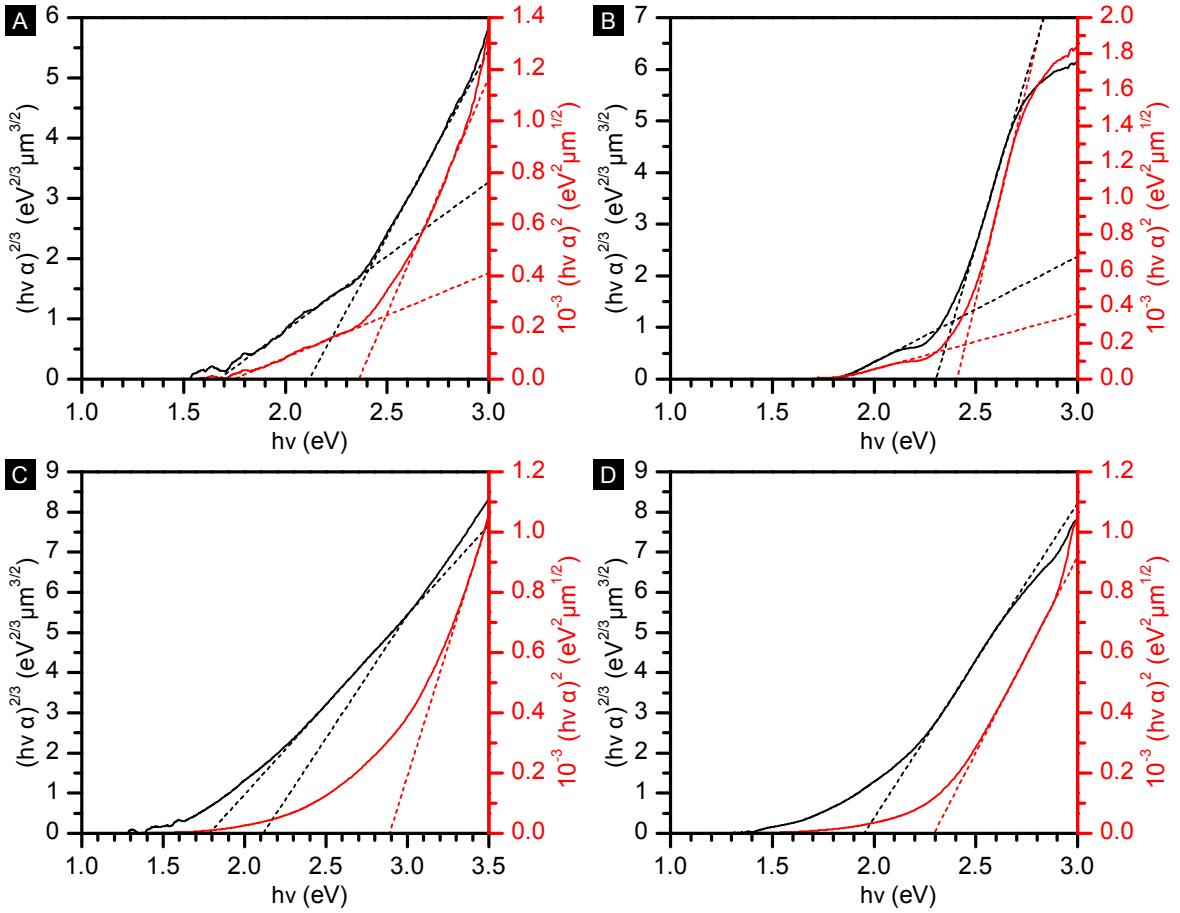

Figure 6.23: Absorption measurements for thermally annealed gyroid-structured copper. Black and red traces correspond to forbidden and allowed direct transitions ($n = 3/2$ and $n = 1/2$) respectively. **(A)** Sample annealed at 70 °C in O_2 for 1 h (P3). **(B)** Sample annealed at 70 °C in air for 8 h (P5). **(C)** Sample annealed at 225 °C in air for 2 h (P3). **(D)** Sample annealed at 350 °C in air for 2 h (P9).

A film thickness of approximately 250 nm was chosen for the calculations and the equivalent spectra are Figure 6.21Db,Fa and Figure 6.22Bb,Da. A Tauc plot, as previously described in Section 5.2.2, plots $(\alpha\hbar\omega)^{1/n}$ versus $\hbar\omega$ where the value of the parameter n describes the type of semiconducting transition. For example, for Cu_2O both forbidden and allowed direct transitions ($n = 3/2$ and $n = 1/2$) have been reported in the literature and as such the Tauc plots shown in Figure 6.23 display calculations for both $n = 3/2$ and $n = 1/2$ (shown in black and red respectively). Care has to be taken when analysing these results since the geometry of the nano-structured samples is very complicated and the absorption of up to three different materials (Cu, Cu_2O and CuO) overlaps to give the observed reflectance and transmittance spectra and the corresponding Tauc plot. The spectral contribution due to each material also changes with annealing protocol as more and more oxidation takes place. However we believe that it is possible to extract some relevant information from the Tauc plots. One or two linear regions are visible in the Tauc plots which correspond to the absorption due the CuO and Cu_2O.

From Figure 6.23 it is possible to determine the band gaps for the Cu_2O and CuO components of the gyroid-structured scaffolds. The determined band gaps (the intersections between the dashed straight lines and the abscissa) are shown in Table 6.4 for protocols P3, P5, P7 and P9, for the forbidden ($n = 3/2$) and allowed ($n = 1/2$) direct transitions and their average values. The band gaps for both the Cu_2O and CuO are blue-shifted compared to their bulk values of 2.0 eV and 1.2 eV [269, 270] which is thought to be due to the confinement caused by the core/shell nature of the nano-structured $Cu/Cu_2O/CuO$ gyroid network.

Protocol	Cu_2O/eV			CuO/eV		
#	n=3/2	n=1/2	average	n=3/2	n=1/2	average
P3	2.12	2.37	2.25	1.67	1.75	1.71
P5	2.30	2.40	2.35	1.80	1.80	1.80
P7	2.12	2.88	2.50	1.80	-	1.80
P9	-	-	-	1.95	2.29	2.12

Table 6.4: Band gaps of copper networks oxidised according to protocols P3, P5, P7 and P9.

Device characterisation

This chapter will present a number of different solar cell configurations including all-inorganic devices and hybrid devices consisting of both solid-state and liquid electrolytes. In general, devices that use a solid-state secondary component, such as ZnO, PCBM and spiro-MeOTAD show a much lower efficiency than the liquid electrolyte devices, most likely due to infiltration issues into the nano-structured Cu/Cu_2O electrodes.

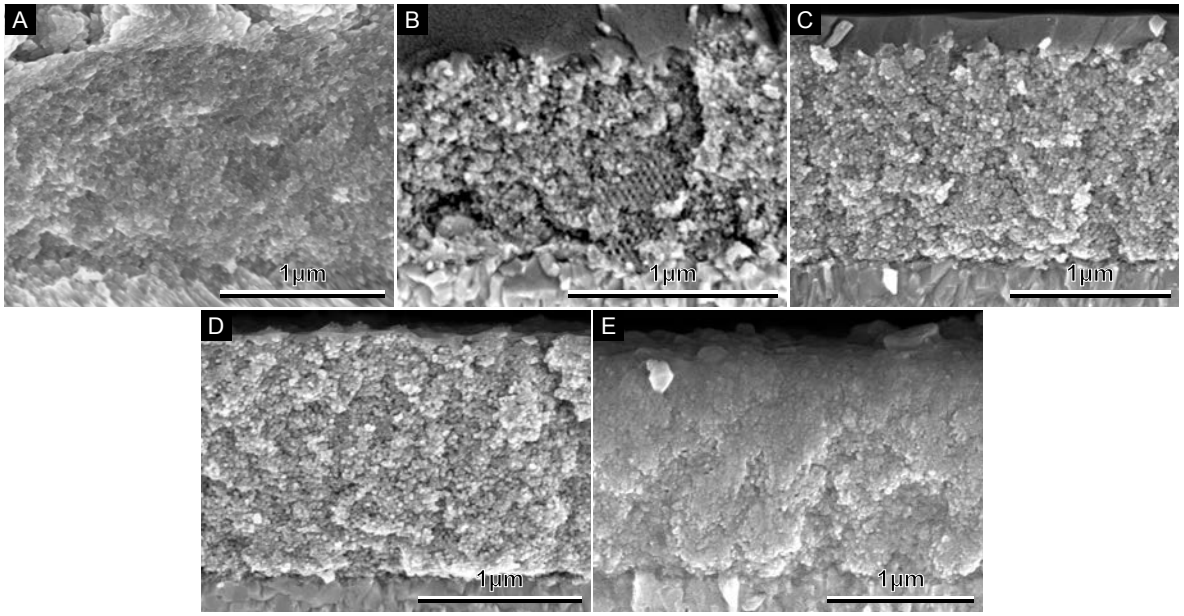

Figure 6.24: Infiltration of solid-state electrolytes in gyroid-structured Cu/Cu_2O electrodes. **(A)** Infiltration of ZnO using atomic layer deposition. **(B)** Partial infiltration of spiro-MeOTAD. **(C)** Full infiltration of spiro-MeOTAD. **(D)** Partial infiltration of PCBM. **(E)** Full infiltration of PCBM.

As ZnO is frequently used as the electron conductor in p-type Cu_2O oxide devices, it is the first choice of material for the fabrication of solar cells based on thermally oxidised gyroid-structured copper scaffolds. The infiltration of ZnO is performed using ALD with long precursor exposure times and as such it can be expected to extend to the bottom of the device. It will however have a tubular rather than a solid cross-section which could possibly limit charge transport. Figure 6.24A shows an SEM cross-section of a copper network oxidised according to protocol P3, infiltrated using ZnO. The absence of porosity, as compared to Figure 6.14A, shows that the infiltration of the ZnO is successful all the way to the FTO substrate.

The I-V curves of samples utilising ZnO are shown in Figure 6.25Aa. The filled and open squares correspond to protocol P3 and P7 respectively. The samples oxidised according to P3 contain a large proportion of copper, and as expected this device in contact with n-type ZnO displays a linear ohmic trace. For P7 samples which are fully oxidised and consist of p-type Cu_2O and CuO, the observed ohmic behaviour is explained by the small feature sizes of the Cu_2O/CuO electrode which prevent the formation of a depletion layer and thus of a rectifying device.

Given the excellent results shown by Shao *et al.* when using Cu/Cu_2O photo-electrodes [237], the same iodine based aqueous electrolyte was also tested with our gyroid-structured photo-electrodes and the I-V spectra are shown in Figure 6.25Ab. The filled and open circles correspond to protocol P3 and P7 respectively. As expected, the LiI/L_2 electrolyte allows both pure p-type (Cu_2O) and n-type (Cu)/p-type (Cu_2O) photo-electrodes to be utilised in successful although not very efficient solar cells. The

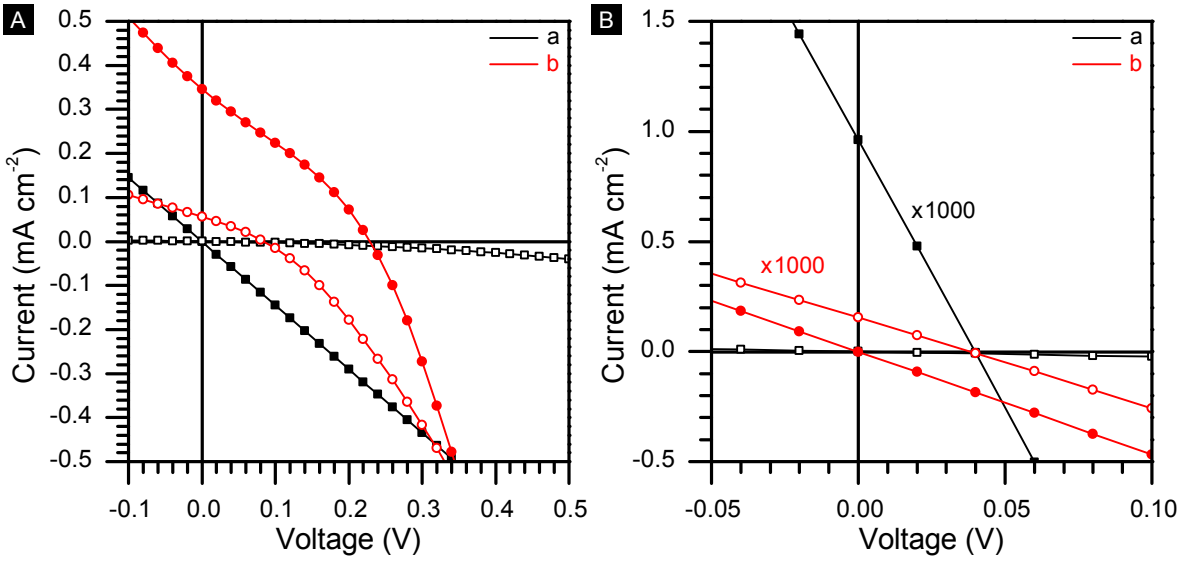

Figure 6.25: I-V measurements of Cu_2O devices. Closed and open markers correspond to samples annealed according to P3 and P7 respectively. **(A)** Devices containing **(a)** ZnO and **(b)** a LiI/I_2 liquid electrolyte. **(B)** Devices containing **(a)** spiro-MeOTAD and **(b)** PCBM.

70 °C oxidised samples (P3) display a short-circuit current and open-circuit voltage of 0.35 mA cm^{-2} and 0.23 V respectively. This is significantly higher than the samples oxidised at 225 °C (P7) which display a maximum short-circuit current and open-circuit voltage of 0.06 mA cm^{-2} and 0.08 V. The difference in short-circuit current is explained by the increased transport through the copper core of the P3 sample. Although the use of an iodine based electrolyte produces working devices, they display a number of drawbacks. Firstly the open-circuit voltage is significantly lower than previously reported for liquid electrolyte Cu_2O devices [219]. Secondly the devices show severe stability issues which are thought to be connected to the instability of Cu_2O in aqueous environments.

Two alternatives to the aqueous iodine-based electrolyte were considered and tested. These are a solid-state PCBM and spiro-MeOTAD electrolyte and a cobalt non-aqueous liquid electrolyte. The reason for using both PCBM and spiro-MeOTAD stems from the fact that conceptually the electrodes can exhibit both n-type and p-type conduction characters depending on the annealing protocol. Considering that the electrodes are core/shell composites, the use of the words n- and p-type are used in the broadest sense to connote that an n-type and p-type electrode transports electrons and holes respectively. For samples annealed according to P3 or P5, the copper core is thought to be surrounded by thin Cu_2O and CuO shells and even though the oxides are p-type, electrons can still be injected into the copper so that the entire electrode can appear n-type. For samples annealed according to P7, no copper core remains, and the electrode will transport any generated holes and appear p-type.

It is known from literature that one of the main limitations for solid-state dye-sensitised solar cells containing spiro-MeOTAD is the infiltration of the electrolyte into the meso-

porous titania scaffold. We believe that the high order of the gyroid will aid the infiltration but that the relatively small pore size will hamper it. This is further compounded for the P7 samples which display a pronounced strut widening which further reduces the available space for the infiltration. To produce the best possible devices using the thermally oxidised copper scaffolds, the infiltration of PCBM and spiro-MeOTAD was optimised by altering the parameters of the spin-coating used for the infiltration. Figure 6.24B,D show the partial infiltration of spiro-MeOTAD and PCBM in P3 samples from a single step spin-coating procedure. If spin-coated in two steps (Section 5.4.2), first with a low and then with a high concentration, a much better infiltration is achieved as shown in Figure 6.24C,E.

The device data for the PCBM and the spiro-MeOTAD solid-state electrolytes are shown in Figure 6.25Ba and Figure 6.25Bb respectively (note the two traces which have been multiplied by a factor of 1000 for clarity). As above, the filled and open circles correspond to protocols P3 and P7 respectively. For both electrolytes, an ohmic behaviour is seen for samples annealed according to P3 and P7 for the PCBM (n-type) and spiro-MeOTAD (p-type) respectively. This is easily understood since in these cases an n-type/n-type or p-type/p-type junction is formed. Conversely rectifying characteristics are seen, albeit with very small short-circuit currents and open-circuit voltages, when the n-type electrodes formed through P3 are used in conjunction with the p-type spiro-MeOTAD and when the p-type electrodes formed through P7 are used with the n-type PCBM. It can also be seen that the n-type electrode with the copper core displays a higher short-circuit current and this is believed to be due to a more efficient transport with fewer losses.

A non-aqueous cobalt electrolyte was successfully used by Xiang *et al.* together with bulk Cu_2O photo-electrodes, fabricated from high temperature oxidation, to produce devices with an open-circuit voltage of 0.82 V and minimal photocorrosion [219]. The most successful devices fabricated in this study utilise the same electrolyte. Results for devices fabricated from samples annealed according to P3 and P7 with an acetonitrile electrolyte containing a $Me_{10}CoCp_2{}^0/Me_{10}CoCp_2{}^+ \cdot PF_6$ redox couple, are shown in Figure 6.26Aa and Figure 6.26Ab respectively. Filled and open circles corresponds to light and dark I-V measurements respectively.

Compared to the LiI/I_2 liquid electrolyte the cobalt electrolyte devices display a much higher open-circuit voltage of 0.74 V which is due to a more suitable offset between the redox potential of the electrolyte and the conduction band of the Cu_2O. As expected from the results seen with the PCBM and spiro-MeOTAD electrolytes, the samples with a copper core surrounded by a Cu_2O/CuO shell (P3) display a much higher short-circuit current which again is believed to be due to the injection into the copper core of electrons photo-generated in the copper oxides. Compared to the PCBM and spiro-MeOTAD devices, both electrodes display characteristic I-V behaviour due to the fact that the redox couple can be both oxidised and reduced and as such can transport both electrons and holes. The light I-V curve for the P3 sample also displays a non-standard shape compared to the expected monotonously decreasing photocurrent for an increasing bias. This will be explained later in this section.

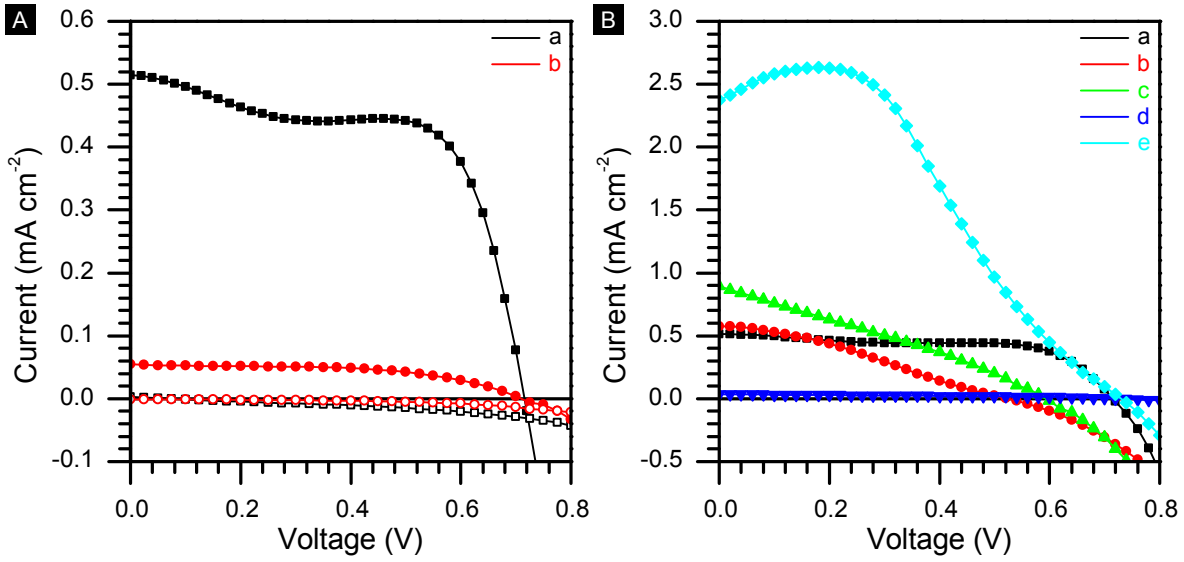

Figure 6.26: I-V measurements of Cu_2O devices with a cobalt electrolyte. **(A)** Illuminated (closed markers) and dark (open markers) I-V curves of devices, fabricated from **(a)** P3 and **(b)** P7. **(B)** The reference device using **(a)** a P3 electrode compared to modifications of the fabrication scheme to improve device performance, including **(b)** D149 dye absorption, **(c)** double electrode thickness, **(d)** 0.5 nm ALD Al_2O_3 barrier layer and **(e)** extended annealing at 70 °C (P5).

It was seen for the samples annealed according to P3 that an increase in performance occurred for extended illumination times. I-V measurements taken just after illumination and up to an illumination time of 12 min are shown in Figure 6.27A. This increase in device performance is due to the fact that extended illumination allows for charge traps to be filled, which increases the measured photo-current and therefore the efficiency. The best performing device using a P3 electrode and the cobalt electrolyte displayed a short-circuit current, open-circuit voltage, fill factor and efficiency of 0.495 mA cm^{-2}, 0.74 V, 63.9 % and 0.234 % respectively. Use of the cobalt electrolyte also remedies the stability problems encountered for the LiI/I_2 electrolyte. Two measurements spaced 24 h apart are seen in Figure 6.27B and no significant change in device performance is seen. However no long-term stability tests were carried out.

Given the success of using the cobalt electrolyte, attempts were made to alter the fabrication parameters toincrease device performance. Results from these attempts together with the reference samples which were annealed according to P3 are shown in Figure 6.26B. Three of the modification routes produced devices that performed worse than the reference and will only be described briefly. In an attempt to increase the open-circuit voltage, the sample was coated with a thin barrier layer of Al_2O_3 using ALD (5 cycles which corresponds to approximately 0.5 nm). As seen in Figure 6.26Bd a small increase in open-circuit voltage is seen, from 0.72 V to 0.78 V. However this is accompanied by a significant reduction in the short-circuit current which is a well-known phenomenon when using wide-band gap barrier layers. By increasing the electrode thickness one can expect an increase in the photocurrent, under the assumption that

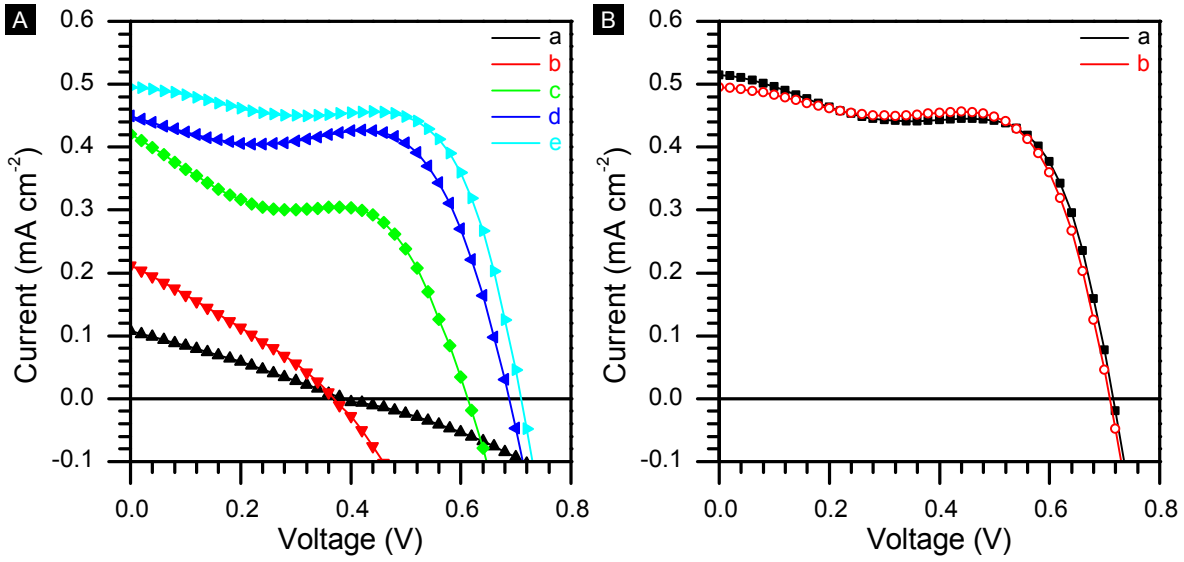

Figure 6.27: Device measurements of P3 electrodes with a cobalt electrolyte. **(A)** I-V curves taken **(a)** 0 min, **(b)** 4 min, **(c)** 8 min, **(d)** 10 min and **(e)** 12 min after the start of the illumination. **(B)** I-V curves taken **(a)** 0 h and **(b)** 24 h after device fabrication. Both curves were taken after 12 min illumination.

recombination does not become too dominant. One such sample is seen in Figure 6.26Bc and an increase in the photocurrent is indeed observed, but a loss in open-circuit voltage and a lowered fill factor produce an overall lowered device performance. Finally an attempt was made to sensitise the electrode using D149, a standard indolene organic dye used in dye-sensitised solar cells. The idea behind this modification was to try to improve the absorption of the device. The I-V measurements are shown in Figure 6.26Bb. However the short-circuit current remained constant and the reduction in the open-circuit voltage and the fill factor indicated increasing losses. This could be due to an increased number of pathways for recombination with the addition of the dye.

One fabrication route which did produce an increased device performance is the use of an extended annealing protocol. After the in-template oxidation at 70 °C in O_2 for 1 h, the template was removed and the sample annealed at 70 °C in air for 8 h (P5). As seen in Figure 6.26Be, the device displays a slightly larger open-circuit voltage of 0.75 V compared to 0.72 V but more importantly a significant increase in the short-circuit current. Although we have not been able to to prove it conclusively, we believe that this increase in short-circuit current is due to a reduction in the probability of recombination due to the extended annealing protocol. As described in Section 6.3.2, XRD measurements of protocol P5 show an increase in the intensity of the copper peaks as well as a decrease in the FWHM compared to the as-deposited copper. We attribute this to a coarsening of the copper crystallites. This coarsening leads to a reduction in the number of grain boundaries which is favourable for lowering the number of recombination events. Secondly the conversion of Cu_2O during P5 into the more thermodynamically stable Cu and CuO, leads to an increased fraction of copper in the

photo-electrode which benefits transport to the FTO electrode. As with the P3 electrodes, an increase in device performance with increasing illumination time is shown in Figure 6.28A. The samples also display similar stability, seen by the two measurements 24 h apart in Figure 6.28B.

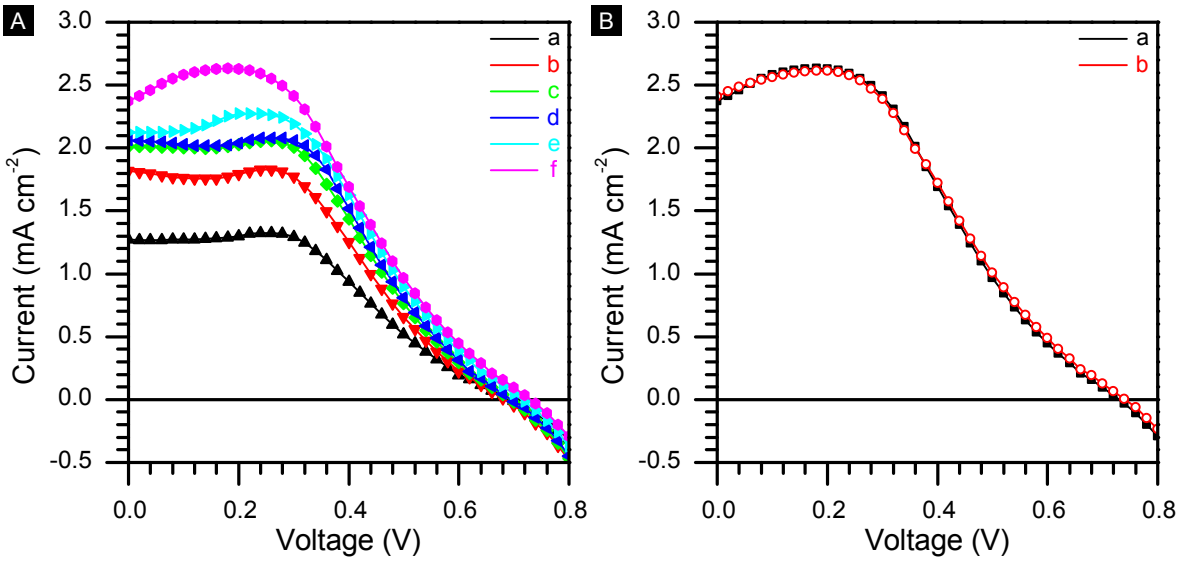

Figure 6.28: Device measurements of P5 electrodes with a cobalt electrolyte. **(A)** I-V curves taken **(a)** 0 min, **(b)** 4 min, **(c)** 8 min, **(d)** 12 min, **(e)** 16 min and **(f)** 20 min after the start of the illumination. **(B)** I-V curves taken **(a)** 0 h and **(b)** 24 h after device fabrication. Both curves were taken after 20 min illumination.

The observed increase in short-circuit current is further confirmed by measurements used to determine the conduction type of copper networks annealed according to protocols P3, P5 and P7 (Figure 6.29). The increase in current density for protocols P5 and P3 compared to P7 confirms an increased conductivity through the former networks due to the presence of copper cores. All three annealing protocols display a cathodic current indicating p-type networks. Although the P3 and P5 samples consist of both copper and Cu_2O/CuO, the observed conduction type is determined by the material at the network electrolyte interface, in this case CuO, explaining the observed behaviour.

For the best-performing device with a P5 electrode, Figure 6.30A and Figure 6.30B show the light (filled squares) and dark (open squares) I-V measurements, and the EQE respectively. The illuminated current trace displays a non-standard shape with a local maximum at approximately 0.25 V. Some insight into the origin of this shape is found in the dark current trace. This trace is also non-standard and a maximum in current appears at about 0.3 V which overlaps with the local maximum seen for the illuminated current trace. Given that the current maximum is seen when no illumination takes place we speculate that it is due to a chemical reaction at the surface of the Cu/Cu_2O electrode. However due to time constraints no further steps have been taken to elucidate the origin of the non-standard current traces. The best performing device displayed a short-circuit current, open-circuit voltage, fill factor and efficiency of 2.37 mA cm^{-2}, 0.73 V, 42.7 % and 0.738 % respectively.

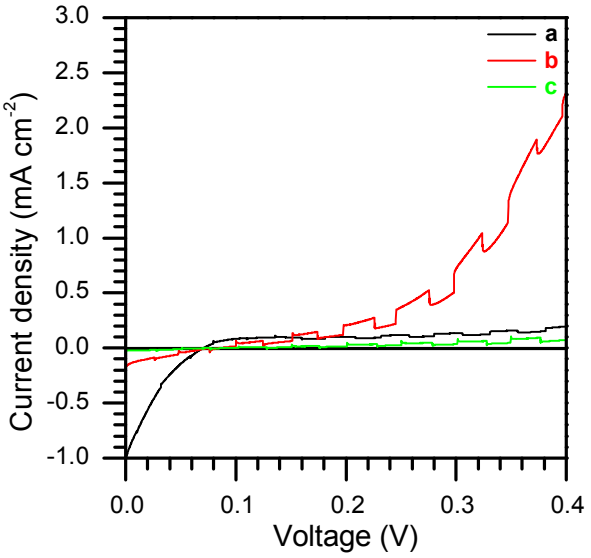

Figure 6.29: Measurements of the conduction type of gyroid-structured networks annealed according to protocol **(a)** P3, **(b)** P5 and **(c)** P7.

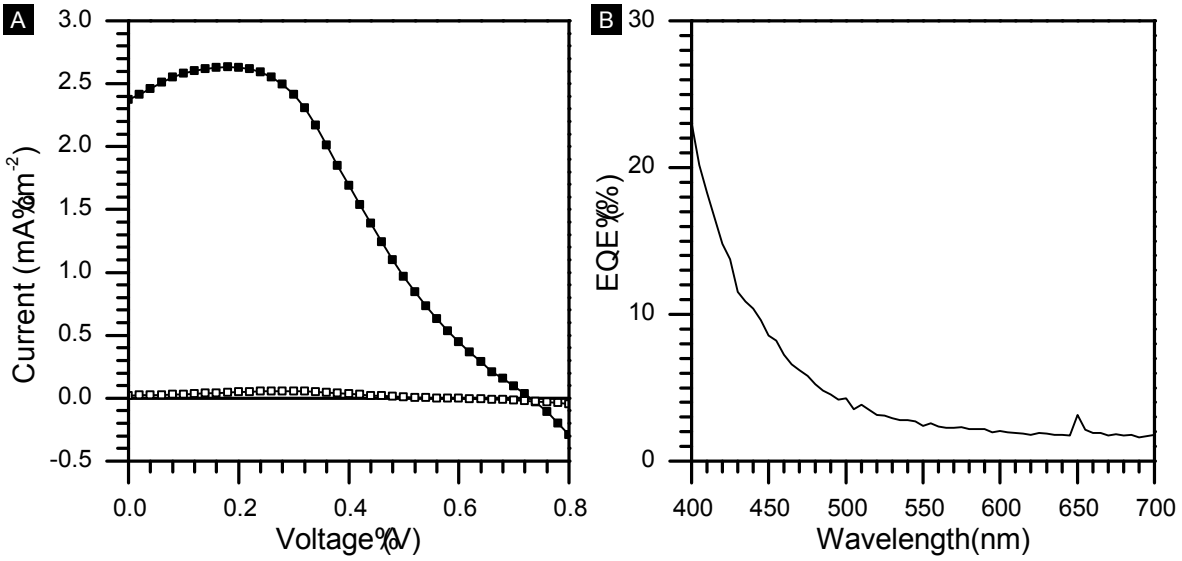

Figure 6.30: Device measurements of P5 electrodes with a cobalt electrolyte. **(A)** Illuminated (closed markers) and dark (open markers) I-V curves. **(B)** External quantum efficiency measurements.

The measured EQE matches the measured transmittance and therefore absorption spectra, (Section 6.3.3) which have a near constant, low absorption for long wavelengths and an onset of increased absorption at approximately 525 nm. This agrees well with the increase in EQE at 500 nm to 550 nm. Given that a relatively thick spacer layer is used in the device fabrication (approximately 300 µm), the low EQE could partially be due to factors such as absorption losses in the liquid electrolyte and reflection losses at both the platinised FTO counter electrode and at the electrode surface itself. Again due to time constraints these losses have not been quantified and the internal quantum

efficiency was not calculated.

Schematics of the band structures of fully assembled devices based on annealing protocols P5 and P7 can be seen in Figure 6.31. The schematics are based on the measured average band gaps together with the formal Nerstian redox potential of the $Me_{10}CoCp_2{}^{0/+}$ electrolyte [218]. It has been assumed that the band gap widening caused by the confinement of the Cu_2O and the CuO is approximately symmetric and that the positions of the conduction band and the valence band shift by equal amounts but in opposite directions [232].

Figure 6.31: Band diagrams of assembled devices consisting of thermally oxidised gyroid-structured copper. **(A)** Sample oxidised at 70 for 8 h under air (P5). **(B)** Sample oxidised at 225 for 2 h under O_2 (P7).

The non-aqueous redox electrolyte used in this study is not involved in the generation of photo-excited species but instead it is only responsible for transport of generated charges and for the value of the equilibrium barrier height of the semiconductor/liquid junction. In a device consisting of a bulk film of Cu_2O more than a couple of micrometres thick, a space charge layer with the accompanied band bending is established in the Cu_2O due to the equilibration of the Fermi level of the Cu_2O and the redox potential of the electrolyte. In such a device, a direct comparison between the Cu_2O/liquid junction and other p-type Cu_2O hetero- and homo-junctions is possible. However in our devices, the length scale of the nano-structured Cu_2O is not sufficient to establish a depletion region and we believe that for the core/shell copper/Cu_2O/CuO devices the copper oxides simply act as sensitisers in an analogous fashion to the dye in a DSSC.

Analogies can also be made between the TiO_2 in a DSSC and the copper core in our samples, both of which incorporate liquid electrolytes. Even though the charge extraction is possibly different in our devices it is still useful to compare the open-circuit voltage in our devices to those of other p-type Cu_2O hetero- and homo-junctions. The observed open-circuit voltage of 740 mV is higher than other reported V_{OC} such as 430 mV for p-n-junction Cu_2O, 400 mV for Cu_2O/alumina doped-ZnO and 595 mV for Cu_2O/ZnO. Previous work onCu_2O/liquid junctions has reported a V_{OC} of 820 mV for p-Cu_2O electrodes fabricated by thermal oxidation of high purity copper foils, in contact with the same cobalt liquid electrolyte. Although our device structures display both a lower short-circuit current and an open-circuit voltage one has to keep in mind the length scales of the Cu_2O for which the results in this study were achieved. Xiang *et al.* achieved a power conversion efficiency of 1.5 % for a Cu_2O oxide thickness of approximately 200 µm. In this work the conversion efficiency is half (0.74 %) but for an effective Cu_2O thickness of only 200 nm or three orders of magnitude thinner than the active layer in the study by Xiang and co-workers.

6.4 Conclusion

This chapter has described the fabrication of core-shell copper/Cu_2O/CuO solar cells. The core-shell structures are formed through the electrodeposition of copper in double-gyroid-structured polystyrene template and the subsequent oxidation of these deposits. The removal of the polystyrene template prior to the copper oxidation requires an in-template oxidation step at 70 °C to prevent loss of the gyroid morphology. The morphological changes upon oxidation were studied using electron microscopy and various spectroscopic techniques. The measurements show a transition from a core-shell Cu/Cu_2O/CuO structure at an annealing temperature of 70 °C to a Cu_2O/CuO structure at 225 °C and finally a CuO-only structure at 350 °C. The oxidations at 225 °C and 350 °C lead to the formation of nano-tubular morphologies due to the nanoscale Kirkendall effect. Various device configurations utilising the oxidised photoanodes were tested, including all-solid-state ZnO devices, PCBM and spiro-MeOTAD devices, aqueous electrolyte LiI/L_2 devices and non-aqueous electrolyte devices containing a cobalt redox couple. Of these configurations, the non-aqueous devices resulted in the highest device performance. The copper networks oxidised at a low temperature (70 °C) showed a higher efficiency than those oxidised at a high temperature (225 °C). This increased device performance is attributed to the presence of a copper core which aids in transport and lowers recombination. The best performing low temperature oxidised device with a cobalt redox couple liquid electrolyte displayed a power conversion efficiency of 0.74 % (short-circuit current, open-circuit voltage and fill-factor of 2.37 mA cm^{-2}, 0.73 V, 42.7 % respectively) for an active Cu_2O thickness of just 200 nm.

7 ALD grown metal oxide networks

This chapter reports on the replication of porous block copolymer thin films with ALD deposited titanium dioxide, aluminium oxide and zinc oxide. It details the characterisation of the novel surface treatment used to achieve a high and uniform nucleation density of ALD growth. ALD grown films with and without the treatment are presented. The chapter concludes by demonstrating the successful incorporation of ALD grown TiO_2 electrodes in dye-sensitised solar cells.

7.1 Introduction

As described in Chapter 4, atomic layer deposition has emerged over the last few decades as a very important thin film deposition technique. An industrial field in which ALD has recently gained importance is the manufacture of solar cells. So far however this has been mainly limited to flat substrates. The aim of this part of the thesis is to apply the benefits of ALD such as atomic layer control and conformality to more complex solar cell device structures, in particular to the TiO_2 electrodes used in dye-sensitised solar cells (Chapter 2).

Despite a marked difference between the record efficiency of the dye-sensitised solar cell and that of the conventional silicon alternative, the DSSC remains one of the main candidates, together with organic solar cells, for the future replacement of fossil fuels by renewable energy sources such as solar energy. This is due to the abundance of titania and therefore the low cost of their constituent titania electrodes. DSSCs are traditionally fabricated from disordered titania nanoparticle networks which, despite their ease of fabrication, suffer from a wide pore size distribution and therefore from potential pore filling problems as described in Section 2.4. Block copolymer templates and in particular the gyroid morphology (Section 3.2.1) present comparably high surface areas but with the added benefit of being highly ordered with a very narrow pore size distribution.

Previous attempts to nano-structure titania using a block copolymer template include the fabrication of double-gyroid-structured TiO_2 electrodes using electrochemical deposition [35, 45]. However these films suffer from limited thicknesses. Since the electroplated TiO_2 is hydrated, the subsequent thermal treatment to crystallise the films leads to delamination of any films thicker than 1 µm. This is due to the induced stresses caused by dehydration.

The technique of post-deposition thermal oxidation of the metal nano-structures that was employed for the electrodeposited copper in Chapter 6 is not applicable for titanium/titania due to the infeasibility of electrochemical titanium deposition.

As such atomic layer deposition of TiO_2 was chosen since it allows for sub-nanometer

thickness control suitable for the small pore diameter of the gyroid templates and since it produces unhydrated amorphous titania deposits even at low temperatures.

Conceptually, the replication of a porous template using ALD and the application of this TiO_2 replica in a dye-sensitised solar cell is straightforward as is depicted in Figure 7.1. A conformal coating with a thickness of up to half the pore diameter should be achieved across the entire template. The polymer template is then removed during the crystallisation of the TiO_2 and a traditional DSSC is assembled from the resulting free-standing scaffold.

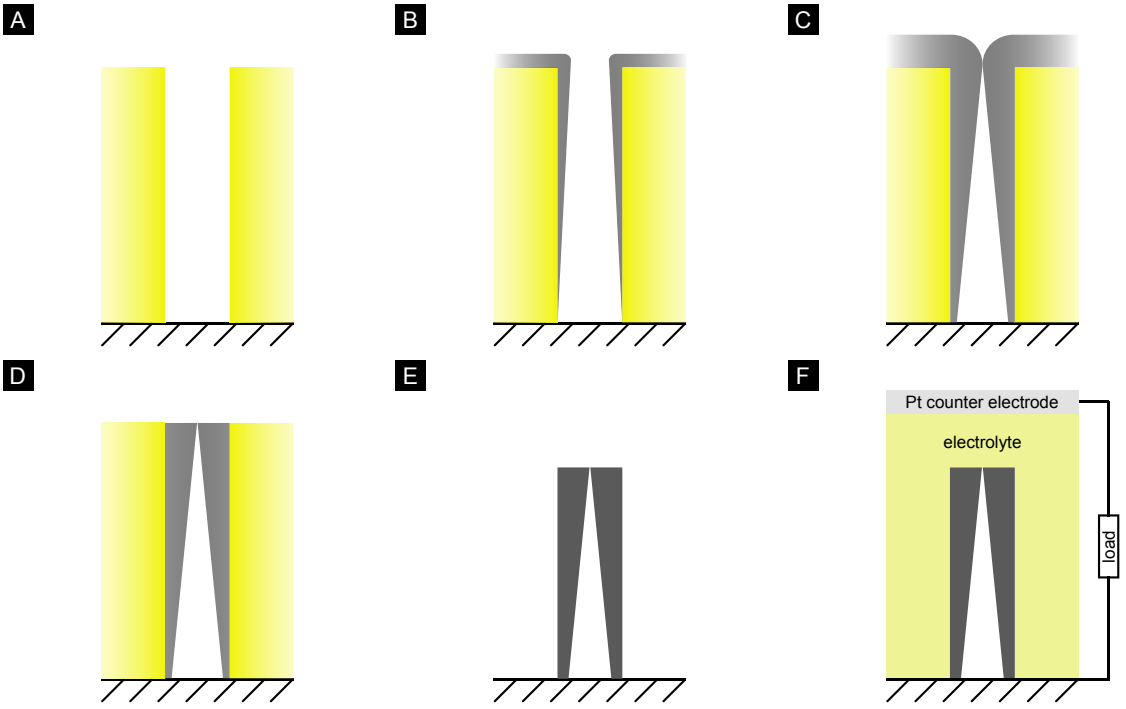

Figure 7.1: Fabrication of ALD deposited double-gyroid-structured TiO_2 dye-sensitised solar cells. The complex network of the double-gyroid is schematically depicted as a single cylinder. **(A)** Surface-functionalised polystyrene template. **(B)** Partial pore filling where the top surface remains porous. **(C)** Further deposition will eventually lead to pore-clogging, after which no further deposition will take place. Despite long pulse and purge times, a gradient in deposition thickness is present. **(D)** The non-porous TiO_2 layer is removed using inductively coupled plasma (ICP)/reactive ion etching (RIE). **(E)** Calcination of the amorphous titania leads to the collapse of the bottom layer of the double-gyroid-structured deposit due to the very thin shell thickness in this region. **(F)** The TiO_2 scaffold is sensitised using a N719 dye and assembled into a standard liquid electrolyte device.

However in practice the replication of the nano-pores in the gyroid-structured templates has proven to be a significant challenge which has taken three years to overcome. The reasons for this difficulty are fourfold. Firstly the styrenic templates used are chem-

ically very inert and provide no functional groups used for the nucleation of ALD, such as -OH or -NH_2 groups, which causes deposits of low quality and conformality. Secondly, due to the voided nature of the templates they have a limited upper processing temperature of approximately 70 °C, well below the glass-transition temperature of the constituent styrenic polymer itself. Thirdly the intrinsically very small initial pore diameter of the template (11 nm) leads to the requirement for very long exposure and purge times in order to allow for a uniform coverage throughout the entire template and to remove excess precursor and reaction by-products. Finally, the assumed regime of free molecular flow is not necessarily correct when the pore diameter, which changes from 11 nm to approximately 4 nm upon deposition, becomes comparable to or within one order of magnitude of the molecular size of the precursors as described in Section 4.6.3.

The solution to the first and second limitations of the styrenic templates is to employ a novel surface modification procedure which combines ozone exposure and thermal annealing to provide the functional groups necessary for uniform ALD nucleation and growth as well as an increased thermal stability via a cross-linking mechanism.

Using this surface modification scheme, the templates were successfully replicated using not only TiO_2 but also Al_2O_3 and ZnO at temperatures up to 120 °C, an increase of 50 °C over the highest processing temperature of the untreated templates. However, even at this elevated temperature, the reactivity and volatility of the titania precursors $TiCl_4$ and H_2O are limited which can lead to non-uniform growth and the incorporation of unreacted precursor ligands and reaction by-products, in this case chlorine. It is this incorporation of chlorine, as well as the shell formed during deposition (thickness of 3 nm to 4 nm) which is thought to lead to the observed lack of crystallinity in the titania and as a consequence to limited device performance in liquid electrolyte DSSCs fabricated from the double-gyroid-structured TiO_2 films.

The work in this chapter was carried out in collaboration with **Maik Scherer**[1].

7.1.1 Chemical surface modification of polystyrene

There are two main motivations for the modification of polystyrene in the literature. Firstly it provides a method for an increased adhesion and growth of cells on polystyrene substrates used in medical and biological research [271, 272]. Secondly chemical modification of polystyrene can be used to improve its thermal and mechanical properties via cross-linking reactions, for example in lithographic applications [273].

A number of procedures for the chemical modification of polystyrene have been reported including nitration [274–278], sulfidation [272], chemical oxidation [279], photo-oxidation [280–284], and plasma and ozone exposures [135, 285–287]. As will be dis-

[1] We contributed equally to the first part of the chapter including the ozone surface functionalisation and the deposition of TiO_2, Al_2O_3 and ZnO in the gyroid-structured templates. The second part including the study of the crystallisation inhibition in thin films and the deposition of TiO_2 in large pore size template was carried out by myself.

cussed in Section 7.3.2, the only modification techniques that proved to be applicable to the nanoporous gyroid-structured polystyrene templates were plasma and ozone exposure.

The main reason for the lack of success of the techniques listed above is that they all partially degrade the polystyrene, leading to the formation of low molecular weight fragments that can easily be washed away during the subsequent liquid processing steps. For the nano-structured block copolymer films, such fragments are comparable to the relatively low molecular weight of the copolymer template itself, and contact with a liquid environment breaks up the film. Plasma and ozone exposures overcome these problems since they are purely gas phase methods without the need for a liquid phase step.

XPS is normally used to determine the functional species, namely those containing O-H, C-O (alcohols, ethers and peroxides), C=O (ketones and aldehydes) and C=O-O (carboxylic acids and esters) groups, which are formed during various modification techniques [288]. For the deposition of TiO_2 using $TiCl_4$ and H_2O, O-H containing species are required, however to the best of our knowledge there are no reports that these species can be detected by XPS.

Plasma treatment of polystyrene is known to produce a high fraction of O-H containing species but it suffers from a limited penetration depth in the porous polymer templates due to the high reactivity and short lifetime of the radicals formed in the plasma (Figure 7.14). Ozone is less reactive and has a longer lifetime than plasma radicals. This allows for Knudsen diffusion of the ozone which enables it to interact with the polystyrene throughout the entire gyroid-structured network. Ozone treatment is not believed to lead to the direct formation of O-H containing species. Thus further modification steps are required to achieve successful ALD nucleation and growth.

The surface modification of the polystyrene using ozone is believed to proceed via the Criegee mechanism [289] in which alkenes react with ozone to form secondary ozonides (SOZ; 1,2,4-trioxolanes) via short-lived primary ozonides (POZ; 1,3,3-trioxolanes) (Reaction 7.1). The SOZ can be transformed into aldehydes/ketones, ketones/carboxylic acids or alcohols via subsequent work-ups using strong reducing or oxidising agents or a post-ozonolysis thermal treatment. As the work-up using liquid phase reducing or oxidising agents led to a complete degradation of the porous films, the thermal treatment route was pursued in this study.

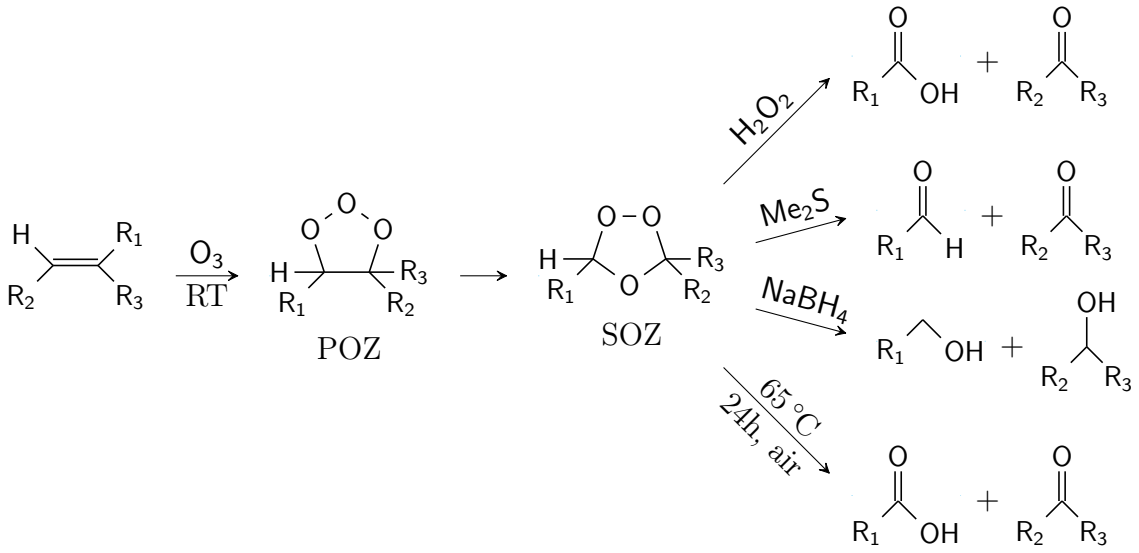

Reaction 7.1: Ozonolysis of a double bond leads to the formation of primary (POZ) and secondary ozonides (SOZ). The SOZ can subsequently be converted into ketones, aldehydes, carboxylic acids and alcohols using a number of work-ups.

7.2 Experimental methods

7.2.1 Materials

The chemicals and materials listed in Table 7.1 were used as received unless otherwise specified.

Chemical	Purity (%)[a]	Abbreviation
1-Methyl-3-propylimidazolium iodide	98 (SA)	PMII
1-Methylbenzimidazole	99 (SA)	NMBI
2-Amino-2-hydroxymethyl-propane-1,3-diol	99 (SA)	TRIS
3-Methoxypropionitrile	98 (SA)	–
Acetonitrile, anhydrous	99.8 (SA)	–
α–Picoline borane	95 (SA)	–
CELLSTAR Petri-dishes (lids only)	– (GBO)	–
D149 indolene-based organic dye	– (SA)	–
Diethylzinc	95 (SA)	DEZ
Dimethyl sulphide	99 (SA)	Me2S
Ethanolamine	99 (SA)	–
Flourine-doped tin oxide (FTO) coated glass	15 $\Omega/\square$ (SR)	FTO

continued

Chemical	Purity (%)[a]	Abbreviation
Guanidine thiocyanate	99 (SA)	GuNCS
Hydrazine hydrate	50–60 (SA)	–
Hydrogen peroxide	30/50 (SA)	–
Iodine	99.8 (SA)	–
Methanol, laboratory reagant grade	– (FS)	–
N719 ruthenium-based dye	– (SR)	–
Nitric acid, laboratory reagent grade	70 (FS)	–
Oxygen	99.999 (BOC)	–
Sodium borohydride	98 (SA)	–
Spiro-MeOTAD, hole conducting material	– (SR)	Spiro
Sulfuric acid, laboratory reagent grade	95 (FS)	–
Titanium isopropoxide	95 (SA)	TIP
Titanium tetrachloride	99 (SA)	–
Toluene, anhydrous	99.8 (SA)	–
Trifluoroethanol	99 (SA)	–
Trimethylaluminium	97 (SA)	TMA
Water, deionised	18 MΩ	DI water

[a] Suppliers are given in brackets: Fisher Scientific, FS; Sigma Aldrich, SA; Greiner Bio-One, GBO; Solaronix, SR.

Table 7.1: Chemicals and materials used in this part of the study.

7.2.2 Surface modification

To determine and optimise the modification parameters, a model system was used, based on the lids of CELLSTAR Petri-dishes. They are fabricated from high-density polystyrene and exhibit an untreated contact angle of $>90°$ which render them unsuitable for ALD growth without further surface modification. Any chemical changes during the various modification schemes, including ozone and plasma treatments, were monitored by attenuated total reflection Fourier transform infrared spectroscopy (ATR-FTIR) and water contact angle measurements. Besides the chemical influence of the treatments, the interaction between the ALD precursor molecules and the modified surfaces and their ability to allow for a uniform and dense nucleation and growth was studied. This was performed using energy-dispersive x-ray spectroscopy (EDX). The EDX was carried out at 15 keV with an integration time of 5 min. Given that the EDX signal of TiO_2 is very weak and that some of its peaks overlap with the peak of oxygen in the EDX spectra, ZnO was chosen as the reference material. The ALD pulse scheme used for the ZnO depositions is shown in Table 7.2.

	Precursors	# cycles	Pulse (s)	Purge (s)
Step 1 (optional)	TMA/H_2O	1	0.5	2
Step 2	DEZ/H_2O	40	0.5	2

Table 7.2: ALD pulsing scheme for EDX measurements.

7.2.3 Ozone treatment

The polystyrene samples were chemically modified by exposure to O_3 (ozone generator BMT 802N, 100% power) at room temperature for between 1 min to 15 min, followed by an optional thermal treatment at 60 °C for 24 h in air.

7.2.4 Polymer template fabrication

The block copolymers used in this study are the PS192 ans PS128 copolymers (Section 5.5). The nanoporous templates were fabricated according to the procedures described in Section 5.6.

7.2.5 ALD depositions

The metal oxide depositions were carried out in a Beneq TFS200 reactor at a pressure of 1.5 torr under a constant N_2 flow (99.999%) of 200 SCCM. The precursors used for the deposition of Al_2O_3, TiO_2 and ZnO and their normal deposition parameters for planar substrates are described in Section 4.7. A number of different deposition schemes were attempted inside the polymeric templates, including extended pulse times, micropulsing (the precursor pulse consists of alternating 100 ms pulses of the precursor and N_2), and pulse&hold where the precursor's residence time inside the reactor is increased by closing the vacuum line valve. The results in this study are mainly based on the pulse&hold scheme and the timings of the schemes for depositions inside the PS192 and PS128 polymers respectively are shown in Table 7.3 and Table 7.4. The deposition temperatures for growth in PS192 and PS128 were 65 °C/100 °C and 100 °C/150 °C respectively. Subsequent to the ALD growth but prior to further imaging or device fabrication, some samples of deposited TiO_2 and ZnO were calcinated at 550 °C (heating rate 20 °C/ min) for 12 h under an O_2 environment to remove the polymeric templates and to crystallise the metal oxide scaffold.

7.2.6 SEM sample preparation

The deposition quality, uniformity and coverage inside the templates was studied by scanning electron microscopy. The samples were fractured and the exposed cross-sections were plasma etched in an oxygen plasma (100W, 0.6 mbar) to remove the

	Precursors	# cycles	Pulse (s)	Hold (min)	Purge (min)
Step 1 (opt)	Precursor 1 and 2	1	15	2	4
Step 2	Precursor 3 and 4	5	10	0	1
Step 3	Precursor 3 and 4	20	10	2	4
Step 4	Precursor 3 and 4	30	10	4	8

Table 7.3: ALD pulsing scheme for depositions inside PS192. Precursor 1 is either TMA or DEZ. Precursors 2 and 4 are H_2O. Precursor 3 is either TMA, $TiCl_4$ or DEZ. Deposition temperature was either 65 °C or 100 °C.

	Precursors	# cycles	Pulse (s)	Hold (min)	Purge (min)
Step 1	Precursor 1 and 2	1	15	2	4
Step 2	Precursor 3 and 4	10	10	0	1
Step 3	Heating to 150 °C				
Step 4	Precursor 3 and 4	100	10	0	1
Step 5	Precursor 3 and 4	20	10	1	2
Step 6	Precursor 3 and 4	20	10	2	4
Step 7	Precursor 3 and 4	20	10	4	8

Table 7.4: ALD pulsing scheme for depositions inside PS128. Precursor 1 is DEZ. Precursors 2 and 4 are H_2O. Precursor 3 is $TiCl_4$. The initial deposition temperature was 100 °C. The chamber was heated to 150 °C for approximately 30 min.

polymer template and expose the metal oxide scaffold. The samples were imaged at 45° or 90° and at an acceleration voltage of 5 kV.

7.2.7 Device characterisation

Both liquid electrolyte DSSCs and solid-state DSSCs were fabricated according to Section 5.4.1 and Section 5.4.1 using TiO_2 replicas of the PS192 and PS128 polymer templates. The characterisation is described in Section 5.4.3.

7.3 Results and discussion

7.3.1 ALD growth in untreated templates

The nanoporous polystyrene templates (PS192) used in the first part of this study are shown in Figure 7.2. The templates display the double-gyroid morphology as described in Chapter 3. The high order, periodicity and tricontinuity of the template is clearly

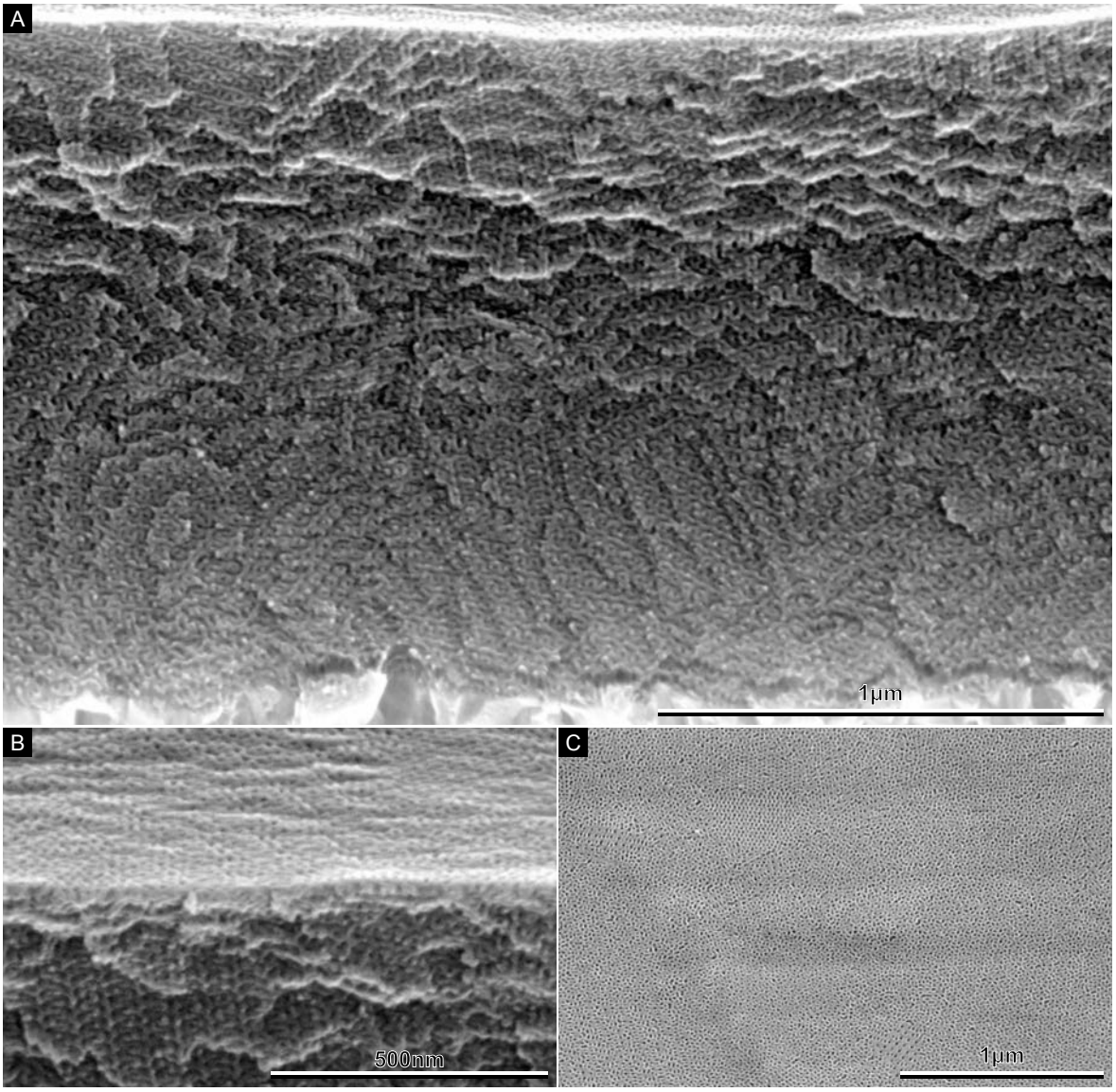

Figure 7.2: Nanoporous double-gyroid thin film polystyrene template. **(A)** Cross-sectional view showing that the porosity extends throughout the entire film. **(B)** Higher magnification view of **A** showing that the porosity extends through the free surface. **(C)** Low magnification view of the top surface of **A** showing that the free surface is highly porous.

visible. The PS192 polymer has a lattice unit cell of approximately 43 nm and a pore size of 10 nm to 11 nm. Contrary to the electrochemical depositions carried out in Chapter 6, where a fully porous substrate/polymer interface was required with only a few pores needed at the free-surface interface for electrolyte infiltration, ALD requires a fully porous free-surface interface to ensure an effective diffusion of precursors and by-products in and out of the templates. This highly porous free-surface interface can be seen in Figure 7.2B,C.

Even though the main advantage of the use of a polymeric template is its easy removal

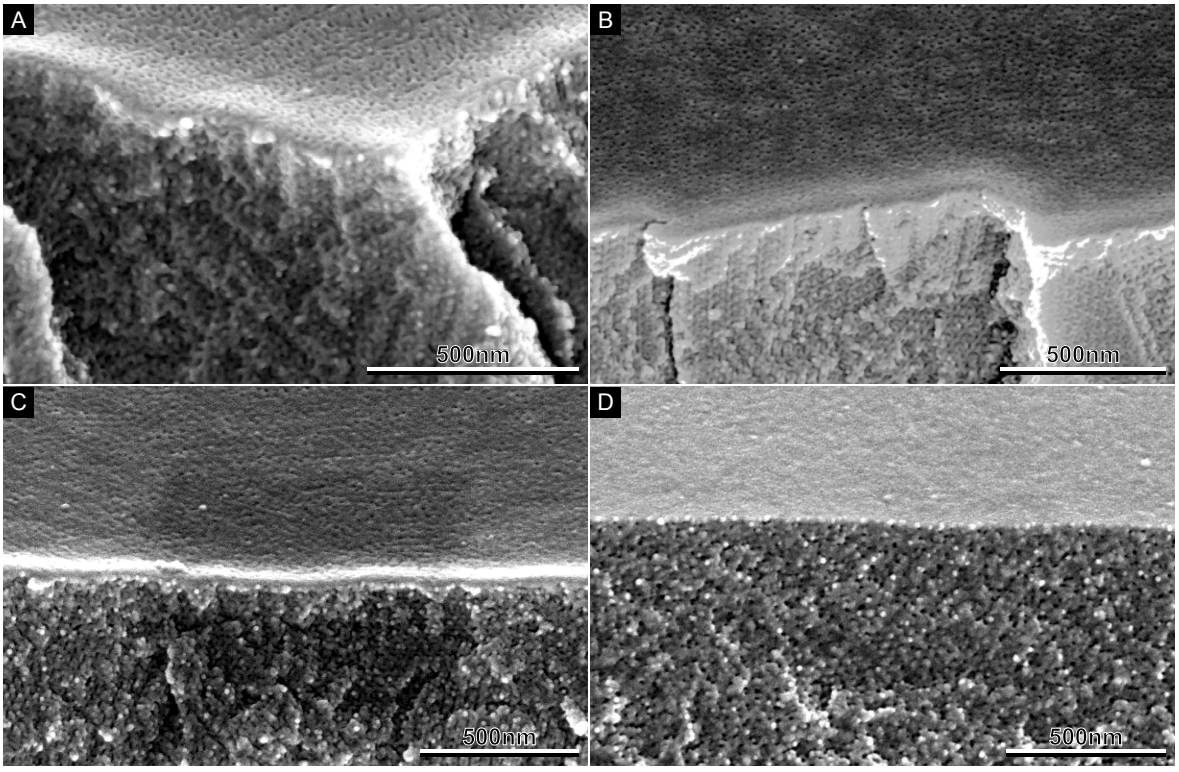

Figure 7.3: Thermal instability and reordering of the mesoporous polystyrene template. All templates were heated for 1 h under vacuum. **(A)** At 65 °C both the bulk and the top surface maintain their order and porosity. **(B)** At 70 °C the bulk maintains its order and porosity whereas the top surface becomes less porous and some order is lost. **(C)** At 75 °C the bulk starts to lose its order and porosity, and the top surface loses further porosity and is completely disordered. **(D)** At 80 °C order is lost in the bulk and the top surface becomes completely non-porous.

after replication or deposition, the low glass transition temperature and low thermal stability of most polymers makes these templates partially or fully incompatible with ALD. This problem is further complicated for the nanoporous voided polystyrene templates used in this work. The glass transition temperature of polystyrene (T_g=104 °C) is further lowered for a porous polymer film which causes the polymer films to reorder at temperatures as low as 70 °C as shown by Zalusky *et al.* [74]. This is not unexpected since the glass transition temperature is a concept normally applied for bulk materials rather than thin porous films. This reordering causes the top surface of the templates to become non-porous (Figure 7.3) which prevents the diffusion of the ALD reactants and the by-product in and out of the template. The thermal instability can be further compounded by random fluctuations in the template's pore diameters at temperatures close to the glass transition. This can lead to exothermic heating of the surrounding polymer volume due to a lowering of the polymer/air interfacial area. This heating softens the surrounding polymer making reordering and the accompanying exothermic heating even more likely. Given the threshold for free-surface reordering of 70 °C to 75 °C (Figure 7.3A,B) the initial ALD growth temperature was chosen to be 65 °C.

Zalusky *et al.* have shown that subsequent to the removal of the PLA component in a PS-b-PLA block copolymer, the connecting group between the two blocks is situated at the newly formed PS/air interface and that the polymer surface is uniformly covered with these groups at a surface density of $0.25\,\mathrm{nm}^{-2}$ [74, 290]. Given that 2-hydroxyethyl-α-bromoisobutyrate (HEBIB) is used as the initiator for the synthesis of the PS192 polymer (Section 5.5), it is expected that -OH containing carboxylic acid groups should be present at the polymer/air interface of PS192 and uniform nucleation and growth of TiO_2 should therefore be feasible without any further requirement for surface treatments.

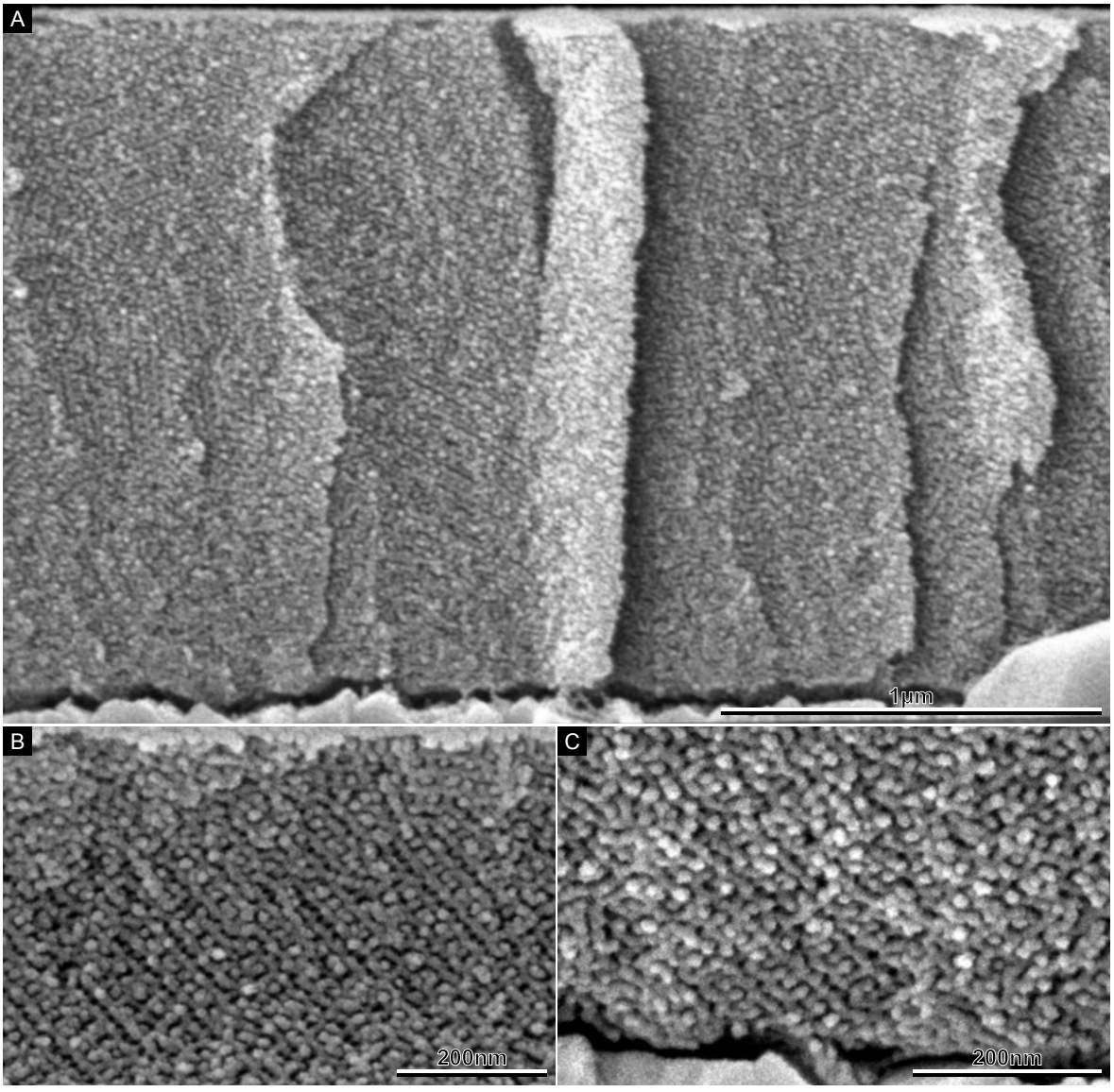

Figure 7.4: ALD growth of Al_2O_3 in untreated PS192 templates using long precursor pulse times. **(A)** The deposition extends throughout the entire template. **(B)** Higher magnification view of **A** near the top surface. **(C)** Higher magnification view of **A** near the FTO substrate.

As described in Section 7.2.5, varying deposition schemes were initially tested. The deposition of Al_2O_3 at 65 °C using exposure times up to 30 s is shown in Figure 7.4.

Even though acceptable replications were achieved using this scheme, the quality of the growth was very varied and mostly produced very poor replicas of the polymer template. The main cause of these disappointing results was initially thought to be a limitation in the precursor residence time in the template. Micro-pulsing, see Section 7.2.5, provides an alternative to increasing this residence time whilst preventing excessive exposure of the precursors to ALD reactor components such as filters and pumps. However micro-pulsing proved unable to improve on previous results.

The third approach to the requirement for long precursor residence times employs a pulse&hold deposition scheme in which the N_2 flow is lowered to 20 SCCM and the vacuum line valve is closed during the precursor pulse and exposure [157]. The precursors are introduced into the reactor with a pulse time t_1 and then held in the reactor for a time t_2. The unreacted precursors and reaction by-products are removed by purging under vacuum for a time t_3. The same procedure is repeated for the H_2O exposure with identical pulse, hold and purge times of t_1, t_2 and t_3. The length of the hold and purge times are increased with increasing numbers of cycles to achieve the highest possible reactant coverage. The pulse, hold and purge length for the PS192 templates are given in Table 7.3.

The deposition of Al_2O_3 and TiO_2 at 65 °C in untreated PS192 templates using the pulse&hold scheme is shown in Figure 7.5 and Figure 7.6. It can been seen that the initial assumption of a sufficient density of functional surface groups on the template surface is incorrect and the deposition displays a grainy texture caused by a low nucleation density and subsequent island growth. The low quality and non-uniformity of the growth is made even more obvious by the perforated nature of the replica with voids clearly present. Even though the deposition appears to have penetrated several micrometers into the templates, the subsequent calcination, which is required for fabrication of crystalline TiO_2 scaffolds, has led to the collapse of the replica down to a very thin film (normally less than 500 nm) with none or little of the original structural order remaining (Figure 7.6C).

Two possible explanations as to why we were unsuccessful in replicating the polymer template are the low deposition temperature which leads to a lowered reactivity of the precursors, and a very low density of functional surface groups on which the ALD growth can nucleate. We now believe that the observed results are due to the latter which is supported by the fact that depositions on plasma-treated templates (Figure 7.14) at the same deposition temperature produce metal oxide replicas that are stable after calcination.

In hindsight the insufficient nucleation should have been expected given the the assumed density of native functional surface groups at the polystyrene/air interface ($0.25\,nm^{-2}$) [74, 290] in comparison to the density of hydroxyl groups on the amorphous native oxide of silicon ($3\,nm^{-1}$ to $5\,nm^{-1}$ [291], a substrate on which ALD displays a dense nucleation and uniform growth.

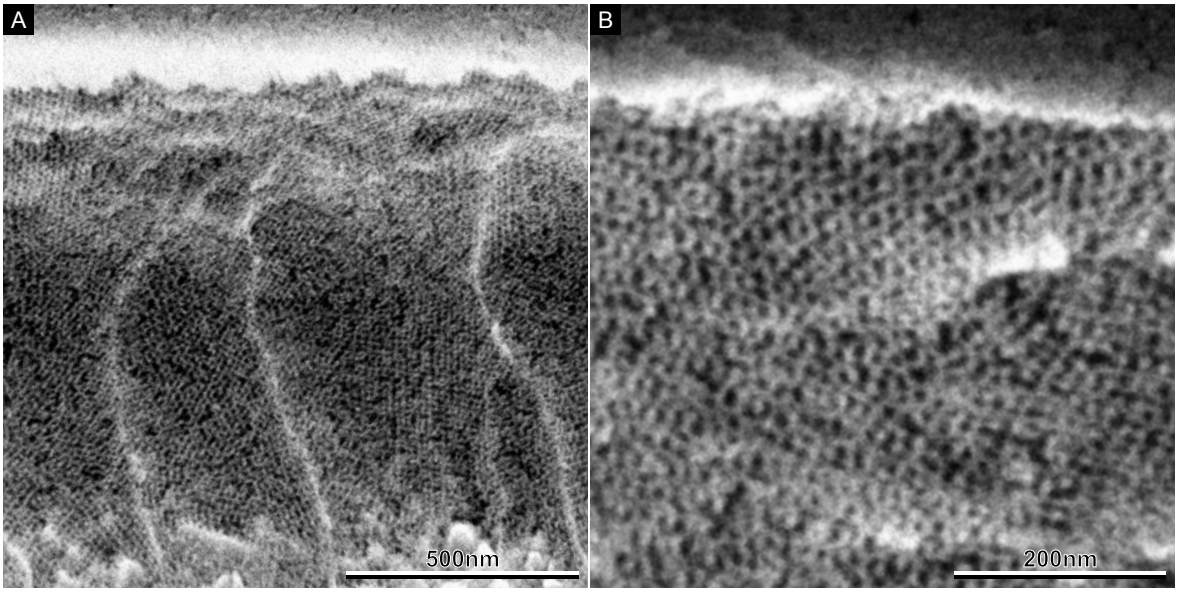

Figure 7.5: ALD growth of Al_2O_3 on untreated PS192 templates using the pulse&hold scheme. **(A)** Cross-sectional image of the Al_2O_3 replica after removal of the polymer template using an O_2 plasma. The deposition is grainy and voids are apparent. **(B)** Higher magnification view of **A**.

These unsuccessful results in replicating the untreated polymer templates prompted the need for a suitable functionalisation technique which could promote a higher density of functional groups and a successful ALD replication.

7.3.2 Chemical modification of polystyrene

As described in the introduction, chemical modification of polystyrene is of particular interest in the biological and medical research communities as a route to promote cell adhesion on culture Petri-dishes. Polystyrene is relatively chemically inert making it difficult to modify, as evidenced the variety of modification routes that exist in the literature. In this study, a large range of different protocols have been tested to determine which have the potential to introduce functional groups compatible with dense ALD nucleation on the surface of polystyrene. As well as chemically altering the surface, the modification also has to maintain the structural integrity of the porous polymer template in order to be considered successful. A significant fraction of the attempted protocols were deemed unsuccessful for either of these two reasons.

The attempted protocols are nitration of the polystyrene phenol rings using either gaseous nitrogen dioxide or ionic nitrites, oxidation using potassium permanganate or sodium hydroxide, sulfonation using concentrated sulphuric acid, photo-oxidation, and plasma and ozone exposures. Besides plasma and ozone exposures, sulfonation and photo-oxidation, all other protocols failed to chemically modify the Petri-dishes and render them hydrophilic, and therefore failed to promote dense ALD nucleation and growth. Sulfonation and photo-oxdiation were deemed unsuccessful since they

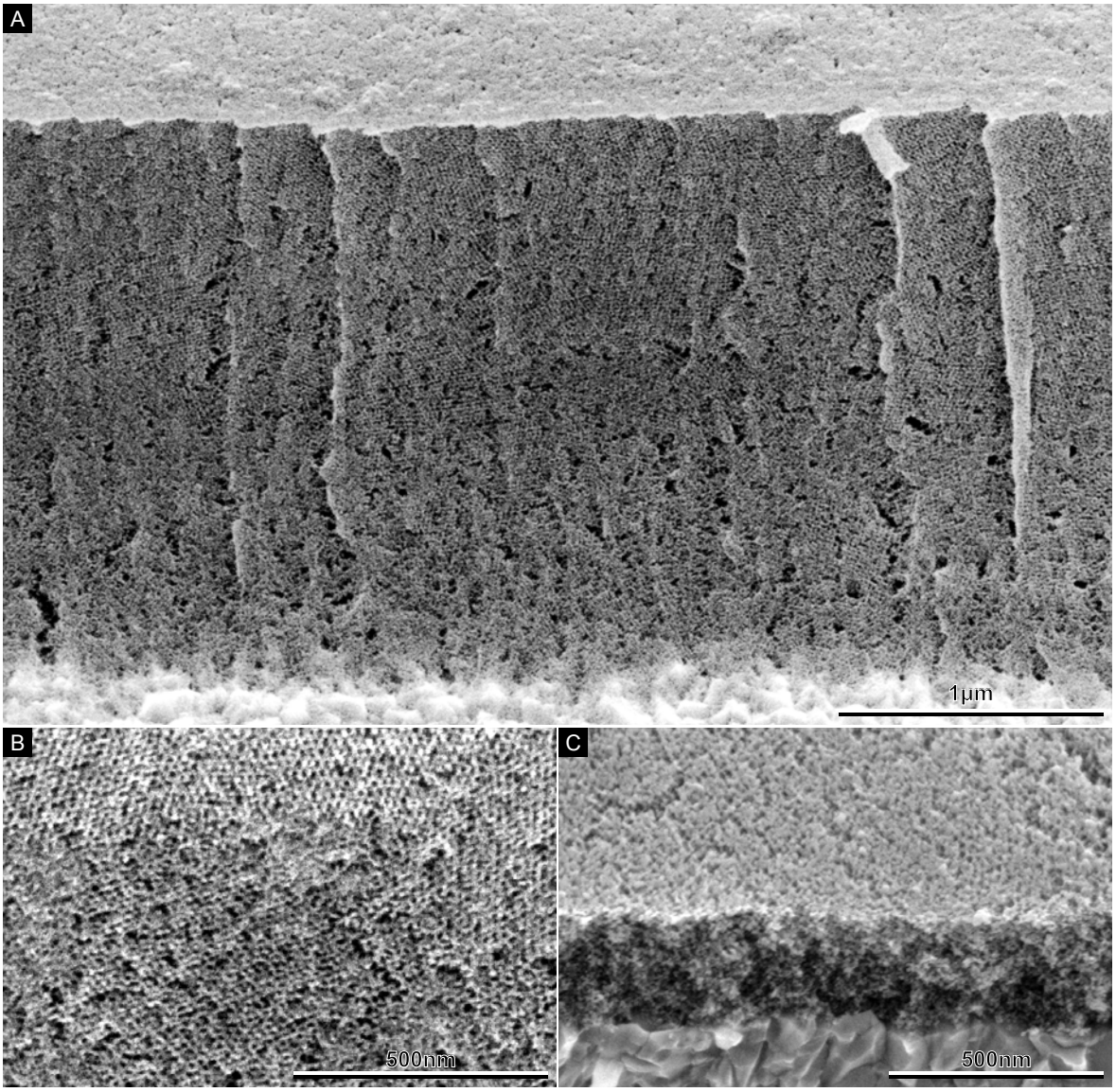

Figure 7.6: ALD growth of TiO_2 on untreated PS192 templates using the pulse&hold scheme. **(A)** Cross-sectional image of the TiO_2 replica after removal of the polymer template using an O_2 plasma. The grainy and voided deposition caused by poor nucleation and island growth is clearly visible. **(B)** Higher magnification view of **A**. **(C)** Calcination at 500 °C under O_2 leads to film collapse and loss of order and porosity.

destroyed the structure of the mesoporous polystyrene templates. The lack of successful modification routes is not unexpected since the tested protocols are normally applied to bulk rather than thin, nanoporous polystyrene films.

As a reference to determine how effective the plasma and ozone exposures are in modifying polystyrene and providing a surface that promotes ALD growth, the EDX spectra of untreated Petri-dishes with and without a coating of 40 cycles of ZnO (DEX/H_2O) are shown in Figure 7.7. The number of ALD cycles was chosen from ALD growth of

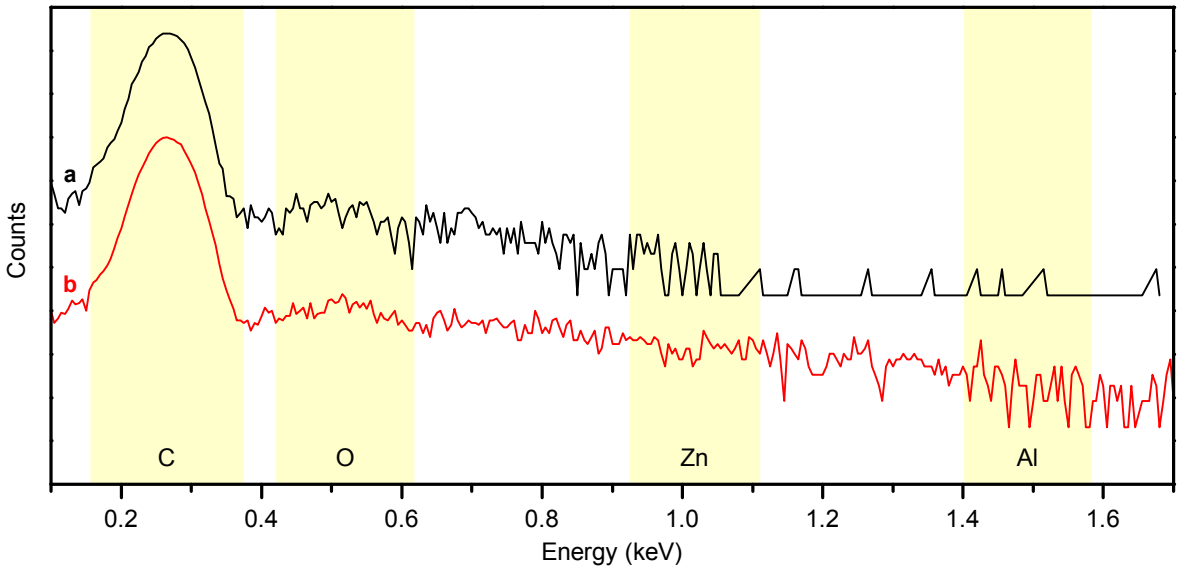

Figure 7.7: EDX spectra of untreated polystyrene Petri-dishes. Spectra are normalised to the carbon K-line at 0.28 keV. **(a)** No ZnO coating. **(b)** 40 cycles of ZnO.

ZnO on silicon, and 40 cycles are sufficient to obtain distinguishable zinc peaks. No zinc peaks are observed for deposition on the untreated substrate (Figure 7.7b). This is explained by the lack of functional groups on the untreated substrate, which is evident from the absence of a pronounced oxygen peak in the untreated film (Figure 7.7a).

Both plasma and ozone exposures are known from the literature to chemically modify polystyrene and produce a hydrophilic surface that lowers the water contact angle [135, 285–287]. Indeed, a short air plasma exposure of 0.5 s (Diener FEMTO MRC 100) reduces the water contact angle of the Petri-dishes to 0° and an oxygen peak is seen by EDX (Figure 7.8a). However no corresponding peaks for C-O, C=O and O-H, which would indicate appropriate functional groups, are seen in ATR-FTIR (Figure 7.9) which is to be expected given the limited penetration depth of the air plasma into the bulk of the polystyrene Petri-dishes and the fact that ATR-FTIR probes bulk properties of materials.

The nucleation and growth of ALD ZnO is significantly improved on the plasma exposed Petri-dishes as seen by the clear zinc peak in Figure 7.8b.

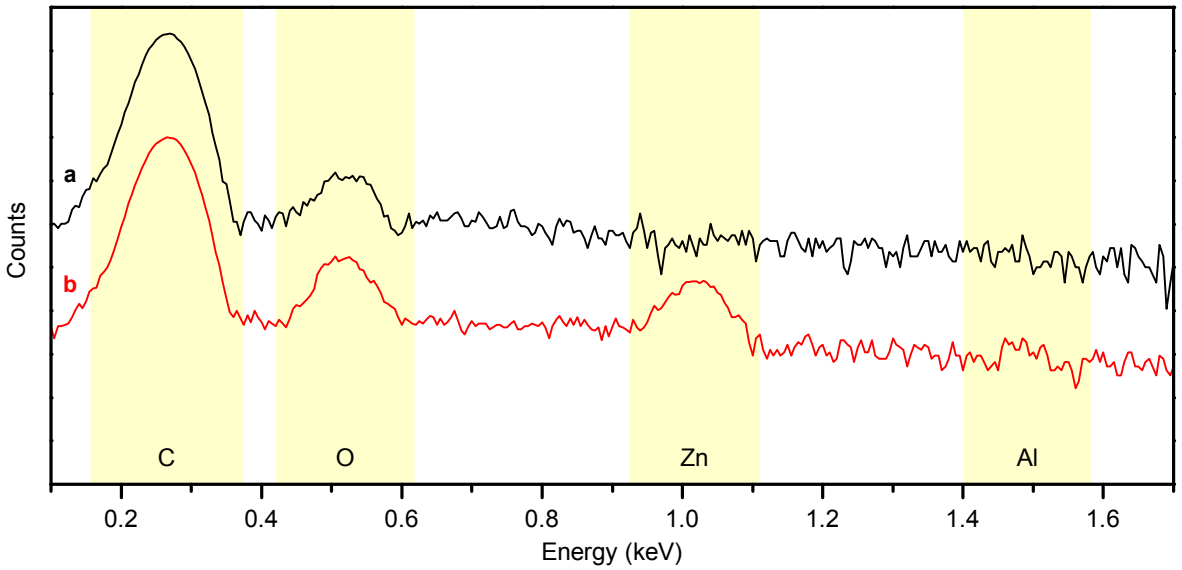

Figure 7.8: EDX spectra of polystyrene Petri-dishes exposed to a 0.5 s air plasma. Spectra are normalised to the carbon K-line at 0.28 keV. **(a)** No ZnO coating. **(b)** 40 cycles of ALD ZnO.

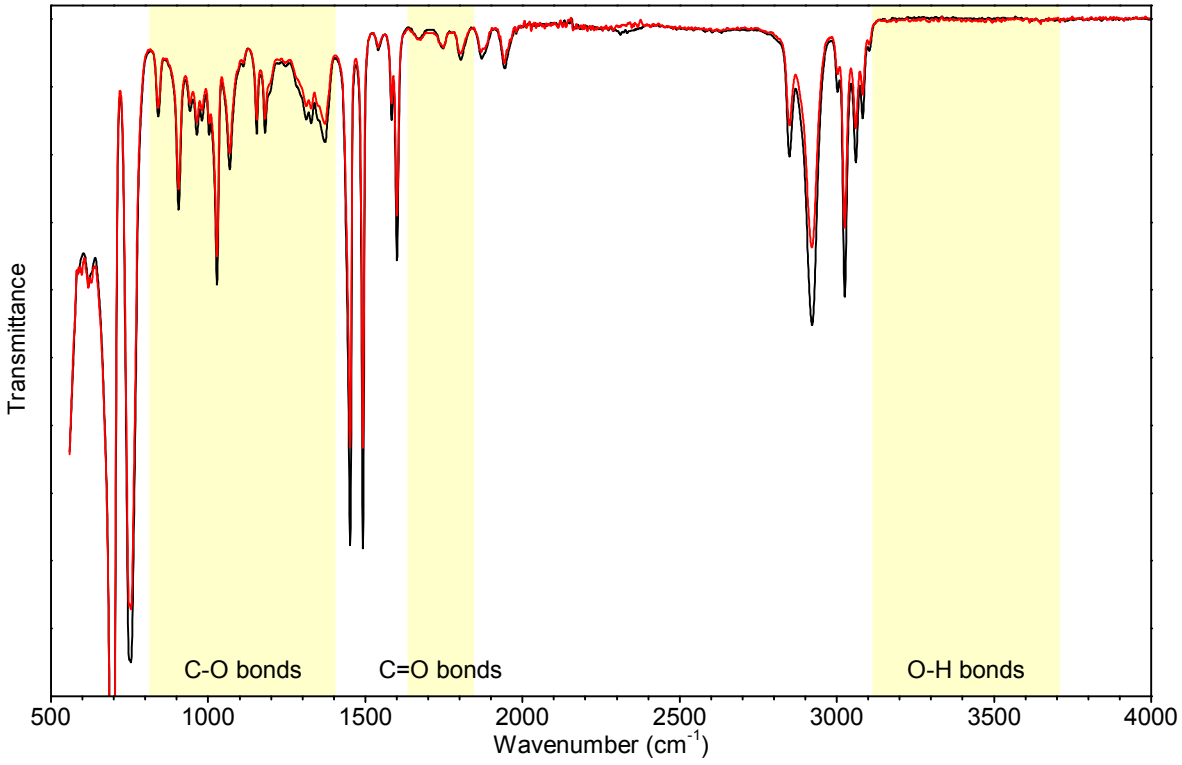

Figure 7.9: ATR-FTIR spectra of polystyrene Petri-dishes exposed to a 0.5 s air plasma. Untreated Petri-dish (—). Plasma exposed Petri-dish (—).

Similarly, an exposure to ozone for 15 min at room temperature reduces the water contact angle of the Petri-dishes and a clearly distinguishable oxygen peak is visible in Figure 7.10a which is due to the incorporation of oxygen containing groups in the Petri-dish. The ozone treatment also produces the expected secondary ozonides as seen by the ATR-FTIR in Figure 7.11. The addition of other oxygen containing bonds is also seen, indicative of the decomposition of the SOZ into ketones, aldehydes and carboxylic acids. However no significant zinc peak is observed in EDX after 40 ZnO cycles (Figure 7.10b). This shows that the ZnO precursor, diethylzinc (DEZ), does not react with the SOZ generated by the initial ozone treatment. Similarly the TiO_2 precursor, $TiCl_4$, does not have sufficient reactivity and no titanium peaks are seen in EDX.

Due to this lack of reactivity between the DEZ and the functional groups, further work-ups are employed to convert the ozonides to more reactive species such as aldehydes and ketones (Section 7.1.1). These work-ups include the oxidative reaction with H_2O_2, the reductive reaction with dimethylsulphide in methanol [292] or $NaBH_4$ in triflouromethanol and the reductive amination of the generated aldehydes and ketones using hydrazine, ethanolamine and 2-amino-2-hydroxymethyl-propane-1,3-diol with α-picoline-borane as the reducing agent. The latter route produces a high density of NH_2 groups on the surface of the Petri-dishes which are known to promote uniform nucleation of ALD growth of both ZnO and TiO_2 [293]. However all of these work-ups require the use of wet chemistry in which the ozone-treated polymer templates are not stable due to the formation of low molecular weight fragments during the ozonolysis.

Trimethylaluminium is known to react with aldehydes according to the reaction mech-

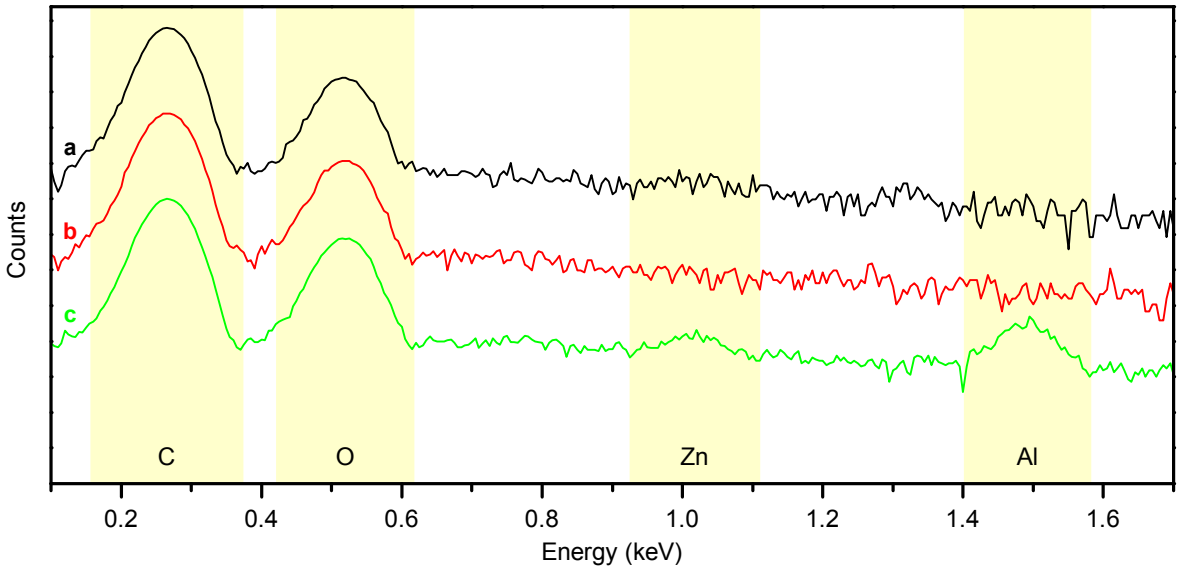

Figure 7.10: EDX spectra of polystyrene Petri-dishes exposed to ozone for 15min at room temperature. Spectra are normalised to the carbon K-line at 0.28 keV. **(a)** No ZnO coating. **(b)** 40 cycles of ZnO. **(c)** 1 cycle of Al_2O_3 and 40 cycles of ZnO.

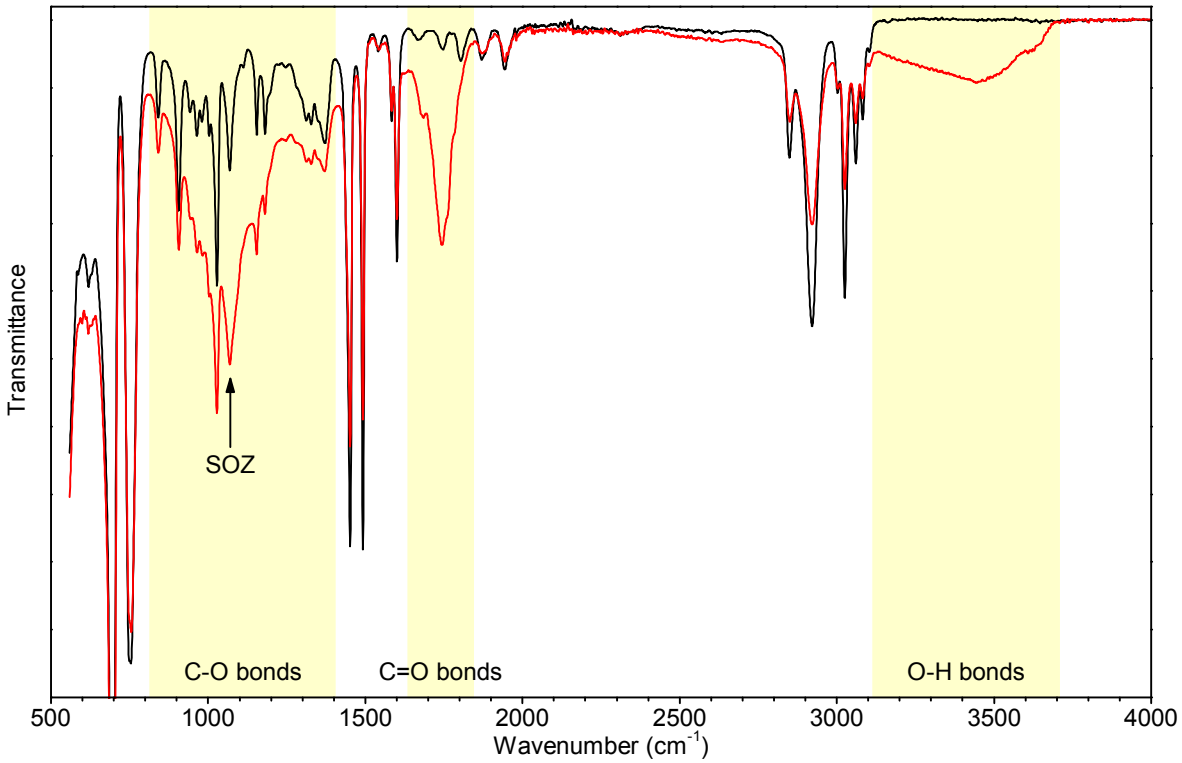

Figure 7.11: ATR-FTIR spectra of untreated (—) and ozone (—) treated Petri-dishes.

anism in Reaction 7.2 [294]. Because of this, exposure to one cycle of TMA/H_2O is attempted as a way to nucleate subsequent growth of ZnO or TiO_2. If successful, the polystyrene surface should be covered with a dense layer of Al-OH groups. Indeed, as seen in Figure 7.10c, the addition of a single Al_2O_3 cycle prior to 40 ZnO cycles enables the ALD growth and a zinc peak is seen in EDX. The stronger interaction between the ozone-treated Petri-dishes and TMA compared to DEZ is believed to stem from the increased reactivity of the TMA which allows it to decompose the SOZ.

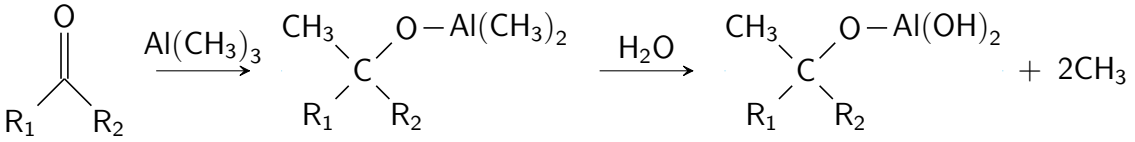

Reaction 7.2: The reaction between trimethylaluminium and ketones and the formation of a seedlayer of Al_2O_3.

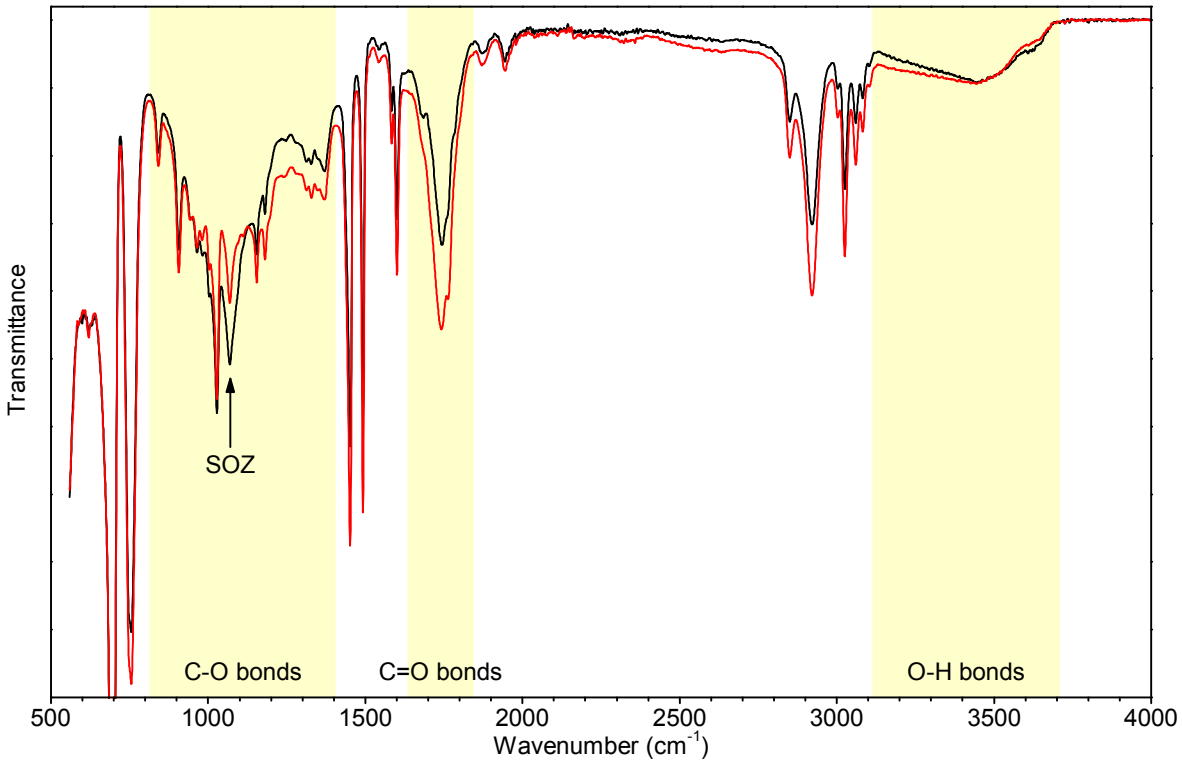

Figure 7.12: ATR-FTIR spectra of ozone-treated Petri-dishes with (—) and without (—) thermal annealing at 65 °C.

This use of a single cycle of TMA/H_2O does however incorporate a significant amount of Al_2O_3 within the Petri-dishes (Figure 7.10c). We therefore attempted to adjust the modification scheme to remove the need for the TMA. The secondary ozonides formed during the ozone treatment are known to be metastable and to decompose upon heating. Indeed, thermal annealing of the Petri-dishes at 65 °C under air for 24 h resulted in a significant decrease in the concentration of SOZ species as well as an increase in oxygen-containing bonds as seen by ATR-FTIR in Figure 7.12, which demonstrates the decomposition of SOZ into alcohols and ketones according to Reaction 7.1.

As seen in Figure 7.13b, the thermal annealing enables a uniform nucleation and growth of 40 cycles of ZnO without the need for an initial TMA cycle. The small aluminium peak in Figure 7.13b is believed to be due to cross-contamination between the Al_2O_3 and ZnO lines on the ALD. However the thermal annealing does not remove the necessity for a TMA or DEZ cycle when depositing TiO_2 using $TiCl_4/H_2O$ due to the lack of reactivity between the $TiCl_4$ and the generated ketones, aldehydes, carboxylic acids and alcohols.

7.3.3 ALD growth in modified templates

The successful use of plasma exposures to promote uniform ALD growth on Petri-dishes warrants its use with the mesoporous polystyrene templates. Compared to the

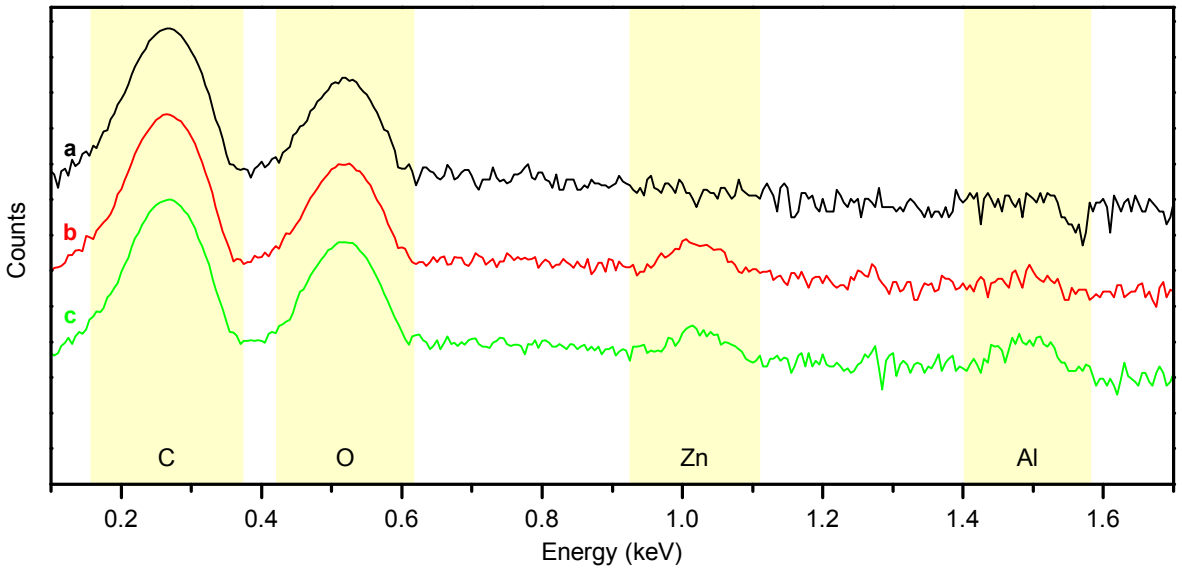

Figure 7.13: EDX spectra of polystyrene Petri-dishes exposed to ozone for 15 min at room temperature and thermally annealed at 65 °C for 24 h in air. Spectra are normalised to the carbon K-line at 0.28 keV. **(a)** No ZnO coating. **(b)** 40 cycles of ZnO. **(c)** 1 cycle of Al_2O_3 and 40 cycles of ZnO.

high-molecular weight of the Petri-dishes where a very short plasma exposure (0.5 s) is sufficient, the convoluted high-aspect-ratio templates require much longer exposure times, between 10 min and 10 h. To limit the probability of detrimental polymer etching due to the plasma exposure and to prevent excessive heating, the plasma power is limited to 40 % (40 W) and the ignition gas pressure is limited to 1 mbar. To further reduce the damaging effect of a direct plasma, an indirect plasma is emulated by placing the samples under a microscope slide inside the plasma chamber. The plasma exposure does not improve the thermal stability of the templates and depositions are therefore carried out at the initial temperature of 65 °C.

SEM images of TiO_2 replicas in plasma treated templates are shown in Figure 7.14. The TiO_2 depositions display a compact and continuous replication of the polymer templates.

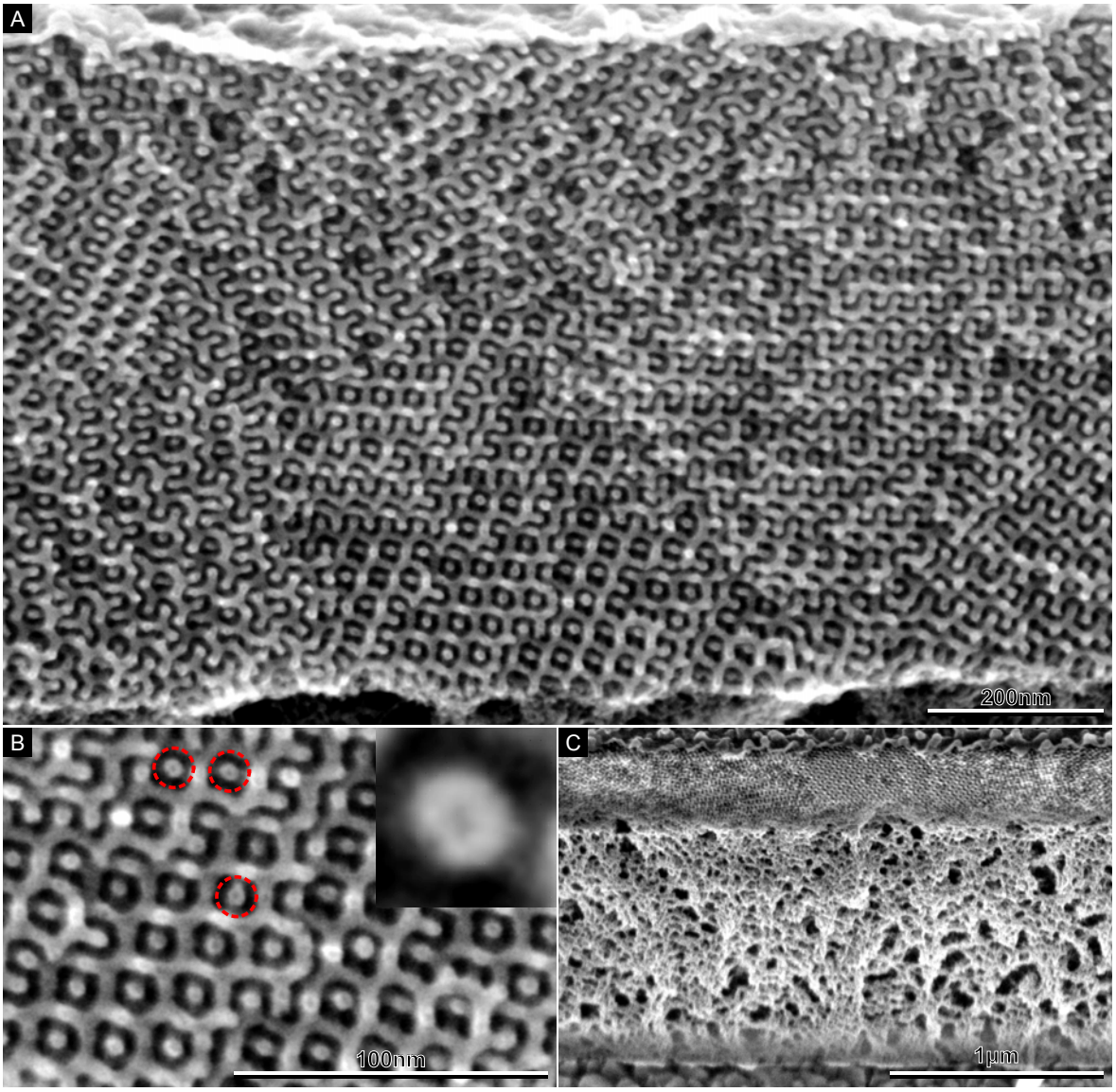

Figure 7.14: ALD TiO_2 deposition in air plasma treated templates. **(A)** Cross-sectional view showing a high quality replica indicating a high ALD nucleation density. **(B)** High magnification view of **A** showing that the struts are hollow as expected from a conformal ALD growth (red circles). The inset shows the end of a single strut. The contrast and brightness have been altered to enhance the strut. **(C)** The transition between deposition and no or poor deposition is clearly seen after removal of the template using an air plasma.

The replicas exhibit a very sharp transition between a region of monolithic replication and a region of very poor or non-existent replication. This deposition behaviour is attributed to the limited penetration depth of the plasma inside the templates. The limited penetration depth is caused by two factors. Firstly the high reactivity of the generated plasma species allows for unwanted recombination with the template surface which limits their life-times. Secondly the generation of the plasma imparts a degree

of directionality to the species which limits their penetration depth inside the template with its high-aspect-ratio network. The limited penetration depth leads to a region 1 µm to 2 µm from the template's free-surface that is densely covered with appropriate ALD functional groups. Below this region the surface chemistry of the initial template is maintained. This binary functionalisation gives the inherently different nucleation densities and growth rates seen in Figure 7.14C. This is contrary to the expected diffusion-limited thickness dependence with depth as described in Section 4.6.3, which is seen for the ozone-treated templates (Section 7.3.3).

Despite attempts to modify the plasma treatment, including the use of various plasma gases such as O_2, N_2 and water vapour, varied exposure times and gas pressures, the plasma penetration depth and therefore the ALD replication depth seldom exceeded 1 µm. In a few instances the replication depth was deeper than 1 µm but no correlation was found between the increased penetration depth and the plasma parameters.

The finite diameter of the precursor molecules ($d_{TiCl_4} = 6.4$ Å, $d_{TMA} = 4$ Å, $d_{DEZ} = 6$ Å, $d_{H_2O} = 3.2$ Å) will eventually lead to pore clogging and the formation of nano-tubes. The formation of a tubular network can be seen in Figure 7.14b. As with the ALD replication of colloidal photonic crystals, where a 100 % filling fraction is not feasible [295], the replication of the gyroid morphology is also limited by a pinch-off phenomenon. Given the thickness of the wall of the generated nano-tube, the deposition rate inside the template at 65 °C is estimated to be 0.8 A per cycle which agrees well with depositions on planar substrates (Section 4.7.2). This shows that the self-terminating nature of the ALD growth is maintained inside the HAR template at this low deposition temperature and that no CVD-like growth behaviour is seen.

As previously described, ALD growth of TiO_2 at temperatures below 150 °C has two unwanted side-effects: non self-limited absorption of $TiCl_4$ molecules which leads to higher deposition rates and possible CVD-like growth behaviour unless very long purge times are used [296]; and a high chlorine content mainly due to unreacted chlorine ligands. The ozone exposure and the subsequent thermal annealing presents one major positive side-effect, an increase in the thermal stability of the templates of up to 120 °C. This is thought to be due to cross-linking reactions which take place during thermal annealing. Cross-linking of polystyrene due to ozone exposures is known to proceed via the generation of carboxyl groups which promote the cross-linking [297]. Cross-linking also causes an increased chemical stability, meaning that the ozone-treated and thermally annealed templates are insoluble in most organic solvents.

Figure 7.15 shows the replication of ozone-treated and thermally annealed templates upon TiO_2 deposition at 100 °C. The replication penetrates throughout the entire film thickness, however uniformity and quality of the replication is lost closer to the substrate as seen by the change in colour in Figure 7.15A. The colour change is due to a change in deposition density and therefore electron contrast where denser regions appear brighter. Upon calcination only the higher density region near the top of the film remains intact (Figure 7.16E). The collapse of the bottom region is due to the fact that only a very thin-walled deposition which can not withstand calcination is present.

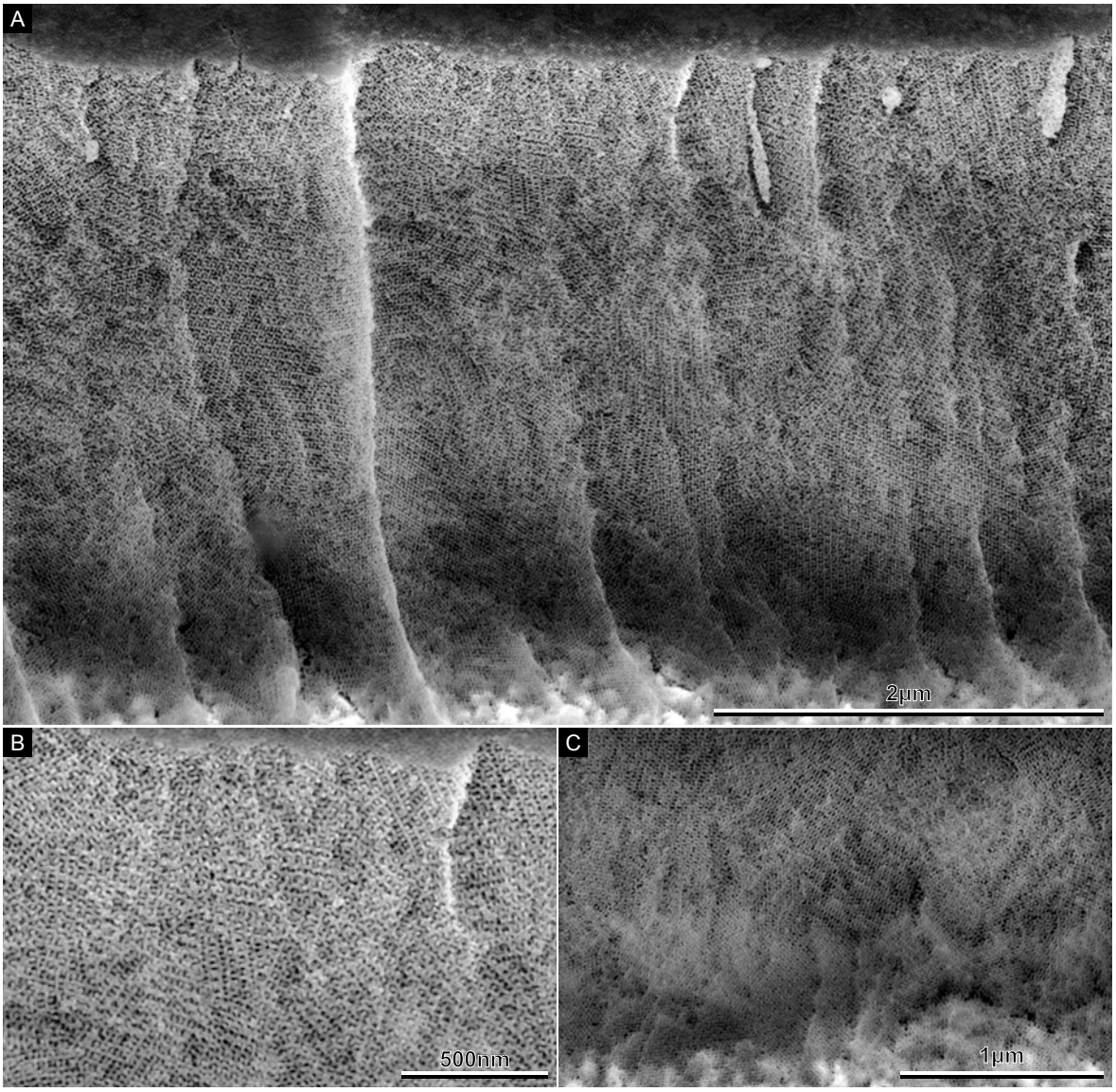

Figure 7.15: ALD growth of TiO_2 at 100 °C in ozone-treated and thermally annealed templates. **(A)** Cross-sectional view of TiO_2 replica after removal of the template using an air plasma. **(B)** High magnification view of region near the top of **A**. The replica appears bright because of a high electron density indicating a high ALD filling fraction. **(C)** High magnification view of region near the bottom of **A**. The replica appears darker than **B** because of a lower ALD filling fraction.

Given the work carried out by Gordon *et al.* and Elam *et al.* [153, 154] (Section 4.6.3), the exposure time required for complete coverage can be estimated. Assume a thickness of the polystyrene template of $L = 5\,\mu m$ and initial and final pore diameters of $d_I = 10.5\,nm$ and $d_F = 3\,nm$ respectively (estimated from the growth in plasma treated templates in Figure 7.14b). Further assume that $T = 373\,K$, $P = 0.2\,mbar$ (based on the pressure increase in the reactor upon precursor pulsing), that the saturated surface densities for $TiCl_4$ and H_2O are $S_{TiCl_4} = (2\sqrt{3})^{-1}\ {r_{TiCl_4}}^{-2} = 2.8 \times 10^{18}\,m^2$ and $S_{H_2O} =$

$11.3 \times 10^{18}\,\mathrm{m}^2$ respectively (assuming a hard closed-packed spheres model of the precursors) and that the reactive sticking coefficient Γ is unity. Given these assumptions, the initial and final minimum exposure times required for complete coverage are $t_{\mathrm{I,TiCl_4}} \approx 5\,\mathrm{s}$, $t_{\mathrm{I,H_2O}} \approx 6\,\mathrm{s}$ and $t_{\mathrm{F,TiCl_4}} \approx 59\,\mathrm{s}$, $t_{\mathrm{F,H_2O}} \approx 75\,\mathrm{s}$ respectively. The approximately equal precursors times are caused by the lower mass of the H_2O molecule being compensated by an increased surface density due to its smaller size.

Although the hold times used for the depositions (Section 7.2.5) are significantly longer than the theoretical minimum times, only approximately the top 1 µm of the replicas has a sufficient wall thickness to avoid collapse upon calcination. This discrepancy between experimental and theoretical exposure times can have two causes. The first is that the reactive sticking coefficient is lower than the assumed value of unity. The second is that templates with a starting pore diameter as small as 10 nm introduce new issues for ALD growth not normally seen for other HAR structures. The rate of change of aspect ratio as a function of deposition cycles is higher for smaller starting pore diameters. This means that the ALD growth very quickly enters into a thermodynamic regime where the pore diameter approaches 1-2 orders of magnitude of the molecular size of the precursors, and therefore the assumed Knudsen diffusion and its associated diffusion equations do not necessarily adequately describe the transport behaviour. In this regime the absorption energy is expected to be up to one order of magnitude higher than for the structures assumed by Gordon and Elam [298, 299]. These very strong interactions between the surface of the template and the precursor molecules can lead to surface diffusion limited transport in which precursor molecules hop from surface site to surface site [300]. It is expected that such a transport mechanism will significantly increase the required exposure times.

The conformality of ALD and the occurence of pore-clogging creates a non-porous TiO_2 layer which covers the top of the template (Figure 7.16A,B). For the subsequent use of the TiO_2 electrode in solar cells, this compact layer has to be removed. This is carried out using an inductively coupled plasma (ICP) etch for 10 s with a gas mixture of SF_6:CHF_3:C_4F_8:O_2 (20:20:20:40 SCCM). The porous top surface resulting from the etch is shown in Figure 7.16C,D. The final step in the post-deposition protocol is the calcination of the samples under an O_2 atmosphere at 500 °C for 3 h. Figure 7.16E,F shows two examples of the gyroid-structured TiO_2 after calcination. The porosity and order of the network remain intact and are clearly visible.

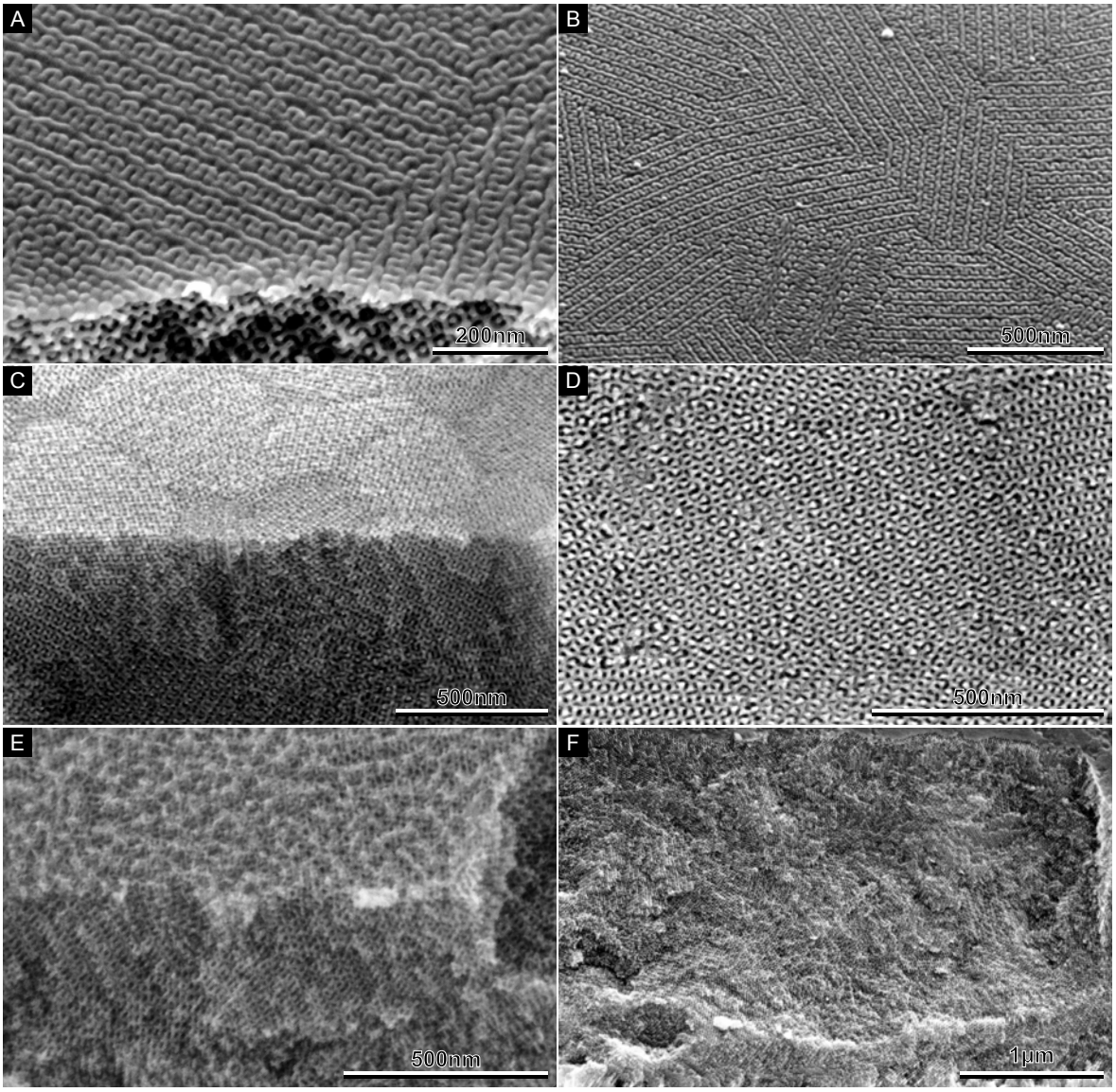

Figure 7.16: Post-processing of ALD growth of TiO_2 at 100 °C in ozone-treated and thermally annealed templates. **(A)** The conformality of ALD is shown by the precise replication of the (211) plane of the top surface. **(B)** The replication is uniform over large areas with multiple domains of the gyroid template visible. **(C)** Removal of the non-porous TiO_2 layer in **A,B** by ICP etching. **(D)** Free surface of **B** displaying the (211) plane. **(E)** Both the bulk and the free surface remain intact after calcination at 550 °C. **(F)** The increased ALD nucleation density due the ozone treatment and thermal annealing assures that the replication of thick polymer templates remains intact during calcination.

In addition to the replication of the templates using TiO_2, Al_2O_3 and ZnO were also successfully deposited. Both TMA and DEZ are more reactive than $TiCl_4$ which allows for depositions at lower deposition temperatures and their by-products, methane and ethane respectively, have a lower boiling point than hydrochloric acid, which leads

to a lower concentrations of contaminants such as unreacted ligands and reaction by-products. The replication using ZnO is shown in Figure 7.17.

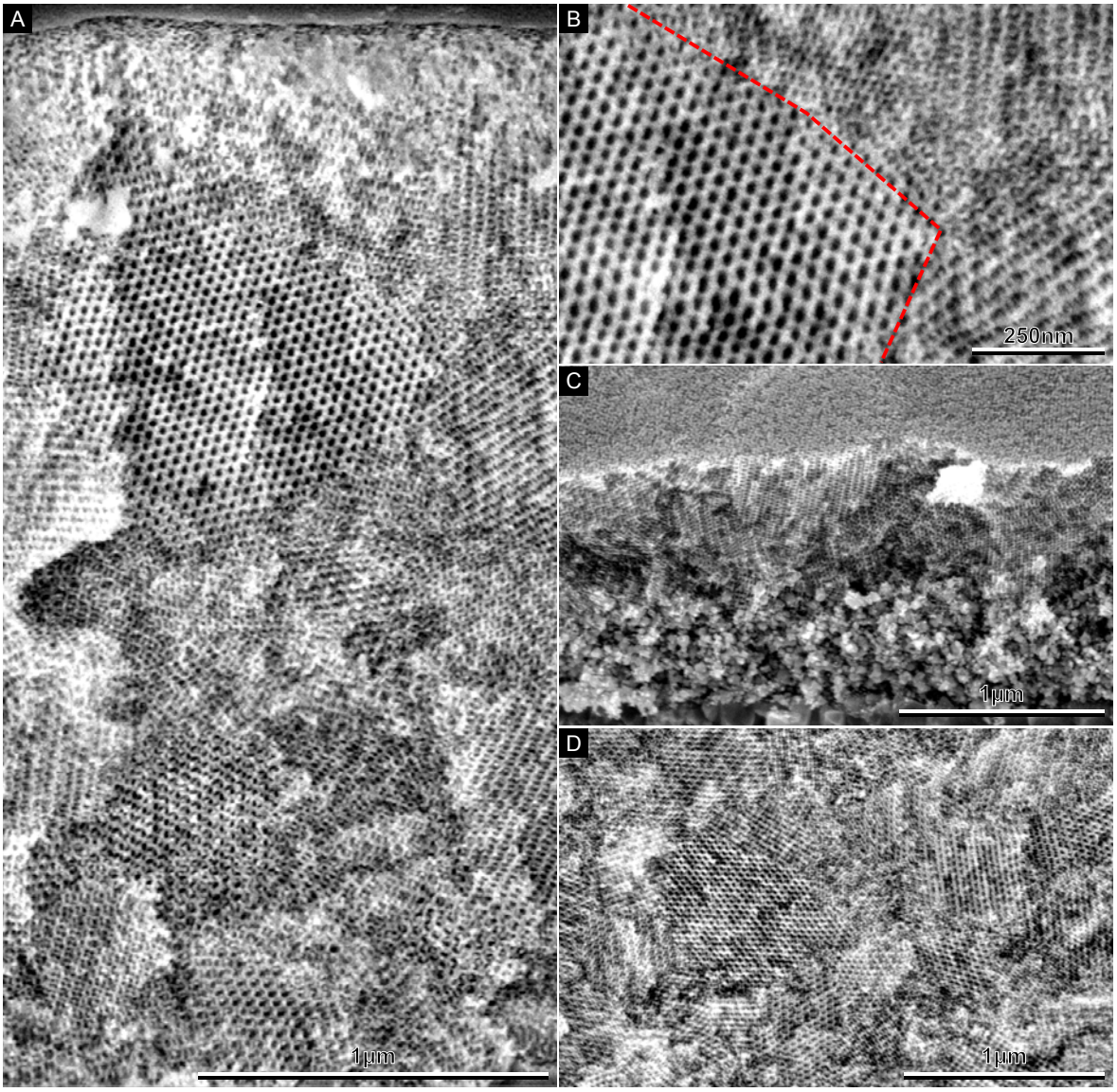

Figure 7.17: ALD growth of ZnO at 100 °C in ozone-treated and thermally annealed templates. **(A)** Cross-sectional view of ZnO replica after removal of the template in an air plasma. **(B)** High magnification view of **A**. The red line separates the double-gyroid morphology ($Ia\bar{3}d$) on the right from a region that is thought to be the *Fddd* diblock copolymer phase. **(C)** ZnO replica after ICP etching and calcination at 500 °C. The bottom of the film has collapsed which indicates a low ALD filling fraction. **(D)** The replica in **A** after calcination displaying a fully intact structure throughout the film.

The deposition displays the best replication seen by any of the three metal oxides. The apparent brightness of the SEM cross-section is more uniform than the TiO_2

deposits in Figure 7.15A which indicates a more uniform nano-pore wall thickness and density. Figure 7.15B shows a high magnification view of the region near the top in Figure 7.15A. A transition between the *Fddd* morphology (left) and the $Ia\bar{3}d$ morphology (right) is indicated by the red dashed line. The uppermost region of the film survives calcination at 500 °C whereas the lower region crumbles and the order is destroyed (Figure 7.15C). This collapse into a disordered structure, rather than the complete removal seen for the TiO_2 replicas, indicates the presence of a thicker wall of the nano-tubular network. Some of the depositions produced samples where larger portions of the film survived calcination and the thickest self-supported ZnO film produced was 2.5 µm (Figure 7.15D).

The deposition of ZnO using ALD or other deposition methods generally results in crystalline films [301–303]. However the as-deposited ZnO inside the polystyrene templates is not crystalline (Figure 7.18a). The lack of crystallisation of ZnO has been observed previously for very thin (fewer than 15 cycles) planar ALD ZnO films [144, 145]. A shell thickness of 4 nm corresponds to 22 cycles, if one assumes a deposition rate of 1.8 Å per cycle. We believe that the increase to the crystalline/amorphous threshold is due to the increased curvature and therefore confinement of the template. Upon annealing at 550 °C for 12 h under O_2, the gyroid-structured ZnO forms the expected hexagonal wurtzite structure with dominant (002) and (101) peaks (Figure 7.18b).

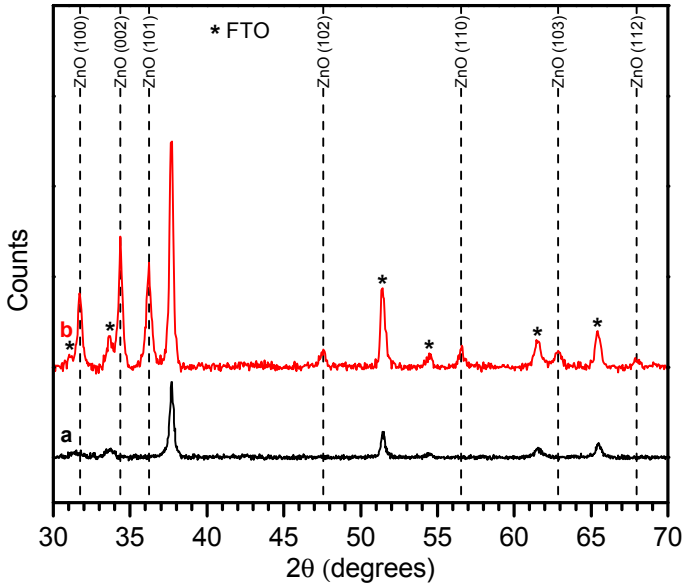

Figure 7.18: XRD spectra of gyroid-structured ZnO replica before (**a**) and after (**b**) calcination at 500 °C for 12 °C.

7.3.4 Crystallisation in ultra-thin TiO_2 films

The inhibition of crystallisation of the as-deposited ZnO replicas described in Section 7.3.3 is also observed in the TiO_2 replicas. This is thought to limit the DSSC device performance shown in Section 7.3.6. For the successful application of the TiO_2

gyroid networks fabricated in Section 7.3.3 in dye-sensitised solar cells, the TiO_2 must be crystalline to support good electronic transport and to suppress the probability of electron/hole recombination as described in Chapter 2. As expected from the deposition of TiO_2 on planar substrates at 120 °C, the as-deposited TiO_2 in the polymer templates is shown by XRD to be amorphous (Figure 7.19a). However, contrary to the gyroid-structured ZnO depositions, calcination of the gyroid-structured TiO_2 at 550 °C for 12 h under an oxygen atmosphere does not result in the expected anatase TiO_2 XRD peaks (Figure 7.19b). Two possible reasons exist for this lack of crystallisation: thickness-induced suppression of nucleation seeds, and an increased crystallisation temperature and time due to impurities present in the titania. According to literature, the incorporation of dopants (or contaminants) in TiO_2 has been shown to lead to both an increase and a decrease in crystallisation temperature [304, 305].

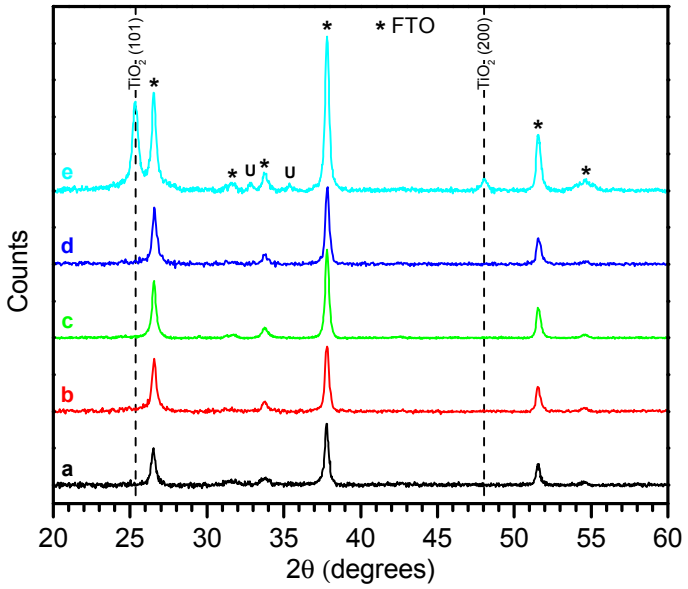

Figure 7.19: XRD spectra of gyroid-structured TiO_2 replicas after calcination. **(a)** FTO-coated glass reference. **(b)** TiO_2 deposited in PS192 using H_2O and $TiCl_4$ at 100 °C. **(c)** TiO_2 deposited in PS192 using H_2O and $TiCl_4$ at 120 °C/150 °C. **(d)** TiO_2 deposited in PS192 using H_2O_2 and $TiCl_4$ at 100 °C. **(e)** TiO_2 deposited in the 21 nm pore size PS128 using H_2O and $TiCl_4$ at 150 °C.

At deposition temperatures below 150 °C, the ALD growth of TiO_2 using $TiCl_4/H_2O$ leads to an incorporation of significant amounts of chlorine impurities in the form of HCl by-products or unreacted chlorine ligands [89, 306]. The amount of chlorine incorporated for deposition on planar substrates from 60 °C to 150 °C using our ALD reactor agrees with values from literature (Figure 4.8). For high-aspect-ratio substrates such as the gyroid templates, we expect the amount of chlorine to be higher due to the requirement for longer pulse and purge times.

However for depositions in plasma treated templates at 65 °C we see an amount of chlorine of approximately 3 % (Figure 7.20a), which is comparable to that seen in flat TiO_2 film deposited at 65 °C (Figure 4.8). This is another indication that the purge

times used are sufficiently long for the growth inside the template to be comparable to flat film growth. Calcination of these films reduces the amount of chlorine to below 1 % (Figure 7.20b). These samples were fabricated on silicon substrates, explaining the silicon peak in Figure 7.20a,b, and the polymer templates were removed prior to EDX using toluene which explains the absence of a carbon peak.

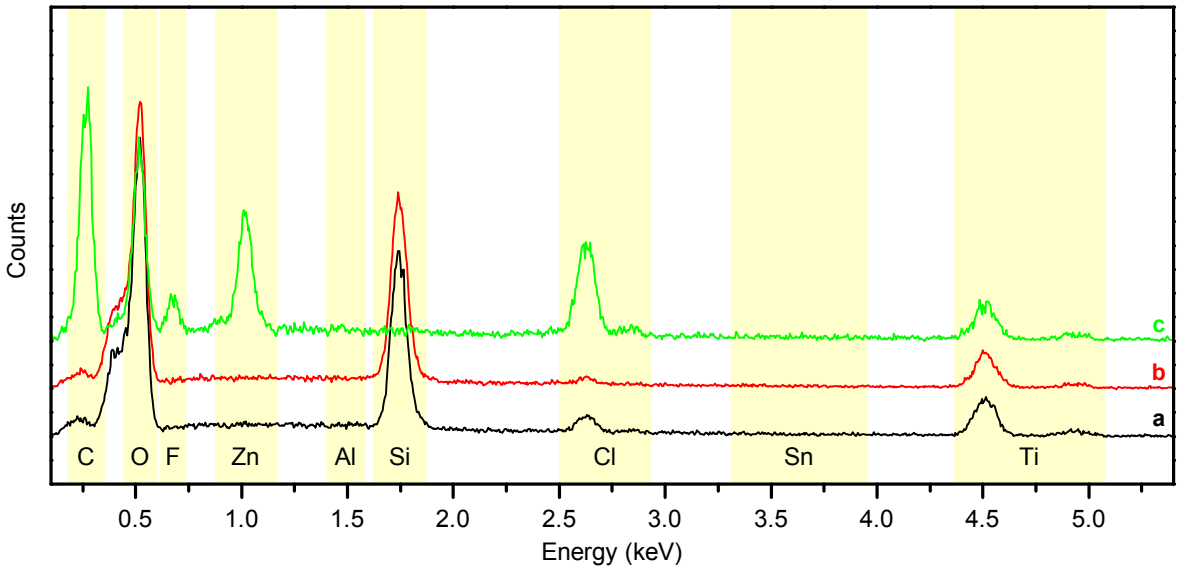

Figure 7.20: EDX spectra of gyroid-structured TiO_2 replicas without ozone treatment. Spectra are normalised to the Ti K-line at 4.5 keV. **(a)** As-deposited TiO_2 replica grown at 65 °C. **(b)** Replica in **a** calcinated at 550 °C. **(c)** TiO_2 replica deposited in ozone-treated templates as a reference.

Contrary to these results, deposition into ozone-exposed and thermally annealed templates at 120 °C leads to a much larger increase in the amount of incorporated chlorine (Figure 7.20c) and an approximate chlorine fraction of 15 %. One single ZnO cycle is used to nucleate the TiO_2 deposition as seen by the addition of a zinc peak in Figure 7.20c compared to Figure 7.20a,b. Given the increased deposition temperature for the ozone-treated templates, one would expect a decrease, not an increase, in the amount of HCl by-products and unreacted chlorine ligands, due to an increased reaction probability between $TiCl_4$ and H_2O and a higher mobility of the by-products.

Further experiments found that the immersion of the as-deposited TiO_2 network (before calcination) in methanol containing 1 M HCl for 5 min causes a significant reduction of both the zinc and chlorine peaks and a chlorine fraction of 4 % (Figure 7.21c). Because of this significant reduction we now believe that the increase in chlorine content is mostly due to a reaction between the single ZnO seed layer deposited prior to the TiO_2 and the HCl by-products. This reaction leads to the formation of $ZnCl_2$, which unlike ZnO is soluble in water and methanol. Immersion of the samples in a methanol/H_2O mixture removes both the $ZnCl_2$ and any remaining ZnO (compare Figure 7.21b to Figure 7.21c).

It is interesting to note that calcination itself is unable to remove all of these chlorine

contaminants (Figure 7.21b) and that a combination of HCl treatment and calcination is required to remove a significant fraction of the chlorine. After these steps the detected amount of chlorine, which varies between samples, is between 0.5 % and the detection limit of the EDX (Figure 7.21d).

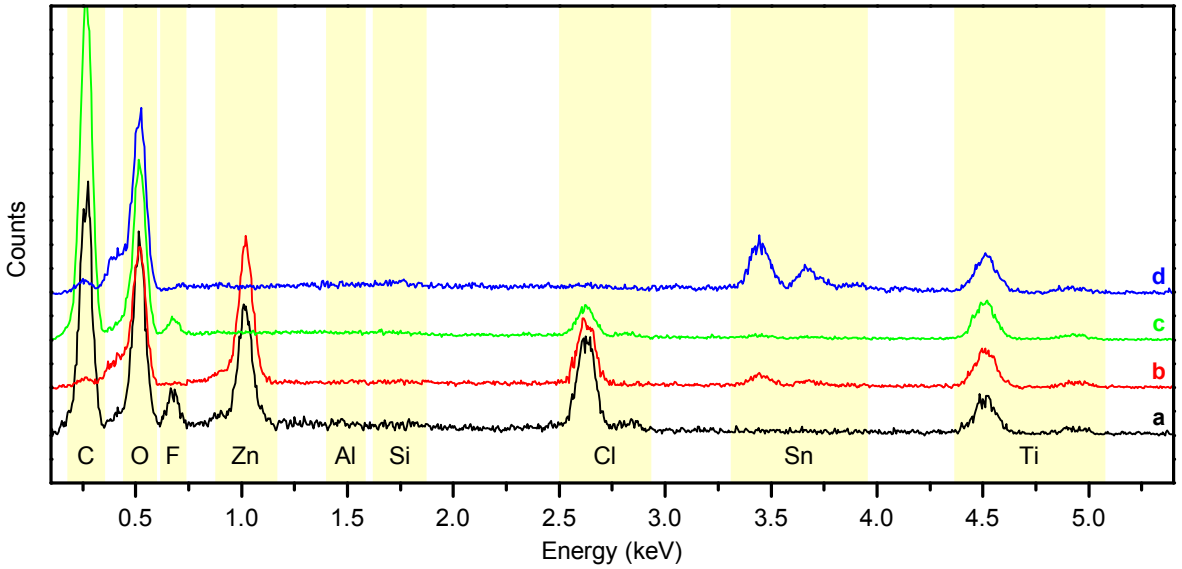

Figure 7.21: EDX spectra of gyroid-structured TiO_2 replicas with the ozone treatment. Spectra are normalised to the Ti K-line at 4.5 keV. **(a)** As-deposited TiO_2 replica grown at 100 °C. **(b)** Replica in **a** calcinated at 550 °C. **(c)** Replica in **a** immersed in 1 M HCl in MeOH for 5 min. **(d)** Replica in **a** exposed to the treatments in **c** and **b**.

There are three different routes to lowering the amount of chlorine contaminations: 1) replacing the H_2O with H_2O_2 which is known to lead to a more complete ligand exchange reaction [176]; 2) using a non-chlorine containing TiO_2 precursor; and 3) increasing the deposition temperature.

The deposition of gyroid-structured TiO_2 using $TiCl_4$ and H_2O_2 is shown in Figure 7.22. The appearance of the deposit is very similar to that deposited using H_2O instead of H_2O_2. Furthermore, the use of H_2O_2 only leads to a small decrease in the amount of chlorine in the as-deposited TiO_2 (Figure 7.23c) compared to the use of H_2O (Figure 7.23a). No additional improvement is seen upon calcination (Figure 7.23d compared to Figure 7.23b).

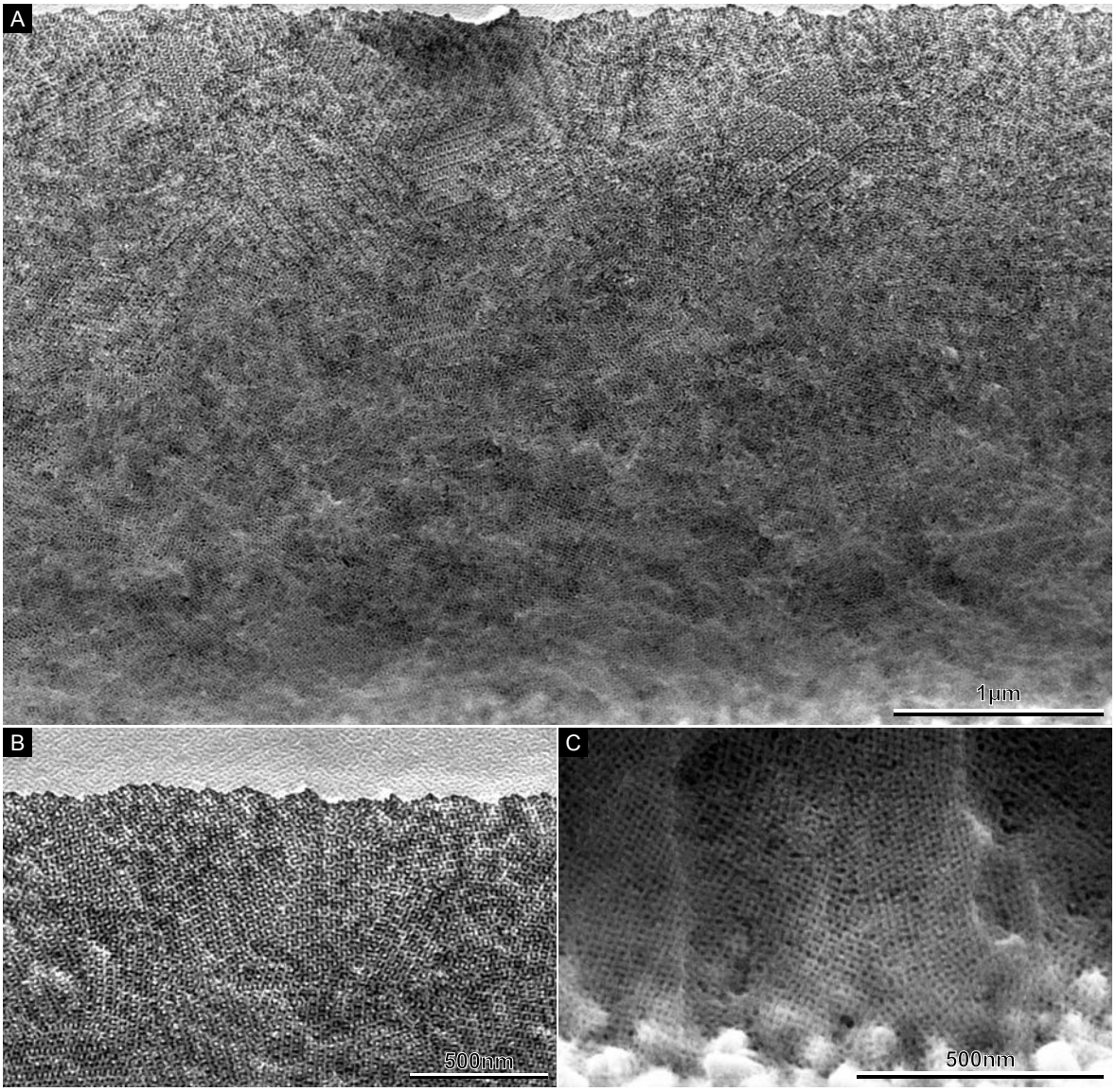

Figure 7.22: TiO_2 replica deposited in ozone-treated templates using $TiCl_4$ and H_2O_2. **(A)** Cross-sectional view of the TiO_2 replica. **(B)** High magnification view of region near the top of **A**. **(C)** High magnification view of region near the bottom of **A**.

The non-chlorine containing precursor titanium isopropoxide was used as a replacement for $TiCl_4$ but resulted in poorer template replication, possibly due to its lowered reactivity compared to $TiCl_4$.

The ozone treatment leads to an increase in thermal stability, and initial tests in which the ozone-treated films were heated under vacuum for 1 h showed that the new temperature limit below which the top surface of the templates remains porous is 120 °C. Further experiments where zero to three cycles of TiO_2 were deposited in the templates at 100 °C (in addition to the seed ZnO cycle) showed an increased template stability and a porous top surface was maintained up to 150 °C. We believe that this increased stabil-

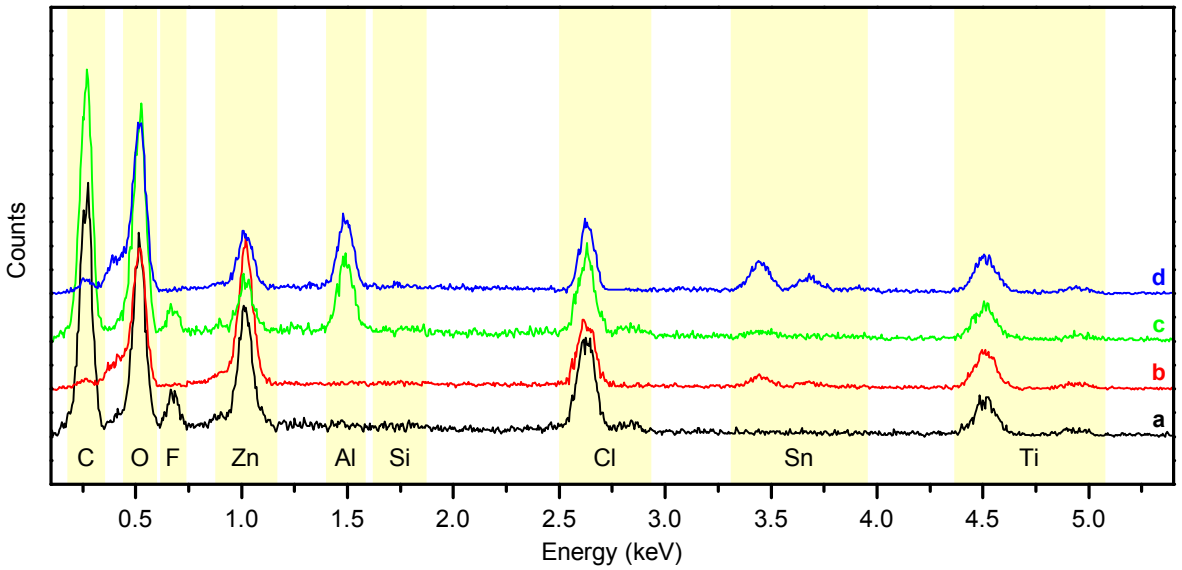

Figure 7.23: EDX spectra of gyroid-structured TiO_2 replicas deposited using $TiCl_4$ and H_2O or H_2O_2. Spectra were normalised to the Ti K-line at 4.5 keV. **(a)** As-deposited TiO_2 replica grown at 100 °C using H_2O. **(b)** Replica in **a** calcinated at 550 °C. **(c)** As-deposited TiO_2 replica grown at 100 °C using H_2O_2. **(d)** Replica in **c** calcinated at 550 °C. The addition of an aluminium peak is due to contamination of TMA during the pre-$TiCl_4$ DEZ pulse.

ity is due to the diffusion of the seed cycle precursor and the $TiCl_4$ into the sub-surface region of the template, creating an organic/inorganic hybrid structure. TiO_2 replicas were fabricated using this new two-step deposition scheme at 100 °C and 150 °C but no change in the level of chlorine contamination was observed and the samples remained amorphous upon calcination at 550 °C (Figure 7.19c).

The second possible cause for the lack of crystallisation in the gyroid-structured TiO_2 stems from thin film inhibition. The inhibition of crystallisation and the associated increase in crystallisation temperature and time in thin amorphous films is well-known [307] but has not been frequently reported for ALD grown thin films [308, 309]. As described in Section 7.3.3, the ALD growth inside the gyroid-structured templates will unavoidably lead to the formation of a thin-walled nano-tubular network rather than the complete filling of the template pores. Extending the annealing times of these tubular networks up to 48 h at 550 °C did not produce anatase TiO_2.

To determine the relative influence of the chlorine impurities and the thin film confinement on the suppression in crystallisation, thin TiO_2 films were deposited with varied film thicknesses, on different substrates and at different temperatures. The film thickness range was chosen as 4 nm to 20 nm so as to include thicknesses from the estimated wall thickness of the nano-tubular network to a thickness which is expected to crystallise. The substrates chosen were bare silicon and silicon coated with an approximately 50 nm thin film of the polystyrene used in the block copolymer template. This was done to emulate growth on the template surface. The polymer coated sub-

strates were exposed to the ozone treatment and thermal annealing. The deposition temperatures were chosen as 100 °C and 150 °C. These temperatures correspond to the normal temperature used for deposition in the porous templates and the highest temperature for which TiO_2 depositions are fully amorphous [138]. The deposition of the TiO_2 on the polymer coated silicon substrates was preceded by a single ZnO seed layer. A summary of the parameters above is given in Table 7.5. All samples were calcinated at 550 °C in an oxygen atmosphere for 48 h to maximise the probability of crystallisation.

Thicknesses (nm)	Substrates	Temperatures (°C)	Technique
4/6/8	Si/PS coated Si	100/150	GI-WAXS
10/20	Si	100/150	WAXS

Table 7.5: Deposition parameters of TiO_2 for thin films crystallisation measurements.

Grazing incident wide-angle x-ray scattering is used for TiO_2 films thinner than 10 nm since they do not provide sufficient intensity for standard wide-angle x-ray scattering. Examples of the two-dimensional scattering patterns as well as the one-dimensional intensity profiles are shown in Figure 7.24.

An incident angle of 0.4° was chosen since at this angle the scattering is dominated by the structure of thin TiO_2 films. Figure 7.24C displays an example of a film where a pronounced Bragg reflection is present at a position corresponding to the crystalline signature of TiO_x. An equivalent film where the crystalline peak is absent is shown in Figure 7.24B. The scattering ring in Figure 7.24C is indicative of a powder-like crystallisation where a preferential face-on direction is found, as shown by the presence of a high intensity halo. A face-on orientation would be expected from crystallisation in thin TiO_2 films where crystal growth preferentially takes place in the plane of the film.

The 1D profiles shown in Figure 7.24D are extracted along the semi-circular path centred on the beamstop as shown in Figure 7.24A and integrated radially between the two white lines. The summary of the results is shown in Table 7.6.

Thickness (nm)	Si		PS coated Si	
	100 °C	150 °C	100 °C	150 °C
4	X	X	X	X
6	X	X	O	o
8	X	X	O	o
10	O	o	n/a	n/a
20	O	o	n/a	n/a

Table 7.6: Results from crystallisation experiments. n/a: no experiment performed, X: no crystallisation seen, o: crystallisation, small crystallites, O: crystallisation, large crystallites.

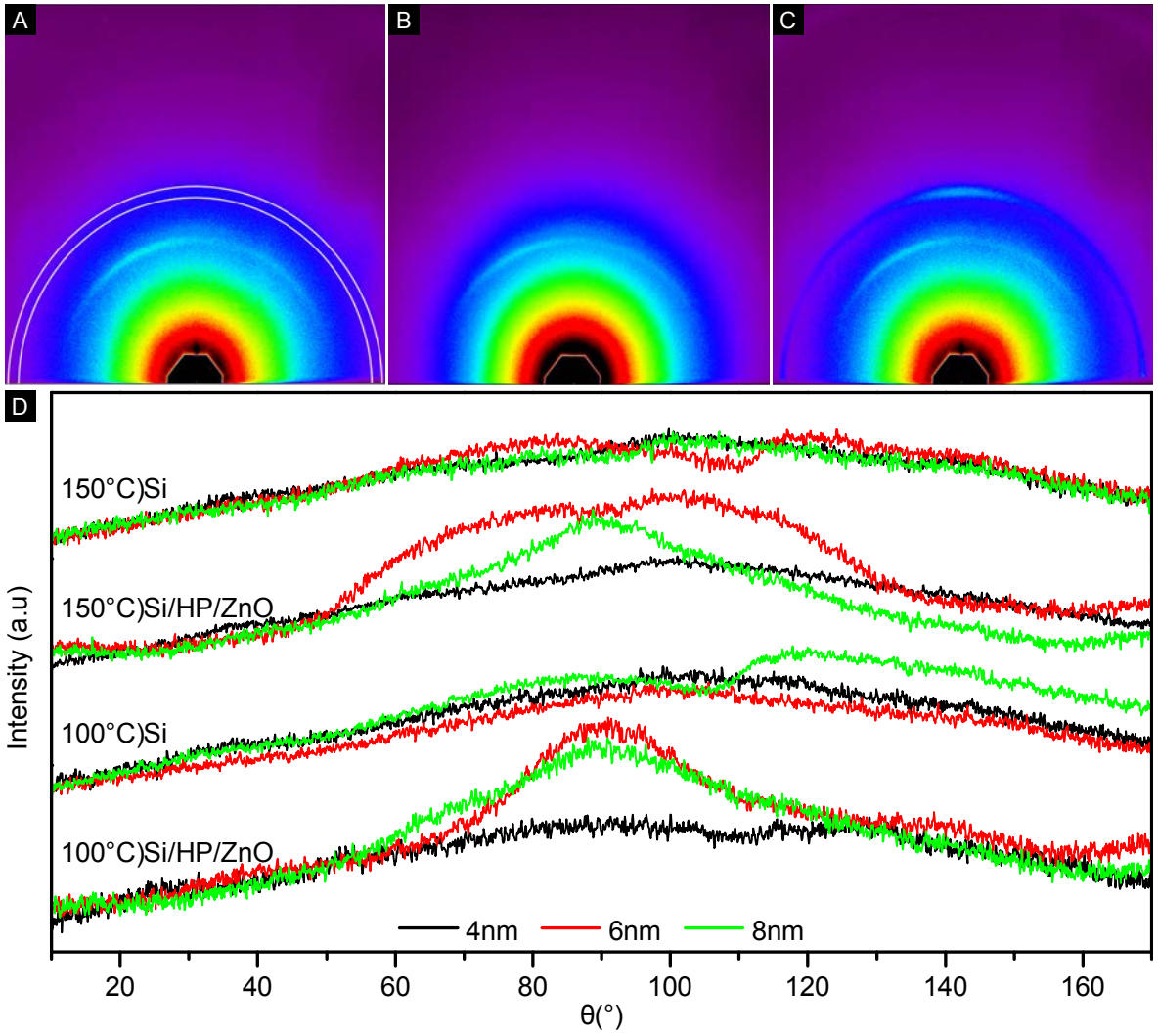

Figure 7.24: GI-WAXS spectra of TiO_2 thin film crystallisation. **(A)** - **(C)** Two-dimensional scattering patterns. **(A)** The white lines are the integration limits for the one-dimensional profiles in **D**. **(B)** A sample where no crystallisation peak is seen. **(C)** A sample with a pronounced crystallisation peak. **(D)** One-dimensional scattering profiles.

For a film thickness of 4 nm (black lines in Figure 7.24D) no crystallisation peaks are seen regardless of substrate or deposition temperature. For intermediate thicknesses of 6 nm and 8 nm shown by the red and green lines respectively in Figure 7.24D, no crystallisation peaks are observed for TiO_2 films on silicon substrates regardless of deposition temperature. For TiO_2 depositions on the polystyrene coated silicon substrates, well-pronounced crystallisation peaks are observed at both deposition temperatures. The lack of crystallisation on a solid substrate and the observed crystallisation on a soft substrate can be explained by the increased compliance of the softer substrate which allows for higher mobility in the amorphous film and a higher probability for crystallisation nuclei to form. Although crystallisation peaks appear for at both deposition temperatures, the peaks for both the 6 nm and 8 nm TiO_2 films deposited

at 100 °C have a smaller full width at half maximum (FWHM) which is indicative of larger crystals. The presence of larger crystals points towards a lower initial density of crystallisation nuclei which is in agreement with reports of inhibited crystallisation due to chlorine impurities.

For the 10 nm and 20 nm TiO_2 films deposited on a silicon substrate, and measured using WAXS, more pronounced crystallisation peaks with a smaller FWHM are seen for depositions at 100 °C (Figure 7.25a,b). This result falls in line with the GI-WAXS data which indicates a lower density of crystallisation nuclei at a lower deposition temperature where a higher concentration of chlorine contaminants are present (Section 4.7.2). This would suggest that for thin ALD grown TiO_2 films, an increased amount of chlorine leads to a suppression of the formation of crystallisation nuclei and the formation of larger crystalline domains.

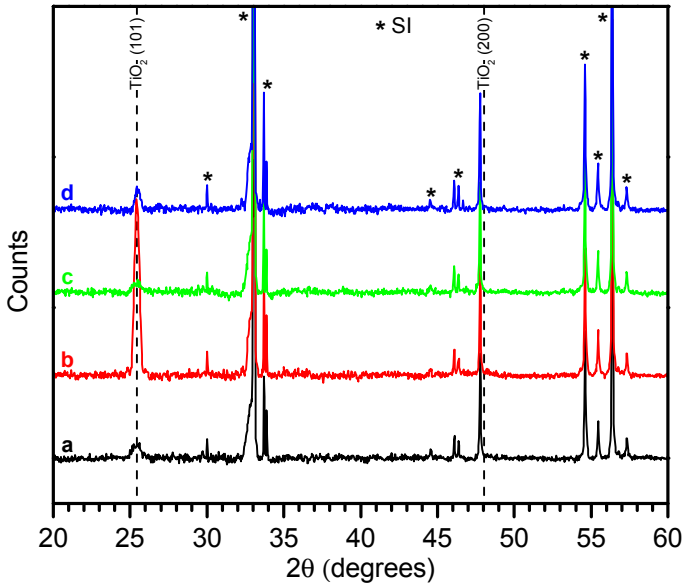

Figure 7.25: XRD spectra of TiO_2 thin films deposited on a silicon substrate. **(a)** 10 nm TiO_2 deposited at 100 °C. **(b)** 20 nm TiO_2 deposited at 100 °C. **(c)** 10 nm TiO_2 deposited at 150 °C. **(d)** 20 nm TiO_2 deposited at 150 °C.

Based on the results above in which no crystallisation is seen for 4 nm TiO_2 films, we believe that the main contribution to the lack of crystallinity in the gyroid-structured TiO_2 replicas is the confinement caused by the thin-walled nano-tube. The added confinement of the high curvature nano-tube makes the probability of crystallisation even lower compared to the flat film results above. The incorporation of a higher concentration of chlorine impurities at 100 °C suppresses the formation of crystallisation nuclei and leads to larger crystalline domains when the film is thick enough to support crystallisation. The incorporation of chlorine can also have a detrimental effect on the DSSC device performance, however the influence of the concentration of chlorine impurities was outside the scope of this study.

7.3.5 ALD growth in large pore size templates

Given that the main explanation for the lack of crystallinity in the PS192 TiO_2 replicas is the formation of a thin-walled nano-tubular network (Section 7.3.3), the obvious solution is to use a larger pore size template which will create a network with thicker tube walls.

The template used in this study is a cylinder forming block copolymer (PS128) which is thermally annealed to achieve a worm-like rather than close-packed morphology described in Section 5.6.2. The template is shown in Figure 7.26A.

Once voided, the template displays a fully porous free-surface interface, as shown in Figure 7.26B, which lends itself well to infiltration and replication using ALD. The deposition of TiO_2 is carried out using a two-step protocol (Table 7.4) at 100 °C and 150 °C to minimise chlorine contamination.

The TiO_2 replica after calcination is shown in Figure 7.26C. ALD has successfully replicated the polystyrene template and the TiO_2 network is fully self-supporting. Figure 7.26D shows the top of the sample after ICP etching of the non-porous TiO_2 compact layer and calcination at 550 °C in O_2 for 12 h. The sample shows very little collapse of the TiO_2 struts, which allows for a successful infiltration of the solid-state hole-conducting material.

The wall thickness of these nano-tubular networks is approximately 8 nm to 9 nm and this increased thickness allows the networks to crystallise upon calcination as shown in Figure 7.19e. Conducting the deposition at 150 °C rather than 100 °Cleads to a lower amount of chlorine contaminations, with a chlorine fraction before and after immersion in HCl/MeOH and calcination of 8 % and 0.1 % respectively as measured by EDX. These thicker walled nano-tubular networks were subsequently used in ssDSSC devices as described in the next section.

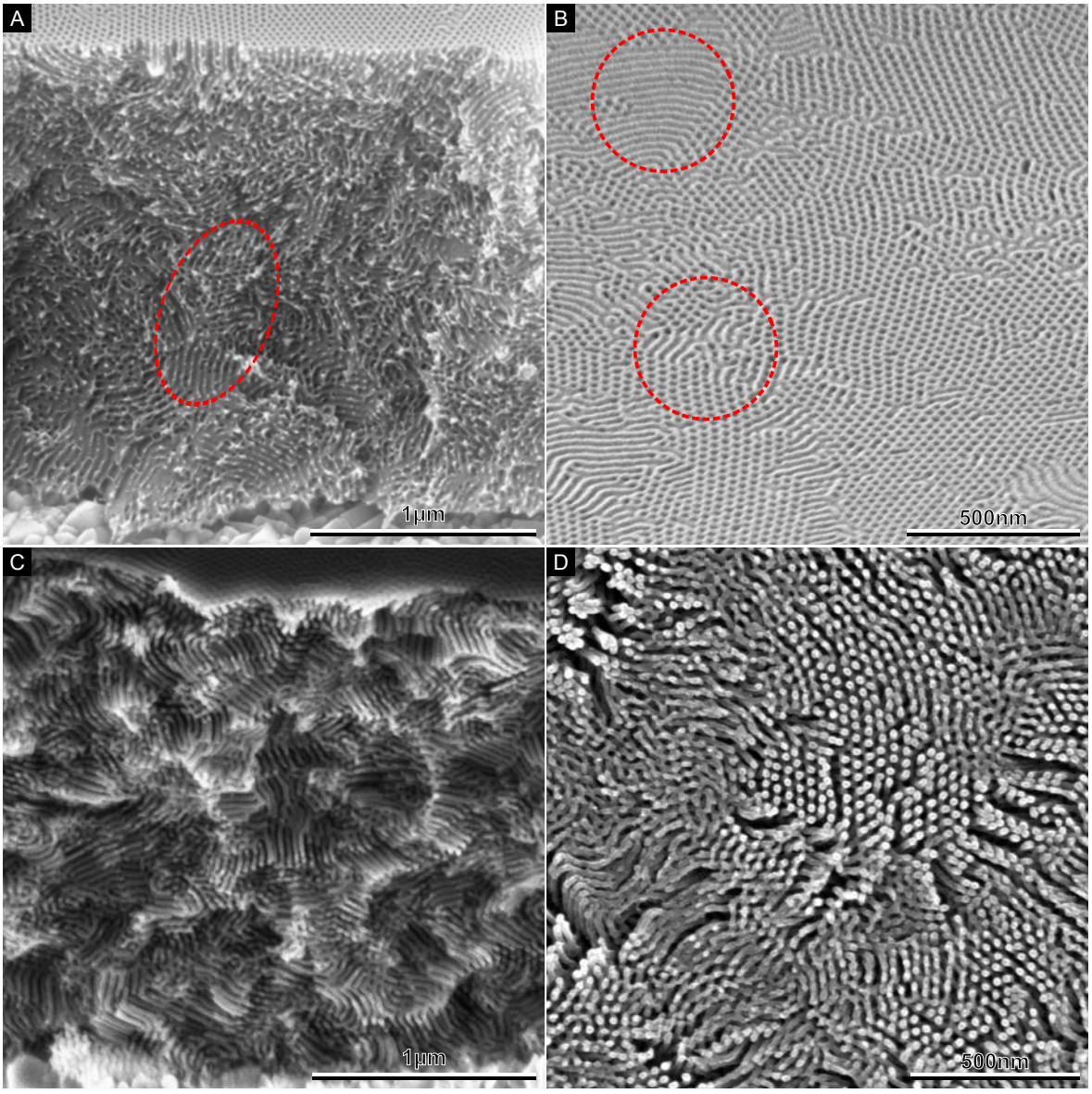

Figure 7.26: TiO_2 deposition in a cylinder forming polystyrene template with a pore diameter of 21 nm. **(A)** Cross-sectional view of a voided thin film template. The network is a non-equilibrium worm-like cylindrical morphology. The encircled area displays a region where the equilibrium close-packed cylindrical morphology can be seen end-on or side-on. **(B)** Free surface of the voided template showing a close-packed arrangement of cylinders perpendicular to the surface with intermittent non-porous regions of lying cylinders parallel to the surface (encircled in red). **(C)** Cross-sectional view of TiO_2 replica of the template in **A** after calcination at 550 °C. **(D)** Top-view of the TiO_2 replica after calcination showing that porosity of the free surface is maintained.

7.3.6 DSSC using ALD grown TiO_2 electrodes

As one of the main goals of this study is to fabricate TiO_2 electrodes for dye-sensitised solar cells, the best ALD processing parameters and template modifications are used to produce both liquid electrolyte and solid-state electrolyte DSSC devices. The device fabrication is described in Section 5.4.1.

Given the small pore size of the TiO_2 replica of the PS192, liquid electrolyte devices were fabricated for ALD grown titania in both the plasma-modified and ozone-treated and thermally annealed templates. Devices fabricated using the plasma etched template with an electrode thickness of 700 nm display a maximum power conversion of 0.5 % (V_{OC} = 0.69 V, I_{SC} = 1.15 A cm^{-2}, ff = 63%) (Figure 7.27A). Devices employing an approximately 600 nm thick TiO_2 electrode fabricated using the ozone-treated template display a power conversion of approximately 0.1 % (V_{OC} = 0.87 V, I_{SC} = 0.27 A cm^{-2}, ff = 42%) (Figure 7.27A).

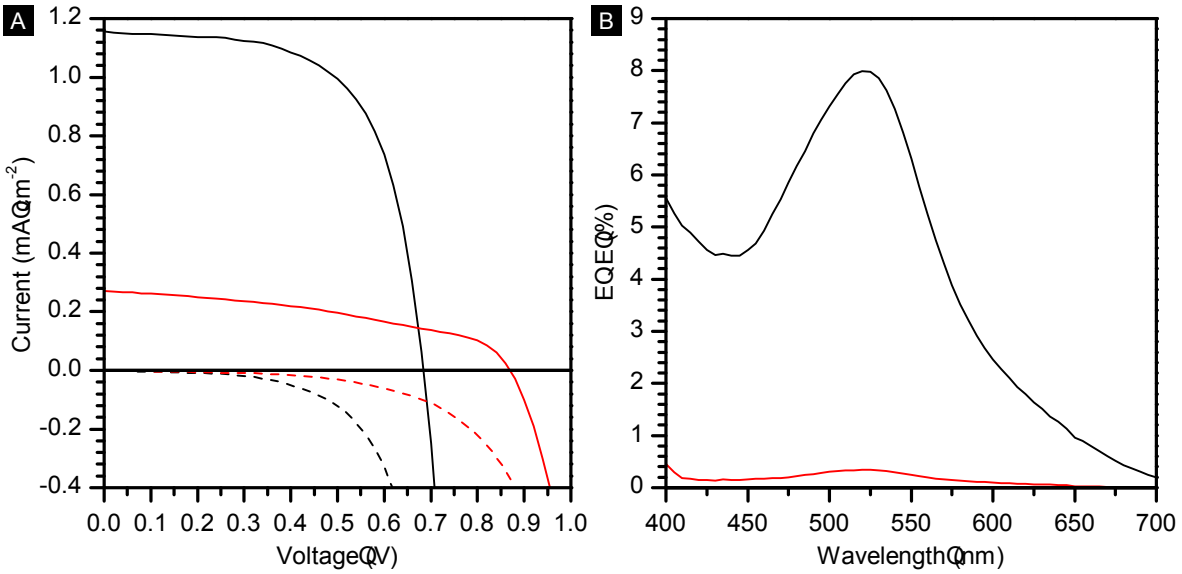

Figure 7.27: Liquid electrolyte DSSC devices fabricated from TiO_2 deposits in plasma-treated (black traces) and ozone-treated (red traces) templates. **(A)** Illuminated (solid) and dark (dashed) I-V curves. **(B)** External quantum efficiency of the devices.

The increased open-circuit voltage of the latter devices is attributed to the single ZnO cycle used to nucleate the ALD growth of TiO_2. As discussed in Section 4.4.1, it has been shown that a thin coating of a wide band gap material, such as Al_2O_3, on the surface of titania DSSCs can increase the open-circuit voltage. However care has to be taken as this coating can also lower the short-circuit current, potentially explaining the low I_{SC} and power conversion efficiencies seen in the latter devices. Devices fabricated using both polystyrene modification routes display very low power conversion efficiencies compared to nano-particle devices of equivalent thicknesses, and this is thought to be due to the lack of crystallinity of the titania replicas. The higher

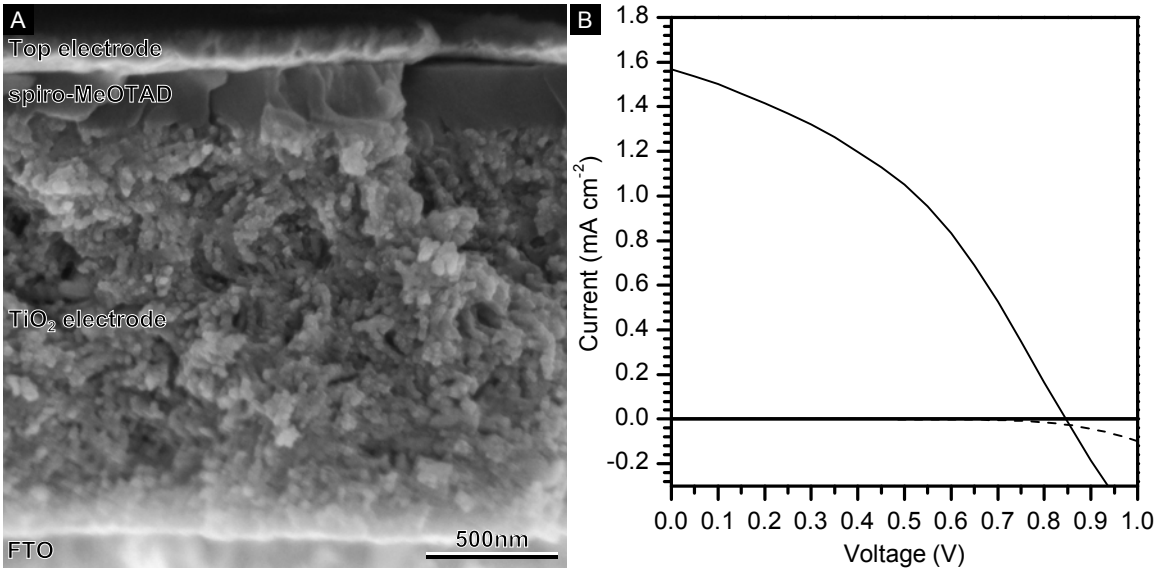

Figure 7.28: Solid-state DSSC fabricated from TiO_2 ALD replica of large pore-size template. **(A)** Cross-section of assembled solid-state electrolyte device. The partial infiltration of the spiro-MeOTAD leaves voids in the TiO_2 layer which are clearly visible. **(B)** Illuminated (solid) and dark (dashed) I-V curves.

efficiency seen in the devices fabricated from the plasma-treated templates compared to those fabricated from the ozone-treated templates is thought to be due to the higher quality and possibly purity of the deposited TiO_2, even though both replicas appear very similar in SEM images.

Devices using titania electrodes deposited in the large pore size template, as described in Section 7.3.5 were assembled using a hole-conducting Spiro-MeOTAD electrolyte. An SEM cross-sectional image of one device is shown in Figure 7.28A.

Devices with an electrode thickness of 1.3 µm displayed a power conversion efficiency of 0.53 % with an open-circuit voltage, short-circuit current and fill-factor of $V_{OC} = 0.85\,V$, $I_{SC} = 1.6\,A\,cm^{-2}$, ff = 40%) respectively (Figure 7.28B). Even though the TiO_2 in these devices is crystalline, the devices fail to perform better than devices fabricated from plasma treated PS192 templates. One possible explanation for the lack of performance is the intrinsically lower performance of solid-state electrolyte devices compared to liquid electrolyte devices. However we believe that the main reason for the poor performance is the low number of devices produced and the absence of optimisation due to time-constraints. For example Figure 7.28A shows an incomplete infiltration of the spiro-MeOTAD in the TiO_2 network which could lower device performance. Further experiments are on-going to optimise the performance of these devices.

7.4 Conclusion

In this chapter we have demonstrated a novel gas phase surface modification technique which introduces functional groups onto the surface of otherwise chemically inert polystyrene by a combination of ozone exposure and thermal decomposition of the ozonite species formed. After the treatment is complete, aldehyde and carboxyl groups are introduced along the polymer backbone. The various reaction steps are confirmed by FTIR. The technique is not limited to polystyrene but is applicable to any other polymers containing carbon-carbon double bonds. The modification takes place in the gas phase which means that it is appropriate for low molecular weight polymers that normally suffer from the strong polymer chain fragmentation associated with other liquid modification protocols such as nitration sulphination or thin polymer films on solid substrates which suffer from cracking and de-lamination. The technique also overcomes difficulties inherent to surface modification of high-aspect-ratio, small pore size polymer thin films or polymer films with non-line of sight regions not accessible by plasma modification techniques.

We have successfully modified the surface of voided polystyrene block copolymer templates with the double-gyroid morphology and a bicontinuous cylindrical morphology. The templates have pore sizes of 10.5 nm and 21 nm and aspect ratios of more than 500:1 and 250:1 respectively. The surface treatment allows atomic layer deposition to be successfully and densely nucleated inside the polystyrene templates. The modified porous polymeric templates were replicated using ALD Al_2O_3, TiO_2 and ZnO and both the bicontinuous cylindrical and the highly ordered gyroid morphologies were maintained after template removal for film thicknesses up to 3 µm. Amorphous TiO_2 deposited in the 10.5 nm gyroid template has a suppressed crystallisation due to thin film confinement whereas the deposition in the 21 nm bicontinuous cylindrical template forms anatase titania upon annealing. This suppression of crystallisation below a deposition thickness of approximately 4 nm imposes a lower bound on the template pore size for the replication using ALD grown crystalline TiO_2. We have further successfully fabricated functioning dye-sensitised solar cells from the ALD grown TiO_2 scaffolds.

8 ALD in photovoltaic applications

This chapter will detail two projects which are still on-going. The first part will cover the installation of an H_2S source, and associated safety aspects, to an existing ALD reactor in order to allow the deposition of metal sulphides. Zinc sulphide is used as a test material to determine the success of the installation. The second part will cover the use of ALD to deposit ultra-thin TiO_2 compact layers for solid-state electrolyte dye-sensitised solar cells.

8.1 ALD using H_2S

Metal oxides constitute the majority of all materials deposited by ALD, but over the last decade there has been increasing interest in the deposition of metal sulphides. For example indium sulphide has been explored as a cadmium-free alternative for barrier layers in CIGS solar cells [310–312]. Copper sulphides have also been deposited using ALD and have applications in photovoltaics, as has antimony sulphide (Sb_2S_3) [129] which was recently incorporated into hybrid solar cells using ALD [114]. The original precursor for the deposition of metal sulphides was elemental sulphur [90, 313] but it has since been replaced by hydrogen sulphide (H_2S).

8.1.1 Motivation

The motivation for introducing a setup to use H_2S with our ALD system, stems from a publication by Grätzel *et al.* [129] in which they demonstrate the use of chemical bath deposition to deposit thin Sb_2S_3 layers on TiO_2 mesoporous scaffolds. The Sb_2S_3 acts as a thin film absorber, and photovoltaic devices using these TiO_2/Sb_2S_3 electrodes together with P3HT showed an impressive efficiency of 5 %. A second motivation is the interesting optical properties seen in certain sulphide compounds such as quantum confinement effects in PbS [314].

During the process of acquiring and installing the H_2S system, work by Bachman *et al.* on the use of ALD Sb_2S_3 in mesoporous TiO_2 devices was published [114]. This publication covers the main aims of this part of the thesis, and as such my own efforts were refocused onto other projects once the installation and testing were complete. Despite this, the successful installation has enabled recent depositions of Sb_2S_3 and will be an asset to the future work of the group.

This section will describe the design of the H_2S process line which includes an H_2S gas cabinet with an Emergency Shutoff Valve and an H_2S scrubber as well as a set of H_2S alarms. The hazards of H_2S as well as potential incompatibilities between the ALD components and H_2S were taken into account during the design. Procedures to safely

vent the ALD were also formulated. Initial results from the deposition of stoichiometric ZnS will be presented.

8.1.2 H_2S hazards

The major drawback of the use of H_2S in an ALD reactor is that it requires special attention to safety protocols due the fact that it is flammable, corrosive and highly toxic. The inhalation of H_2S can lead to damage to the repository tract and lungs, the central nervous system and may even cause death depending on the exposure level. The allowed short and long term exposure limits as specified by the HSE are 5 ppm and 10 ppm respectively [315]. Above a concentration of 100 ppm H_2S is considered dangerous to life and health [315]. The gas has a characteristic smell of 'rotten eggs' but the human sense of smell suffers from olfactory fatigue at higher concentration [316–318] and as such the odour itself is not a sufficient nor acceptable warning system for humans of potentially harmful exposure levels.

Besides the potential danger to human health via inhalation, H_2S is also highly flammable. The lower and upper explosive limits (LEL and UEL) are 4.3 % and 46 % respectively. Furthermore the autoignition temperature of pure H_2S is 232 °C which lies within the temperature range of common ALD deposition temperatures. Further the by-product of the H_2S/water reaction is acidic which compounds the safety issues since this can compromise the integrity of the sealed ALD reactor. To minimise the risk from both the toxicity and flammability hazards, a 3.5 % concentration of H_2S in a N_2 ballast is used in this study.

8.1.3 ALD reactor

A large fraction of the ALD reactors which are capable of using H_2S are custom-built rather than obtained commercially and the safety issues of H_2S have in these cases been taken into account throughout the design of the entire reactor. In this work H_2S was added as an additional precursor onto a commercially obtained Beneq TFS200 research reactor. Besides liquid precursors, the TFS200 comes equipped with a number of process lines for gaseous precursors, one of which was used for the addition of the H_2S process line. Information regarding the compatibility between H_2S and the components in the reactor was acquired from Beneq. For the installation of H_2S in a custom-built ALD reactor see the the excellent review by Dashupta *et al.* [319]

Special care has to be taken when using metal components with H_2S. Above process temperatures of 260 °C, the corrosion of carbon steel due to sulphidation of the metal becomes an issue [320] Because of this, low-carbon and annealed steel is recommended for applications which use H_2S at elevated temperatures. All of the wetted metal components in our Beneq reactor are 316L stainless steel which has excellent corrosion resistance. Fittings for the 1/4" steel tubing are Swagelok VCR® stainless steel gasket face seals which are designed for high vacuum systems.

Hydrogen sulphide is also know to interact with the elastomer materials used in O-rings present throughout the reactor, from the main chamber lid to the vacuum line and the pump. The O-rings used in the reactor are Viton®, as is the case in most ALD reactors due to its relatively good corrosion resistance and temperature stability. However H_2S is known to cause severe swelling in Viton and is normally not recommended for use. This swelling is reported for 100% H_2S and for extended exposure times. Despite the swelling issue, the use of Viton O-rings was considered low risk due to the low concentration of the H_2S source (3.5 % in N^2) in combination with the high ratio between the carrier gas flow and the H_2S flow (10:1) which reduces the concentration further, and the sequential nature of the ALD reaction which lowers the total exposure time. The integrity of the main O-rings in the reactor are monitored on a regular basis to determine the influence of the H_2S exposure.

Prior to use, the ALD reactor fitted with the additional gas line, gas cabinet, and H_2S scrubber, was leak tested in two separate ways. First all of the valves between the H_2S cylinder and the reactor were opened and the system pumped to its lowest possible base pressure overnight. The vacuum pump valve was then closed and the reactor pressure monitored to detect any changes in the base pressure which would indicate a leak. A total pressure change of less than 0.1 mbar was measured over 1 h which correspond to a fully sealed system without any leaks. The system was also pressurised to 2 bar with helium and a helium 'sniffer' was used to detect any leaks around all seals. This procedure will also be repeated after for example pump maintenance to assure the integrity of the full system.

A schematic of the reactor, the gas cabinet and process line (Section 8.1.4), the H_2S scrubber (Section 8.1.5) and the alarm system (Section 8.1.6) is shown in Figure 8.1.

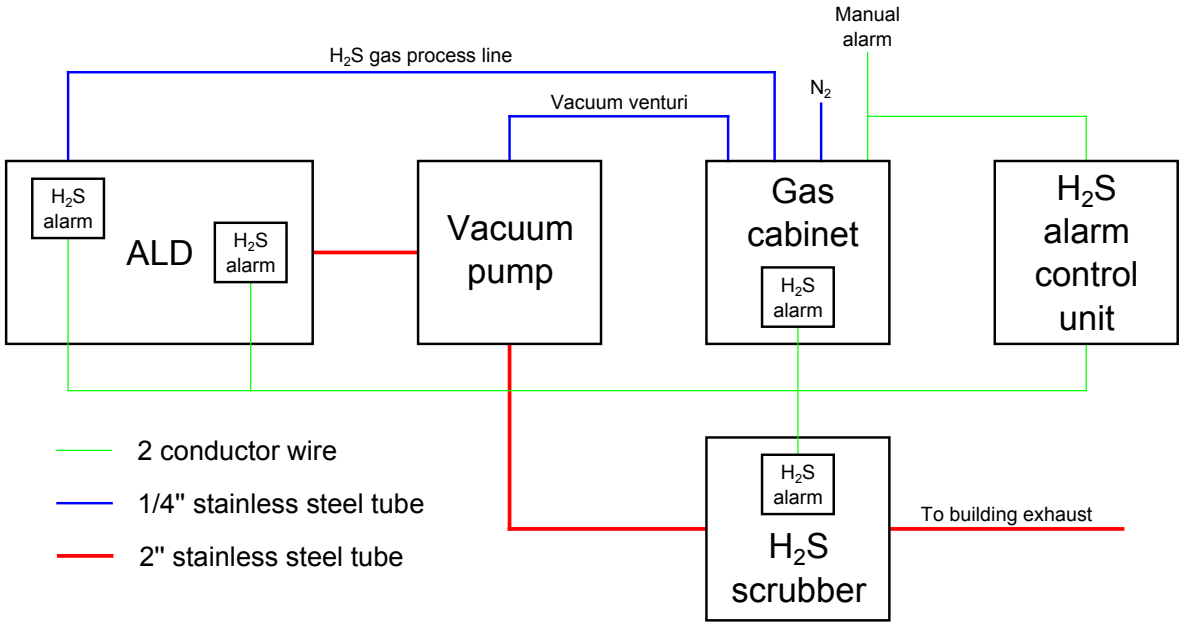

Figure 8.1: Schematic of the H_2S installation. The ALD reactor is upgraded with a gas process line as well as by the addition of an H_2S gas cabinet and scrubber and an H_2S alarm system with a detection threshold of 5 ppm.

8.1.4 H_2S gas cabinet and process line

The H_2S was purchased from BOC Speciality Gases in size AY cylinders (200 bar, 15 L water capacity). To minimise the risk associated with cylinder changeovers and to allow for an effective and safe purging of the H_2S gas line, a commercial gas cabinet from Spectron Gas Control Systems Ltd was installed (Figure 8.2A).

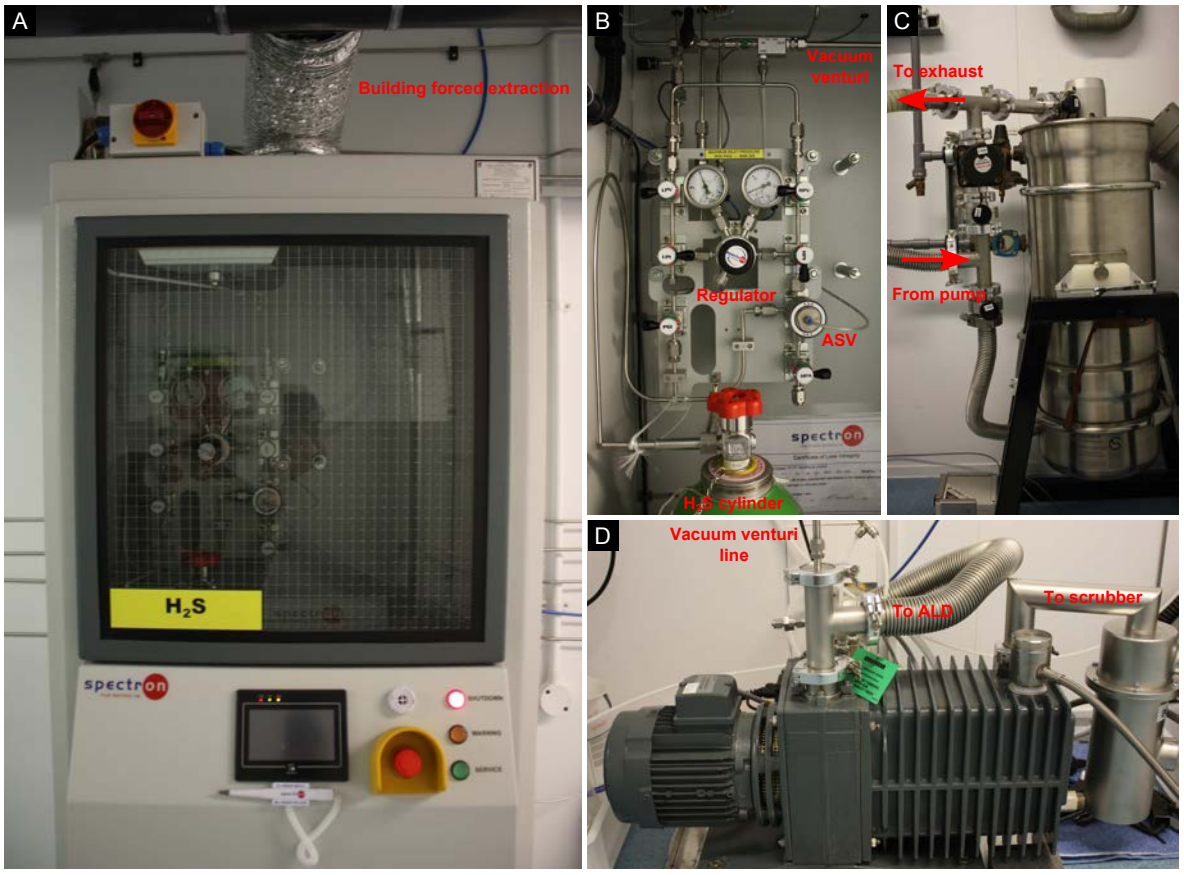

Figure 8.2: Components of the H_2S installation. **(A)** Forced extraction H_2S gas cabinet. **(B)** H_2S gas panel with gas cylinder, regulator and Automatic Shutoff Valve. **(C)** H_2S scrubber with by-pass line. **(D)** Vacuum pump with added vacuum venturi line.

The gas cabinet is connected to the building's forced extraction and the cabinet is under negative pressure during normal operation. The gas cabinet comes equipped with an automatic shutoff valve (ASV) as well as an H_2S-rated regulator and a vacuum venturi purging line (Figure 8.2B). Additional safety features include a regulator over-pressure gauge to detect regulator faults, an over-flow gauge which limits the total gas flow to 100 SCCM and a flow gauge which detects issues with the forced extraction. All of these gauges as well as the H_2S alarms in Section 8.1.6 can trigger the ASV. In addition to the pre-installed panel, an H_2S compatible needle valve was installed to allow the flow to be reduced to below 10 SCCM.

The H_2S gas line from the cabinet to the reactor consisted of Swagelok® 316L stainless

steel flexible tubing lined with PTFE to improve its mechanical integrity. To minimise the risk of a leak, the gas line only has two connection points, at the gas cabinet and at the ALD. The H_2S operating pressure in the line was kept below atmospheric pressure, at 0.6 mbar. This was done to assure a flow of air into the line rather than H_2S out of it in case of a leak.

8.1.5 Purging procedures and H_2S removal

To prevent H_2S from entering into the building's exhaust line two additions were made on the reactor vacuum line. Firstly a gas ballast was connected to the pump to further dilute the H_2S. Secondly an H_2S scrubber was installed between the vacuum pump and the building's exhaust line (Figure 8.2C,D). The CLEANSORB® scrubber was purchased from CS Clean Systems AG. The scrubber can reduce 100% H_2S to below 5 ppm. Based on the initial H_2S concentration of 3.5 % in a nitrogen ballast, the ratio between carrier gas flow and H_2S flow, the vacuum pump gas ballast and the H_2S pulse and purge lengths, the time averaged H_2S concentration before the scrubber was estimated to be below 500 ppm.

Prior to venting the reactor, the H_2S gas line and the reactor are purged using an extended purging protocol. The gas line and the cabinet gas panel are purged by alternately pressurising them with N_2 and evacuating them with the vacuum venturi purge line. This procedure is repeated 30 times. The reactor is purged by increasing the pressure to 700 mbar to dilute and remove any residual H_2S and then evacuating it to below 5 mbar. This process is repeated 5 times.

8.1.6 Additional safety features

To further lower the risks associated with the use of H_2S, an alarm system was also installed. Four electrochemical H_2S sensors together with a 4 channel control unit were purchased from Frontline Safety UK Ltd. The alarm set point was chosen to be 5 ppm in accordance with the maximum long term exposure limit. Upon activation, the control unit will trigger the ASV as well as sounding a visible and audible alarm. An emergency stop button was also implemented to activate the alarm manually. To prevent any unintentional introduction of H_2S into the reactor, an extra manual on/off valve was introduced between the gas line and the ALD. The four alarms were placed at (Figure 8.1): 1) below the manual valve described above; 2) below the main reactor chamber; 3) inside the gas cabinet; and 4) below the H_2S scrubber.

After venting the reactor but before opening the main chamber lid fully, hand-held H_2S sensors are used to measure the H_2S concentration in the chamber to determine if the purge was successful.

8.1.7 ZnS depositions

To determine if the relatively low concentration of H_2S used (3.5 % in N_2) was sufficient for uniform depositions, zinc sulphide was deposited from diethyl zinc (95 % supplied from Sigma Aldrich) and H_2S (3.5 % in N_2 supplied from BOC) at 120 °C. A cycle scheme used to deposit 500 cycles of ZnS is shown in Table 8.1. The film thickness was measured using spectroscopic ellipsometry and found to be 34 nm which corresponds to a deposition rate of 0.68 Å per cycle. The refractive index at 632.8 nm was measured to be 2.52. The deposition rate is lower than reported in literature possibly due to non-saturated dose times [321]. The refractive index agrees with literature values of ZnS [322]. EDX and XRD (Figure 8.3A,B) were also used to determine stoichiometry and crystallinity of the ZnS deposit.

	Precursor	Pulse (s)	Purge (s)
Step 1	DEZ	0.5	5
Step 2	H_2S	1	5

Table 8.1: Pulsing scheme for depositions of ZnS using diethylzinc and hydrogen sulphide.

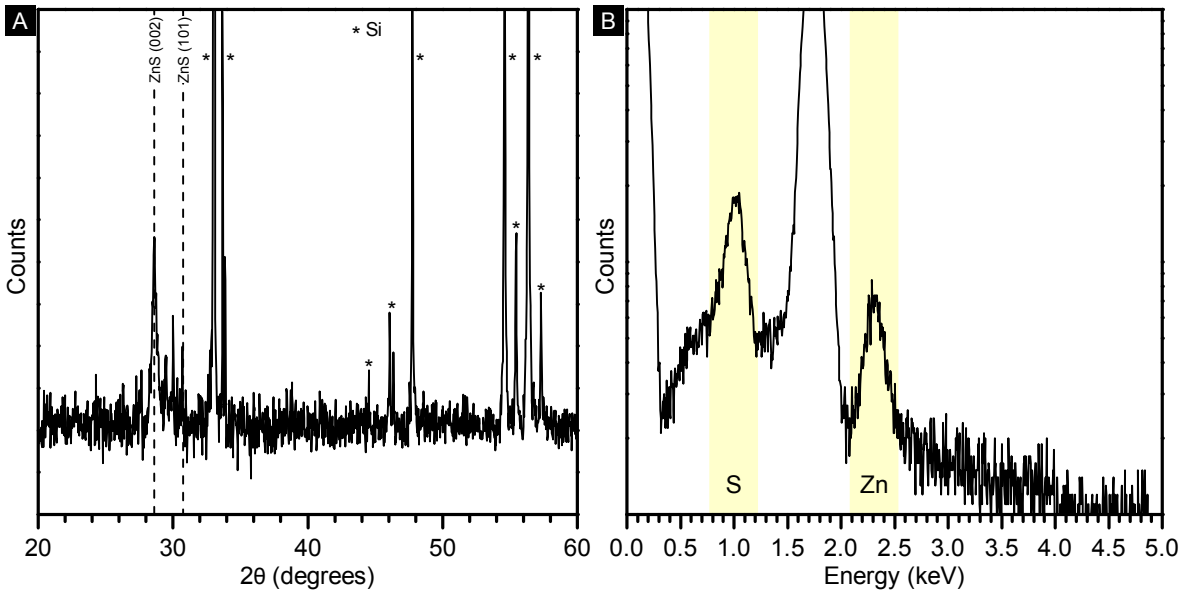

Figure 8.3: ZnS deposited using DEZ and H_2S. **A)** XRD spectrum. **B)** EDX spectrum.

EDX measurements showed a stoichiometry of $Zn_{0.49}S_{0.51}$ with no carbon contaminants present. A small amount of oxygen was measured but this is attributed to the native oxide layer on the silicon substrate. XRD showed a wurtzite structure with the preferential orientation being the (002) direction. This demonstrates that the non-flammable mixture of 3.5 % H_2S in a N_2 ballast is sufficient for the successful reaction with the ligands in the diethyl zinc. Further tests, not included here because of time constraints, have shown that the H_2S gas mixture can also be used to deposit Sb_2S_3.

8.1.8 Conclusion

Hydrogen sulphide was successfully added as a secondary precursor to a commercial Beneq ALD reactor. The hazards and risks associated with the use of H_2S were analysed and appropriate component and safety measures were chosen and implemented to minimise the risk. A dedicated H_2S gas cabinet was installed which houses a size AY cylinder of 3.5 % H_2S in a N_2 ballast. The cabinet contains an automatic shutoff valve connected to the gas cylinder which can be triggered either manually or by a set of H_2S alarms. The H_2S alarm sensors are positioned in appropriate key positions by the ALD, and the alarm set point was chosen to be 5 ppm. To prevent H_2S from entering the building's exhaust line, an H_2S solid-state scrubber was installed after the reactor's vacuum pump, which lowers the H_2S concentration to below 5 ppm which is the long term exposure limit.

To determine if a concentration of 3.5 % H_2S in N_2 was sufficient for ALD depositions, ZnS was successfully deposited from diethyl zinc and H_2S. The deposited ZnS displayed the expected stoichiometry and crystal structure.

8.2 ALD deposited TiO_2 compact layers

8.2.1 Introduction

The following section of the chapter describes the use of atomic layer deposition to deposit ultra-thin TiO_2 compact layers.

As described in Section 2.4, the dye-sensitised solar cell consists of five constituent components, the mesoporous metal oxide scaffold, the monolayer of absorbed dye, the liquid or solid-state electrolyte, a platinum-coated counter electrode and the compact or blocking layer covering the substrate (normally FTO-coated glass). Up until the last decade the majority of the research efforts towards more efficient solar cells have been focused on the first four of these areas. However it has been shown that parameters such as compact layer thickness, choice of material and crystallinity can significantly alter the device performance.

There are four main interfaces in a DSSC which can lower the conversion efficiencies: the mesoporous TiO_2/dye molecule interface, the dye molecule/electrolyte interface, the Pt-coated counter electrode/electrolyte interface and the mesoporous TiO_2/FTO interface. To achieve high power conversion efficiencies a unidirectional flow of charge across all of these interfaces is required. Charge transport in the opposite direction or charge recombination processes occur mainly at the mesoporous TiO_2/dye molecule and FTO/mesoporous TiO_2 interfaces. The recombination at the mesoporous TiO_2/dye molecule interface is considered insignificant for the device performance since the injection of generated photoelectrons is considerably faster than charge transfer in the opposite direction, i.e. from the mesoporous TiO_2 to the dye molecules [323, 324]. However at the FTO/mesoporous TiO_2 interface, charge recombination can take place due to the physical contact between the surface of the FTO and the electrolyte. This is caused by the porous structure of the TiO_2 which allows the electrolyte to percolate to the surface of the FTO. Suppression of electron leakage at the FTO/porous TiO_2 interface is thus important to improve the power conversion efficiency of dye-sensitised solar cells.

An effective method to prevent this recombination is to introduce a thin compact layer situated between the FTO and mesoporous TiO_2 film [325, 326]. A significant amount of research has been carried out on the fabrication of metal oxide layers which could act as efficient blocking layers. Metal oxides used as blocking layers include TiO_2 [327–329], ZnO [330] and Nb_2O_5 [331]. Amongst the metal oxides used, TiO_2 has been shown to be the most effective and is also the most studied material. Besides successfully preventing recombination, the use of a TiO_2 compact layer also increases the adhesion between the mesoporous titania layer and the substrate which enhances the transfer of electrons from the TiO_2 electrode to the FTO. The decrease in recombination leads to an increase in the short-circuit current and an increase in the electron density in the TiO_2 conduction

band, which in turn raises the Fermi level and increases the open-circuit voltage [329].

There are a number of existing fabrication routes for the production of TiO_2 compact layers. These include sol-gel processing [327], spray pyrolysis [326, 329], layer-by-layer processing [324], electrochemical deposition [332], dip-coating [333], various sputtering techniques such as microwave and inductively coupled plasma (ICP)-assisted DC magnetron sputtering [327, 334] and atomic layer deposition [125]. The majority of the techniques require high-temperature heat treatments (exceptions include assisted forms of DC magnetron sputtering and ALD).

The type of electrolyte and dye used affects the effectiveness of the compact layer. The traditional dye-sensitised solar cell contains a ruthenium-based dye and an iodine/iodide redox couple containing liquid electrolyte. Work by Ito *et al.* has shown that for devices containing the sensitiser bis-tetrabutylammonium cis-dithiocyanato-N,N'-bis-2,2'-bi-pyridine-4-carboxylic acid, 4'-carboxylate ruthenium(II), or N719, the introduction of a compact layer only causes a small amount of suppression of the surface charge recombination. The explanation for this observation is that the dye itself screens the electrons in the FTO from the iodine species present in the liquid electrolyte [335]. Ab initio calculations have shown that for the N719 ruthenium dye, the highest occupied molecular orbital (HOMO) is shared between the isothiocyanate ligands (NCS) and the ruthenium-containing metal centre which is indicative that the positive charge is spread out over both the metal centre and the NCS ligands [336]. The bulkiness of the ruthenium dye in combination with the strong interaction between the FTO surface and the bis-2,2'-bi-pyridine-4-carboxylic acid group causes a physical separation of the injected electrons and the iodine species in the electrolyte.

On the other hand, devices containing organic dyes, which have lately received a significant amount of attention for being environmentally friendly and cheaper to produce, necessarily require a compact metal oxide layer to reduce charge recombination losses. This fundamentally different behaviour compared to the ruthenium dyes was explained by Burke *et al.* [337] They show through FTIR studies that for the organic dye (4E)-4-{[3-(2-carboxy-ethyl)-1,1-dimethyl-1H-benzo[e]indolium-2-yl]methylene}-2-{(E)-[3-(2-carboxyethyl)-1,1-dimethyl-1,3-dihydro-2H-benzo[e]indol-2-ylidene]methyl}-3-oxocyclobut-1-en-1-olate triethylammonium salt, the dye molecules absorb with either their x or z axes parallel to the surface normal. They estimate, for absorption with the x axis parallel to the surface normal, that the maximum separation caused by the dye between the FTO and the electrolyte is less than 7 Å, which is smaller than the separation observed for the ruthenium dyes [338]. They further argue that bulkier, less planar dyes, with attachments groups along the long direction would lead to larger separation distances and improved device performance. It has further been shown by Ito *et al.* that one such bulkier dye, the indolene dye D149 from Uchida, functions well even in the absence of a TiO_2 blocking layer [339].

The type of electrolyte also affects the effectiveness of a blocking layer. In a liquid electrolyte device, the iodine/iodide redox couple has a strong over-potential at the electrolyte/FTO interface. This creates a barrier which prevents the recombination of the photo-generated charges. However, in a solid-state electrolyte device, the spiro-

MeOTAD forms an ohmic contact with the FTO which makes recombination highly probable. Thus, in the latter device, the use of a compact layer is essential to avoid recombination and short circuiting, and it thereby leads to improvements in the current output of three to four orders of magnitude.

The results by Burke *et al.* and Ito *et al.* show that the separation between the FTO and the electrolyte caused by the absorbed dye molecules improves device performance. However what is of particular importance is that this improvement occurs for very small separation distances, less than 2 nm [338]. Since this improvement is caused by just a thin layer of dye, one might expect that, similarly, the use of very thin metal oxide compact layers could also allow for such an improvement in device effectiveness.

A few studies have been reported where the performance of dye-sensitised solar cells is measured as a function of the compact layer thickness, however thicknesses were still limited to more than 20 nm [324, 326]. The primary fabrication technique suited for a comprehensive study of the device performance as a function of compact layer thickness is ALD. This is due to its ability to produce high quality and conformal films with a low pin-hole density whilst maintaining a thickness control of less than 1 Å. ALD has been used a handful of times to produce TiO_2 blocking layers with thicknesses varying from 4 nm to 35 nm [110, 340, 341].

During the process of writing this thesis a study was published by Kim *et al.* which overlaps with this work [125]. They show, for a 18 µm thick TiO_2 mesoporous film with an N719 dye and an iodine-based electrolyte, that an optimum compact layer thickness of 10 nm yields a power conversion efficiency of 8.5 % compared to 7 % with no blocking layer. However no direct comparison of efficiency was made between the ALD deposited compact layers and traditional fabrication routes such as spray pyrolysis and spin coating.

In this study we have gone outside of the scope presented by Kim *et al.* The thickness range is extended to sub-nanometre film thicknesses and the temperature to four different deposition temperatures both above and below the amorphous to crystalline transition at approximately 165 °C. The reasons for these extended thickness and temperature ranges are three-fold. Firstly deposition of both amorphous and crystalline films can affect the (re)crystallisation behaviour of the ALD films during the calcination of the mesoporous TiO_2 electrodes. Secondly, as shown in Section 7.3.4, the amount of chlorine varies with deposition temperature, and is known to affect both the crystallisation behaviour [342] and the electronic properties by acting as a dopant [304]. Thirdly, as has also been shown in (Section 7.3.4), the deposition of ultra-thin films allows for the formation of films which remain amorphous even at elevated temperatures (550 °C) and overextended periods of time (48 h).

8.2.2 Experimental methods

Materials

The chemicals and materials listed in Table 8.2 were used as received unless otherwise specified.

Chemical	Purity(%)[a]	Abbreviation
Acetonitrile, anhydrous	99.8 (SA)	–
Chlorobenzene, anhydrous	99.8 (SA)	–
D149 indolene-based organic dye	– (SA)	–
Ethanol	95 (SA)	–
Flourine-doped tin oxide (FTO) coated glass	15 Ω/□ (SR)	FTO
Gold	99.999 (KL)	–
Hydrochloric acid	37 (SA)	–
Lithium bis(trifluoromethanesulfonyl)imide	– (SA)	–
Spiro-MeOTAD hole conducting material	– (SR)	Spiro
Tert-butylpyridine	96 (SA)	–
TiO_2 paste, 18 NTR	– (DL)	–
Titanium diisopropoxide bis(acetylacetonate)	75 (SA)	TAA
Titanium tetrachloride	99 (SA)	–
Water, deionised	18 MΩ	DI water
Zinc, powder	99 (SA)	–

[a] Suppliers are given in brackets: Sigma Aldrich, SA; Solaronix, SR; Kurt Lesker, KL; Dyesol, DL.

Table 8.2: Chemicals and materials used in this part of the study.

Device fabrication

The FTO substrate was cleaned and etched according to Section 5.4.1. ALD compact layers were then deposited using $TiCl_4$ and H_2O at 120 °C, 150 °C, 200 °C and 300 °C. The range of cycles was 10, 20, 40, 60, 100, 200, 500, and 1000 which corresponds to compact layer thicknesses of approximately 0.5 nm, 1 nm, 2 nm, 3 nm, 5 nm, 10 nm, 20 nm and 50 nm assuming a deposition rate of 0.5 Å per cycle (Section 4.7.2). The deposition rate does vary with temperature and as such the exact deposition thickness was determined by ellipsometric measurement of a piece of silicon placed in the ALD reactor during depositions. Reference substrates were also fabricated according to the procedure in Section 5.4.1.

The solid-state dye-sensitised solar cells were produced according to Section 5.4.1 and Section 5.4.1. The fabricated mesoporous TiO_2 films had an approximate thickness of

1.6 µm. The ALD deposited compact layers were not calcinated prior to the assembly of the mesoporous layer.

The device characterisation was performed according to Section 5.4.3.

8.2.3 Results and discussion

Due to time constraints the results presented here are only initial findings and further work is currently being carried out to verify and extend the results of this thesis.

Figure 8.4 shows a cross-section through a typical assembled device. The TiO_2 electrode is clearly visible and the lack of porosity shows the successful infiltration of the spiro-MEOTAD solid-state hole conductor.

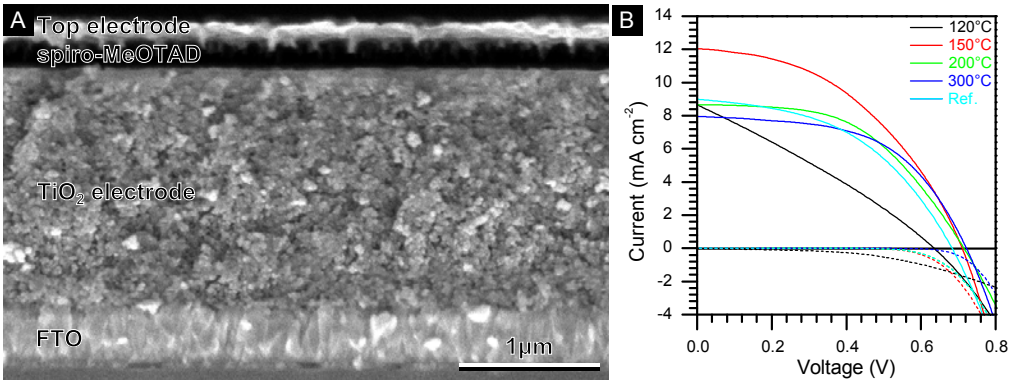

Figure 8.4: **(A)** Cross-sectional scanning electron micrograph of a solid-state electrolyte DSSC assembled on an ALD deposited TiO_2 compact layer. The lack of voids shows the complete infiltration of the spiro-MeOTAD hole conductor. **(B)** I-V traces for illuminated (solid lines) and dark (dashed lines) conditions for the best performing compact layer for each deposition temperature as well as the reference device.

The best I-V curves collected for the four deposition temperatures and the eight compact layer thicknesses are shown in Figure 8.5. From all sets of I-V curves we extracted averaged short-circuit currents, open-circuit voltages, fill-factors and power conversion efficiencies. They are shown in Figure 8.6 as a function of the compact layer thickness for the four deposition temperatures. The performance of the reference devices are shown by the dashed lines.

Neither the devices utilising the ALD compact layers nor the devices utilising the spray-pyrolysis compact layer perform as well as state-of-the-art ss-DSSC [343], which is not surprising given that these are non-optimised devices utilising standard dyes and electrolytes. However it is interesting to compare the ALD compact layer devices with the reference spray-pyrolysis ones. For thick ALD compact layers, the devices perform worse than the reference devices regardless of the deposition temperature as shown in Figure 8.6. This agrees with the results by Kim *et al.* (although care has to

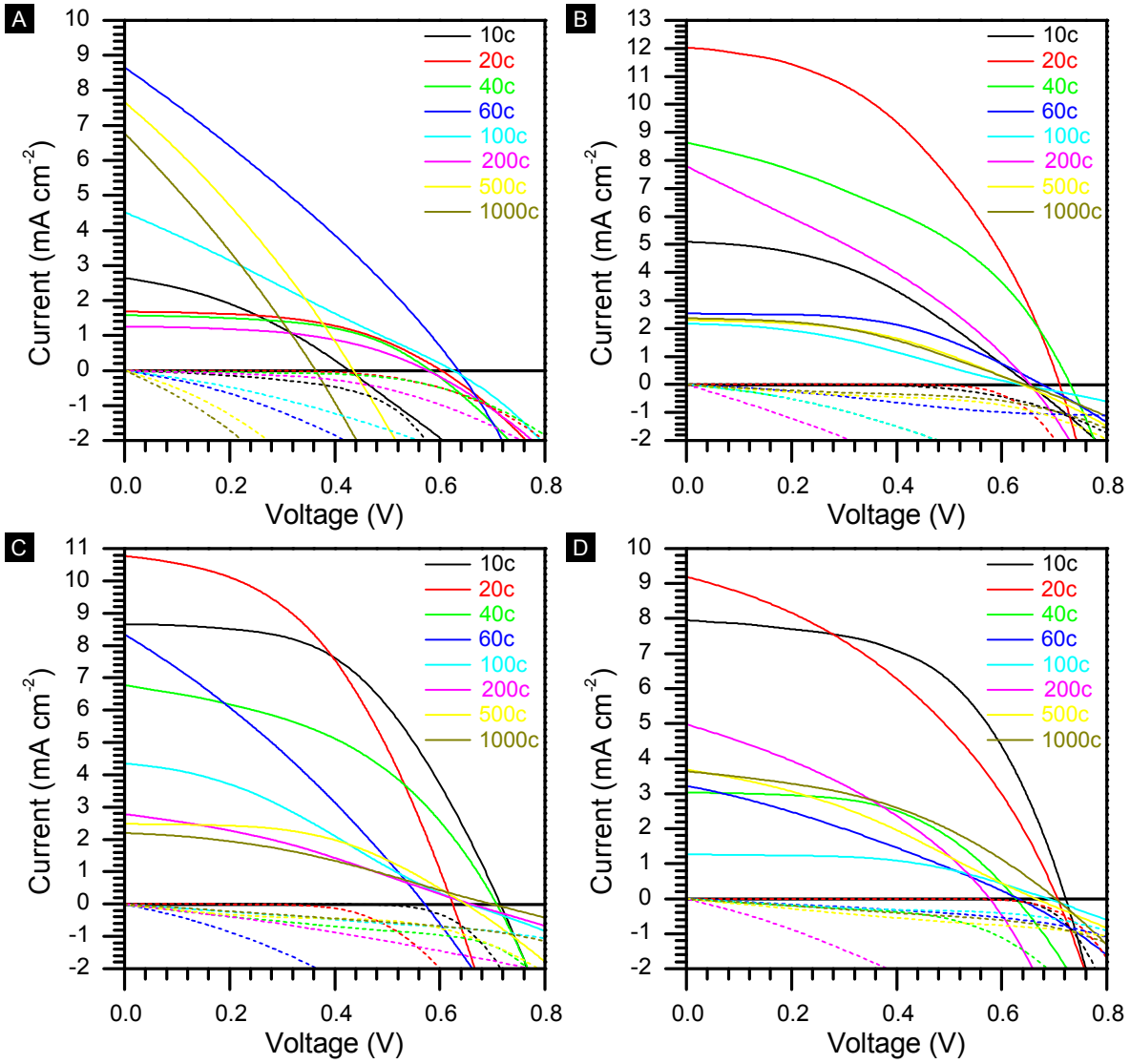

Figure 8.5: I-V measurements under illuminated (solid lines) and dark (dashed lines) conditions for devices with ALD compact layers. The number of ALD deposition cycles are 10, 20, 40, 60, 100, 200, 500 and 1000. The deposition temperatures are **(A)** 120 °C, **(B)** 150 °C, **(C)** 200 °C and **(D)** 300 °C.

be taken when comparing results from liquid electrolyte and solid-state electrolyte devices). This decrease in performance for thicker films is thought to be due to decreased transmittance and lowered tunnelling effects. The lower density of the spray-pyrolysis TiO_2 leads to a higher transmittance compared to the ALD grown TiO_2.

There is a clear difference between devices with compact layers deposited at 120 °C and those with compact layers deposited at higher temperature. For the 120 °C compact layers the efficiency is approximately 1 % regardless of the number of ALD cycles whereas at higher deposition temperatures there is a general trend showing power conversion efficiencies which match or better those of the reference devices for 10, 20 and 40 ALD cycles with a decrease to approximately 1 % for higher numbers of cycles. We

attribute the constantly low efficiency at 120 °C to a higher concentration of chlorine impurities and a higher density of pin-holes in the TiO_2 compact layer film.

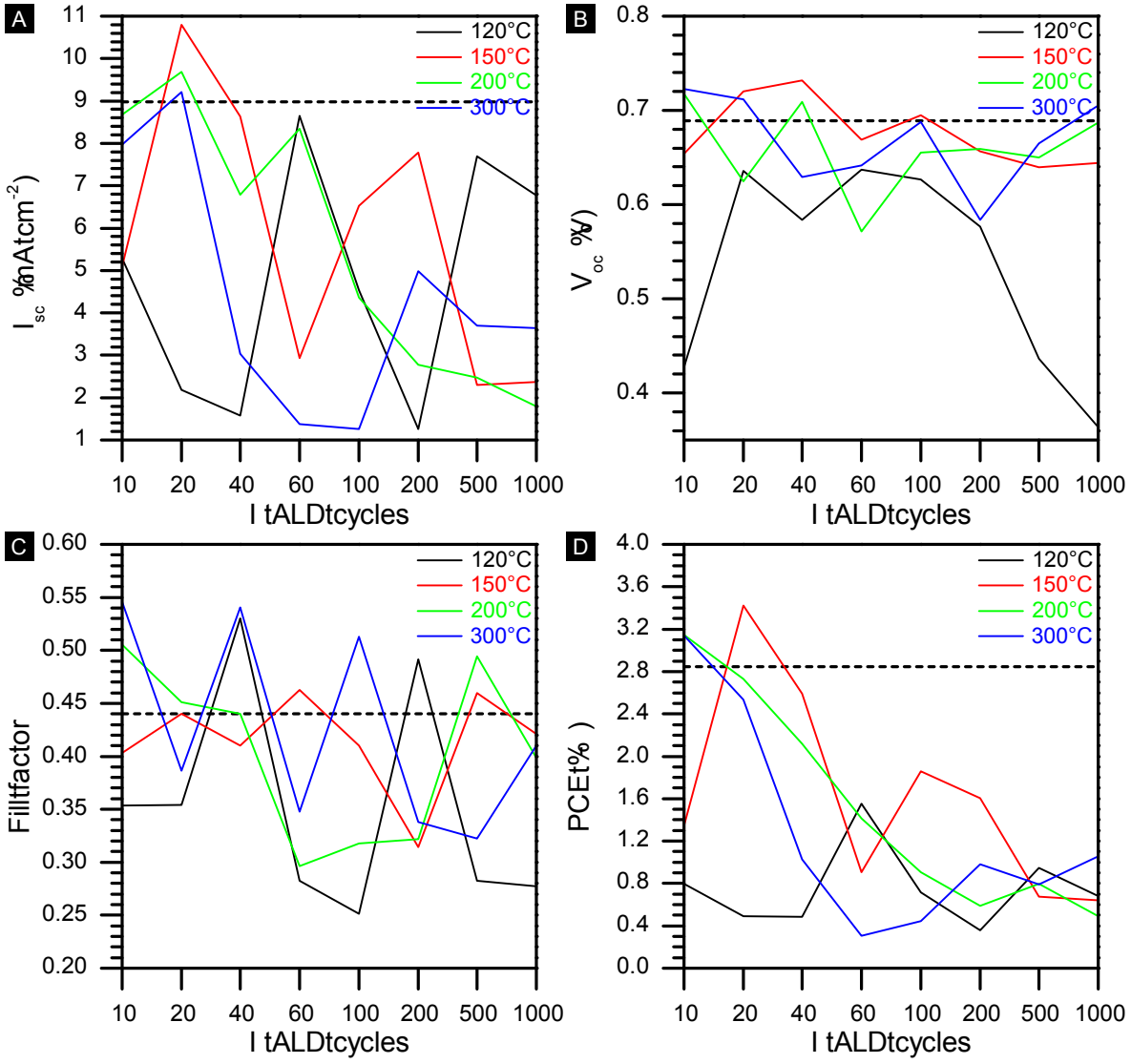

Figure 8.6: Device characteristic of ALD compact layers deposited at 120 °C, 150 °C, 200 °C and 300 °C. The dashed lines denote the characteristics of the reference device. The characteristics are **(A)** short-circuit current, **(B)** open-circuit voltage, **(C)** fill factor and **(D)** power conversion efficiency.

The best performing device with an ALD compact layer displays a power conversion efficiency of 3.42 % with a short-circuit current, open-circuit voltage and fill-factor of 10.8 mA cm^{-2}, 0.72 V and 0.44 respectively. This device consist of a 1.1 nm (20 ALD cycles) compact layer deposited at 150 °C and displays an increase in power conversion efficiency compared the reference devices of 20 %.

We believe that the main reason for the equal or improved performance compared to the spray pyrolysis reference devices lies in the fact that the ultra-thin compact layers

remain amorphous despite the higher temperature calcination of the mesoporous TiO_2 film. The amorphous layer successfully prevents recombination whilst being sufficiently thin to allow effective tunnelling of electrons through it. The ultra-thin compact layers also ensure that the transmittance is very close to the uncoated FTO.

As described in the introduction, the purpose of a compact or blocking layer is to prevent recombination between electrons injected into the FTO and the electrolyte in the device. Thus the ideal compact layer from a recombination point of view consists of a thick film of a material with a low conductivity. However the electrons transported through the mesoporous TiO_2 scaffold require a thin compact layer with a high conductivity to allow for an effective injection of the electrons into the FTO and a low series resistance. Thus a compromise has to be found in term of the thickness of the compact layer and its conductivity. We hypothesise that the improved performance shown by our devices can be explained by their resolution of these opposing requirements.

As shown in Section 7.3.4, the confinement imposed by ultra-thin ALD deposited TiO_2 films leads to a significant suppression in crystallisation, and films below 4 nm do not crystallise despite calcination at 550 °C for 48 h. It is this suppression that we think could be responsible for the impressive performance of the ultra-thin compact layer devices.

The schematic for our hypothesis is shown in Figure 8.7. Prior to calcination of the mesoporous TiO_2 electrode, the TiO_2 compact layer is amorphous, regardless of ALD deposition temperature, as long as the film thickness is approximately 4 nm or thinner (which corresponds to roughly 70 ALD cycles). Upon calcination with the TiO_2 film assembled on top of the compact layer, only regions of the compact layer in contact with TiO_2 nanoparticles crystallise. This is because the nanoparticles act as nucleation points for the crystallisation of the compact layer. The regions in between these contact points, between the mesoporous layer and the compact layer, remain amorphous. This leads to an effective lowering of the recombination between electrons in the FTO and the electrolyte due to the conformal nature and low pin-hole density of the ALD TiO_2, whilst also promoting effective transport from the TiO_2 scaffold to the FTO.

The threshold for the crystalline/amorphous transition described in Section 7.3.4 is based on TiO_2 ALD films grown on silicon substrates and we expect the threshold to be thinner for depositions on rougher substrates such as FTO. The different lattice matching of the FTO/TiO_2 interface could also influence the crystallisation behaviour. This agrees which the results in Figure 8.6D which show impressive power conversion efficiencies for compact layers up to 40 cycles or 2.2 nm. Compact layers with a thickness above approximately 3 nm are expected to be crystalline which increases the recombination rate as well as removing the possibility of the binary crystalline/amorphous compact layer configuration described above.

To the extent of our knowledge, the successful use of sub-2 nm compact layers in dye-sensitised solar cells has not been reported previously. Nor have we found any reference to the concept of a binary crystalline/amorphous compact layer or a potential route to fabricate such a layer. We believe that with further work and optimisation, this use of ultra-thin atomic layer deposited compact layers could become a useful route

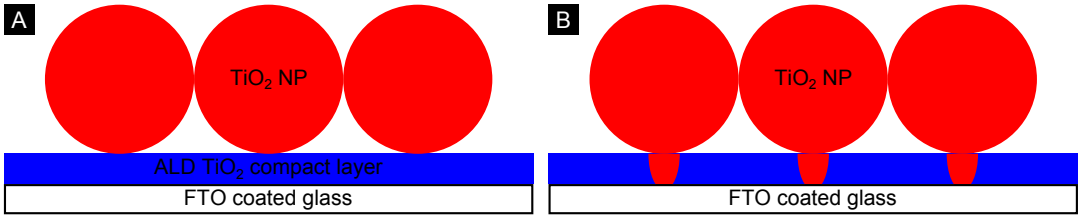

Figure 8.7: Schematic of selective crystallisation of a TiO_2 compact layer. Crystalline and amorphous regions are denoted by red and blue respectively. The sizes are not to scale. **(A)** The FTO/compact layer/TiO_2 scaffold interface prior to calcination. The ALD compact layer is amorphous since its thickness is below the threshold for crystallisation suppression. **(B)** As the device is calcinated at 500 °C in air for 3 h the parts of the compact layer which are in contact with the TiO_2 nanoparticles crystallise, whereas the rest remains amorphous. This binary crystallisation behaviour leads to improved device performance.

to improve the performance of dye-sensitised solar cells as well as organic solar cells. The technique could also be used for other metal oxide scaffolds such as ZnO DSSCs. Moreover, dopants could be used to further increase the conductivity of the TiO_2 and potentially extend the suppression threshold to thicker films, which could in turn improve the suppression of recombination. These low temperature depositions of very thin compact layers could also have uses in low temperature devices fabricated on temperature sensitive polymeric substrates.

8.2.4 Conclusion

In this section it has been shown that ultra-thin TiO_2 films of less than 3 nm, deposited using ALD from $TiCl_4$ and H_2O,can successfully be used as compact or blocking layers in solid-state dye-sensitised solar cells. We believe that this is the thinnest TiO_2 compact layer used in a functioning DSSC reported so far. The ultra-thin compact layer devices equal and even out-perform otherwise identical devices which utilise a 50 nm thick compact layer formed through spray-pyrolysis. We believe that this enhanced performance is due to the reduced recombination rate of an amorphous compact layer and the formation of a binary amorphous/crystalline compact layer upon calcination, where the contact points between the mesoporous TiO_2 scaffold and the compact layer act as nucleation seeds for the crystallisation of the otherwise amorphous layer. This selectivity ensures an amorphous compact layer at the electrolyte/FTO interface which suppresses recombination, and a crystalline compact layer at the TiO_2 electrode/FTO interface which leads to an efficient electron injection. The combination of these effects leads to improved device performances compared with traditional devices with compact layers fabricated using spray pyrolysis.

9 Biomimicry of the *Papilio Blumei*

Up until this point the use of atomic layer deposition has been mainly focused on photovoltaic applications. In the following study a similar process of ALD growth on self-assembled structures is utilised in an optical application. The chapter will describe the biomimicry of the wing scales of the *Papilio Blumei* butterfly. This is accomplished using well-studied experimental techniques including assembly of colloidal monolayers, electrochemical deposition of metals and atomic layer deposition. The results of an alternative fabrication route which produced a very striking colour response will also be presented.

9.1 Introduction

Over the last few decades, research into micro- and nano-structured fabrication has more and more frequently taken inspiration from structures found in nature. This trend has included the design of novel device structures such as bio-inspired optics and dynamic device architectures [344], and direct biomimetic replication [345]. One particular field of biomimetics that has received an increased interest is the biomimicry of structural colours. The major reason for the appeal of research in this field is its potential industrial and commercial relevance, for example in anti-counterfeiting security features, cosmetics and paints [346, 347].

Vivid, pure and intense colours play a very import role in nature amongst both animals and plants. In animals, colours are normally used as an intra-species form of communication as an offensive cue between males as well as a visual selection criterion between males and females for reproduction [348]. Colours can also have an inter-species function as both warning signs and camouflage [349–351]. In plants colours are normally used as a means to attract pollinators [352] but examples of more intricate evolutionary functions such as UV-protection can also be found [353].

The majority of colours seen in both animals and plants have a pigment-based origin, however the use of pigments makes the production of bright and vivid colours more difficult. Instead, these vivid colours arise from the interaction between light and structures on the micrometre and nanometre length scale [354–356]. Colours produced in this manner are normally termed 'structural colours'. Compared to pigment-based colours, the structures in structural colours are normally formed from materials that display low light absorption. The main physical effects responsible for structural colours are diffraction, multilayer interference and coherent scattering. Normally these effects are coupled with wavelength specific absorption to enhance certain optical features [357–359]. Through evolutionary development, nature has fine-tuned the ideal structures to include varying amounts of disorder, thus enhancing certain spectral features as well as producing a broader angular response. A large number of design architectures, such as multilayers, perforated multilayers, disordered scattering films, structures that

mix features with different length scales and photonic crystals are employed in nature to achieve not only bright colours but also to enhance reflectivity, light polarisation, strong scattering to form pure whiteness and strong absorption to form deep blackness [69, 347, 360–363]. The *Morpho* butterfly is a stark example [357] of the incorporation of structural colour.

The work of this chapter is focussed on the biomimcry of one species of butterfly, the *Papilio blumei*, and in particular on the successful replication of the colour mixing seen on its wings. Although the physical underpinnings that describe the observed spectral response are well understood, the actual replication of these structures has previously presented a significant challenge. Some attempts have been carried out to replicate the multilayer structure and colour mixing seen in the *Blumei* butterfly. One approach similar to the one carried out in this chapter has been recorded by Crne *et al.* where breath-figures are used to replicate the wing scale concavities [364]. Butterfly wing scales have also been directly replicated using ALD, however this route does not replicate the intricate multilayer structure seen in the *Blumei* [365]. The work presented in this chapter was undertaken in collaboration with **Mathias Kolle** and **Maik Scherer**[1].

9.1.1 *Papilio blumei* and *papilio palinurus*

The wings of both the *Papilio blumei* and the *Papilio palinurus* display striking green areas against a dark or black background, as shown in Figure 9.1A. Higher magnification optical microscopy of the individual wing scales (Figure 9.1B,C) reveal microstructures on the surface of the scales. These microstructures reflect yellow-green light from the centres and blue light from the edges, as seen in Figure 9.1E and it is this mixing of sources of yellow and blue light that causes the observed green colour on the millimetre length scale. The microstructures are in fact concavities (Figure 9.1D), approximately 5 µm to 10 µm in size, which are conformally coated with a multilayer consisting of alternating layers of cuticle and air/cuticle which gives the required refractive index contrast. The cuticle and air multilayer displays a reflection maximum under normal incidence illumination at $\lambda = 525\,\text{nm}$ which moves to $\lambda = 477\,\text{nm}$ when the incident angle is shifted to 45° (Figure 9.1I). The wing scales display a reflectance peak bandwidth of approximately 105 m which is slightly wider than expected from a flat cuticle/air multilayer, $\lambda_{\text{ml}} = 2/\pi\overline{\lambda}\Delta n/\overline{n} \approx 74\,\text{nm}$ where Δn and $\overline{n}$ are the refractive index difference and average refractive index respectively and $\overline{\lambda}$ is the centre wavelength of the reflectance peak [358].

From an assumed refractive index of the cuticle of $n_{\text{cut}} = 1.56$, the refractive index of the air/cuticle layer of the multiayer was calculated to be approximately 1.25. This value agrees with values from literature [355]. Light that is reflected from the centre

[1]The majority of the fabrication steps, including the photolithography, the assembly of colloidal crystals, the electrochemical depositions and the atomic layer deposition, were carried out by myself. Optical and spectral characterisation and imaging was carried out by **Mathias Kolle**. The figures in this thesis are based on these measurements.

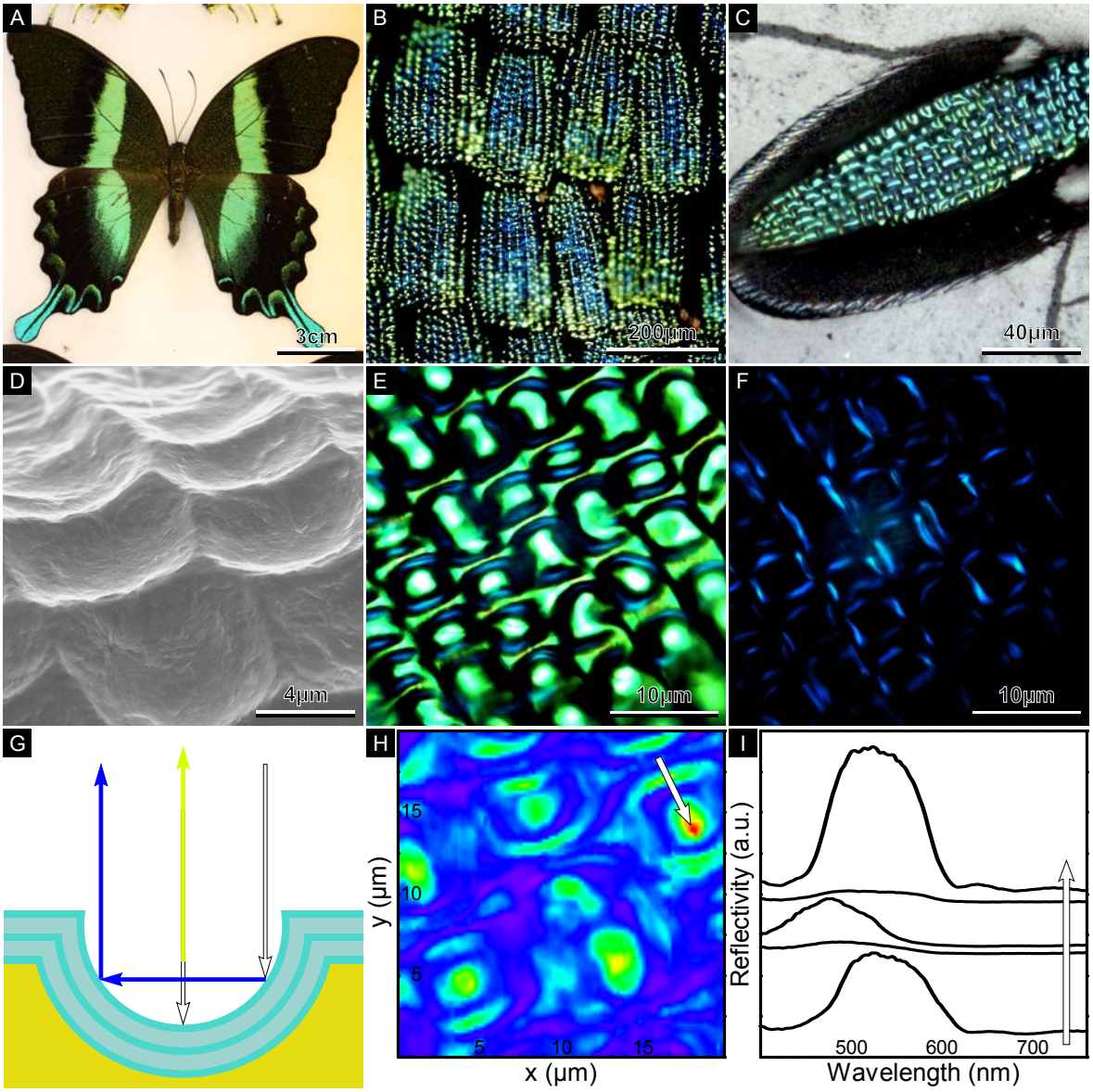

Figure 9.1: Optical response of the *Papilio blumei* butterfly. **(A)** The butterfly displays stunning green areas caused by structural colours on its wings. **(B,C)** High magnification optical micrographs of the green areas. The intricate microstructure responsible for the colour is clearly visible. **(D)** Scanning electron micrograph of the cuticle and air multilayers. **(E)** Optical micrograph of the concavities under co-linear polarisers displaying their yellow-green centres and blue rims. **(F)** Optical micrograph of the concavities under crossed polarisers. The four blue segments along the concavity rim are caused by a double polarisation rotation. **(G)** Schematic of light reflection in a concavity causing the central yellow-green colour and the blue colour along the rim. **(H)** Two-dimensional spectroscopic scan at 466 nm of a 20 µm×20 µm section of a wing scale. **(I)** Spectra measured along the arrow in **H**. The red curve displays the spectral response of the wing scale multilayer predicted from simulations.

of the concavity inpinges on the multilayer at normal incidence and the retro-reflected light from these regions is thus yellow-green. On the other hand, light incident on the edges of the concavity inpinges the multilayer at a non-normal, close to 45° angle which causes the observed blue colour as well as a double reflection as shown in Figure 9.1G. Besides the spectral filtering caused by the multilayer near the edge of the concavities, the double reflection off these areas also causes a geometrical rotation of the polarisation of the incident light [366]. If the concavities are observed under crossed polarisers, light from the central regions is extinguished (Figure 9.1F) since no polarisation change is expected from a normal incident reflection. However light incident at the outer edges of the concavities is retro-reflected as four distinct regions all at 90° to each other (Figure 9.1F) [355, 366]. This phenomenon is explained by the polarisation rotation mentioned above. Light incident with a polarisation angle of θ relative to a defined incident reference plane will acquire a total polarisation change of 2θ through the double bounce which leads to an intensity distribution of $\cos 2\theta$ and thus the four observed blue regions.

Upon comparison of the spectral response seen in the *Papilio blumei* and *Papilio palinurus* to other butterflies such as the *Papilio ulysses*, an absence of colour mixing and polarisation rotation is observed in the latter. This is caused by the shallower concavities of the *Ulysses*, with smaller angles between the sides and the top of the concavities, which can not support a double reflection.

9.1.2 Biomimetical replica

The aim of this study was to mimic the spectral response of the *Blumei* rather than the complete wing scale structure, which allowed for a certain degree of freedom over choice of materials. For the most part, inorganic materials were chosen for the replication which significantly simplified the fabrication procedure. The cuticle/air multilayer was substituted by a TiO_2/Al_2O_3 Bragg multilayer deposited using ALD. TiO_2 and Al_2O_3 both have the advantage that they do not display any significant absorption in the visible spectrum. The concavities themselves were fabricated using a combination of colloidal self-assembly, which will be described in more detail in the following section, and electrochemical deposition of gold or platinum.

Besides the successful mimicry of the colour response of the butterfly, this chapter will also describe the fabrication of a variant to the morphology of the *Blumei* butterfly through a conceptually very simple modification to the fabrication procedure, which displays a much stronger colour variation than its natural inspiration.

9.1.3 Fabrication of colloidal monolayers

A number of fabrication methods exist to grow colloidal monolayers, including spin coating [367, 368] and evaporation deposition [369, 370]. The main problem with these methods is that it is very hard to achieve monolayers when the colloidal particle size

is smaller than 2μm. To avoid this problem, together with other complications such as long fabrication times, a different fabrication technique was used in this study. tjis technique is known as the suspension-pulling technique and will be detailed below.

In order to understand this fabrication technique, it is first necessary to review the physics of colloidal crystallisation. A range of physical processes including electrostatic repulsion and Van der Waals forces have been suggested to be responsible for the colloidal crystallisation process. In 1992 Denkov *et al.* showed that the main driving force for the close packing of the colloidal particles is the capillary force occurring when the solvent evaporates [371]. As the liquid evaporates, the particles become partially immersed, which leads to the eventual formation of a meniscus between neighbouring particles as seen in Figure 9.2A.

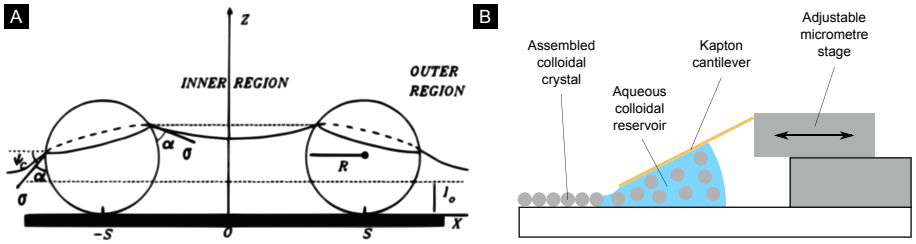

Figure 9.2: **(A)** Hexagonal close-packing of colloidal particles partially immersed in a liquid. The particles are pulled together because of attractive forces caused by the deformation of the meniscus between the two particles. Modified from [371]. **(B)** Experimental setup of the suspension-pulling technique. The cantilever is slowly withdrawn using the micrometre screw to form the colloidal layer. The formation of multilayers can be prevented by controlling the amount of water vapour in the air above the sample. Modified from [75].

The shape of the meniscus depends on the undisturbed liquid depth (I_0), the contact angle of the solid in the liquid (α), the particle separation ($2S$) and the radius of the particles (R). There are two contributions to the attractive driving force between two colloidal particles. The smaller of the two is a pressure force arising from the differing liquid heights inside and outside of the two particles. The major contribution is due to an imbalance in the forces arising from the surface tension of the gas/liquid/solid contact line. The imbalance leads to an attractive force which can be shown to be

$$F_{\mathrm{x}} = \frac{2\pi\sigma r_{\mathrm{c}}}{2S}\sin^2(\psi_{\mathrm{c}}), \tag{9.1}$$

where $2\pi r_{\mathrm{c}}$ is the circumference of the circular gas/liquid/solid contact line and ψ_{c} is the average angle between the meniscus and a plane parallel to the substrate. Since the attractive force is inversely proportional to the particle separation the attraction continues until the particles touch. Once touching the particles are held in close proximity by van der Waals interactions. This pair-wise attraction occurs between all the nearest neighbour particles in the systems which leads to an equilibrium hexagonally close-packed state which minimises the average inter-particle distances.

The crystal growth is sustained by an influx of particles from the region where the particles are still fully immersed. The influx is caused by a movement of liquid towards a region of high evaporation rate from the already assembled crystal.

The technique used to fabricate the colloidal monolayers is called the suspension-pulling technique and was developed by Maik Scherer [75] but has also been separately described by Zhang *et al.* [372]. It allows the user to control two parameters: the height of the suspension reservoir, and the evaporation rate of the water. This in turn controls the formation of either monolayers or multilayers. The experimental setup is shown in Figure 9.2B above. The method works by pulling a suspension of colloids in water over a flat substrate using a hydrophobic cantilever. The cantilever allows for the formation of a thin layer of water on the substrate with a well-defined thickness, as well as trapping the suspension between the cantilever and the substrate thus forming a reservoir of colloids. A linear scratch is made in the substrate perpendicular to the movement of the cantilever, and this acts as the nucleation point for the crystal growth. As the cantilever is slowly moved away from the scratch using the micrometre screw shown in Figure 9.2B the crystal grows at the tip of the cantilever.

9.2 Experimental methods

9.2.1 Materials

The chemicals and materials listed in Table 9.1 were used as received unless otherwise specified.

Chemical	Purity (%)[a]	Abbreviation
Polystyrene colloids, 5 µm	10 (DS)	–
Gold plating solution, ECF60	– (ML)	–
Hexachloricoplatinic acid	99.9 (SA)	–
SU-8 2000.5	– (MC)	–
Titanium tetrachloride	99 (SA)	–
Trimethylaluminium	97 (SA)	TMA
Water, deionised	18 MΩ	DI water

[a] Suppliers are given in brackets: Metalor, ML; Sigma Aldrich, SA; MicroChem, MC, Duke Scientific, DS.

Table 9.1: Chemicals and materials used in this part of the study.

9.2.2 Sample fabrication

The template used for the fabrication of the ordered concavities consists of 5 µm polystyrene colloids assembled in a monolayer on gold coated silicon substrates using the method described in Section 9.1.3. Approximately 20 µL of the colloidal suspension in water is placed under a 15 mm wide Kapton cantilever which produces colloidal monolayers approximately 15 mm × 20 mm.

The template is subsequently replicated by electrochemical deposition of a 2.0 µm to 2.5 µm thick layer of platinum or gold into the interstitial spaces between the colloids Figure 9.3 [356, 373, 374]. A three-electrode setup with a Ag/AgCl reference electrode and a platinum mesh counter electrode is used. The deposition electrolytes are a 50 mM aqueous hexachloroplatinic acid solution and a commercial plating solution (Metalor ECF60 with the addition of 0.5 vol/vol% E3 brightener) for the platinum and gold depositions respectively.

Two different routes may then be followed depending on the type of sample as shown in Figure 9.3. For the direct replica of the *Blumei* the polystyrene colloids were removed by sonication in dimethylformamide, resulting in close-packed metal concavities Figure 9.3C. The gold or platinum surface was covered with a 20 nm film of amorphous carbon. The thin layer of carbon acts as an absorption layer limiting unwanted reflections from the gold as well as counterproductive destructive interference which would limit the optical appearance of the sample. The metal concavity template was then conformally coated with a TiO_2 and Al_2O_3 Bragg mirror using atomic layer deposition Figure 9.3D. In the second fabrication route, instead of removing the polystyrene colloids prior to the ALD deposition, the sample was heated to 200 °C, melting the colloids in order to create a planar top surface onto which the ALD multilayer was deposited Figure 9.3E,F.

9.2.3 Sample characterisation

The morphology of the produced replicas are determined using SEM. Prior to imaging at 45° and 90° the samples are coated with a thin layer of gold/palladium.

Spatial spectroscopic information is obtained using an Olympus BX-51 microscope setup with a spot-size of approximately 1 µm (using a 100x objective and a 50 µm core optical fiber) equipped with computer-controlled translational stage. A halogen lamp serves as the light source.

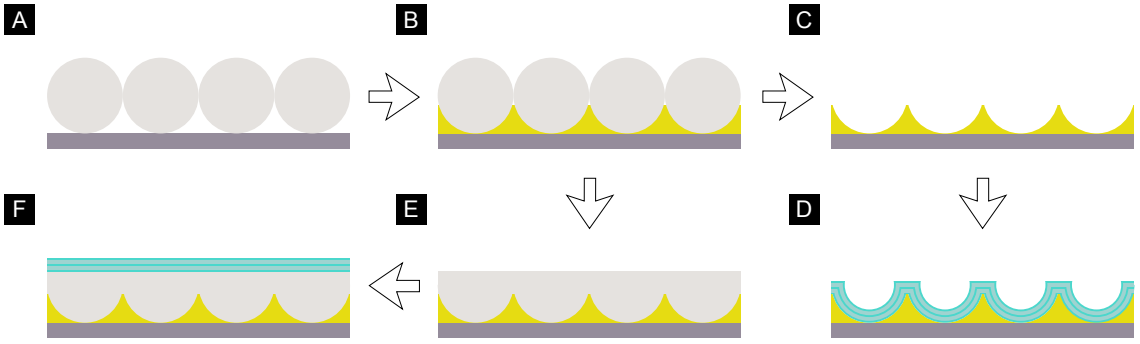

Figure 9.3: Fabrication routes for the biomimetic replication of the *Papilio blumei* butterfly. **(A)** A monolayer of 5 µm polystyrene colloids are assembled on gold-coated silicon using the technique described in Section 9.1.3. **(B)** Gold or platinum is electrochemically deposited through the colloidal template to just under half-colloid height. **(C)** For the standard replication route the colloids are removed using sonication in DMF. A thin layer of amorphous carbon (3 nm to 5 nm) is then deposited on the metal concavities to lower the reflectivity of the concavity surface. **(D)** A Bragg multilayer stack consisting of 11 layers of Al_2O_3 and TiO_2 is conformally deposited on the surfaces of the concavities. **(E)** For the modified replication route the polystyrene colloids are melted at 200 °C to produce a flat polymer cavity on top of the metal concavities. **(F)** A planar Bragg stack is then deposited on the polystyrene cavity using the same processing parameters as in **D**.

9.3 Results and discussion

9.3.1 A direct biomimetic replication

The artificial concavities can be seen in Figure 9.4A. Although a colloid size of 5 µm is used, the gold replicated concavities have diameters of approximately 4.5 µm due to a deposition thickness of 2.3 µm which is below half-colloid height as seen in Figure 9.4B. The multilayer deposited on the concavities using ALD as shown in Figure 9.4B consists of 11 layers, alternating TiO_2 and Al_2O_3 (the first and last layers being Al_2O_3). The layer thicknesses and refractive indices of the TiO_2 and Al_2O_3 are measured using ellipsometry to be $d_{TiO_2} = 57 \pm 4$ nm, $n_{TiO_2} = 2.5 \pm 0.1$ and $d_{Al_2O_3} = 82 \pm 4$ nm, $n_{Al_2O_3} = 1.7 \pm 0.1$ respectively. The layer thicknesses were chosen, based on the measured refractive indices of the TiO_2 and Al_2O_3, as to produce a stop-band that matches the reflectance of the *Blumei*, which has a band centre at about 525 nm, as closely as possible. The measured normal incidence reflectance peak is determined to be 550 nm which agrees well with predictions from modelling. The optical appearance of the multilayer coated concavities at normal and grazing incidence are shown in Figure 9.4C,D. The normal incidence optical response qualitatively matches the colour of *Blumei* very well. For the grazing incidence the perceived colour is blue-shifted as expected as well as displaying iridescence.

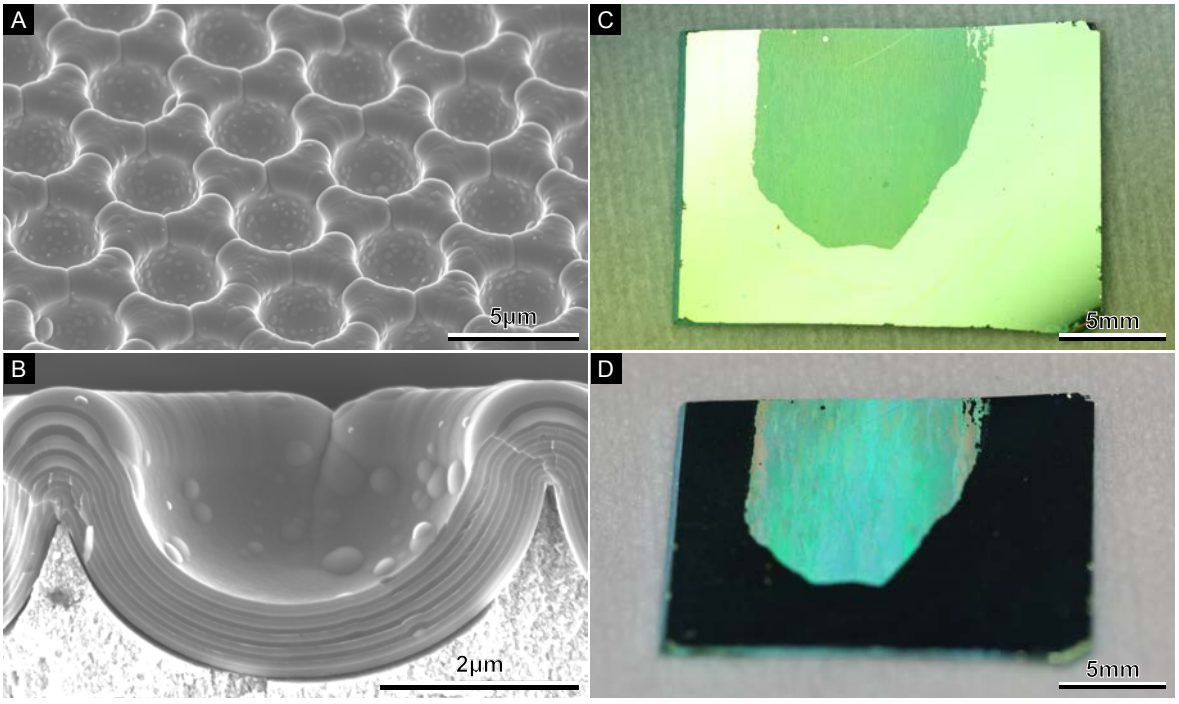

Figure 9.4: Biomimetic replication of the *Papilio blumei* butterfly. **(A)** SEM image taken at 45° of the top surface of the multilayer coated metal concavities showing the large area conformality of ALD. **(B)** Cross-sectional SEM image of a single concavity showing that the ALD multilayer conformally coats the metal concavity. **(C)** Image of a $1\,\mathrm{cm}^2$ biomimetic replica at normal incidence displaying a striking green colour due to the colour mixing from the edges and centres of the concavities. **(D)** Image of the same sample as in **C** taken at grazing incidence which blue-shifts the optical response. The sample also displays some iridescence.

While the bandwidth of the original butterfly wingscales is $\Delta\lambda = 105\,\mathrm{nm}$, the replica displays a reflection bandwidth of 140 nm (calculated value of $\Delta\lambda_{\mathrm{ml}} = \frac{2}{\pi}\overline{\lambda}\frac{\Delta n}{n} = 134\,\mathrm{nm}$). This difference is expected due to the larger value of $\Delta n/\overline{n}$ for the TiO_2 and Al_2O_3 multilayer.

Higher magnification microscopy of the replica concavities also agree with the natural original, with the centres and the edges reflecting yellow-green and blue respectively as shown in Figure 9.5A. This is further confirmed by the spectral map in Figure 9.5B and the observed peak-shift in Figure 9.5C. Spectroscopy of the replica under cross polarisers also matches the spectral features of the butterfly with only light incident on four distinct regions of the edge of the concavities being reflected (Figure 9.5D). As expected for a multilayer illuminated at non-normal incident (45°) the reflected light is shifted to a shorter wavelength than the light reflected from the centre of the concavities (Figure 9.5E). This shows that the inorganic replica displays the same spectral behaviour as its natural counterpart.

As well as replicating the optical features of the butterfly, the replica also displays an

additional optical feature. This is the double-peak seen in the reflection spectrum under crossed polarisers (Figure 9.5F). To understand this set of observed peaks one has to look at the behaviour of the complex reflection coefficients, r_s and r_p, as the s- and p-components of the incident light are reflected from the curved multilayer surface. It is possible to model the full reflectivity of a single multilayer concavity using a transfer matrix model with the assumption that all of the incident light is reflected via single-, double- and triple-bounces. A triple bounce is possible if the incident light is at an angle of 60° with respect to the normal. The reflection spectra are calculated for linearly polarised incident light and for the detection through no polariser and with a polariser parallel and perpendicular to the incident light.

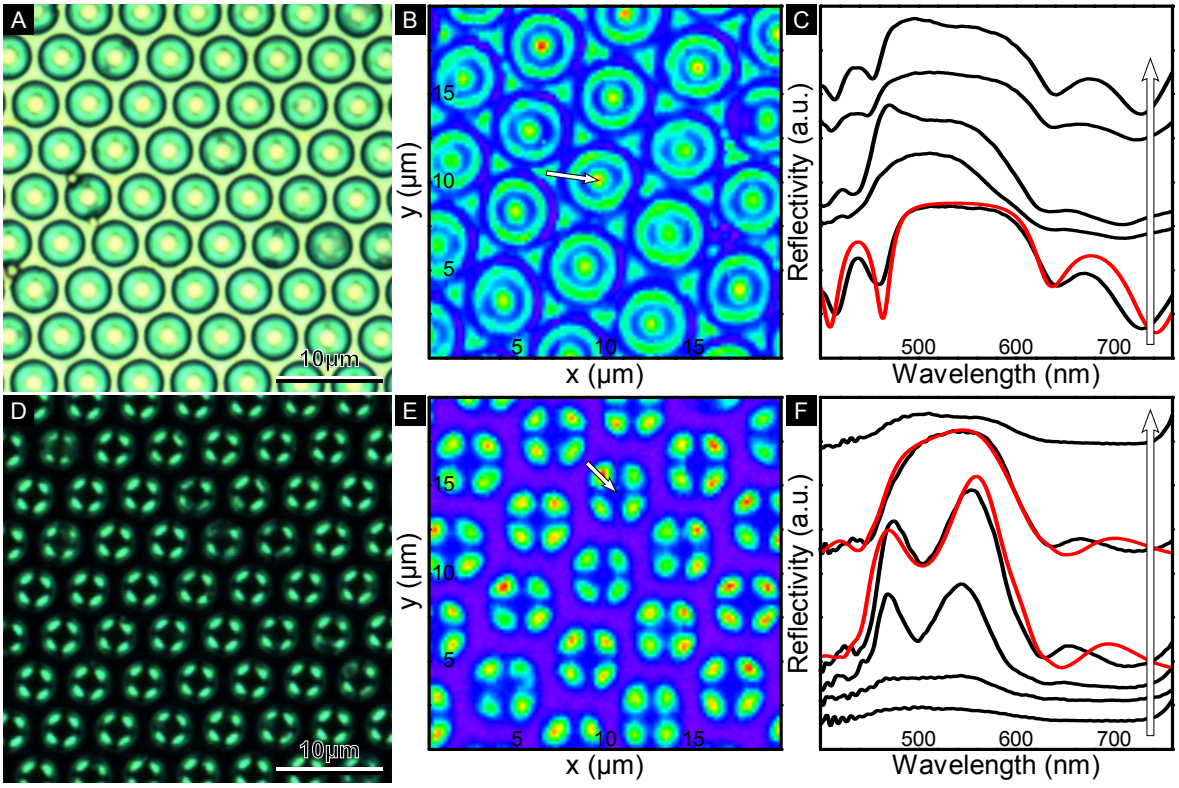

Figure 9.5: Optical response of biomimetic replica. **(A)** High-magnification microscopy image taken using un-polarised light of multilayer-coated concavities. The yellow-green centres and blue edges are clearly visible. **(B)** 2D spectral map at 450 nm of an array of concavities in **A**. **(C)** Spectra taken along the arrow **B** from the interstitial space between three concavities to a concavity centre. **(D)** The area in **A** imaged under crossed polarisers. Four distinct regions are visible which are due to the polarisation rotation caused by the incidence light impinging at the multilayer at non-normal incidence at the edge of the concavities. **(E)** 2D spectral map at 450 nm taken under crossed polarisers of the area in **B**. **(F)** Spectra along the arrow in **E** taken from the interstitial space between two concavities to a concavity centre.

In summary, the results show that a triple bounce is needed to result in the observed

double-peak feature of the sample under crossed polarisers (for the full results see the thesis of **Mathias Kolle** [375]). Simulations of triple bounces agree well with the measured reflection spectrum as shown by the red curve in Figure 9.5F. The reason for why this double-peak reflection is not observed in the reflection spectrum of the butterfly is two-fold. Firstly the refractive indices of the cuticle/air multilayer leads to only a very shallow dip in the broad reflection peak. Secondly the butterfly wing scales consist of concavities with varying sizes and orientations which means that a mix of double and triple bounces are present, further reducing the double-peak shape of the reflection peak.

As mentioned previously, the macroscopically observed colour is a mixture of the reflections of the centre and edges of the concavities. The maximum wavelength separation between these two colours can be calculated given the expression for the wavelength of the peak reflectance as a function of the incident angle,

$$\lambda(\theta_\mathrm{i}) = \frac{2}{m}\left[d_1\sqrt{{n_1}^2 - \sin^2\theta_\mathrm{i}} + d_2\sqrt{{n_2}^2 - \sin^2\theta_\mathrm{i}}\right] \tag{9.2}$$

where d_1, d_2, n_1 and n_2 are the thicknesses and refractive indices of the two multilayer components, m is a positive integer and θ_i is the incident angle of the illumination. Given the refractive indices and thicknesses of the TiO_2 and Al_2O_3 multilayer and incident angles of 0° and 45° at the centre and edge of the concavities respectively, a maximum colour separation of 35 nm is possible. This can be compared to a maximum shift of 60 nm for the butterfly multilayer. The colour shift could be extended further by altering the refractive index of one of the two layers, for example by replacing the Al_2O_3 layer with a material with a lower refractive index.

The perceived hue of the reflected colours can also be improved by utilising two materials with a smaller refractive index contrast which in turn leads to a narrower band width. However the use of materials with a smaller refractive index contrast has the unwanted side effect of resulting in a lower reflectivity unless more layers are used in the Bragg stack.

9.3.2 An alternative fabrication route

As mentioned in Section 9.1.2, a relatively small modification to the fabrication procedure leads to a large change in the spectral response of the sample. The modification takes place before the deposition of the TiO_2 and Al_2O_3 multilayer. Instead of removing the polystyrene colloids using dimethyl formamide (DMF), the sample is heated to 200 °C, melting the colloids and forming a flat surface for the multilayer deposition (Figure 9.3C). The formation of this polystyrene spacer layer fills the concavities completely, creating polystyrene resonance cavities between the planar multilayer and the curved gold concavity surface as shown in Figure 9.6B. This modification in the fabrication procedure leads to a striking colour response (Figure 9.6C,D). The observed colour is a function of the position of the observer relative to the light source. If observed in specular reflection, including at normal incidence, the sample appears a vidid blue

whereas in observation through retro-reflections the sample displays a vivid red colour. Figure 9.6E displays a schematic of the possible optical paths through the modified replica for both normal and non-normal incidence light, which explains the observed colours.

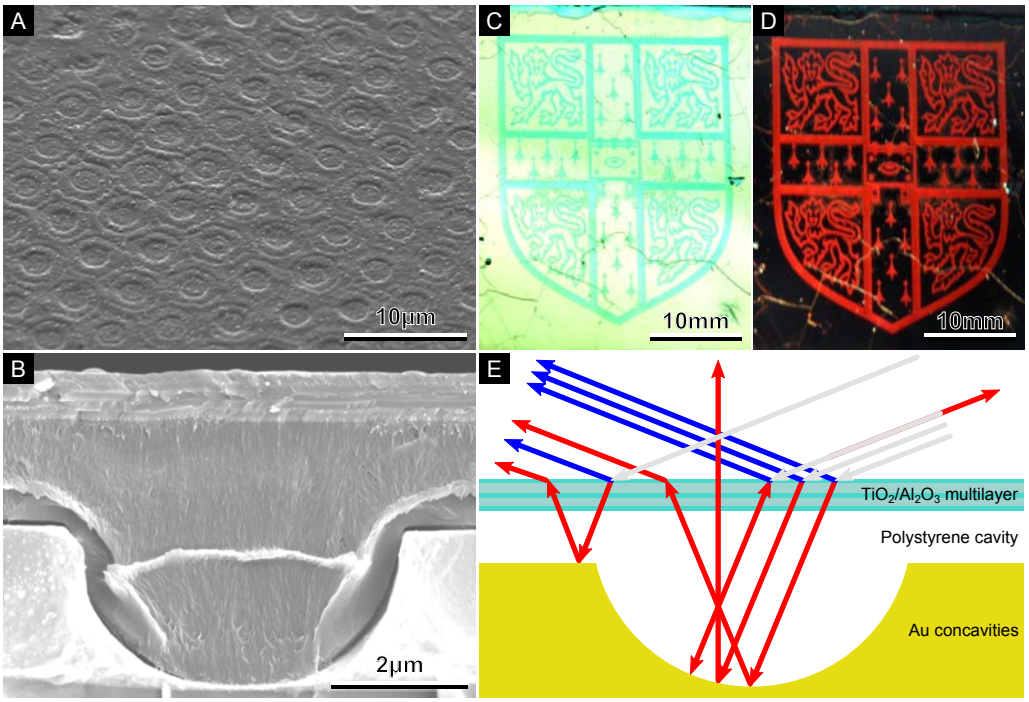

Figure 9.6: Modified fabrication procedure of the *Blumei* replica. **(A)** SEM image taken at 45° of the modified replica. Projections of the concavities are still visible due to small height variations of the polystyrene cavity across each concavity. **(B)** Cross-sectional SEM image of a single concavity. The polystyrene cavity and the Bragg multilayer stack are clearly visible. **(C)** Modified replica displaying the crest of the University of Cambridge templated using an SU-8. The sample displays a vibrant blue colour under specular reflection. **(D)** The sample in **C** displays a striking red colour when observed in retro-reflection. **(E)** Schematic of the optical paths through the modified replica under non-normal incidence illumination (light grey arrows). Specular reflection leads to a vibrant blue colour whereas retro-reflection and observation at normal incidence displays a striking red colour.

This study has devised a route which allows the patterning of the observed colour change using optical lithography with a resolution of less than 50 µm. This is achieved by electrically insulating the gold coated silicon substrate with a thin layer of SU-8 prior to the assembly of the colloidal monolayer. The thin SU-8 layer does not interfere with the colloidal assembly but it instead prevents the electrochemical deposition of gold or platinum in the covered areas. The samples still retain the striking colour change from specular to retro-reflection as seen by the patterned logo of the University of Cambridge in Figure 9.6C,D.

Spectral maps of the modified fabrication procedure replica display similar spectral features to the unmodified replica under both un-polarised light and under crossed polarisers. The main optical difference between the two replicas is the method by which the observed colours are produced. In the unmodified replica, the change in colour from the centre to the edges of the concavities is linked to a non-normal light incidence, as described by Equation (9.2). In the modified version, the planar multilayer acts as a spectral filter reflecting the blue part of the spectrum, which explains the observed blue colour in specular reflection (Figure 9.7A).

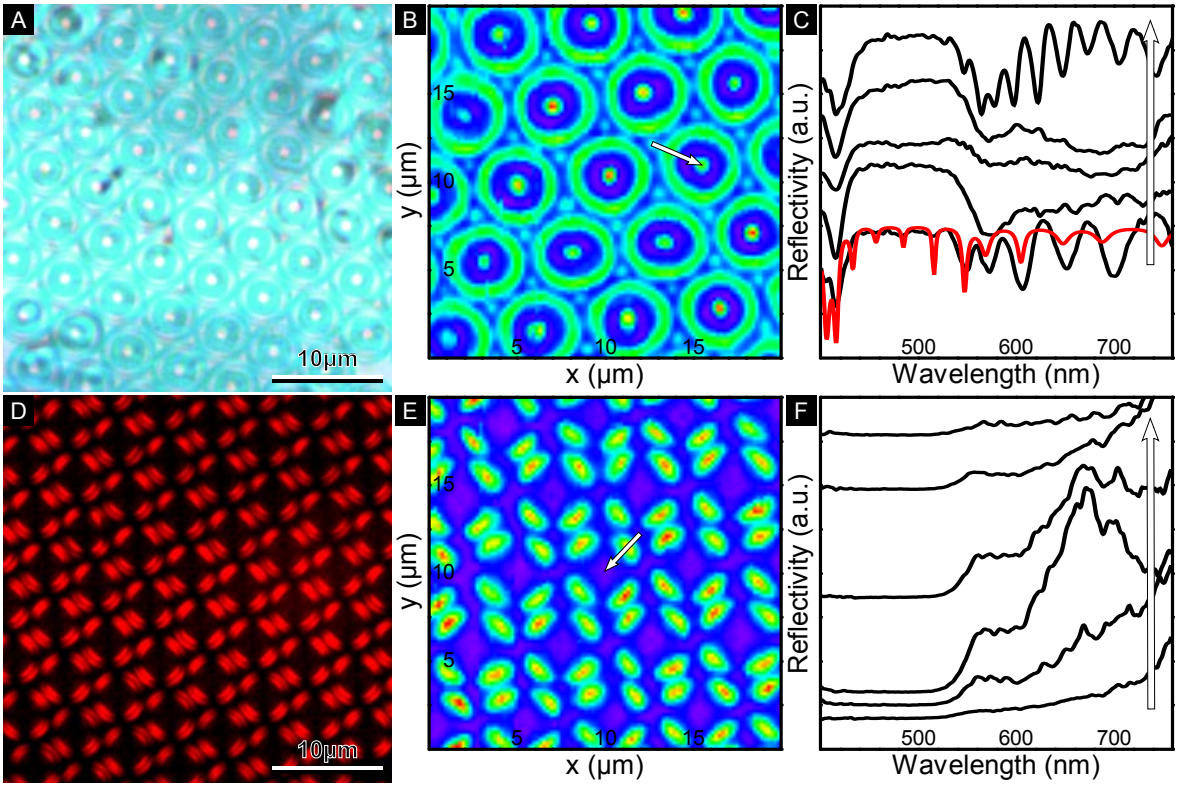

Figure 9.7: Optical response of the modified biomimetic replica. **(A)** High-magnification microscopy image taken using un-polarised light. The spectral filtering of the multilayer in combination with the polystyrene cavity causes the edges and centres of the concavities to appear blue and white respectively. **(B)** 2D spectral map at 750 nm of an array of concavities in **A**. **(C)** Spectra taken along the arrow in **B** from the interstitial space between three concavities to a concavity centre. **(D)** The area in **A** imaged under crossed polarisers. Four distinct regions are visible which are due to the polarisation rotation caused by the red light filtered by the multilayer impinging at the concavity surface at non-normal incidence at the edges of the concavities. **(E)** 2D spectral map at 750 nm of the area in **B** taken under crossed polarisers. **(F)** Spectra along the arrow in **E** taken from the interstitial space between three concavities to a concavity centre.

However the red part of the spectrum, which is the complimentary colour to the reflected light, is transmitted through the multilayer where it is retro-reflected off the gold concavities. The circular concavities ensure that this retro-reflection can take place over a large range of non-normal incident angles. Little scattering of the red light from the gold surface is observed. As expected from non-normal incidence illumination, both the reflected and transmitted light from the multilayer are shifted to shorter wavelengths, thus moving the observed colour in retro-reflection from red to orange.

Resonance features caused by the polystyrene cavity modes are also present in the spectra taken with un-polarised light, as shown by the 2D spectral maps in Figure 9.7B,C. These features are more prominent in the centre of the concavities and the flat regions between the concavities since these areas present a cavity between two relatively parallel surfaces. Measurements under crossed polarisers display similar optical features as the standard replica with four red regions at 90° to each other (Figure 9.7D). The retro-reflection of the transmitted red light at normal incidence illumination explains the observed appearance of the concavities under high magnification with the centre of each concavity appearing white whilst the edges appear blue (Figure 9.7A). This is also seen in the top- and bottom-most spectra in Figure 9.7C which display a uniform intensity across the visible spectrum compared to the middle three spectra.

Measurements were also taken of the modified replica under dark field conditions where the illumination is at a incident angle of more than 70°. The numerical aperture of the objective used, $n_A = 0.9$, limits the collection angle to 65°. A collection angle smaller than the illumination angle means that the blue specular reflection is filtered out. However it is possible for red light that has passed through the multilayer to reflect back within the 65° collection cone as shown in Figure 9.8A. A spectral map of the sample in this dark field configuration is shown in Figure 9.8B together with the measured spectra from a concavity edge to its centre (Figure 9.8C).

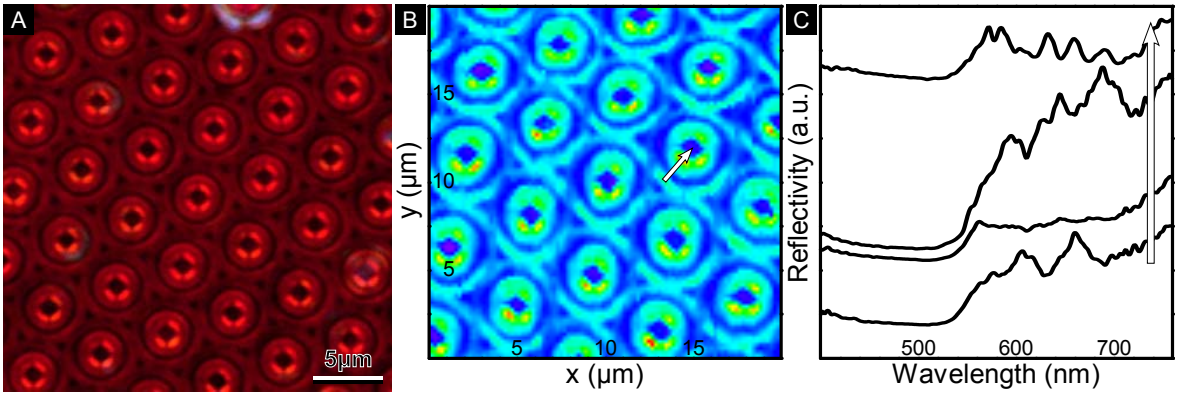

Figure 9.8: Dark field optical response of the modified biomimetic replica. **(A)** Dark field optical micrograph. **(B)** 2D spectral map at 688 nm of an array of concavities in **A**. **(C)** Spectra taken along the arrow in **B** from the interstitial space between three concavities to a concavity centre.

In summary the modified replica displays a vivid blue colour in specular reflection and at normal incidence whereas a red colour is seen in non-specular directions and

especially in retro-reflection.

9.4 Conclusion

This chapter has shown that a biomimetic replica of the *Papilio blumei* butterfly can be fabricated using common and well-studied fabrication techniques including colloidal self-assembly, electrochemical deposition of metals, and atomic layer deposition of aluminium oxide and titanium dioxide. The inorganic biomimetic replica matches that found in nature both visually with a striking green colour observed by eye due to the mixing of blue and yellow-green colours from the edge and centre of each concavity, and spectrally under both un-polarised and cross-polarised illumination. The use of simple fabrication techniques allows for samples to be produced in a scalable fashion over areas larger than the $1\,\mathrm{cm}^2$ produced in this study.

The chapter has further shown that a minor modification of the fabrication procedure leads to a biomimetic structure that has a much more striking colour response than its natural inspiration. The modified replica appears blue in specular reflection with the colour changing to a striking red when observed under retro-reflection. This pair of colours can easily be altered by changing the materials or thicknesses of the Bragg multilayer stack. The striking colour response as a function of the observer's position relative to the sample and the light source could have significant potential commercial applications.

10 Summary and future work

This thesis has studied the crossover between the fields of atomic layer deposition, block copolymer self-assembly and photovoltaics. The central research question asked was how the technique of atomic layer deposition (ALD) could be incorporated into the creation of nano-structured functional materials and devices, more specifically in the areas of photovoltaics and biomimetics.

The aim of the work was to explore the capabilities of ALD as a strategy for overcoming two main challenges: the creation of extremely thin conformal metal oxide layers and the replication of complex high-surface-area templates. The use of ALD to deposit thin conformal metal oxide film was implemented in four different studies. The main experimental results and conclusions from these chapters and indications of potential future work will be summarised below.

Chapter 6 described the study of post-deposition thermal oxidation of metal nano-structures. The nano-structures consisted of copper electrochemically deposited in double-gyroid-structured polystyrene templates. The gyroid-structured copper networks were subjected to a range of thermal oxidation treatments. Electron microscopy and scattering experiments showed that low temperature oxidation at 70 °C resulted in the formation of a core-shell copper/Cu_2O/CuO structure whereas oxidation at 225 °C and 350 °C resulted in Cu_2O/CuO and CuO-only structures. These structures were used to fabricate solar cells incorporating aqueous and non-aqueous liquid and solid-state electrolytes. ALD was used to deposit both Al_2O_3 barrier layers and ZnO n-type photoelectrodes. The best performing devices were those consisting of an acetonitrile-based electrolyte containing a cobalt redox couple. The copper/Cu_2O/CuO core-shell networks also performed better than the Cu_2O/CuO containing ones, and this improved performance can be explained by the injection of photoelectrons generated in the copper oxides into the copper core. The maximum measured power conversion efficiency was 0.74 % for an active Cu_2O thickness of 200 nm.

One of the limiting factors of the fabrication route described in this chapter is the electrochemical deposition of copper in the gyroid-structured polystyrene templates. Not only is electrochemical deposition not easily scalable but the use of a highly-ordered template which requires thermal annealing to achieve its equilibrium morphology also makes the fabrication process time consuming. One possible extension of the work carried out in this chapter would be the transfer of the post-deposition thermal oxidation concept to a mesoporous nanoparticular network similar to those used in TiO_2 DSSCs. This would allow for the formation of copper/Cu_2O core-shell networks using traditional fabrication techniques such as screen printing. To prevent the oxidation of the nanoparticles prior to the assembly of the network, which would limit transport between neighbouring nanoparticles, the fabrication and assembly would have to be carried out under an inert atmosphere. The matrix material used for the network formation would also have to be carefully designed since pyrolysis is not a viable removal technique. One possible route includes the use of polystyrene as the matrix material

and the use of UV-light and/or ozone to achieve chain scission, which would allow for its removal at low temperatures.

Chapter 7 described the deposition of metal oxides including Al_2O_3, TiO_2 and ZnO in double-gyroid-structured polystyrene templates with a pore diameter of 11 nm. The intrinsically low density of functional groups on the surface of polystyrene makes nucleation and homogenous ALD growth difficult, and as a result the initial depositions inside the templates were of poor quality which did not survive high temperature calcination. This triggered the need for a functionalisation route which would result in a high density of functional groups on the template surface. Of a number of functionalisation schemes tested, only plasma exposure and ozone exposure with a thermal post-treatment produced functional groups whilst maintaining the structural stability of the templates. ALD growth inside functionalised templates produced Al_2O_3, TiO_2 and ZnO replicas with an aspect ratio of up to approximately 400:1 which survived calcination. Attempts to include the TiO_2 replicas in DSSCs elicited very low device performances, due to a lack of crystallinity caused by confinement in the nano-tubular networks formed during the depositions. From this we are able to deduce that inhibition of crystallisation imposes a lower bound on the pore size of polystyrene templates used in the formation of anatase TiO_2 structures by ALD. The ozone-based functionalisation scheme devised in this chapter is expected to work with most carbon-carbon double bond containing polymers and as such could be utilised for the deposition of homogeneous thin films using ALD on a variety of polymeric substrates.

Chapter 8 described two ongoing projects. The first project dealt with the upgrade of a commercial Beneq TFS200 reactor to enable the deposition of metal sulphides through the use of H_2S. Given that H_2S is a highly toxic and flammable gas, the safety aspects of the installation were considered carefully . A number of measures were taken to reduce potential hazards. Firstly the H_2S was supplied as a 3.5 % mixture in a N_2 mixture. Secondly a forced extracted cabinet was installed to house the H_2S cylinder and regulator. The cabinet was equipped with an automatic shut-off valve as an extra safety measure. Thirdly a solid-state scrubber was installed before the building's exhaust, which allows the H_2S level to be reduced to less than 5 ppm. Fourthly H_2S alarms were also installed at the cabinet, the scrubber and the ALD, and the alarm set-point was chosen as 5 ppm in line with HSE regulations. As a test of the feasibility of using a 3.5 % mixture of H_2S for sulphide deposition, stoichiometric ZnS was successfully deposited. This installation will greatly extend the capabilities of the ALD and projects are already underway to deposit antimony sulphide as a thin film sensitiser and lead sulphide for optical applications.

In the second project ALD was used to deposit ultra-thin compact layers for solid-state electrolyte dye-sensitised solar cells using $TiCl_4$ and H_2O as the ALD precursors. The study spanned a large range of deposition temperatures (120 °C to 300 °C) and film thicknesses (0.5 nm to 50 nm). It was demonstrated that devices utilising ultra-thin ALD grown compact layers (below 4 nm) show comparable or better device performances than devices with a traditional compact layer fabricated through spray pyrolysis. We believe that the reason for the impressive performance of the ultra-thin TiO_2 layers is twofold. Firstly crystallisation of the TiO_2 is inhibited due to confinement

and the amorphous nature of the compact layers reduces recombination. Secondly we hypothesise that a binary crystalline/amorphous structure is formed upon calcination of the mesoporous TiO_2 scaffold of the device. The areas of the compact layer which are in contact with the titania nanoparticles crystallise, leaving the rest amorphous. This allows for a successful lowering of the recombination between the solid-state electrolyte and the FTO whilst maintaining an effective injection of electrons from the TiO_2 scaffold to the FTO.

Current work to extend the use of these ultra-thin ALD grown compact layers to organic solar cells is ongoing. One potential new direction for this project could be the introduction of dopants in the TiO_2 compact layer films. The correct choice of dopant levels could allow for improved conductivity and transport of the titania, and could also extend the amorphous-to-crystalline transition threshold to even thicker films, resulting in an even greater reduction in recombination.

Chapter 9 described the use of ALD in the biomimetic replication of the spectral response of the wing scales of the *Papilio Blumei* butterfly. A combination of well-studied experimental techniques were utilised in the fabrication, including the assembly of colloidal monolayers, the electrochemical deposition of gold and platinum and the growth of conformal thin Al_2O_3 and TiO_2 films using atomic layer deposition. The standard fabrication route consisting of gold concavities (approximately 5 µm in diameter) conformally coated with an ALD-grown Al_2O_3/TiO_2 Bragg stack, successfully replicated the colour-mixing spectral response of the butterfly wings. An alternative fabrication route was developed, in which a polystyrene cavity was introduced between a planar Bragg stack and the gold concavities, producing an even stronger optical response. The samples now appeared a vivid blue in specular reflection and a striking red in retro reflection. We further showed that it is possible to pattern these optical features on the 50 µm length scale which would enable the use of these structures in security features such as anti-counterfeiting measures.

This thesis has successfully shown the capability of ALD to produce conformal and ultra-thin metal oxide and metal sulphide films for a variety of applications in the fields of photovoltaics and biomimetics.

Bibliography

[1] B. D. Gates, Q. Xu, M. Stewart, D. Ryan, C. G. Willson, G. M. Whitesides, *Chem. Rev.* **2005**, *105*(4), 1171–1196.

[2] M. Li, C. K. Ober, *Mater. Today* **2006**, *9*(9), 30–39.

[3] L. Schmidt-Mende, J. L. MacManus-Driscoll, *Mater. Today* **2007**, *10*(5), 40–48.

[4] S. H. Ko, D. Lee, H. W. Kang, K. H. Nam, J. Y. Yeo, S. J. Hong, C. P. Grigoropoulos, H. J. Sung, *Nano Lett.* **2011**, *11*(2), 666–671.

[5] M. Sommer, S. Hüttner, S. Wunder, M. Thelakkat, *Adv. Mater.* **2008**, *20*(13), 2523–2527.

[6] M. Sommer, S. Huettner, M. Thelakkat, *J. Mater. Chem.* **2010**, *20*(48), 10788–10797.

[7] M. Templin, A. Franck, A. D. Chesne, H. Leist, Y. Zhang, R. Ulrich, V. Schädler, U. Wiesner, *Science* **1997**, *278*(5344), 1795–1798.

[8] J. Lee, M. Christopher Orilall, S. C. Warren, M. Kamperman, F. J. DiSalvo, U. Wiesner, *Nat. Mater.* **2008**, *7*(3), 222–228.

[9] J. Nelson, *The Physics of Solar Cells*, ICP, Imperial College Press, **2003**.

[10] R. R. King, D. C. Law, K. M. Edmondson, C. M. Fetzer, G. S. Kinsey, H. Yoon, R. A. Sherif, N. H. Karam, *Appl. Phys. Lett.* **2007**, *90*(18), 183516.

[11] J. Zhao, A. Wang, M. A. Green, F. Ferrazza, *Appl. Phys. Lett.* **1998**, *73*(14), 1991–1993.

[12] M. Tucci, G. de Cesare, *J. Non-Cryst. Solids* **2004**, *338-340*, 663–667.

[13] B. A. Gregg, *J. Phys. Chem. B* **2003**, *107*(20), 4688–4698.

[14] R. D. Schaller, V. I. Klimov, *Phys. Rev. Lett.* **2004**, *92*(18), 186601.

[15] X. Yang, J. Loos, *Macromolecules* **2007**, *40*(5), 1353–1362.

[16] K. M. Coakley, M. D. McGehee, *Chem. Mater.* **2004**, *16*(23), 4533–4542.

[17] N. S. Sariciftci, D. Braun, C. Zhang, V. I. Srdanov, A. J. Heeger, G. Stucky, F. Wudl, *Appl. Phys. Lett.* **1993**, *62*(6), 585–587.

[18] M. A. Green, K. Emery, Y. Hishikawa, W. Warta, *Prog. Photovoltaics* **2011**, *19*(1), 84–92.

[19] H. Hoppe, N. S. Sariciftci, *J. Mater. Chem.* **2006**, *16*(1), 45–61.

[20] W. U. Huynh, J. J. Dittmer, A. P. Alivisatos, *Science* **2002**, *295*(5564), 2425–2427.

[21] A. L. Linsebigler, G. Lu, J. T. Yates, *Chem. Rev.* **1995**, *95*(3), 735–758.

[22] X. Chen, S. S. Mao, *Chem. Rev.* **2007**, *107*(7), 2891–2959.

[23] B. O'Regan, M. Grätzel, *Nature* **1991**, *353*(6346), 737–740.

[24] A. C. Arango, S. A. Carter, P. J. Brock, *Appl. Phys. Lett.* **1999**, *74*(12), 1698–1700.

[25] K. Coakley, Y. Liu, M. McGehee, K. Frindell, G. Stucky, *Adv. Funct. Mater.* **2003**, *13*(4), 301–306.

[26] S. Zhang, X. Yang, Y. Numata, L. Han, *Energy Environ. Sci.* **2013**, *6*(5), 1443–1464.

[27] M. K. Nazeeruddin, S. M. Zakeeruddin, R. Humphry-Baker, M. Jirousek, P. Liska, N. Vlachopoulos, V. Shklover, C.-H. Fischer, M. Grätzel, *Inorg. Chem.* **1999**, *38*(26), 6298–6305.

[28] H. J. Snaith, L. Schmidt-Mende, *Adv. Mater.* **2007**, *19*(20), 3187–3200.

[29] J. Bisquert, D. Cahen, G. Hodes, S. Rühle, A. Zaban, *J. Phys. Chem. B* **2004**, *108*(24), 8106–8118.

[30] B. E. Hardin, H. J. Snaith, M. D. McGehee, *Nat. Photonics* **2012**, *6*(3), 162–169.

[31] A. Yella, H.-W. Lee, H. N. Tsao, C. Yi, A. K. Chandiran, M. K. Nazeeruddin, E. W.-G. Diau, C.-Y. Yeh, S. M. Zakeeruddin, M. Grätzel, *Science* **2011**, *334*(6056), 629–634.

[32] S. Rani, P. K. Shishodia, R. M. Mehra, *J. Renew. Sust. Energ.* **2010**, *2*(4), 043103–043103–8.

[33] U. Bach, D. Lupo, P. Comte, J. E. Moser, F. Weissörtel, J. Salbeck, H. Spreitzer, M. Grätzel, *Nature* **1998**, *395*(6702), 583–585.

[34] U. Bach. *Solid-state dye-sensitized mesoporous TiO_2 solar cells*, EPFL Lausanne, **2000**.

[35] E. J. W. Crossland, M. Kamperman, M. Nedelcu, C. Ducati, U. Wiesner, D. M. Smilgies, G. E. S. Toombes, M. A. Hillmyer, S. Ludwigs, U. Steiner, H. J. Snaith, *Nano Lett.* **2009**, *9*(8), 2807–2812.

[36] H. Kokubo, B. Ding, T. Naka, H. Tsuchihira, S. Shiratori, *Nanotechnology* **2007**, *18*(16), 165604.

[37] J. Wang, Z. Lin, *Chem. Mater.* **2008**, *20*(4), 1257–1261.

[38] H. Wang, C. C. Oey, A. B. Djurišić, M. H. Xie, Y. H. Leung, K. K. Y. Man, W. K. Chan, A. Pandey, J.-M. Nunzi, P. C. Chui, *Appl. Phys. Lett.* **2005**, *87*(2), 023507.

[39] M. Zukalová, A. Zukal, L. Kavan, M. K. Nazeeruddin, P. Liska, M. Grätzel, *Nano Lett.* **2005**, *5*(9), 1789–1792.

[40] M. Wei, Y. Konishi, H. Zhou, M. Yanagida, H. Sugihara, H. Arakawa, *J. Mater. Chem.* **2006**, *16*(13), 1287–1293.

[41] K. Zhu, N. R. Neale, A. Miedaner, A. J. Frank, *Nano Lett.* **2007**, *7*(1), 69–74.

[42] Y. Leprince-Wang, A. Yacoubi-Ouslim, G. Wang, *Microelectr. J.* **2005**, *36*(7), 625–628.

[43] X. Zhang, B. Yao, L. Zhao, C. Liang, L. Zhang, Y. Mao, *J. Electrochem. Soc.* **2001**, *148*(7), G398–G400.

[44] B. T. Holland, C. F. Blanford, A. Stein, *Science* **1998**, *281*(5376), 538–540.

[45] E. J. W. Crossland, M. Nedelcu, C. Ducati, S. Ludwigs, M. A. Hillmyer, U. Steiner, H. J. Snaith, *Nano Lett.* **2009**, *9*(8), 2813–2819.

[46] M. R. J. Scherer, L. Li, P. M. S. Cunha, O. A. Scherman, U. Steiner, *Adv. Mater.* **2012**, *24*(9), 1217–1221.

[47] D. Wei, M. R. J. Scherer, C. Bower, P. Andrew, T. Ryhänen, U. Steiner, *Nano Lett.* **2012**, *12*(4), 1857–1862.

[48] M. R. J. Scherer, U. Steiner, *Nano Lett.* **2012**, *13*(7), 3005–3010.

[49] Q. Zhang, C. S. Dandeneau, X. Zhou, G. Cao, *Adv. Mater.* **2009**, *21*(41), 4087–4108.

[50] A. Birkel, Y.-G. Lee, D. Koll, X. V. Meerbeek, S. Frank, M. J. Choi, Y. S. Kang, K. Char, W. Tremel, *Energy Environ. Sci.* **2012**, *5*(1), 5392–5400.

[51] A. Sacco, A. Lamberti, R. Gazia, S. Bianco, D. Manfredi, N. Shahzad, F. Cappelluti, S. Ma, E. Tresso, *Phys. Chem. Chem. Phys.* **2012**, *14*(47), 16203–16208.

[52] P. J. Flory, *J. Chem. Phys.* **1941**, *9*(8), 660–660.

[53] M. L. Huggins, *J. Chem. Phys.* **1941**, *9*(5), 440.

[54] M. Takenaka, T. Wakada, S. Akasaka, S. Nishitsuji, K. Saijo, H. Shimizu, M. I. Kim, H. Hasegawa, *Macromolecules* **2007**, *40*(13), 4399–4402.

[55] The Scientific Graphics Project, **2013**. URL http://archive.msri.org/about/sgp/jim/models/copolymers/morphologies/index.html.

[56] F. S. Bates, G. H. Fredrickson, *Phys. Today* **1999**, *52*(2), 32–38.

[57] T. Hashimoto, M. Shibayama, H. Kawai, *Macromolecules* **1980**, *13*(5), 1237–1247.

[58] M. W. Matsen, M. Schick, *Phys. Rev. Lett.* **1994**, *72*(16), 2660–2663.

[59] M. W. Matsen, F. S. Bates, *Macromolecules* **1996**, *29*(4), 1091–1098.

[60] A. K. Khandpur, S. Foerster, F. S. Bates, I. W. Hamley, A. J. Ryan, W. Bras, K. Almdal, K. Mortensen, *Macromolecules* **1995**, *28*(26), 8796–8806.

[61] M. W. Matsen, *Phys. Rev. Lett.* **2007**, *99*(14), 148304.

[62] D. M. Cooke, A.-C. Shi, *Macromolecules* **2006**, *39*(19), 6661–6671.

[63] N. A. Lynd, M. A. Hillmyer, *Macromolecules* **2005**, *38*(21), 8803–8810.

[64] E. J. W. Crossland. *Block Copolymer Patterning of Functional Materials*, University of Cambridge, **2008**.

[65] A. S. Finnemore, M. R. J. Scherer, R. Langford, S. Mahajan, S. Ludwigs, F. C. Meldrum, U. Steiner, *Adv. Mater.* **2009**, *21*(38-39), 3928–3932.

[66] M. Scherer. *Synthesis and Applications of Double-Gyroid-Structured Functional Materials*, University of Cambridge, **2012**.

[67] P. J. Gandy, J. Klinowski, *Chem. Phys. Lett.* **2000**, *321*(5–6), 363–371.

[68] M. Wohlgemuth, N. Yufa, J. Hoffman, E. L. Thomas, *Macromolecules* **2001**, *34*(17), 6083–6089.

[69] K. Michielsen, D. G. Stavenga, *J. R. Soc. Interface* **2008**, *5*(18), 85–94.

[70] Z. Almsherqi, F. Margadant, Y. Deng, *Interface Focus* **2012**, *2*(5), 539–545.

[71] V. Luzzati, P. A. Spegt, *Nature* **1967**, *215*(5102), 701–704.

[72] E. L. Thomas, D. B. Alward, D. J. Kinning, D. C. Martin, D. L. Handlin, L. J. Fetters, *Macromolecules* **1986**, *19*(8), 2197–2202.

[73] A. Nykänen, M. Nuopponen, A. Laukkanen, S.-P. Hirvonen, M. Rytelä, O. Turunen, H. Tenhu, R. Mezzenga, O. Ikkala, J. Ruokolainen, *Macromolecules* **2007**, *40*(16), 5827–5834.

[74] A. S. Zalusky, R. Olayo-Valles, J. H. Wolf, M. A. Hillmyer, *J. Am. Chem. Soc.* **2002**, *124*(43), 12761–12773.

[75] M. Scherer. *Nanostructured Materials via Self-Assembled Templates*, University of Cambridge, **2008**.

[76] T. H. Epps, E. W. Cochran, T. S. Bailey, R. S. Waletzko, C. M. Hardy, F. S. Bates, *Macromolecules* **2004**, *37*(22), 8325–8341.

[77] T. Goldacker, V. Abetz, *Macromolecules* **1999**, *32*(15), 5165–5167.

[78] M. J. Bluemle, G. Fleury, T. P. Lodge, F. S. Bates, *Soft Matter* **2009**, *5*(8), 1587–1590.

[79] O. Olabisi, L. M. Robeson, M. T. Shaw, *Polymer - Polymer Miscibility*, Academic Press, **1979**.

[80] W. van Zoelen, G. A. van Ekenstein, E. Polushkin, O. Ikkala, G. ten Brinke, *Soft Matter* **2005**, *1*(4), 280.

[81] O. Ikkala, G. ten Brinke, *Chem. Commun.* **2004**, *19*, 2131–2137.

[82] W. H. Binder, *Monatsh. Chem.* **2005**, *136*(1), 1–19.

[83] I. Podariu, A. Chakrabarti, *J. Chem. Phys.* **2003**, *118*(24), 11249–11257.

[84] Y. Yin, P. Sun, R. Jiang, B. Li, T. Chen, Q. Jin, D. Ding, A.-C. Shi, *J. Chem. Phys.* **2006**, *124*(18), 184708.

[85] H.-W. Park, J. Jung, T. Chang, K. Matsunaga, H. Jinnai, *J. Am. Chem. Soc.* **2009**, *131*(1), 46–47.

[86] E. J. W. Crossland, S. Ludwigs, M. A. Hillmyer, U. Steiner, *Soft Matter* **2010**, *6*(3), 670–676.

[87] E. J. W. Crossland, P. Cunha, S. Scroggins, S. Moratti, O. Yurchenko, U. Steiner, M. A. Hillmyer, S. Ludwigs, *ACS Nano* **2010**, *4*(2), 962–966.

[88] E. Kessels, M. Putkonen, *MRS Bull.* **2011**, *36*(11), 907–913.

[89] G. Triani, J. Campbell, P. Evans, J. Davis, B. Latella, R. Burford, *Thin Solid Films* **2010**, *518*(12), 3182–3189.

[90] J. Antson, T. Suntola. Method for producing compound thin films, **1977**. US4058430 A.

[91] S. G. Lindfors, A. J. Pakkala, T. S. Suntola. Method for performing growth of compound thin films, **1983**. US4413022 A.

[92] A. Ott, J. Klaus, J. Johnson, S. George, *Thin Solid Films* **1997**, *292*(1–2), 135–144.

[93] V. Aleskovskii, V. Drozd, V. Kiselev, S. Kozlov, S. Kol'tsov, A. Petrov, G. Plotnikov, *Sov. Phys. Semicond+.* **1979**, *13*(7), 1397–1401.

[94] H. Kim, H.-B.-R. Lee, W.-J. Maeng, *Thin Solid Films* **2009**, *517*(8), 2563–2580.

[95] M. Knez, K. Nielsch, L. Niinistö, *Adv. Mater.* **2007**, *19*(21), 3425–3438.

[96] L. Niinistö, J. Nieminen, M.Päiväsaari, J. Niinistö, M. Putkonen, M. Nieminen, *Phys. Status Solidi A* **2004**, *201*(7), 1443–1452.

[97] H. Wojcik, C. Hossbach, C. Kubasch, P. Verdonck, Y. Barbarin, U. Merkel, J. W. Bartha, R. Hübner, H.-J. Engelmann, M. Friedemann, *Microelectron. Eng.* **2013**, *110*, 29–34.

[98] O. Sneh, R. B. Clark-Phelps, A. R. Londergan, J. Winkler, T. E. Seidel, *Thin Solid Films* **2002**, *402*(1–2), 248–261.

[99] R. L. Puurunen, J. Saarilahti, H. Kattelus, *ECS Trans.* **2007**, *11*(7), 3–14.

[100] B. Davidson, D. Seghete, S. George, V. Bright, *Sensor. Actuat. A-Phys.* **2011**, *166*(2), 269–276.

[101] TCO for Photovoltaics | Beneq. URL http://www.beneq.com/tco-photovoltaics.html.

[102] D. P. Gaillot, C. J. Summers. In N. Pinna, M. Knez, editors, *Atomic Layer Deposition of Nanostructured Materials*, 345–376. Wiley-VCH, **2011**.

[103] J. A. v. Delft, D. Garcia-Alonso, W. M. M. Kessels, *Semicond. Sci. Technol.* **2012**, *27*(7), 074002.

[104] J. R. Bakke, K. L. Pickrahn, T. P. Brennan, S. F. Bent, *Nanoscale* **2011**, *3*(9), 3482–3508.

[105] G. Eldallal, M. Abou-Elwafa, M. Elgammal, S. Bedair, *Renew. Energ.* **1995**, *6*(7), 713–718.

[106] Y. Ohtake, K. K. Ichikawa, A. Yamada, M. Konagai, *Jpn. J. Appl. Phys.* **1995**, *34*(Part 1, No. 11), 5949–5955.

[107] B. Sang, K. Dairiki, A. Yamada, M. Konagai, *Jpn. J. Appl. Phys.* **1999**, *38*(Part 1, No. 9A), 4983–4988.

[108] L. J. Antila, M. J. Heikkilä, V. Mäkinen, N. Humalamäki, M. Laitinen, V. Linko, P. Jalkanen, J. Toppari, V. Aumanen, M. Kemell, P. Myllyperkiö, K. Honkala, H. Häkkinen, M. Leskelä, J. E. I. Korppi-Tommola, *J. Phys. Chem. C* **2011**, *115*(33), 16720–16729.

[109] A. B. F. Martinson, J. W. Elam, J. Liu, M. J. Pellin, T. J. Marks, J. T. Hupp, *Nano Lett.* **2008**, *8*(9), 2862–2866.

[110] C. Y. Jiang, W. L. Koh, M. Y. Leung, S. Y. Chiam, J. S. Wu, J. Zhang, *Appl. Phys. Lett.* **2012**, *100*(11), 113901–113901–4.

[111] T. W. Hamann, A. B. F. Martinson, J. W. Elam, M. J. Pellin, J. T. Hupp, *J. Phys. Chem. C* **2008**, *112*(27), 10303–10307.

[112] T. W. Hamann, A. B. F. Martinson, J. W. Elam, M. J. Pellin, J. T. Hupp, *Adv. Mater.* **2008**, *20*(8), 1560–1564.

[113] S. K. Sarkar, J. Y. Kim, D. N. Goldstein, N. R. Neale, K. Zhu, C. M. Elliott, A. J. Frank, S. M. George, *J. Phys. Chem. C* **2010**, *114*(17), 8032–8039.

[114] H. Wedemeyer, J. Michels, R. Chmielowski, S. Bourdais, T. Muto, M. Sugiura, G. Dennler, J. Bachmann, *Energy Environ. Sci.* **2012**, *6*(1), 67–71.

[115] C. Prasittichai, J. T. Hupp, *J. Phys. Chem. Lett.* **2010**, *1*(10), 1611–1615.

[116] T.-C. Tien, F.-M. Pan, L.-P. Wang, F.-Y. Tsai, C. Lin, *J. Phys. Chem. C* **2010**, *114*(21), 10048–10053.

[117] V. Ganapathy, B. Karunagaran, S.-W. Rhee, *J. Power Sources* **2010**, *195*(15), 5138–5143.

[118] L. J. Antila, M. J. Heikkilä, V. Aumanen, M. Kemell, P. Myllyperkiö, M. Leskelä, J. E. I. Korppi-Tommola, *J. Phys. Chem. Lett.* **2010**, *1*(2), 536–539.

[119] T.-C. Tien, F.-M. Pan, L.-P. Wang, C.-H. Lee, Y.-L. Tung, S.-Y. Tsai, C. Lin, F.-Y. Tsai, S.-J. Chen, *Nanotechnology* **2009**, *20*(30), 305201.

[120] C. Lin, F.-Y. Tsai, M.-H. Lee, C.-H. Lee, T.-C. Tien, L.-P. Wang, S.-Y. Tsai, *J. Mater. Chem.* **2009**, *19*(19), 2999–3003.

[121] K. Ellmer, *Mater. Lett.* **2012**, *6*(12), 809–817.

[122] F. Kurdesau, G. Khripunov, A. da Cunha, M. Kaelin, A. Tiwari, *J. Non-Cryst. Solids* **2006**, *352*(9–20), 1466–1470.

[123] L. Chongmu, *J. Korean Phys. Soc.* **2010**, *56*(2), 576.

[124] D.-J. Lee, K.-J. Kim, S.-H. Kim, J.-Y. Kwon, J. Xu, K.-B. Kim, *J. Mater. Chem. C* **2013**, *1*(31), 4761–4769.

[125] D. H. Kim, M. Woodroof, K. Lee, G. N. Parsons, *ChemSusChem* **2013**, *6*(6), 1014–1020.

[126] A. B. F. Martinson, M. S. Góes, F. Fabregat-Santiago, J. Bisquert, M. J. Pellin, J. T. Hupp, *J. Phys. Chem. A* **2009**, *113*(16), 4015–4021.

[127] M. Nanu, L. Reijnen, B. Meester, J. Schoonman, A. Goossens, *Chem. Vapor. Depos.* **2004**, *10*(1), 45–49.

[128] R. B. Yang, J. Bachmann, M. Reiche, J. W. Gerlach, U. Gösele, K. Nielsch, *Chem. Mater.* **2009**, *21*(13), 2586–2588.

[129] J. A. Chang, J. H. Rhee, S. H. Im, Y. H. Lee, H.-j. Kim, S. I. Seok, M. K. Nazeeruddin, M. Gratzel, *Nano Lett.* **2010**, *10*(7), 2609–2612.

[130] R. L. Puurunen, *J. Appl. Phys.* **2005**, *97*(12), 121301.

[131] V. Miikkulainen, M. Leskelä, M. Ritala, R. L. Puurunen, *Appl. Phys. Rev.* **2013**, *2013*(1), 2–2.

[132] M. D. Groner, F. H. Fabreguette, J. W. Elam, S. M. George, *Chem. Mater.* **2004**, *16*(4), 639–645.

[133] A. Rahtu, T. Alaranta, M. Ritala, *Langmuir* **2001**, *17*(21), 6506–6509.

[134] R. L. Puurunen, M. Lindblad, A. Root, A. O. I. Krause, *Phys. Chem. Chem. Phys.* **2001**, *3*(6), 1093–1102.

[135] H. Kumagai, M. Matsumoto, Y. Kawamura, K. Toyoda, M. Obara, *Jpn. J. Appl. Phys.* **1994**, *33*(Part 1, No. 12B), 7086–7089.

[136] R. Kuse, M. Kundu, T. Yasuda, N. Miyata, A. Toriumi, *J. Appl. Phys.* **2003**, *94*(10), 6411–6416.

[137] R. L. Puurunen, *Appl. Surf. Sci.* **2005**, *245*(1–4), 6–10.

[138] J. Aarik, A. Aidla, T. Uustare, V. Sammelselg, *J. Cryst. Growth* **1995**, *148*(3), 268–275.

[139] N. Taewook, K. Jae-Min, K. Min-Kyu, K. Hyungjun, K. Woo-Hee, *J. Korean Phys. Soc.* **2011**, *59*(21), 452.

[140] M. Ritala, M. Leskelä, E. Nykänen, P. Soininen, L. Niinistö, *Thin Solid Films* **1993**, *225*(1–2), 288–295.

[141] J. Aarik. *Atomic layer deposition of titanium, zirconium and hafnium dioxides: growth mechanisms and properties of thin films*, University of Tartu, Tartu, **2007**.

[142] V. Lujala, J. Skarp, M. Tammenmaa, T. Suntola, *Appl. Surf. Sci.* **1994**, *82–83*, 34–40.

[143] B. Sang, M. Konagai, *Jpn. J. Appl. Phys.* **1996**, *35*(Part 2, No. 5B), L602–L605.

[144] Y.-M. Chang, S.-R. Jian, H.-Y. Lee, C.-M. Lin, J.-Y. Juang, *Nanotechnology* **2010**, *21*(38), 385705.

[145] J. Libera, J. Elam, M. Pellin, *Thin Solid Films* **2008**, *516*(18), 6158–6166.

[146] X. Jiang, S. F. Bent, *J. Phys. Chem. C* **2009**, *113*(41), 17613–17625.

[147] E. Färm, M. Kemell, M. Ritala, M. Leskelä, *J. Phys. Chem. C* **2008**, *112*(40), 15791–15795.

[148] D. B. Farmer, R. G. Gordon, *Nano Lett.* **2006**, *6*(4), 699–703.

[149] S. Jandhyala, G. Mordi, B. Lee, G. Lee, C. Floresca, P.-R. Cha, J. Ahn, R. M. Wallace, Y. J. Chabal, M. J. Kim, L. Colombo, K. Cho, J. Kim, *ACS Nano* **2012**, *6*(3), 2722–2730.

[150] M. Puttaswamy, K. B. Haugshøj, L. Højslet Christensen, P. Kingshott, *Chem-Eur. J.* **2010**, *16*(47), 13925–13929.

[151] C. A. Wilson, R. K. Grubbs, S. M. George, *Chem. Mater.* **2005**, *17*(23), 5625–5634.

[152] J.-S. Park, H. Chae, H. K. Chung, S. I. Lee, *Semicond. Sci. Technol.* **2011**, *26*(3), 034001.

[153] J. W. Elam, D. Routkevitch, P. P. Mardilovich, S. M. George, *Chem. Mater.* **2003**, *15*(18), 3507–3517.

[154] R. Gordon, D. Hausmann, E. Kim, J. Shepard, *Chem. Vapor. Depos.* **2003**, *9*(2), 73–78.

[155] C. Detavernier, J. Dendooven, S. P. Sree, K. F. Ludwig, J. A. Martens, *Chem. Soc. Rev.* **2011**, *40*(11), 5242–5253.

[156] S. K. Karuturi, L. Liu, L. T. Su, Y. Zhao, H. J. Fan, X. Ge, S. He, A. T. I. Yoong, *J. Phys. Chem. C* **2010**, *114*(35), 14843–14848.

[157] S. K. Karuturi, L. Liu, L. T. Su, A. Chutinan, N. P. Kherani, T. K. Chan, T. Osipowicz, A. I. Y. Tok, *Nanoscale* **2011**, *3*(12), 4951–4954.

[158] J. Bachmann, Jing, M. Knez, S. Barth, H. Shen, S. Mathur, U. Gösele, K. Nielsch, *J. Am. Chem. Soc.* **2007**, *129*(31), 9554–9555.

[159] M. Daub, M. Knez, U. Goesele, K. Nielsch, *J. Appl. Phys.* **2007**, *101*(9), 09J111–09J111–3.

[160] T. Scharf, S. Prasad, M. Dugger, P. Kotula, R. Goeke, R. Grubbs, *Acta Materialia* **2006**, *54*(18), 4731–4743.

[161] H. Shin, D.-K. Jeong, J. Lee, M. M. Sung, J. Kim, *Adv. Mater.* **2004**, *16*(14), 1197–1200.

[162] Z. A. Sechrist, B. T. Schwartz, J. H. Lee, J. A. McCormick, R. Piestun, W. Park, S. M. George, *Chem. Mater.* **2006**, *18*(15), 3562–3570.

[163] J. Biener, T. F. Baumann, Y. Wang, E. J. Nelson, S. O. Kucheyev, A. V. Hamza, M. Kemell, M. Ritala, M. Leskelä, *Nanotechnology* **2007**, *18*(5), 055303.

[164] S. O. Kucheyev, J. Biener, T. F. Baumann, Y. M. Wang, A. V. Hamza, Z. Li, D. K. Lee, R. G. Gordon, *Langmuir* **2008**, *24*(3), 943–948.

[165] The International Centre for Diffraction Data. URL http://www.icdd.com/.

[166] SAS / GISAS Analysis Package. URL http://steiner.bss.phy.cam.ac.uk/facilities/sas-gisas-analysis-package.

[167] P. Busch, M. Rauscher, D.-M. Smilgies, D. Posselt, C. M. Papadakis, *J. Appl. Crystallogr.* **2006**, *39*(3), 433–442.

[168] G. E. Stein, E. J. Kramer, X. Li, J. Wang, *Macromolecules* **2007**, *40*(7), 2453–2460.

[169] T. Xu, J. T. Goldbach, M. J. Misner, S. Kim, A. Gibaud, O. Gang, B. Ocko, K. W. Guarini, C. T. Black, C. J. Hawker, T. P. Russell, *Macromolecules* **2004**, *37*(8), 2972–2977.

[170] M. Li, K. Douki, K. Goto, X. Li, C. Coenjarts, D. M. Smilgies, C. K. Ober, *Chem. Mater.* **2004**, *16*(20), 3800–3808.

[171] B. Lee, I. Park, J. Yoon, S. Park, J. Kim, K.-W. Kim, T. Chang, M. Ree, *Macromolecules* **2005**, *38*(10), 4311–4323.

[172] I. Park, B. Lee, J. Ryu, K. Im, J. Yoon, M. Ree, T. Chang, *Macromolecules* **2005**, *38*(25), 10532–10536.

[173] V. N. Urade, T.-C. Wei, M. P. Tate, J. D. Kowalski, H. W. Hillhouse, *Chem. Mater.* **2007**, *19*(4), 768–777.

[174] D. Smilgies, P. Busch, C. M. Papadakis, D. Posselt, *Synchrotron Radiat. News* **2002**, *15*(5), 35–42.

[175] R. M. A. Azzam, N. M. Bashara, *Ellipsometry and polarized light*, North-Holland, **1987**.

[176] D. M. King, X. Du, A. S. Cavanagh, A. W. Weimer, *Nanotechnology* **2008**, *19*(44), 445401.

[177] J. Ahmad Banday, *Am. J. Anal. Chem.* **2012**, *03*(03), 204–209.

[178] T. Watanabe, *Nano-plating: microstructure control theory of plated film and data base of plated film microstructure*, Elsevier, Amsterdam, **2004**.

[179] S. Trasatti, O. Petrii, *J. Electroanal. Chem.* **1992**, *327*(1–2), 353–376.

[180] A. Lasia. In B. E. Conway, J. O. Bockris, R. E. White, editors, *Modern Aspects of Electrochemistry*, number 32 in Modern Aspects of Electrochemistry, 143–248. Springer US, **2002**.

[181] A. J. Bard, L. R. Faulkner, *Electrochemical Methods: Fundamentals and Applications*, Wiley, **2000**.

[182] G. H. A. Therese, P. V. Kamath, *Chem. Mater.* **2000**, *12*(5), 1195–1204.

[183] L. Vayssieres, *On Solar Hydrogen and Nanotechnology*, John Wiley & Sons, **2010**.

[184] T. Pauporté, A. Goux, A. Kahn-Harari, N. de Tacconi, C. Chenthamarakshan, K. Rajeshwar, D. Lincot, *J. Phys. Chem. Solids* **2003**, *64*(9–10), 1737–1742.

[185] L. Kavan, M. Grätzel, *Electrochim. Acta* **1995**, *40*(5), 643–652.

[186] Y. Ren, Y.-Z. Zheng, J. Zhao, J.-F. Chen, W. Zhou, X. Tao, *Electrochem. Commun.* **2012**, *16*(1), 57–60.

[187] M. K. Nazeeruddin, A. Kay, I. Rodicio, R. Humphry-Baker, E. Mueller, P. Liska, N. Vlachopoulos, M. Graetzel, *J. Am. Chem. Soc.* **1993**, *115*(14), 6382–6390.

[188] D. Kuang, S. Ito, B. Wenger, C. Klein, J.-E. Moser, R. Humphry-Baker, S. M. Zakeeruddin, M. Grätzel, *J. Am. Chem. Soc.* **2006**, *128*(12), 4146–4154.

[189] H. J. Snaith, L. Schmidt-Mende, M. Grätzel, M. Chiesa, *Phys. Rev. B* **2006**, *74*(4), 045306.

[190] W. A. Braunecker, K. Matyjaszewski, *Prog. Polym. Sci.* **2007**, *32*(1), 93–146.

[191] K. Matyjaszewski, N. V. Tsarevsky, *Nat. Chem.* **2009**, *1*(4), 276–288.

[192] N. E. Kamber, W. Jeong, R. M. Waymouth, R. C. Pratt, B. G. G. Lohmeijer, J. L. Hedrick, *Chem. Rev.* **2007**, *107*(12), 5813–5840.

[193] J.-S. Wang, K. Matyjaszewski, *J. Am. Chem. Soc.* **1995**, *117*(20), 5614–5615.

[194] M. Szwarc, *Nature* **1956**, *178*(4543), 1168–1169.

[195] M. A. White, J. A. Johnson, J. T. Koberstein, N. J. Turro, *J. Am. Chem. Soc.* **2006**, *128*(35), 11356–11357.

[196] C. Jérôme, P. Lecomte, *Adv. Drug. Deliver. Rev.* **2008**, *60*(9), 1056–1076.

[197] R. C. Pratt, B. G. G. Lohmeijer, D. A. Long, P. N. P. Lundberg, A. P. Dove, H. Li, C. G. Wade, R. M. Waymouth, J. L. Hedrick, *Macromolecules* **2006**, *39*(23), 7863–7871.

[198] L. O. Grondahl. Unidirectional current-carrying device, **1927**. 1640335.

[199] C. F. Klingshirn, *Semiconductor Optics*, Springer, **2007**.

[200] W. H. Brattain, *Rev. Mod. Phys.* **1951**, *23*(3), 203–212.

[201] D. Trivich, L. Papadimitriou, N. A. Economou, *Sol. Cells* **1981**, *3*(1), 73–80.

[202] C. Wadia, A. P. Alivisatos, D. M. Kammen, *Environ. Sci. Technol.* **2009**, *43*(6), 2072–2077.

[203] L. Olsen, F. Addis, W. Miller, *Sol. Cells* **1982**, *7*(3), 247–279.

[204] B. Rai, *Sol. Cells* **1988**, *25*(3), 265–272.

[205] A. Mittiga, E. Salza, F. Sarto, M. Tucci, R. Vasanthi, *Appl. Phys. Lett.* **2006**, *88*(16), 163502.

[206] L. C. Olsen, R. C. Bohara, M. W. Urie, *Appl. Phys. Lett.* **1979**, *34*(1), 47–49.

[207] K. Akimoto, S. Ishizuka, M. Yanagita, Y. Nawa, G. K. Paul, T. Sakurai, *Sol. Energy* **2006**, *80*(6), 715–722.

[208] J. Herion, E. Niekisch, G. Scharl, *Sol. Energ. Mater.* **1980**, *4*(1), 101–112.

[209] J. A. Assimos, D. Trivich, *Phys. Status Solidi A* **1974**, *26*(2), 477–488.

[210] L. M. Wong, S. Y. Chiam, J. Q. Huang, S. J. Wang, J. S. Pan, W. K. Chim, *J. Appl. Phys.* **2010**, *108*(3), 033702.

[211] S. W. Boettcher, J. M. Spurgeon, M. C. Putnam, E. L. Warren, D. B. Turner-Evans, M. D. Kelzenberg, J. R. Maiolo, H. A. Atwater, N. S. Lewis, *Science* **2010**, *327*(5962), 185–187.

[212] J. R. Maiolo, B. M. Kayes, M. A. Filler, M. C. Putnam, M. D. Kelzenberg, H. A. Atwater, N. S. Lewis, *J. Am. Chem. Soc.* **2007**, *129*(41), 12346–12347.

[213] J. R. Maiolo, H. A. Atwater, N. S. Lewis, *J. Phys. Chem. C* **2008**, *112*(15), 6194–6201.

[214] M. J. Price, S. Maldonado, *J. Phys. Chem. C* **2009**, *113*(28), 11988–11994.

[215] M. Pourbaix, *Thermodynamics of dilute aqueous solutions*, E. Arnold, **1949**.

[216] J. L. Sculfort, D. Guyomard, M. Herlem, *Electrochim. Acta* **1984**, *29*(4), 459–465.

[217] Y. Tachibana, R. Muramoto, H. Matsumoto, S. Kuwabata, *Res. Chem. Intermediat.* **2006**, *32*(5-6), 575–583.

[218] J. L. Robbins, N. Edelstein, B. Spencer, J. C. Smart, *J. Am. Chem. Soc.* **1982**, *104*(7), 1882–1893.

[219] C. Xiang, G. M. Kimball, R. L. Grimm, B. S. Brunschwig, H. A. Atwater, N. S. Lewis, *Energy Environ. Sci.* **2011**, *4*(4), 1311–1318.

[220] A. Musa, T. Akomolafe, M. Carter, *Sol. Energ. Mat. Sol. C.* **1998**, *51*(3–4), 305–316.

[221] M. O'Keeffe, W. J. Moore, *J. Chem. Phys.* **1962**, *36*(11), 3009–3013.

[222] G. K. Paul, Y. Nawa, H. Sato, T. Sakurai, K. Akimoto, *Appl. Phys. Lett.* **2006**, *88*(14), 141901.

[223] R. P. Wijesundera, *Semicond. Sci. Technol.* **2010**, *25*(4), 045015.

[224] Y. Tang, Z. Chen, Z. Jia, L. Zhang, J. Li, *Mater. Lett.* **2005**, *59*(4), 434–438.

[225] R. Wijesundera, M. Hidaka, K. Koga, M. Sakai, W. Siripala, *Thin Solid Films* **2006**, *500*(1–2), 241–246.

[226] N.A. Economou, R.S. Toth, R.J. Komp, D. Trivich. In *Photovoltaic cells of electrodeposited cuprous oxide*. New York, **1982** 1180–1185.

[227] S. Jeong, A. Mittiga, E. Salza, A. Masci, S. Passerini, *Electrochim. Acta* **2008**, *53*(5), 2226–2231.

[228] K. P. Musselman, A. Marin, L. Schmidt-Mende, J. L. MacManus-Driscoll, *Adv. Funct. Mater.* **2012**, *22*(10), 2202–2208.

[229] L. Tsakalakos, J. Balch, J. Fronheiser, B. A. Korevaar, O. Sulima, J. Rand, *Appl. Phys. Lett.* **2007**, *91*(23), 233117.

[230] S. Ishizuka, K. Suzuki, Y. Okamoto, M. Yanagita, T. Sakurai, K. Akimoto, N. Fujiwara, H. Kobayashi, K. Matsubara, S. Niki, *Phys. Status Solidi C* **2004**, *1*(4), 1067–1070.

[231] S. Suzuki, T. Miyata, T. Minami. In *Papers from the 49th International Symposium of the American Vacuum Society*, volume 21. AVS, Denver, Colorado (USA), **2003** 1336–1341.

[232] Y. Nakano, S. Saeki, T. Morikawa, *Appl. Phys. Lett.* **2009**, *94*(2), 022111.

[233] F. Biccari. *Defects And Doping In Cu_2O*, University of Rome, Sapienza, **2010**.

[234] J.-W. Chen, D.-C. Perng, J.-F. Fang, *Sol. Energ. Mat. Sol. C.* **2011**, *95*(8), 2471–2477.

[235] L. Papadimitriou, N. A. Economou, D. Trivich, *Sol. Cells* **1981**, *3*(1), 73–80.

[236] B. M. Fariza, J. Sasano, T. Shinagawa, H. Nakano, S. Watase, M. Izaki, *J. Electrochem. Soc.* **2011**, *158*(10), D621–D625.

[237] F. Shao, J. Sun, L. Gao, J. Luo, Y. Liu, S. Yang, *Adv. Funct. Mater.* **2012**, *22*(18), 3907–3913.

[238] R. N. Briskman, *Sol. Energ. Mat. Sol. C.* **1992**, *27*(4), 361–368.

[239] A.D. Smigelskas, E.O. Kirkendall, *Trans. AIME* **1947**, *171*, 130–142.

[240] H. J. Fan, U. Gösele, M. Zacharias, *Small* **2007**, *3*(10), 1660–1671.

[241] H. Jin Fan, M. Knez, R. Scholz, K. Nielsch, E. Pippel, D. Hesse, M. Zacharias, U. Gösele, *Nat. Mater.* **2006**, *5*(8), 627–631.

[242] Y. Ren, W. K. Chim, S. Y. Chiam, J. Q. Huang, C. Pi, J. S. Pan, *Adv. Funct. Mater.* **2010**, *20*(19), 3336–3342.

[243] A.-A. El Mel, M. Buffière, P.-Y. Tessier, S. Konstantinidis, W. Xu, K. Du, I. Wathuthanthri, C.-H. Choi, C. Bittencourt, R. Snyders, *Small* **2013**, *2013*, 1–6.

[244] S. R. Chun, W. A. Sasangka, M. Z. Ng, Q. Liu, A. Du, J. Zhu, C. M. Ng, Z. Q. Liu, S. Y. Chiam, C. L. Gan, *Small* **2013**, *2013*, 1–7.

[245] Y. Shi, H. Li, L. Chen, X. Huang, *Sci. Technol. Adv. Mater.* **2005**, *6*(7), 761.

[246] S. Kumar, D. Saini, G. S. Lotey, N. Verma, *Superlattice. Microst.* **2011**, *50*(6), 698–702.

[247] X. Liu, Y. Zhou, *J. Mater. Res.* **2005**, *20*(09), 2371–2378.

[248] A. Keilbach, J. Moses, R. Köhn, M. Döblinger, T. Bein, *Chem. Mater.* **2010**, *22*(19), 5430–5436.

[249] S. Valizadeh, J. George, P. Leisner, L. Hultman, *Electrochim. Acta* **2001**, *47*(6), 865–874.

[250] G. Gunawardena, G. Hills, I. Montenegro, *Electrochim. Acta* **1978**, *23*(8), 693–697.

[251] P. Keil, D. Lützenkirchen-Hecht, R. Frahm. In *Investigation of Room Temperature Oxidation of Cu in Air by Yoneda-XAFS*, volume 882. AIP, **2007** 490–492.

[252] V. Jović, B. Jović, *J. Electroanal. Chem.* **2003**, *541*, 13–21.

[253] M. Schlesinger, *Modern electroplating*, Wiley, Hoboken, NJ, **2010**.

[254] J. T. Hinatsu, F. R. Foulkes, *J. Electrochem. Soc.* **1989**, *136*(1), 125–132.

[255] D. Grujicic, B. Pesic, *Electrochim. Acta* **2002**, *47*(18), 2901–2912.

[256] M. E. T. Molares, V. Buschmann, D. Dobrev, R. Neumann, R. Scholz, I. U. Schuchert, J. Vetter, *Adv. Mater.* **2001**, *13*(1), 62–65.

[257] Z. Liu, Y. Bando, *Chem. Phys. Lett.* **2003**, *378*(1–2), 85–88.

[258] W. Dong, J. Zhang, J. Zheng, J. Sheng, *Mater. Lett.* **2008**, *62*(10–11), 1589–1591.

[259] J. M. E. Harper, C. Cabral, P. C. Andricacos, L. Gignac, I. Noyan, K. Rodbell, C.-K. Hu, *J. Appl. Phys.* **1999**, *86*(5), 2516–2525.

[260] N. A. Weir, *J. Macromol. Sci. B* **1975**, *11*(4), 553–563.

[261] Y.-I. Lee, Y.-S. Goo, C.-H. Chang, K.-J. Lee, N. V. Myung, Y.-H. Choa, *J. Nanosci. Nanotechnol.* **2011**, *11*(2), 1455–1458.

[262] S. Poulston, P. M. Parlett, P. Stone, M. Bowker, *Surf. Interface Anal.* **1996**, *24*(12), 811–820.

[263] Lee S.Y., Mettlach N., Nguyen N., Sun Y.M., White J.M., *Appl. Surf. Sci.* **2003**, *206*(1), 102–109.

[264] D. B. Pedersen, S. Wang, S. H. Liang, *J. Phys. Chem. C* **2008**, *112*(24), 8819–8826.

[265] B. P. Rai, *Phys. Status Solidi A* **1987**, *99*(1), K35–K39.

[266] S. Vignolini, N. A. Yufa, P. S. Cunha, S. Guldin, I. Rushkin, M. Stefik, K. Hur, U. Wiesner, J. J. Baumberg, U. Steiner, *Adv. Mater.* **2012**, *24*(10), OP23–OP27.

[267] S. Salvatore, A. Demetriadou, S. Vignolini, S. S. Oh, S. Wuestner, N. A. Yufa, M. Stefik, U. Wiesner, J. J. Baumberg, O. Hess, U. Steiner, *Adv. Mater.* **2013**, *25*(19), 2713–2716.

[268] S. Santucci, P. Picozzi, *Thin Solid Films* **1984**, *113*(3), 243–250.

[269] Y. Abdu, A. O. Musa, *Bayero J. Pure Appl. Sci.* **2009**, *2*(2), 8–12.

[270] J. Pierson, A. Thobor-Keck, A. Billard, *Appl. Surf. Sci.* **2003**, *210*(3–4), 359–367.

[271] V. Hendrick, E. Muniz, G. Geuskens, J. Wérenne, *Cytotechnology* **2001**, *36*(1-3), 49–53.

[272] A. S. Curtis, J. V. Forrester, C. McInnes, F. Lawrie, *J. Cell Biol.* **1983**, *97*(5 Pt 1), 1500–1506, PMID: 6355120.

[273] W. Zhao, H. Y. Low, P. S. Suresh, *Langmuir* **2006**, *22*(12), 5520–5524.

[274] D. L. Bunbury, *Can. J. Chem.* **1965**, *43*(6), 1714–1719.

[275] K. Watanabe, H. Ishikawa, W. Ando, *B. Chem. Soc. Jpn.* **1978**, *51*(4), 1253–1254.

[276] J. Mack, J. R. Bolton, *J. Photoch. Photobio. A* **1999**, *128*(1–3), 1–13.

[277] N. Jayaswal, S. Sinha, A. Kumar, *J. Appl. Polym. Sci.* **2001**, *79*(10), 1735–1748.

[278] D. Vione, V. Maurino, C. Minero, D. Borghesi, M. Lucchiari, E. Pelizzetti, *Environ. Sci. Technol.* **2003**, *37*(20), 4635–4641.

[279] A. Hambardzumyan, S. Biltresse, Y. Dufrêne, J. Marchand-Brynaert, *J. Colloid. Interface. Sci.* **2002**, *252*(2), 443–449.

[280] B. W. Callen, M. L. Ridge, S. Lahooti, A. W. Neumann, R. N. S. Sodhi, *J. Vac. Sci. Technol. A* **1995**, *13*(4), 2023–2029.

[281] B. Mailhot, J. L. Gardette, *Macromolecules* **1992**, *25*(16), 4119–4126.

[282] D. O. H. Teare, C. Ton-That, R. H. Bradley, *Surf. Interface Anal.* **2000**, *29*(4), 276–283.

[283] M. Davidson, S. Mitchell, R. Bradley, *Surf. Sci.* **2005**, *581*(2–3), 169–177.

[284] J. López-Gejo, H. Gliemann, T. Schimmel, A. M. Braun, *Photochem. Photobiol.* **2005**, *81*(4), 777–782.

[285] M. L. Steen, A. C. Jordan, E. R. Fisher, *J. Membrane Sci.* **2002**, *204*(1–2), 341–357.

[286] E. S. Brandt, J. M. Grace, *J. Vac. Sci. Technol. A* **2012**, *30*(1), 01A137.

[287] E. Partouche, D. Waysbort, S. Margel, *J. Colloid. Interface. Sci.* **2006**, *294*(1), 69–78.

[288] S. Mitchell, A. Poulsson, M. Davidson, R. Bradley, *Colloids Surface B* **2005**, *46*(2), 108–116.

[289] R. Criegee, *Angew. Chem. Int. Edit.* **1975**, *14*(11), 745–752.

[290] J. Rzayev, M. A. Hillmyer, *J. Am. Chem. Soc.* **2005**, *127*(38), 13373–13379.

[291] A. Londergan, *Atomic Layer Deposition Applications 4*, The Electrochemical Society, **2008**.

[292] M. Tajbakhsh, R. Hosseinzadeh, H. Alinezhad, S. Ghahari, A. Heydari, S. Khaksar, *Synthesis* **2010**, *2011*(03), 490–496.

[293] S. Sato, T. Sakamoto, E. Miyazawa, Y. Kikugawa, *Tetrahedron* **2004**, *60*(36), 7899–7906.

[294] Vahak Abedi. *Development of aldehyde selective organoaluminum reagents for organic synthesis*, University of Florida, **1991**.

[295] A. Brzezinski, Y.-C. Chen, P. Wiltzius, P. V. Braun, *J. Mater. Chem.* **2009**, *19*(48), 9126–9130.

[296] H. Kim, E. Pippel, U. Gösele, M. Knez, *Langmuir* **2009**, *25*(23), 13284–13289.

[297] A. Ravve, *Principles of Polymer Chemistry*, Springer, **2012**.

[298] E. G. Derouane, *Micropor. Mesopor. Mat.* **2007**, *104*(1–3), 46–51.

[299] A. Lucas, I. Derycke, P. Lambin, J.-P. Vigneron, L. Leherte, M. Elanany, J.-M. André, A. Larin, D. Vercauteren, *J. Mol. Catal. A-Chem.* **2009**, *305*(1–2), 16–23.

[300] D. N. Jaguste, S. K. Bhatia, *Chem. Eng. Sci.* **1995**, *50*(2), 167–182.

[301] H.-C. Wang, C.-H. Liao, Y.-L. Chueh, C.-C. Lai, P.-C. Chou, S.-Y. Ting, *Opt. Mater. Express* **2013**, *3*(2), 295–306.

[302] N. Yoshii, A. Nakamura, S. Hosaka, J. Temmyo, *J. Electrochem. Soc.* **2009**, *156*(7), K117–K120.

[303] J. Malm, E. Sahramo, J. Perälä, T. Sajavaara, M. Karppinen, *Thin Solid Films* **2011**, *519*(16), 5319–5322.

[304] M. Long, W. Cai, H. Chen, J. Xu, *Front. Chem. China* **2007**, *2*(3), 278–282.

[305] X. Jiang, B. P. Bastakoti, W. Weng, T. Higuchi, H. Oveisi, N. Suzuki, W.-J. Chen, Y.-T. Huang, Y. Yamauchi, *Chemistry* **2013**, *2013*, 1–8.

[306] S. D. Gendt, S. F. Bent, A. Delabie, J. W. Elam, S. B. Kang, A. Londergan, O. van der Straten, *Atomic Layer Deposition Applications 5*, The Electrochemical Society, **2009**.

[307] R. Kuzel, L. Nichtova, Z. Matej, J. Musil, *Thin Solid Films* **2010**, *519*(5, SI), 1649–1654.

[308] Y. S. Kim, S. Jin Yun, *J. Cryst. Growth* **2005**, *274*(3–4), 585–593.

[309] D. R. G. Mitchell, G. Triani, D. J. Attard, K. S. Finnie, P. J. Evans, C. J. Barbé, J. R. Bartlett, *Smart Mater. Struct.* **2006**, *15*(1), S57.

[310] E. Yousfi, T. Asikainen, V. Pietu, P. Cowache, M. Powalla, D. Lincot, *Thin Solid Films* **2000**, *361–362*, 183–186.

[311] N. Naghavi, R. Henriquez, V. Laptev, D. Lincot, *Appl. Surf. Sci.* **2004**, *222*(1–4), 65–73.

[312] S. Spiering, D. Hariskos, S. Schröder, M. Powalla, *Thin Solid Films* **2005**, *480–481*, 195–198.

[313] M. Leskelä, M. Ritala, *J. Phys. IV* **1999**, *09*(PR8), Pr8–837–Pr8–852.

[314] N. P. Dasgupta, W. Lee, F. B. Prinz, *Chem. Mater.* **2009**, *21*(17), 3973–3978.

[315] Great Britain, *a practical guide*, Health and Safety Executive (HSE) : [distributor] HSE Books, Merseyside, **2009**.

[316] M. G. Costigan, *Occup. Environ. Med.* **2003**, *60*(4), 308–312.

[317] R. J. Reiffenstein, W. C. Hulbert, S. H. Roth, *Annu. Rev. Pharmacol.* **1992**, *32*(1), 109–134.

[318] A. R. Hirsch, G. Zavala, *Occup. Environ. Med.* **1999**, *56*(4), 284–287.

[319] N. P. Dasgupta, J. F. Mack, M. C. Langston, A. Bousetta, F. B. Prinz, *Rev. Sci. Instrum.* **2010**, *81*(4), 044102.

[320] A. Seidel, editor, *Kirk-Othmer Encyclopedia of Chemical Technology*, Sulfur Compounds: Hydrogen Sulfide, Wiley-Interscience, Hobo-ken, 5 edition, **2007**.

[321] J. Bakke, J. King, H. Jung, R. Sinclair, S. Bent, *Thin Solid Films* **2010**, *518*(19), 5400–5408.

[322] H. H. Li, *J. Phys. Chem. Ref. Data* **1984**, *13*(1), 103–150.

[323] M. Grätzel, *Inorg. Chem.* **2005**, *44*(20), 6841–6851.

[324] A. Patrocínio, L. Paterno, N. Murakami Iha, *J. Photoch. Photobio. A* **2009**, *205*(1), 23–27.

[325] E. Palomares, J. Clifford, S. Haque, T. Lutz, J. Durrant, *J. Am. Chem. Soc.* **2003**, *125*(2), 475–482.

[326] B. Peng, G. Jungmann, C. Jäger, D. Haarer, H.-W. Schmidt, M. Thelakkat, *Coordin. Chem. Rev.* **2004**, *248*(13-14), 1479–1489.

[327] J. Hart, D. Menzies, Y.-B. Cheng, G. Simon, L. Spiccia, *Cr. Chim.* **2006**, *9*(5-6), 622–626.

[328] R. Hattori, H. Goto, *Thin Solid Films* **2007**, *515*(20-21), 8045–8049.

[329] P. Cameron, L. Peter, *J. Phys. Chem. B* **2005**, *109*(15), 7392–7398.

[330] S.-J. Roh, R. S. Mane, S.-K. Min, W.-J. Lee, C. D. Lokhande, S.-H. Han, *Appl. Phys. Lett.* **2006**, *89*(25), 253512.

[331] J. Xia, N. Masaki, K. Jiang, S. Yanagida, *J. Phys. Chem. C* **2007**, *111*(22), 8092–8097.

[332] N. Suzuki, S. Karuppuchamy, S. Ito, *J. Appl. Electrochem.* **2009**, *39*(1), 141–146.

[333] W. Y. Gan, S. W. Lam, K. Chiang, R. Amal, H. Zhao, M. P. Brungs, *J. Mater. Chem.* **2007**, *17*(10), 952–954.

[334] H.-J. Kim, J.-D. Jeon, D. Y. Kim, J.-J. Lee, S.-Y. Kwak, *J. Ind. Eng. Chem.* **2012**, *18*(5), 1807–1812.

[335] S. Ito, P. Liska, P. Comte, R. Charvet, P. Péchy, U. Bach, L. Schmidt-Mende, S. M. Zakeeruddin, A. Kay, M. K. Nazeeruddin, M. Grätzel, *Chem. Commun.* **2005**, (34), 4351–4353.

[336] A. Hagfeldt, M. Grätzel, *Acc. Chem. Res.* **2000**, *33*(5), 269–277.

[337] A. Burke, S. Ito, H. Snaith, U. Bach, J. Kwiatkowski, M. Grätzel, *Nano Lett.* **2008**, *8*(4), 977–981.

[338] V. Shklover, Y. E. Ovchinnikov, L. S. Braginsky, S. M. Zakeeruddin, M. Grätzel, *Chem. Mater.* **1998**, *10*(9), 2533–2541.

[339] S. Ito, S. M. Zakeeruddin, R. Humphry-Baker, P. Liska, R. Charvet, P. Comte, M. K. Nazeeruddin, P. Péchy, M. Takata, H. Miura, S. Uchida, M. Grätzel, *Adv. Mater.* **2006**, *18*(9), 1202–1205.

[340] T. W. Hamann, O. K. Farha, J. T. Hupp, *J. Phys. Chem. C* **2008**, *112*(49), 19756–19764.

[341] K. Miettunen, J. Halme, P. Vahermaa, T. Saukkonen, M. Toivola, P. Lund, *J. Electrochem. Soc.* **2009**, *156*(8), B876–B883.

[342] J. Aarik, A. Aidla, H. Mändar, T. Uustare, *Appl. Surf. Sci.* **2001**, *172*(1–2), 148–158.

[343] I. Chung, B. Lee, J. He, R. P. H. Chang, M. G. Kanatzidis, *Nature* **2012**, *485*(7399), 486–489.

[344] A. Sidorenko, T. Krupenkin, J. Aizenberg, *J. Mater. Chem.* **2008**, *18*(32), 3841–3846.

[345] A. R. Parker, H. E. Townley, *Nat. Nanotechnol.* **2007**, *2*(6), 347–353.

[346] S. Berthier, J. Boulenguez, Z. Bálint, *Appl. Phys. A* **2007**, *86*(1), 123–130.

[347] L. P. Biro, K. Kertesz, E. Horvath, G. I. Mark, G. Molnar, Z. Vertesy, J.-F. Tsai, A. Kun, Z. Balint, J. P. Vigneron, *J. R. Soc. Interface* **2010**, *7*(47), 887–894.

[348] G. S. Butcher, S. Rohwer. In D. M. Power, editor, *Current Ornithology*, number 6 in Current Ornithology, 51–108. Springer US, **1989**.

[349] R. R. Baker, G. A. Parker, *Phil. Trans. R. Soc. Lond. B* **1979**, *287*(1018), 63–130.

[350] T. Guilford, *Am. Nat.* **1988**, *131*, S7–S21.

[351] K. L. Prudic, A. K. Skemp, D. R. Papaj, *Behav. Ecol.* **2007**, *18*(1), 41–46.

[352] P. G. Kevan, H. G. Baker, *Annu. Rev. Entomol.* **1983**, *28*(1), 407–453.

[353] J. P. Vigneron, M. Rassart, Z. Vértesy, K. Kertész, M. Sarrazin, L. P. Biró, D. Ertz, V. Lousse, *Phys. Rev. E Stat. Nonlin. Soft. Matter. Phys.* **2005**, *71*(1 Pt 1), 011906.

[354] P. Vukusic, *Curr. Biol.* **2006**, *16*(16), R621–R623.

[355] S. M. Doucet, M. G. Meadows, *J. R. Soc. Interface* **2009**, *6*(Suppl 2), S115–S132.

[356] M. G. Meadows, M. W. Butler, N. I. Morehouse, L. A. Taylor, M. B. Toomey, K. J. McGraw, R. L. Rutowski, *J. R. Soc. Interface* **2009**, *6*(Suppl 2), S107–S113.

[357] P. Vukusic, J. R. Sambles, C. R. Lawrence, R. J. Wootton, *P. R. Soc. B-Biol. Sci.* **1999**, *266*(1427), 1403.

[358] R. O. Prum, R. H. Torres, S. Williamson, J. Dyck, *Nature* **1998**, *396*(6706), 28–29.

[359] S. Berthier, *Iridescences: The Physical Colors of Insects*, Springer, **2007**.

[360] P. Vukusic, B. Hallam, J. Noyes, *Science* **2007**, *315*(5810), 348–348.

[361] P. Vukusic, J. R. Sambles, C. R. Lawrence, *P. Roy. Soc. Lond. B Bio.* **2004**, *271*(Suppl 4), S237–S239.

[362] V. Sharma, M. Crne, J. O. Park, M. Srinivasarao, *Science* **2009**, *325*(5939), 449–451.

[363] K. Michielsen, H. De Raedt, D. G. Stavenga, *J. R. Soc. Interface* **2010**, *7*(46), 765–771.

[364] M. Crne, V. Sharma, J. Blair, J. O. Park, C. J. Summers, M. Srinivasarao, *EPL* **2011**, *93*(1), 14001.

[365] D. P. Gaillot, O. Deparis, V. Welch, B. K. Wagner, J. P. Vigneron, C. J. Summers, *Phys. Rev. E Stat. Nonlin. Soft. Matter. Phys.* **2008**, *78*(3 Pt 1), 031922.

[366] M. Srinivasarao, *Chem. Rev.* **1999**, *99*(7), 1935–1962.

[367] D. Wang, H. Möhwald, *Adv. Mater.* **2004**, *16*(3), 244–247.

[368] P. Jiang, M. J. McFarland, *J. Am. Chem. Soc.* **2004**, *126*(42), 13778–13786.

[369] X. Chen, Z. Sun, L. Zheng, Z. Chen, Y. Wang, N. Fu, K. Zhang, X. Yan, H. Liu, L. Jiang, B. Yang, *Adv. Mater.* **2004**, *16*(18), 1632–1636.

[370] H. Fudouzi, Y. Xia, *Langmuir* **2003**, *19*(23), 9653–9660.

[371] N. Denkov, O. Velev, P. Kralchevski, I. Ivanov, H. Yoshimura, K. Nagayama, *Langmuir* **1992**, *8*(12), 3183–3190.

[372] X. Zhang, A. V. Whitney, J. Zhao, E. M. Hicks, R. P. Van Duyne, *J. Nanosci. Nanotechnol.* **2006**, *6*(7), 1920–1934.

[373] M. F. Land, *Prog. Biophys. Mol. Biol.* **1972**, *24*, 75–106.

[374] H. Ghiradella, *J. Morphol.* **1974**, *142*(4), 395–409.

[375] M. Kolle. *Photonic structures inspired by nature*, University of Cambridge, **2010**.

Related publications

P. M. S. Cunha♣, M. R. J. Scherer♣, U. Steiner, Ozone surface modification for enhanced atomic layer deposition in polymer templates, in preparation, ♣these authors contributed equally.

P. M. S. Cunha, M. R. J. Scherer, S. Pathak, A. Sepe, Y. Vaynzof, U. Steiner, Gyroid-structured $Cu/Cu_2O/CuO$ core-shell solar cells, in preparation.

P. M. S. Cunha, M. R. J. Scherer, S. Pathak, A. Sepe, U. Steiner, Atomic layer deposition of sub-2nm blocking layers for dye-sensitised solar cells, in preparation.

M. R. J. Scherer, P. M. S. Cunha, U. Steiner, Labyrinth-Induced Faceted Growth, *Science*, **2013**, submitted.

S. Vignolini, N. A. Yufa, P. S. Cunha, S. Guldin, I. Rushkin, M. Stefik, K. Hur, U. Wiesner, J. J. Baumberg, U. Steiner, A 3D Optical Metamaterial Made by Self-Assembly, *Adv. Mater.* **2012**, *24*(10), OP23-OP27.

A. Finnemore, P. Cunha, T. Shean, S. Vignolini, S. Guldin, M. Oyen, U. Steiner, Biomimetic layer-by-layer assembly of artificial nacre, *Nat. Commun.* **2012**, *3*, 966.

M. R. J. Scherer, L. Li, P. M. S. Cunha, O. A. Scherman, U. Steiner, Enhanced electrochromism in Gyroid-Structured vanadium pentoxide, *Adv. Mater.* **2012**, *24*(9), 1217-1221.

M. Kolle, P. M. Salgard-Cunha, M. R. J. Scherer, F. Huang, P. Vukusic, S. Mahajan, J. J. Baumberg, U. Steiner, Mimicking the colourful wing scale structure of the papilio blumei butterfly, *Nat. Nano.* **2010**, *5*(7), 511-515.

E. J. W. Crossland, P. Cunha, S. Scroggins, S. Moratti, O. Yurchenko, U. Steiner, M. A. Hillmyer, S. Ludwigs, Soft-etch mesoporous hole-conducting block copolymer templates, *ACS Nano* **2010**, *4*(2), 962-966.